JOURNAL OF CONDENSED MATTER NUCLEAR SCIENCE

Experiments and Methods in Cold Fusion

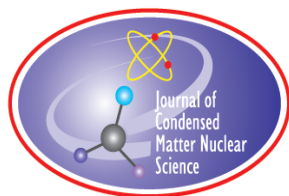# JOURNAL OF CONDENSED MATTER NUCLEAR SCIENCE

Experiments and Methods in Cold Fusion

JOURNAL OF CONDENSED MATTER NUCLEAR SCIENCE

Volume 27, November 2018

JOURNAL OF CONDENSED MATTER NUCLEAR SCIENCE

Volume 27   2018

CONTENTS

PREFACE

RESEARCH ARTICLES

Preface

Are we at the threshold of a major breakthrough in the field of Condensed Matter Nuclear Science? After almost 30 years of work by passionate scientists and a lot of false hopes, maybe, finally we are seeing the light at the end of the tunnel, and it is not an oncoming train! This new volume of the Journal of Condensed Matter Nuclear Science shows the increased interest in the field by theoreticians and experimentalists. It should be noted that there are a variety of ways to consider the phenomenon of Low Energy Nuclear Reactions, indicating that the phenomenon is more general than thought of at the beginning.

Sincerely,

Dr. Jean-Paul Biberian
November 2018

Research Article

Nuclear Metamorphosis in Mercury: Rare Earths Production[*]

F. Cardone[†]

Istituto per lo Studio dei Materiali Nanostrutturati (ISMN- CNR), Via dei Taurini, 00185 Roma, Italy

G. Albertini[‡]

Università Politecnica delle Marche (UNIVPM) Via Brecce Bianche, 60131 Ancona, Italy

D. Bassani

SIDOM S.A .S., Via Volta 34, 12010 Cervasca CN, Italy

G. Cherubini[§] and F. Rosetto

ARPA Radiation and Chemical Laboratories, Via Montezebio,?01100 Viterbo, Italy

E. Guerriero

CNR, Area Ricerca Roma 1, Montelibretti Roma, Italy

R. Mignani[¶]

Università degli Studi "Roma Tre", Dipartimento di Matematica e Fisica – Sezione di Fisica, Via della Vasca Navale 84, 00146 Roma, Italy

Abstract

In two previous papers, we described the equipment and the results of an experiment in which nuclear reactions occurred in a mole of mercury, in a condition of Local Lorentz Invariance breakdown. The elemental analyses performed after the
© 2018 ISCMNS. All rights reserved. ISSN 2227-3123

Keywords: Deformed space–time, Local Lorentz invariance breakdown, Mercury, Nuclear reactions, Rare earths production

(Continuation of Authors and their Affiliations)

M. Monti and V. Sala

STARTEC Srl, Via Libero Grassi, 1 - 23875 Osnago LC, Italy

A. Petrucci, A. Rosada and E. Santoro

Agenzia Nazionale per le nuove Tecnologie, l'Energia e lo Sviluppo Economico sostenibile (ENEA),
Via Anguillarese, 301, 00123 Roma, Italy

F. Ridolfi

Institut für Mineralogie, Leibniz Universität Hannover, Callinstr. 3, D-30167 Hannover, Germany

G. Spera

CRA-IS.Pa. Ve., Chemical Section, Via C. G. Bertero, 22, 00156 Roma, Italy

(continuation of Abstract from page 1) experiment showed the presence of elements which were not part of the set-up before the treatment. However, some of the detected elements were not reported in the results as they needed further analysis. In this final paper, all the elements detected in the above-mentioned experiment are presented along with their concentration measured in the analysed samples. Of particular interest is the presence of some rare earth elements among them.

1. Introduction

In the last few years, Low Energy Nuclear Reactions (LENR) were reported to occur under different experimental conditions. Due to the different methods used to produce these effects, different names were used for them: cold fusion [1,2], piezonuclear reactions [3–6], Condensed Matter Nuclear Science [7] and E-Cat [8]. They have not been widely accepted by the scientific community, mainly because they do not seem to follow the known laws of physics.

Recently, the Deformed Space–Time (DST) theory was suggested [9] as a general theory able to explain the occurrence of all these phenomena.

This theory can be considered as a generalization of General Relativity (GR), which predicts the gravitational interaction as a curvature of space–time. According to the DST theory [10,11], all interactions can deform space–time, thus changing the 4D-metric parameters of the local Minkowskian frame. In this sense, the Riemannian curvature of GR is only a particular case of deformation and not unique [12].

A local deformation of space-time corresponds to a violation of the Local Lorentz Invariance (LLI), which, on the contrary, assumes that space–time is locally isotropic, homogeneous and flat.

Energy [10,11] and energy density [6] in space and in time play a fundamental role in this deformation. Four different energy thresholds were deduced [10,11], each one for each of the four different fundamental interactions, starting from the experimental data collected in experiments specifically dedicated to the study of these interactions: the pure leptonic decay of the meson K_0 short for the weak nuclear interaction; the pion pair production obtained in 1984 by the UA1 collaboration at CERN for the strong interaction; the superluminal propagation of electromagnetic

waves in conducting waveguides with variable section for the electro-magnetic interaction; the relative rates of clocks at different heights in the gravitational field of Earth for the gravitational interaction.

The DST reactions possess three peculiar characteristics: the existence of an energy density threshold to be reached and overtaken, which may also result in a delay of the reaction start; the spatial anisotropy; the time asymmetry and asynchrony, which correspond to the emission of aperiodic intense beams having a very short life-span and different chronological structure rather than continuous emissions of particles.

Besides, in the case of DST nuclear reactions, the absence of gamma radiation has also been always experimentally verified [4,9,19,20] and can be considered as a further signature of the DST nuclear reactions. Some or all of these characteristics have been also reported [9] by several authors in LENR.

Following a previous experiment [13–15], where the anisotropic emission of neutrons from a steel bar subjected to ultrasound was attributed to the LLI breakdown, a new experiment was conceived [16]. The target was to induce the breakdown of LLI in a mole of mercury and hence the initiation of DST nuclear reactions.

The striking result of this experiment consisted in finding in the matrix of mercury chemical elements whose presence had already been excluded by the initial blank analyses. The atomic mass of these elements was both heavier and lighter than that of mercury. This fact is unusual as nuclear fusion reactions usually produce heavier nuclei, but not heavier then iron, while nuclear fission reactions produce lighter nuclei, but not lighter then iron. In this case, on the contrary, reactions could occur in both directions, irrespective of the position with respect to iron.

After 180 s of treatment of the mole of mercury, some solid material appeared floating on top of the still liquid mercury. A thorough and careful elemental analysis of each part of the experimental equipment (initial mercury, container, ultrasound conveying implements, final mercury and of the course the solid material) was carried out by different analytical techniques.

An element of this solid material was considered as a reliable reaction product if it was detected by at least two different techniques and if it was neither present in the initial mercury pool nor in the container nor in the used tools.

This data rejection rate is very severe since an element which does not comply with the requirements above is excluded also when it is present as a different isotope. Besides, it is also excluded even if the element is detected by different investigators in different laboratories if their instruments use the same technique.

A subsequent paper [17] announced the results obtained in a laboratory enabled to release official certification. They confirmed previously reported results.

Due to the stringent requirements adopted to accept an element as a reliable reaction product, several elements and isotopes were discarded and hence not reported in the previous two papers [16,17]. In contrast, for the sake of completeness and in order to gain the global picture of the outcomes collected in this experiment, all the elements and isotopes detected as reaction products, with the only limitation of not being part of the blank, are listed in this paper.

We point out that we are not presenting a new set of experiments confirming the results of those previously reported, but we present new information about the results obtained by analysing the material produced after the previous experiment.

2. Experimental

One mole of mercury (0.2 kg) from SPHERAE SRL (Gorizia, Italy) declared 99.99% pure, was treated making use of the Startec reaction system dedicated to DST reactions and built up according to the patents reported in [16].

Due to the restrictions connected to the patent, the technological details of the reaction system cannot be described here. However, the physics and the scientific details that are the basis of the instrument are reported in Section 1, and are widely discussed in the papers related to DST-theory.

We are aware of this limitation, which is usually not widely discussed in the scientific literature. Nowadays, the distance between Science and Technology is becoming shorter and shorter since the time interval between the scientific

finding and the technological application is shorter than in the past. However, different laws rule the two worlds that, in this sense, are widely separated. We think that respecting the rules of the technological world is a duty of the scientist, so we will just summarize the related patents, without giving details.

The experiment lasted 3 min and was repeated 10 times in one year, between 2012 and 2013. Each time, a solid material formed and was extracted from the remaining liquid phase.

The initial temperature was $20\pm2°$C while the final temperature was $260\pm2°$C. They were measured by infrared thermometer Fluke 68 IR.[a]

In the year 2016, the spatial concentration of energy was slightly modified in three trials although the same source, the same power and the same total energy released to the sample were used. In these cases, no formation of solid material was observed and the temperature increase was smaller ($20\pm2°$C–$80\pm2°$C).

As forecast in the DST-theory, the energy concentration rather than the total energy is of fundamental importance. In these cases, the necessary conditions to create the LLI breakdown were not attained and the DST-reactions did not occur. For this reason, the corresponding three samples were not further considered.

In the first instance, the composition of the formed solid phase was analysed together with some residual part of Mercury. In the second instance, before analysing this material, it was heated at $400°$C in Nitrogen flux inside a Pyrex container (the so-called stripping procedure), with the aim of eliminating mercury.

The latter procedure, however, also eliminated other elements. In particular, Bromine was detected by three different techniques in the first step while it was not detected in the second one.

The composition of solid material was investigated by using different techniques in different Italian institutions:

- Inductively coupled plasma optical emission spectroscopy (ICP-OES).

Instrument: Perkin Elmer optical emission spectrometer OPTIMA 8300/at Università Politecnica delle Marche – Ancona (UNIVPM).

- Inductively coupled plasma mass spectroscopy (ICP-MS).

Instrument: Thermo Fisher X series II/at National Council for Researches, Rome (CNR).

- ICP-MS.

Instrument: Perkin Elmer OPTIMA 2100 DV/at CNR.

- ICP-MS.

Instrument: Agilent 7005C octopole reaction system/at CNR.

- Environmental scanning electron microscopy with energy dispersive spectroscopy (ESEM+EDS).

Instrument: FEI Quanta 200/at University of Urbino.

- ESEM+EDS.

Instrument: LEO 1450 VP LAIKA Cambridge at Università di Roma 1 – Rome.

- Scanning electron microscopy with energy dispersive spectroscopy (SEM+EDS).

Instrument: FEI x120 with EDAX ECON 4 EDS/at UNIVPM.

---

[a]By the way, in a previous paper [16] it was erroneously quoted as model 69.

- Scanning electron microscopy (SEM).

Instrument: SEM Cambridge Stereoscan 250 MK3/at ENEA-Rome.

- X-ray fluorescence (XRF).

Instrument: Spectro x-Lab2000/at CNR.

- Instrumental neutron activation analysis (INAA).

Instrument: Gamma detector with high purity Ge by ORTEC (HPGe ORTEC) at nuclear reactor TRIGA Mark II-upgrade/at ENEA- Casaccia.

These techniques were also used to determine the elemental composition of the blank: mercury from the initial pool; pieces of the vessel containing the mercury in the reaction device; parts of the tools in contact with mercury inside the device; parts of the same tools not in contact with mercury.

Further analyses [17] were performed at the CAIM laboratory (Follonica – Grosseto, Italy), accredited by Accredia as lab.#0437. In fact, International agreements ensure the validity and credibility of accreditation as an effective instrument of qualification of operators and of conformity assessment on the European and world market. They used the standard method UNI EN 13656:2004, which defines the mineralization of a solid sample, necessary before feeding it into an analytical device, by using a microwave digestion system (in this case: mineralization system Ethos 1 - Advanced Microwave Digestion System), and the standard method UNI EN ISO 17294-2:2005, which describes the instrumental measurement of metals by using ICP-MS (in this case: model 7700 – Agilent Technologies).

3. Results

As explained in the introduction, only the elements that were detected by two different techniques, and that were not among the elements of the blank, were considered reliable reaction products. These are reported in [16]. Further results satisfying less stringent conditions were also reported in [17], as explained in Section 2.

Both data are gathered in the second column of Table 1. On the other hand, the results relevant to the present paper can be found in the third column of the same table. This column contains a list of elements or isotopes that had been detected but were not reported in the previous works, due to the severe conditions imposed on the determination of the suspected reaction products.

When allowed by the detecting technique (INAA or ICP-MS), the isotopes of the elements are reported in the table. In this case, the position of the isotope by natural abundance on the Earth is also indicated. The concentration of the reported isotope can be evaluated from that measured of the corresponding element by considering the natural abundance.

The fifth column of Table 1 shows the techniques by which the element or isotope was detected.

Calcium (^{43}Ca) was also detected among the products. However, it is not reported in Table1, as it is usually considered ubiquitously present.

4. Discussion

Ninety are the natural elements on the Earth: among them, 19 were excluded from the reaction products because they were present in the devices and original mercury pool; 11 are gaseous at room temperature and pressure and thus could not be detected in our experimental conditions. Among the remaining 60 elements, Table 1 shows that 28

Table 1. Reaction products of the DST-reactions in mercury ordered by atomic number Z. The elemental concentrations in column 4 is related to the analysed sample, not the whole mole of mercury. In bracket, isotope position by natural abundance on the Earth: 1st, 2nd, 3rd, ... isotope; mono represents naturally monoisotopic element on the Earth.

Z	Element/isotope in [16,17]	Other detected element/isotope	Elemental concentration	Detecting techniques
3	^{7}Li (1st)		0.40±0,05 ppb	ICP-OES ICP-MS
4		^{9}Be (mono)	0.004 ± 0,001 ppb	ICP-MS
22	^{47}Ti (3rd)		7800 ± 800 ppm	ICP-OES ICP-MS ESEM
23	^{51}V (1st)		0.10 ± 0,03 ppb	ICP-MS INAA
27	^{59}Co (mono)		34 ± 2 ppm	ICP-OES, INAA XRF
28	^{58}Ni (1st)		186 ± 20 ppm	ICP-OES INAA XRF ICP-MS
31	^{69}Ga (1st) ^{71}Ga (2nd)		84 ± 10 ppm	ICP-MS XRF INAA
32		Ge	2780 ± 300 ppm	XRF
34	^{78}Se (2nd) ^{82}Se (4th)		240 ± 25 ppm	ICP-MS XRF
35	^{79}Br (1st)		77 000 ± 5000 ppm	ESEM INAA XRF
37		Rb	335 ± 35 ppm	XRF
39		^{89}Y (mono)	56 ± 8 ppm	ICP-MS INAA
42		^{95}Mo (3rd) ^{98}Mo (1st)	1113 ± 3 ppm	ICP-MS INAA
48		^{111}Cd (3rd)	6 ± 2 ppm	ICP-MS XRF
49		^{113}In (2nd)	10820 ± 120 ppm	INAA
50	^{118}Sn (2nd) ^{124}Sn (6th)		6 ± 0.6 ppm	ICP-MS INAA XRF
51		^{121}Sb (1st) ^{123}Sb (2nd)	0.30 ± 0.13 ppm	ICP-MS INAA
58	^{138}Ce (3rd) ^{140}Ce (1st)		34.5 ± 4,0 ppm	INAA ICP-MS
63		^{151}Eu (2nd)	31 ± 7 ppb	INAA
64		^{152}Gd (7th) ^{158}Gd (1st)	417 ± 17 ppm	INAA
70		^{174}Yb (4th)	57 ± 24 ppm	INAA
71		^{176}Lu (2nd)	141 ± 37 ppm	INAA
72	^{177}Hf (3rd)		450 ± 50 ppm	INAA XRF
75		^{185}Re (3rd)	30 ± 3 ppm	INAA
78		^{190}Pt (6th) ^{195}Pt (1st) ^{196}Pt (3rd)	1332 ± 9 ppm	INAA ICP-MS INAA
79	^{197}Au (mono)		0.07 ± 0,01 ppb	ICP-MS INAA
90	^{232}Th (mono)		35 ± 5 ppm	INAA XRF
92	^{238}U (1st)		114 ± 20 ppm	ICP-MS XRF

are considered reaction products. Calcium could have also been counted in, as it was only detected in the produced material.

Beside the ability of DST-reactions to produce both lighter and heavier nuclei from those of the starting material, as already remarked in previous works [16,18], it is also interesting to note that six of the 17 rare earths[b] were also detected in the formed material: yttrium, cerium, europium, gadolinium, ytterbium and lutetium. This fact could be the starting point for a new way to produce them, thus also eliminating the troubles related to their supply.

Among the 31 elements that were not found, the absence of caesium is particularly important, as it is a harmful product of other nuclear reactions.

A quantitative prediction of the reaction products in a single experiment is not yet possible. In fact, the elements of Table 1 were found inside the solid material obtained from one run. In this sense, the reported uncertainty concerns only the investigated amount of produced material and is not obtained over different runs.

Moreover, the primary reactions, supposed to occur in conditions of LLI breakdown, could produce elements that, in turn, produced other elements in secondary reactions. These last could either occur in condition of LLI breakdown or in accordance with the LLI.

We can thus argue that, although the control of the conditions producing DST-reactions is attained in this experiment, a fine determination of the reaction paths would require long systematic investigations, which now are out of the aims of our study.

In any case, the DST nuclear reactions, which have also been observed to occur without concomitant dangerous gamma emissions [4,9,19,20], appear to be very promising both from a fundamental and an applicative point of view.
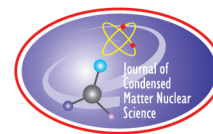
Finally, we remark that the occurrence of nuclear reactions in mercury subjected to some kind of stress was also reported by other authors (see [21,22] and references therein). Similarly to our case, those investigations can be classified as "LENR in mercury" due to the types of reactions and the characteristics of the experimental apparatus.

References

[1]   M. Fleischmann, S. Pons and M. Hawkins, Electrochemically induced nuclear fusion of deuterium. *J. Electroanal. Chem.* **261**(2A) (1989) 301–308. doi:10.1016/0022-0728(89)80006-3, and errata in Vol. 263.
[2]   M. Fleischmann, S. Pons, M.W. Anderson, L.J. Li and M. Hawkins, *J. Electroanal. Chem.* **287** (1990) 293.
[3]   F. Cardone, G. Cherubini and A. Petrucci, Piezonuclear neutrons, *Phys. Lett.* A **373** (2009) 862–866.
[4]   F. Cardone, G. Cherubini, R. Mignani, W. Perconti, A. Petrucci, F. Rosetto and G. Spera, Neutrons from piezonuclear reactions, *Annales de la Fondation Louis de Broglie* **34** (2009) 183 and arXiv:0710.5115 (physics.gen-ph).
[5]   F. Cardone, V. Calbucci and G. Albertini, Possible evidence of Piezonuclear alpha emission, *J. Adv. Phys.* **2**(1) (2013) 20–24, doi: http://dx.doi.org/10.1166/jap.2013.1029.
[6]   F. Cardone, V. Calbucci and G. Albertini, Deformed space time of the piezonuclear emissions, *Mod. Phys. Lett.* B **28** (2) (2014), DOI: 10.1142/S0217984914500122.
[7]   Jean-Paul Biberian, Condensed matter nuclear science (cold fusion): an update, *Int. J. Nucl. Energy Sci. Technol.* **3** (1) (2007) 31.
[8]   G. Levi, E. Foschi, B. Höistad, R. Pettersson, L. Tegnér and H. Essén, Observation of abundant heat production from a reactor device and of isotopic changes in the fuel, 2014.
           http://www.sifferkoll.se/sifferkoll/wpcontent/uploads/2014/10/LuganoReportSubmit.pdf .
[9]   G. Albertini and D. Bassani, Deformed space–time reactions and their phenomenology, *Phys. J.* **1** (3) (2015) 382–387.
[10]   F. Cardone and R. Mignani (Eds.), *Energy and Geometry*, World Scientific, Singapore, 2004.
[11]   F. Cardone and R. Mignani (Eds.), *Deformed Space–time*, (Ed.), Springer, Dordrecht, The Netherlands. ISBN 978-1-4020-6282-7 (HB) ISBN 978-1-4020-6283-4 (e-book) (2007).

---

[b]If one considers scandium and yttrium too as rare earths.

[12] Gianni Albertini, Domenico Bassani and Fabio Cardone, Two questions about a non-flat nuclear space-time, *Eur. Phys. J. Plus* **133** (2018) 39. DOI 10.1140/epjp/i2018-11871-9.

[13] A. Petrucci, A. Rosada and E. Santoro, Asymmetric neutron emissions from sonicated steel, *Mod. Phys. Lett*. B **29** (2015) 1550067. DOI: http://dx.doi.org/10.1142/S0217984915500670.

[14] A. Petrucci and A.Rosada, Ultrasonic neutron emissions, *J. Adv. Phys.* **5** (2016) 63–68.

[15] F. Cardone, G. Cherubini, M. Lammardo, R. Mignani, A. Petrucci, A. Rosada, V. Sala and E. Santoro, Violation of local Lorentz invariance for deformed space–time neutron emission, *Eur. Phys. J. Plus* **130** (2015) 55. doi:10.1140/epjp/i2015-15055-y.

[16] F. Cardone, G. Albertini, D. Bassani, G. Cherubini, E. Guerriero, R. Mignani, M. Monti, A. Petrucci, F. Ridolfi, A. Rosada, F. Rosetto, V. Sala, E. Santoro and G. Spera, Nuclear metamorphosis in mercury, *Int. J. Mod. Phys*. B **29** (2015) 1550239. DOl: 10.1142/S0217979215502392.

[17] F. Cardone, G. Albertini, D. Bassani, G. Cherubini, E. Guerriero, R. Mignani, M. Monti, A. Petrucci, F. Ridolfi, A. Rosada, F. Rosetto, V. Sala, E. Santoro and G. Spera, Deformed space–time transformations in mercury, *Int. J. Mod. Phys*. B **31** (2017) 1750168. DOI: 10.1142/S0217979217501685.

[18] Gianni Albertini and Riccardo Capotosto, Deformed space–time reactions: towards nuclear metabarysis, *J. Adv. Phys.* **5** (2016) 84–89.

[19] F. Cardone, R. Mignani, M. Monti, A. Petrucci and V. Sala, Piezonuclear neutrons from iron, *Mod. Phys. Lett.* A **27** (18) (2012).

[20] Gianni Albertini, Fabio Cardone, Monica Lammardo, Andrea Petrucci, Filippo Ridolfi, Alberto Rosada, Valter Sala and Emilio Santoro, Atomic and isotopic changes induced by ultrasounds in iron, *J. Radioanal. Nucl. Chem*. **304** (2) (2015) 955–963. DOI: 10.1007/s10967-014-3341-5. ISSN 0236-5731 (print), 1588-2780 (on-line-2014).

[21] C.D. West, 2000 Report Oakridge Nat. Lab. – Cavitation in a Mercury Target, 2000. http://web.ornl.gov/~. webworks/cpr/rpt/108523_.pdf. DOI: 10.2172/ 885870.

[22] F. Moraga and R.P. Taleyarkhan, Static and transient cavitation threshold measurements for mercury, in *Proc. 3rd Int. Topical Meeting on Accelerator Applications (AccApp '99)*, Long Beach, California, 1999, pp. 301–307.

Research Article

Improved Stability and Performance of Surface-Modified Constantan Wires, by Chemical Additions and Unconventional Geometrical Structures

Francesco Celani[∗], B. Ortenzi, S. Pella and A. Spallone[†]

INFN-LNF, Via E. Fermi 40, 00044 Frascati (RM)-Italy

G. Vassallo[‡], E. Purchi, S. Fiorilla, L. Notargiacomo, C. Lorenzetti, A. Calaon, A. Spallone[§], M. Nakamura, A. Nuvoli, P. Cirilli and P. Boccanera

International Society for Condensed Matter Nuclear Science (ISCMNS-UK); Via Cavour 26, 03013 Ferentino (FR), Italy

Abstract

At INFN-LNF, starting in 2011, we have investigated the behavior of the Constantan (Cst) alloy ($Cu_{55}Ni_{44}Mn_1$; ISOTAN44) with hydrogen and/or deuterium (H_2/D_2) absorption and the generation of anomalous excess heat (AHE) at high temperatures (i.e. $>200°C$). To further improve the intrinsic, excellent catalytic proprieties of Cst in $H_2 \rightarrow 2H$ dissociation, we subjected the surface to repeated cycling of "flash" oxidation (pulsed power up to 20 kVA/g), obtaining sub-micrometric particles of *mixed composition* ($Cst–NiO_x–CuO_y–Cu_xNi_yO_z$) and reducing deleterious self-sintering problems with nano-materials at high temperatures. Despite the fact that results with thin, long wires ($\Phi = 200\ \mu m$, $l = 100$ cm) were generally positive and excess power (10–20%) was frequently recorded (5–10 W at 50 W input), reproducibility remained unsatisfactory. Later, we realized that iron impurities (up to 1% in the old, pre-1970 batch of Cst) enhanced AHE generation, especially at $T > 500°C$. Since 2014, we added $Fe(NO_3)_3$ solutions both to the Cst sub-micrometric surfaces (during flash oxidation process),and to borosilicate glass sheaths (SIGI-Fabier; micrometric fibers, previously wetted-dried with $Sr(NO_3)_2$ solution) where wires were inserted (as electrical (continue on p.10)
© 2018 ISCMNS. All rights reserved. ISSN 2227-3123

Keywords: Anomalous Excess Heat (AHE); Electro-migration phenomena, H_2 and/or D_2 absorption at high temperatures into Constantan, $H_2 \rightarrow 2H$ dissociation by Constantan, High-temperature H storage into Fe, Low working function materials, Spontaneous voltage generation along hydrogen-absorbing wires, Surface-modified Cu–Ni–Mn alloy

[∗]Corresponding author. E-mail: franzcelani@libero.it. Also at: International Society for Condensed Matter Nuclear Science (ISCMNS-UK); Via Cavour 26, 03013 Ferentino (FR), Italy.

[†]Also at: International Society for Condensed Matter Nuclear Science (ISCMNS-UK); Via Cavour 26, 03013 Ferentino (FR), Italy.

[‡]Also at: Department of Ind. and Dig. Innov., Univ. of Palermo - Viale delle Scienze 90128 Palermo (PA)-Italy.

[§]Also at :INFN-LNF, Via E. Fermi 40, 00044 Frascati (RM)-Italy.

insulation). Recently, we adopted the methodology of making several knots along wires (holes 150–200 μm), later coated multiple times with an iron solution. We introduced potassium into the solution (which is known as a promoter of iron catalytic performance) and, eventually, manganese to prevent or decrease potassium evaporation. H^+ electro-migration, due to large current (>2 A) flowing along the Cst wires as well as high magnetic fields at the center of the knots and on iron micro-particles (absorbing hydrogen at high temperatures) deposited inside micro-holes of Cst, is supposed to play a role in AHE. The cylindrical thick-glass wall reactor had a volume of 250 cm^3; operating pressures were 0.1–3 bar; the gases used were helium (for calibration), D_2, pure or mixed with xenon (which has ultra-low thermal conduction). In a difference from our previous experiments, we employed *only* D_2 and not H_2. The three wires we used were: platinum for calibration purposes and "indirect heating" of Cst wires, and Cst with 41 and 71 knots. Input power range was 10–90 W. Up to now we have observed that the AHE, measured at the external wall of the reactor, reached the largest values (over 85 W, by *comparison/extrapolation* with platinum under helium, isoperibolic procedure) when the highest input power (90 W) was applied to the 71-knots Cst in D_2 *mixed with xenon*. Further work is necessary to evaluate the effects of: I versus J, numbers of knots, gas mixtures, temperature (including electron emission from SrO: inspired by Iwamura's experiments**,** and the Richardson law).

1. Introduction

The main motivations for our new experimental work were as follows.

(1) Improving the reproducibility of results after realizing (in 2014) that some iron impurities in the main material (Constantan, an alloy with composition $Cu_{55}Ni_{44}Mn_1$, brand name ISOTAN44 from Isabellenhutte) and potassium (at low concentration, about 10% atomic in respect to Fe), are crucial to get positive results.

(2) Increasing the amount of the Anomalous Heat Effect (AHE) previously (2011) detected by our group using the Constantan (Cst) with its surface modified (sub-micrometric shape) and exploring the role of wire knots.

(3) Further studying the spontaneous anomalous voltage and current detected along wires once they absorbed hydrogen or deuterium.

Aside from other effects, AHE is mainly due to the interaction of hydrogen (H_2) or deuterium (D_2) gas absorbed and/or adsorbed by the Cst itself and/or on host sites, by enhancing the effect of nanostructures (pioneered by Y. Arata), under forced *non-equilibrium conditions*, even local, of any type. Up to now, the following phenomena leading to non-equilibrium conditions have been explored in the LENR field: electrical (everybody); thermal (everybody); hydrogen or deuterium electro-migration (F. Celani); deuterium flux (Y. Iwamura); magnetic; laser (Cravens and Letts; L. Holmlid and S. Olafsson; others); radiation stimulation (several); ultrasound (R. Stringham); fractures (A. Carpinteri [1]); nano-magnetism and energy localization (Brian Ahern); femto-chemistry (F. Celani); etc.

We note that in our experience, the AHE origin and process with Cst is similar to that with palladium. Nevertheless, Cst has the advantages of a significantly lower cost and higher robustness; in fact, AHE was still present after months of experiments and after repeatedly cycling the wires between several hundred degrees Celsius and room temperature. Unfortunately, we also observed that the catalytically active surface tends to become less effective upon exposure to high temperatures under vacuum or in the presence of an inert gas, probably due to sintering and loss of the key nanostructured surface produced by current pulses during wire preparation.

As described in our previous reports, we selected Cst because of its catalytic activity in hydrogen dissociation [2], providing around 3 eV for the dissociation of H_2 (or molecular deuterium, D_2) from molecular to atomic state ($H_2 \rightarrow 2H$). We typically used Cst in the shape of long ($l =100$ cm) and thin ($\Phi = 0.2$ mm) wires, with weight 278 mg. Their surface was made sub-micrometric (some particles have dimensions less than 200 nm, see SEM in Fig. 10) by means of high-peak power and electric-thermal treatments: the typical energy was as large as 600–1000 J/g of Cst and produced several hundred times by pulses with a width of 50 ms [3]. Because of such powerful, fast rise/fall times

(<1 μs) and short duration pulses, the wires incandesce in red (indicating a temperature of about 800–900°C), oxidize in some milliseconds of time and rapidly quench at the end of the pulse. In air, the oxidation conditions vanish at about 600°C. The energy density (J/g) is evaluated assuming no *skin effects*, but the effective density is larger. For some aspects the flash oxidation we developed is similar to the "explosive" preparation procedure adopted for production of nanomaterials, because of the formation of craters at the surfaces.

The procedure we developed resembles the highly sophisticated, melt-spinning and quenching procedure adopted and optimized by Prof. Yoshiaki Arata and other groups (Osaka and Tohoku University, Japan) since 1995, to produce nano-powders of Pd and Pd–Zr in the field of Solid State Fusion (the name given to LENR by Prof. Arata) [4]. We were inspired by this procedure and modified it for the use with wires.

In previous successful experiments, after prolonged cycling at high-low temperatures, under H_2 gas at high temperature, the SEM of the wires showed the presence of fracturing phenomena due to hydrogen embrittlement: the typical dimensionality of the particles was *smaller* with respect to an untreated sample used as reference, then, a useful effect.

2. Description of Experimental Set-up: Some Key Details

The experimental set-up is basically similar to that developed and published since 2011 [3]. In addition, we performed several modifications to the wire geometry with the introduction of knots and adopted a new procedure for the chemical impregnation of the borosilicate glass sheaths. In the following, we describe only the most recent set-up (started on 20/05/2016, and still in operation). We used only D_2, not H_2. D_2O was also employed in the preparation of the solution for impregnating the sheaths and coating the knots. It is possible that some residual hydrogen is coming both from HNO_3 used for preparing iron nitrate and from water adsorbed by the hygroscopic glass sheaths (when assembling the reactor). From the isotopic point of view, H_2, HD, D_2 will be present, at different concentrations. The amount of radioactive tritium, i.e. tritiated water (T_2O) in the heavy water (D_2O) that we used is quite low: measurements by Liquid Scintillation Counting (LSC) gave values <250 dpm/ml (disintegrations per minute/milliliter), i.e. <4 Bq/ml. The half-life of T, a β emitter, is 12.3 years and its specific activity (in the gas phase at *RT*) is 3.6×10^{14} Bq/g. Local internal excitation by β-radiation (end point at 18.59 keV) appears unlikely. For radiation stimulation we used a weak (10 kBq), γ-source (decay of natural Th^{232}, sintered with tungsten, i.e. usual TIG electrodes used for welding), well enclosed inside a thick SS cylinder, just positioned outside the wall of the glass reactor.

The overall system, which is quite complex and was developed using several unconventional procedures, is based on the following features and facts:

(1) Thick wall (3 mm) borosilicate glass tube (Schott-Duran, further processed by glass blowers Spaziani Rolando Srl), $l = 25$ cm, $\Phi = 32$–40 mm. Gas pressures: vacuum, pressurized. The maximum pressure depends on glass temperature for safety limits: e.g. <3 bar ABS at 300°C of glass-tube wall temperature.

(2) Platinum wire (usually $l = 100$ cm; $\Phi = 100$ μm). In this specific experiment $l = 102.5$ cm. Platinum has multi-purpose uses: 1) power calibration of the system using inert gas (He); 2) indirect heating of the Cst wires; 3) evaluation of mean wire temperature (i.e. platinum used also as thermometer).

(3) Two Cst wires, $\Phi = 200$ μm. One with 41 knots, the other with 71 knots nominal. The initial length (without knots) were 113 and 127 cm. After tying the knots, the length was reduced to 102.5 and 108.5 cm. During assembly, the length of all wires was equalized to 102.5 cm: the number of knots in the 71-knot wire was reduced to 65. (Because of the previous convention in our log-book, we kept the identification "Cst71.")

(4) Usually, one wire is polarized and the other is left unconnected and used to measure the so-called "spontaneous voltage" (using a high-resolution Fluke 187 multimeter) or current (with a 2-Ω shunt resistance in the milliampere range). The current is limited only by the internal resistance of the wire (about 17–21 ?). The resistance decreases when D_2 is absorbed, similarly to previous (2011–2012) experiments with H_2.

Reactor assembly

Fig. 1

1) Wire weighting
2) Manufacture wide knots

Constantan wire

Fig. 2

3) Insertion 0.21 mm copper wires

4) Pull slightly (the Constantan wire) every four knots while oscillating, until the knots are firmly closed around the copper wires

Fig. 3

5) Remove the copper wires
6) High power conditioning and repeated filling into the knots by Fe-K-Mn
7) Insert the Constantan wire into the borosilicate sheath

Pin (connected through the Macor insulator of the support)

Fig. 4

Borosilicate sheath (Ø 1 mm) impregnated by Sr, Fe-K-Mn

Constantan

Alumina sheath (Ø 2 mm)

Copper retainer

Fig. 5

8) Insert the complete wire into the alumina sheath
9) Crimp terminals
10) Make braid
11) Insert braid in 12 mm sheath
12) Wave the braid around the S.S. support

Figure 1: Preparation of the knots in the Constantan wire.

Figure 2: Insertion of the copper wires in order not to completely tighten the knot.

Figure 3: Critical point of tightening the node due to possible stress of the Constantan wire.

Figure 4: After conditioning, insertion of the wires inside the several glass sheaths.

Figure 5: Braid of the three wires to be weaved around the SS support.

(5) Each wire is inserted inside a borosilicate glass multi-filamentary flexible sheath (made by SIGI & Favier) with $\Phi = 1$ mm. Each porous filament has a diameter of 5 μm. The weight of the 1-mm diameter sheath, after burning the oil used to produce the texture of fibers by SIGI, is 1.9135 g/m. Each fiber is immersed in $Sr(NO_3)_2$ solution (made by us, starting from decomposition of $SrCO_3$ by 65% HNO_3 and diluted by D_2O).
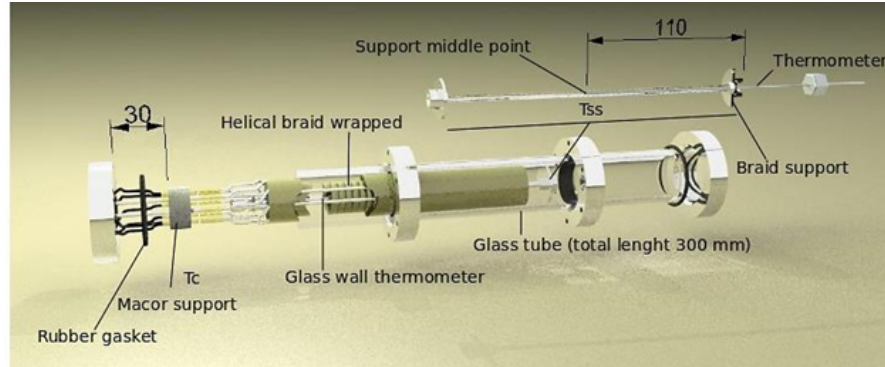
Figure 6. Overview of the reactor once assembled. Regarding temperatures, T_c is external, T_{ss} is internal to the reactor core.

After drying/heating (to 400°C) and the partial dissociation of $SrNO_3$ to SrO (a low work function material for electron emission, similar to CaO used by Yasuhiro Iwamura since 2000, [5] and references therein), the weight increases 44 mg per each meter of wire.

(6) Our conjecture is that SrO, at nanometric size, could have a work function (W) even lower than the value usually reported (about 2.1 eV), similarly to what happens when using cesium [6]. According to this hypothesis, large electron emissions may occur at significantly smaller temperatures (i.e., 500°C instead of the usual 800–900°C) than those enabling emissions from low work function metals (generally mixtures of Ba, Sr, Ca oxides used in vacuum tubes). The electron emission in vacuum follows the well-known law developed by Owen Willans Richardson:

$$J = A_C T^2 \exp\left(-\frac{W}{k_B T}\right),$$

where J is the current density (A/m^2), $A_C = \lambda_r A_0$ a constant with λ_r usually 0.5 and $A_0 = 4\pi m_e k_B^2 e/h^3 = 1.2017 \times 10^6$ A m^{-2} K^{-2}, T the absolute temperature (Kelvin); m_e the electron mass ($9 \times 10^9 \times 10^{-31}$ kg), e the electron charge (1.602×10^{-19} C), k_B the Boltzmann constant (1.38×10^{-23} J K^{-1}), and h is the Planck constant (6.626×10^{-34} J s).

(1) We had seen indications since 2013 that the glass sheaths can play a key-role in the whole reaction [7] and Reference 4 therein), also following the very detailed work of Irving Langmuir on hydrogen absorption on glass bulb surfaces ($H_2 \rightarrow 2H$ dissociation by tungsten filament at $T > 2000$ K). Accordingly, the multi-filamentary borosilicate sheaths could absorb huge amounts of H/D just because of the extremely large values of surface (over 10^4 cm^2 for each sheath covering the wire) and its favorable geometry, being almost in contact with the Cst that dissociates the molecular H_2/D_2 to atomic H/D.

(2) *NEW PROCEDURE.* Three wires are inserted into sheaths, and then immersed in a solution of $Fe(NO_3)_3 + KMnO_4$ in D_2O. The atomic ratio of Fe:K–Mn is 10:1. Potassium is used as a "promoter" of activation for the absorption or desorption reactions of H/D by Fe_xO_Y (mixed oxides, like FeO, Fe_2O_3, Fe_3O_4), similarly to the Cst dissociation properties. Hydrogen is adsorbed inside the iron lattice at high temperatures
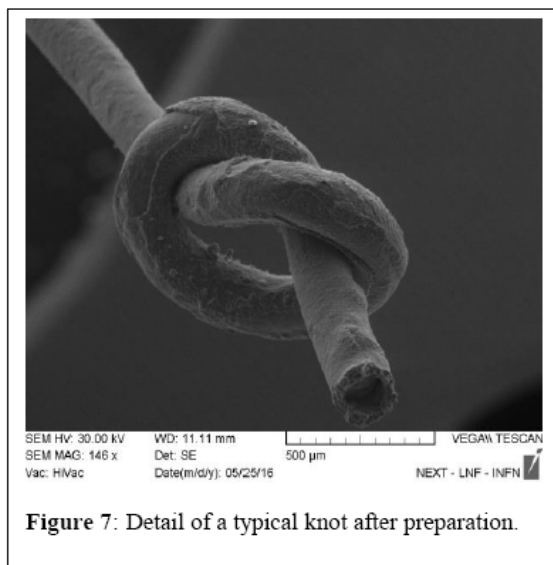
Figure 7: Detail of a typical knot after preparation.
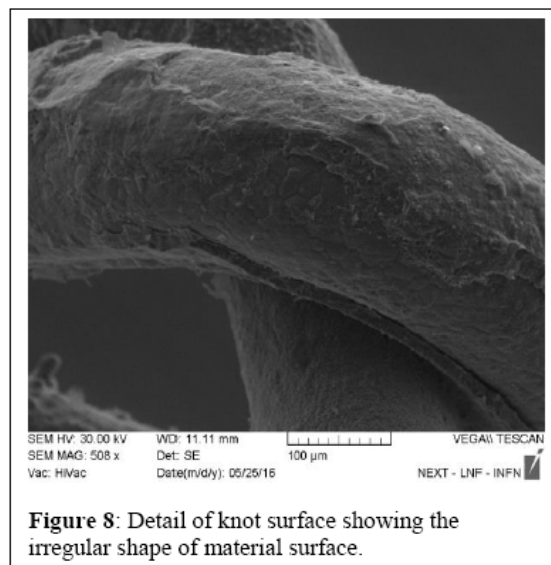
Figure 8: Detail of knot surface showing the irregular shape of material surface.
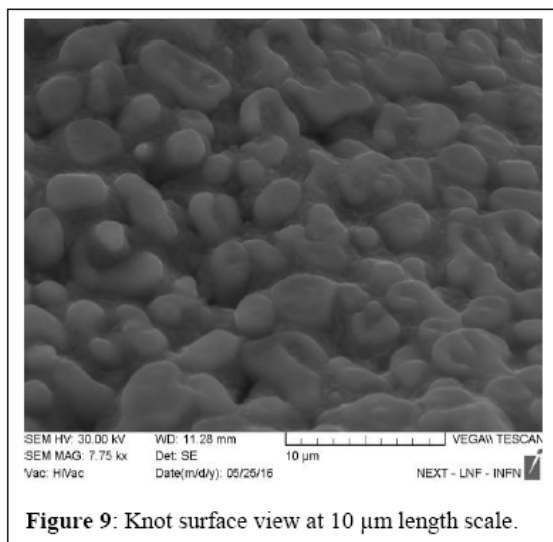
Figure 9: Knot surface view at 10 μm length scale.
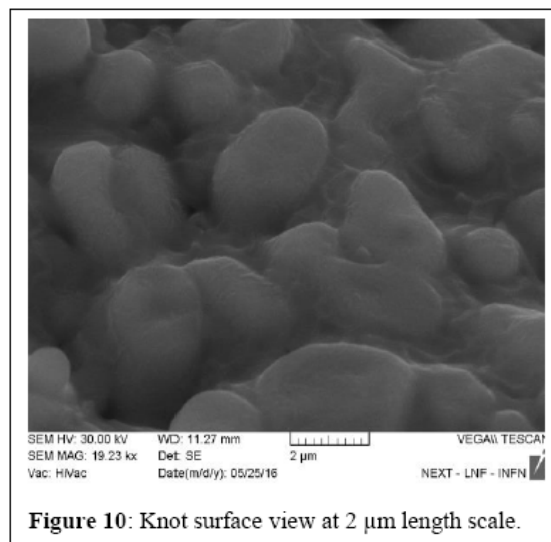
Figure 10: Knot surface view at 2 μm length scale.

Figures 7–10.

($> 500°$C). Manganese is mainly used to reduce potassium "evaporation", keeping the reactivity of Fe–K quite stable over time [8].

(3) In separate tests, we measured an increase of 10–20 mg/m of weight of sheaths due to $Fe_{10}K_1Mn_1O_x$ deposited on the fiber surface, after drying and the partial decomposition of nitrate and the (partial) oxidation at 500°C. The glass sheaths are mechanically stable up to about 60°C.
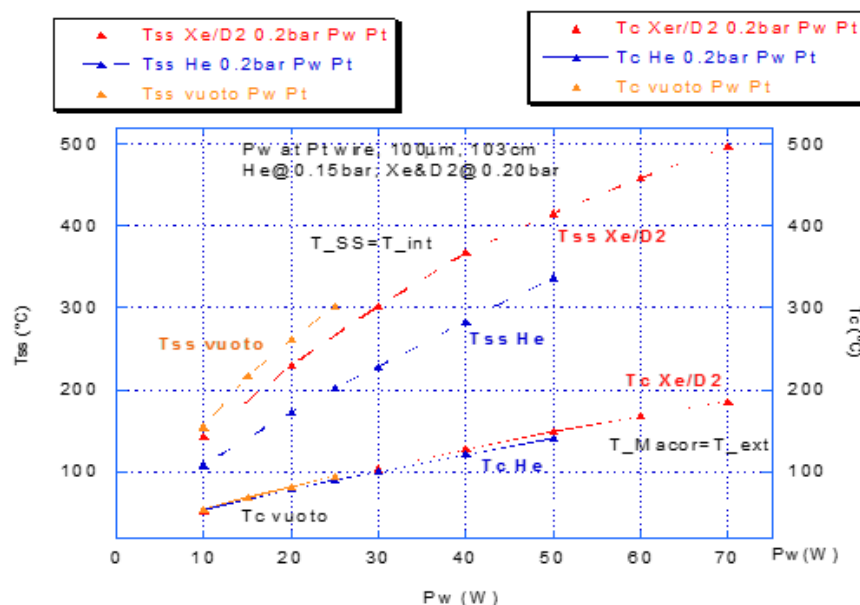
Figure 11.

(4) After drying/heating at 500°C, the glass sheath is inserted into another sheath ($\Phi = 2$ mm), consisting of Al_2O_3, able to withstand without self-damaging, up to 1200°C in continuous operations: avoiding dispersion of glass sheaths (at $T > 650$°C) FeKMn, Cst mixed-composition surface, improved electrical insulation.

(5) The three sheaths were closely braided around each other (Fig. 5) and inserted inside another sheath of 12 mm diameter, which provides mechanical stability and further thermal homogeneity.

(6) At their ends, the sheaths are rolled up around the SS tube ($\Phi = 4$–2 mm) central support (covered by a glass sheath). To reduce the problem of sulfur content of AISI 304 ($<0.015\%$), all the SS materials were conditioned at 700°C several times: cleaned with acid etching and ultrasound. Sulfur is usually deleterious to catalysts.

(7) A K-type thermocouple (made gas tight with a SS sheath) is inserted inside the SS tube to measure the inner temperature of the reactor ("T_{ss}" nomenclature in the following).

(8) The three wires are interconnected to external ambient using a MACOR® cylinder ($\Phi = 7$–24 mm) inside the reactor: it is heavy (10 g). Aside from the central hole (4 mm) there are other eight small holes ($\Phi = 1.6$ mm, like the cylinder of a revolver). The MACOR® cylinder is not in direct contact with the main glass-tube wall: there is a 5 mm gap. An overview of the reactor, with MACOR location and the key thermometers, is shown in Fig. 6.

3. Procedure for Wire Preparation: Some Details

The steps of wire preparation procedure, which is quite elaborate, is detailed in Figs. 1–5.

In Fig. 1, steps 1, 2, we show the initial procedure, i.e. accurate weighing of the wire and tying of knots.

In Fig. 2, step 3, we detail the insertion of the copper wire ($\Phi = 0.21$ mm, gold color), in reference to the "*main hole*" see also steps 5 and 6 in Fig. 3.

In Fig. 3, we describe steps 4 and 5 for "locking" the reference copper wire without causing too large stress in the
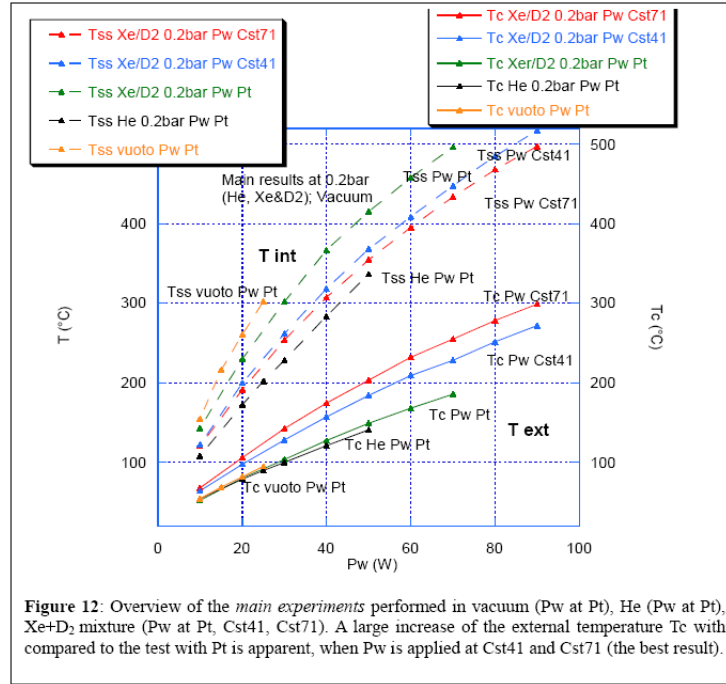
Figure 12: Overview of the *main experiments* performed in vacuum (Pw at Pt), He (Pw at Pt), Xe+D_2 mixture (Pw at Pt, Cst41, Cst71). A large increase of the external temperature Tc with compared to the test with Pt is apparent, when Pw is applied at Cst41 and Cst71 (the best result).
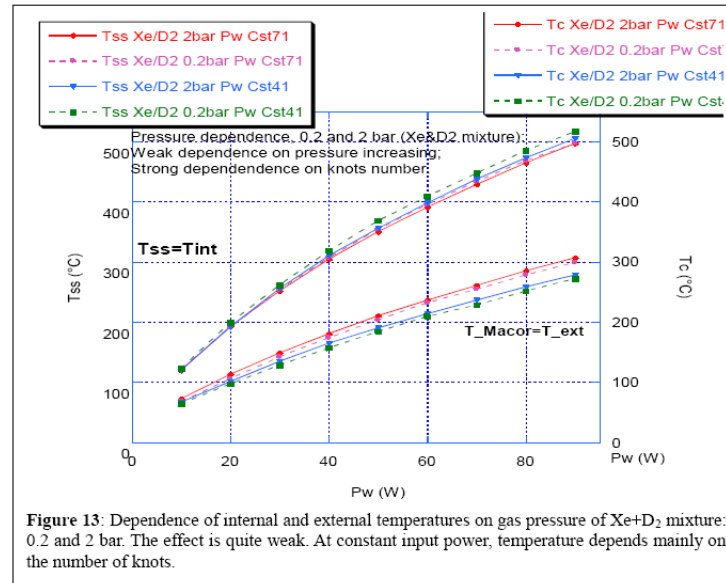
Figure 13: Dependence of internal and external temperatures on gas pressure of Xe+D_2 mixture: 0.2 and 2 bar. The effect is quite weak. At constant input power, temperature depends mainly on the number of knots.

wire. Such steps are the most critical and delicate part of the assembly.

In Fig. 4, steps 6 and 7, we report the *key* processes for "conditioning" the Cst in order to modify the surface from smooth to sub-micrometric (by "flash oxidation" electric pulses) with different chemical compositions (Cst, CuO_x, NiO_y, $Cu_xNi_yO_z$). The main hole and the micro-holes generated by explosive-like pulses on the wire surface are filled with liquid Fe–K–Mn solution several times. Such steps are the most tedious, time consuming (several hours) and risky part of the assembly: the wire can get destroyed because of the combined effects of aggressive chemicals (e.g. liquid nitrate, $KMnO_4$) and extreme thermal and mechanical stresses (e.g. pulsing to very high temperatures up to 900-1000°C and cooling in a few milliseconds). The Cst wires are inserted inside a borosilicate sheath (from SIGI-Favier; $\Phi = 1$ mm), previously wetted and dried, sequentially, with a solution of $Sr(NO_3)_2$ and Fe–K–Mn both in D_2O. At step 8 the borosilicate sheath is inserted into another sheath of Al_2O_3, $\Phi = 2$ mm able to withstand continuously up to 1200°C. At step 9, the ends of the wires are crimped with a gold plated mini-connector. At step 10, the three wires are braided around each other and put, at step 11, inside another borosilicate sheath ($\Phi = 12$ mm) for mechanical stability and thermal homogeneity. (This configuration is not shown.)

In Fig. 5, step 12 the ($\Phi = 12$ mm) sheath is rounded at the SS support, previously covered by a ($\Phi = 4$ mm) glass sheath. The rounded sheath is, at the end, covered with a ($\Phi = 25$ mm) final sheath with an internal diameter of 34 mm (not shown) for mechanical stability and overall thermal homogeneity toward the borosilicate thick-glass reactor.

4. SEM Images

Figures 7–10 show an overview of a typical Cst wire after thermal treatments (for oxidation and structuring of the micrometric surfaces) and Fe–KMn depositions. The actual diameter of the main hole is 160 μm, less than the "stated" 200 μm of the copper reference wire in Fig. 3.

After several cycles of hydrogen/deuterium loading and deloading at high temperatures, the diameter of the particles decreases in a remarkable way, supposing no sintering due to vacuum or inert gases happened. We guess that the "new" addition of Fe–KMn compound at the surface of the wires reduces the "weakness" of Cst toward sintering problems. We note that hydrogen is adsorbed at high temperatures (>500°C) inside iron lattice. Perhaps, the addition of potassium to iron can even reduce the starting temperature of absorption.

5. Main Results

After calibration under vacuum and helium gas with power applied *only* to platinum to avoid sintering of the nanoparticles at the Cst surface (due to high temperatures in vacuum or inert/noble gas atmosphere), the experiments were performed using D_2 at high (2 bar) and low (0.2 bar) pressures. The combined effect of pure D_2 (a cracking agent to reduce dimensionality of surface nanomaterials) and several LowHighLow temperature cycles further promotes deuterium absorption into the bulk of Cst, obtaining *useful aging effects*.

In order to increase the wire temperature, which enhances the AHE, while keeping the external power applied as low as possible, we added xenon gas to pure D_2 at 50% ratio. Among other useful and strange effects, to be fully explored and reconfirmed by us, this noble gas has an extremely low value of thermal conductivity. Most of the results we report are obtained with a Xe–D_2 mixture, mainly at a total pressure of 0.2 bar. Since 2010 [9], we added high-Z noble gas (e.g. argon) to reduce the thermal conductivity of the reactors. We observed that such addition even improved the AHE, but the results were too low in absolute values for us to completely sure they are real. For this reason we moved from argon to xenon (although the latter is quite expensive). Since then, we have speculated about the role of noble gases but we have not reached any firm conclusions.

The results are shown in Figs. 11–15.

Figure 14 shows the behavior of the so-called spontaneous voltage, which increases with the loading of the wire, the concentration of atomic deuterium and temperature.

Figure 14: Spontaneous voltages (with 10 MΩ load) measured at the ends of Cst71 wire, *not* connected. The current produced (at 2 Ω load) depends only on the internal resistance of the wire (around 18 Ω). Aside from internal temperature, voltage increases with gas pressure and with the "amount" of atomic D allowable: when Pw is applied at Cst41 (which we assumed is a good catalytic material) the results are larger than with Pt.

Figure 15: Case with the 2 Cst wires connected in series (green lines). It can be argued that the AHE, at constant Pw, is *not* strongly related to the internal temperatures (Tss) of wires (individually lower because of lower voltage drop) due to the current.

6. Highlights

The addition of Fe–Mn–K mixed oxides to our experimental set-up has caused a significant increase of the AHE compared to our previous similar experiments. The data point toward a complex of phenomena mediated by atomic

hydrogen/deuterium formation, transport and recombination despite pressure and temperature (unfavorable for atomic hydrogen). In fact the energy gain seems to strongly correlate with the process of dissociation and recombination of atomic hydrogen or deuterium.

We also have early indications that the migration of the active species is enhanced by current and voltage in the Constantan.

On the basis of our observations we propose a simplified model of the experiment where atomic hydrogen/deuterium is first formed by exothermic adsorptive dissociation on the surface of Constantan (Ni/Cu), then migrates toward the Fe–Mn–K impregnated fiberglass sheath and exothermically recombines (especially on MACOR ceramic) (**??**). The energy to sustain this process comes in the form of current on Constantan (via Joule heating and a possible electrochemical factor) and from a *yet unknown process, possibly at electron Compton wavelength scale, explaining perhaps the apparent excess heat.*

Future work will be dedicated to identifying and better understanding the active sites of energy generation. At the same time, special care will be given to exclude any "electrochemical" Peltier-like effect capable of mimicking some of the reported thermal anomalies In that respect we consider particularly valuable the work of Dr. Groszek that has been recently brought to our attention. In [10,11] he has recently described experiments where hydrogen absorbed on transition metal catalysts reacts with oxygen, releasing a heat pulse far beyond the enthalpy of combustion. Having said that, we suppose that in our experiments we are continuously regenerating the catalyst and the reagents of a Groszek-type experiment allowing a steady excess heat release. Future work will be dedicated to identify and better understand the active sites of energy generation and the role of the mixed oxides.

7. Final Remarks

Transport of atomic hydrogen may possibly occur from dissociation to recombination sites. These transport phenomena appear to be enhanced by current in Constantan, hence calling for a possible role of charged hydrogen/deuterium
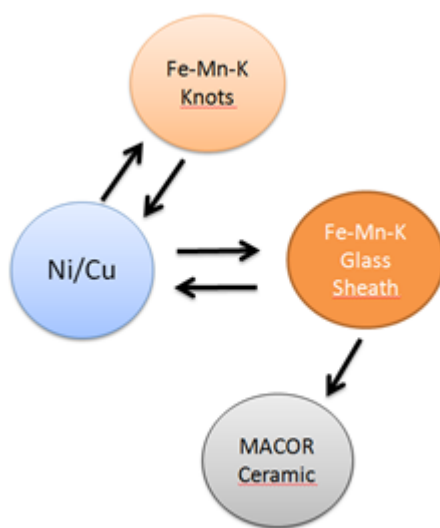
Figure 16. Possible exchange of atomic hydrogen in the current experiment.

species. Dissociation/transport/recombination make it difficult to identify sites where excess heat occurs. A minor risk for some sort of Peltier-like effect mimicking certain observations cannot be excluded yet.

8. Addendum

Recently, after of ICCF20, by chance it came to our attention that a researcher from Germany Horst Preusker, [12] claimed in a short patent that xenon acts as a catalyst for the nuclear reaction $D_2+D_2 {}^4_2He$ with emission of a large amount of energy, once D_2 gas is ionized. So far, we have not observed elements to judge whether the claims by Preusker are correct. In any case, we have experimental evidence of a performance increase *after* the introduction of xenon inside the reactor, even at low concentration, especially when power is applied to Cst.

Because of the possible effect of xenon, and others high-Z noble gases as co-catalytic agents of the AHE reactions (at least in our specific environment), we repeated previous tests (since 2013) to confirm the role of argon and xenon. Additionally, after taking into account a possible role of water which we may always consider present in traces in our experiment (mostly coming from the glass sheaths and the mixed oxides), we intentionally added D_2O again in the reactor chamber. Table 1 summarizes some thermal data collected at a fixed input power (Pw) of 50 W on Cst. We can argue that the additions of argon and, even better, of xenon gas to D_2, *really are effective in increasing AHE, beyond any doubt*. Water is also very effective and a synergistic effect with xenon can be observed. How all these compounds are interacting with the wire and mixed oxides is under investigation.

9. Conclusions

(1) One of the weakest points of LENR studies in general, i.e. the not at all satisfactory reproducibility, in our specific experimental situation seems to be overcome with the addition of some Fe–K–Mn to our Constantan wires and glass sheaths (saturated with SrO, whose role is the emission of electrons even at low temperatures, i.e. 600°C).

(2) The effect appears also related to the concentration (or hyper-concentration according to some authors such as Leif Holmlid and Svein Olafsson) of hydrogen or deuterium in specific sites including iron (absorbing hydrogen only at high temperatures, >500°C), once H_2 or D_2 are dissociated *in situ*.

(3) The role of glass sheaths, due to their specific composition and geometry and porosity, seems to be important, similar to that of alumina "support" in the field of automobile catalytic converters used to condition exhaust gases.

(4) The observation of "strange" nuclear effects, even including a reduction of ambient radioactivity and/or the emission of some low energy photons (<250 keV), has to be fully elucidated yet. Anyway, such phenomena arise only after the reactor is operated for a *long* time (several months) with large and stable "loading".

(5) The effect of the so-called "spontaneous or thermionic voltage", first observed accidentally by us on June 2014, has been confirmed and, since the first measures it has been increased by over one order of magnitude. This effect seems to arise from the Thermionic emission of Constantan wire in presence of hydrogen or deuterium, and could lead to interesting applications such as Thermionic Generators driven by AHE.

(6) Further *multidisciplinary* work is mandatory to exploit the full potentialities of our Cst configuration and LENR in general. Several phenomena are really unexpected and are *not* experimental errors:

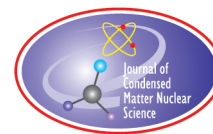*Some of the new phenomena observed have the potential for practical applications.*

Acknowledgments

cannot forget the kindness, hospitality and useful scientific exchanges of information with our Japanese Colleagues (Y. Iwamura, J. Kasagi, H. Yoshino, T. Mizuno, A. Takahashi, A. Kitamura and several co-workers) before and during ICCF20. Several discussions with Prof. Renato Burri (Perugia University, Italy) helped us to clarify some peculiarities of the atomic and even ionized hydrogen. The replications and results of some of our experiments, performed since 2012 by M. Valat and B. Greyner (MFMP), helped us to elucidate some of the problems using Constantan wires. We are indebted with Prof Giorgio Trenta (recently retired from LNF-INFN) for in-depth discussions on radiation emissions from our cell, including enhanced $\gamma-$stimulation. SEM analysis and microphotography were performed by Antonino Cataldo and Federico Micciulla from NEXT Laboratory at INFN-LNF, Italy. Finally, we would like to thank Jed Rothwell for his helpful support in editing and revising this paper. *Finally, we note that several Italian politicians (in the Lower and Higher House, notwithstanding their party affiliations) made very notable "recommendations" and political pressure to allow the survival of LENR scientific studies in Italy.*

References

[1] A. Carpinteri, G. Lacidogna and A. Manuello, *Acoustic, Electromagnetic, Neutron Emissions from Fracture and Eartquakes,* Springer, Berlin, 2015, ISBN: 978-3-319-16954-5.

[2] S. Romanowski, W.M. Bartczak and R. WesoÅĆkowski, Density functional calculations of the hydrogen adsorption on transition metals and their alloys. An application to catalysis, *Langmuir* **15** (18) (1999) 5773–5780.

[3] F. Celani, E.F. Marano, A. Spallone, A. Nuvoli, B. Ortenzi, S. Pella, E. Righi, G. Trenta, F.4 Micciulla, S. Bellucci, S. Bartalucci, M. Nakamura, E. Purchi, G. Zangari, S. Cupellini, A. Mancini, F. Maggiore and A. Ovidi, Experimental results on sub-micro structured Cu–Ni alloys under high temperatures hydrogen/deuterium interactions, *Chem. Maetrials Res.* **3**(3) (2013) 25–76, ISSN: 2225-0956.

[4] Y. Arata and Y.-C. Zhang, Development of "Ds-Reactor" as the practical reactor of "Cold Fusion" based on "DS-cell" with DS-cathode, *Condens. Matter Nucl. Science*, World Scientific, Singapore, 2006, pp. 44–56, ISBN: 978-981-256-901-1.

[5] Y. Iwamura, T. Itoh, M. Sakano and S. Sakai, Observation of low energy nuclear reactions induced by D_2 gas permeation through Pd complexes, in The Ninth International Conference on Cold Fusion, Beijing, 2002.

[6] R. Swensson and L. Holmlid, Very low work function surfaces from condensed excited states: Rydberg matter of cesium, *Surface Science* **269/270** (1992) 695–699,

[7] F. Celani, A. Spallone, B. Ortenzi, S. Pella, E. Purchi, F. Santandrea, S. Fiorilla, A. Nuvoli, M. Nakamura, P. Cirilli, P. Boccanera and L. Notargiacomo, Observation of macroscopic current and thermal anomalies, at high temperatures, by hetero-structures in thin and long constantan wires under H_2 gas, *J. Condensed Matter Nucl. Sci.* **19** (2016) 29–45, ISSN 2227-3123.

[8] A. Kotarba, I. Kruk and Z. Sojka, How the iron oxide catalyst for EBDH is stabilized via Mn addition, *J. Catalysis* **221** (2004) 650–652.

[9] F. Celani, M. Nakamura, W.J.M. F. Collis, O.M. Calamai, A. Spallone, A. Nuvoli, E.F. Marano, E. Purchi, V. Andreassi, B. Ortenzi, E. Righi, G. Trenta and A. Mancini, Flow calorimetric measurements of interaction of H_2, D_2 and He with nano-coated wires of Ni and Pd-alloy at temperatures up to 850∘C, in *ICCF16 Proceedings*, Mahadeva Srinivasan and Jean Paul Biberian (Eds.), pp.70–80, 2011, ISBN 1-892925-06-0.

[10] A.J. Groszek, Abnormally high heat generation by transition metals interacting with hydrogen and oxygen molecules, *Adsorption* **19** (2013) 235–240.

[11] Erwin Lalik, Oscillatory behavior and anamalous heat evolution in recombination of H_2 and O_2 on Od based catalysts, *Ind. Eng. Chem. Res.* **54** (2015) 7047–7058.

[12] Horst Preusker, *Design of a helium fusion reactor*, DE4300016, Jan. 02, 1993.

Research Article

Increase of an Anti-Stokes Peak at the Cathode of an Electrically Driven, Active Aqueous Nickel/H$_2$O/Pt System

Mitchell R. Swartz*

JET Energy Inc., Wellesley Hills, MA 02481, USA

Abstract

Coherent Multiwavelength Optical Reflection Electric-driven (CMORE) spectroscopy offers investigators of condensed matter nuclear science a new diagnostic – in addition to calorimetry and detection of classic emissions. The fact that these discerning spectra occur at the beginning of an experimental run before the temperature and calorimetry can respond in both nanomaterials, and now aqueous systems as reported here, is of tremendous potential value to experimentalists because it may enable avoiding inactive modes and undesired quenching reactions.

© 2018 ISCMNS. All rights reserved. ISSN 2227-3123

Keywords: Anti-Stokes, CMORE spectroscopy, Excess heat mode, Lattice assisted nuclear reactions, Nickel/H$_2$O/Pt, Phonon gain, PHUSOR®-type component, Spectroscopy

1. Introduction

Coherent Multiwavelength Optical Reflection Electric-driven (CMORE) spectroscopy is capable of rapidly differentiating inactive and active states in CF/LANR nanomaterials and aqueous systems. Previous results include ZrO$_2$PdD NANOR®-type preloaded components driven in the desired, active "Excess Heat" mode, as described elsewhere [1,2]. This report expands that knowledge and shows (cf. Fig. 1) that for successful LANR in an aqueous Nickel/H$_2$O/Pt system containing ordinary water of natural deuteron abundance. Its "excess heat" mode is indicated by a unique signature using dual wavelength electric-driven volume-enhanced reflection spectroscopy. Shown in Fig. 1 are two spectra of the same LANR component resolved by dual wavelength CMORE spectroscopy. The two modes (responses) are the undriven "off"-state, and the optimal operational state, the "Desired Active Mode", where "excess" energy is being released. The "Excess Heat" (XSH) Mode can be distinguished in its CMORE spectra observed by a unique reflected optical backscatter along with the reflected optical beams. Note the increase of the anti-Stokes Peak from the active state of an aqueous Nickel/H$_2$O/Pt system.

---

*Mitchell R. Swartz ScD, MD, EE, E-mail: mica@theworld.com.
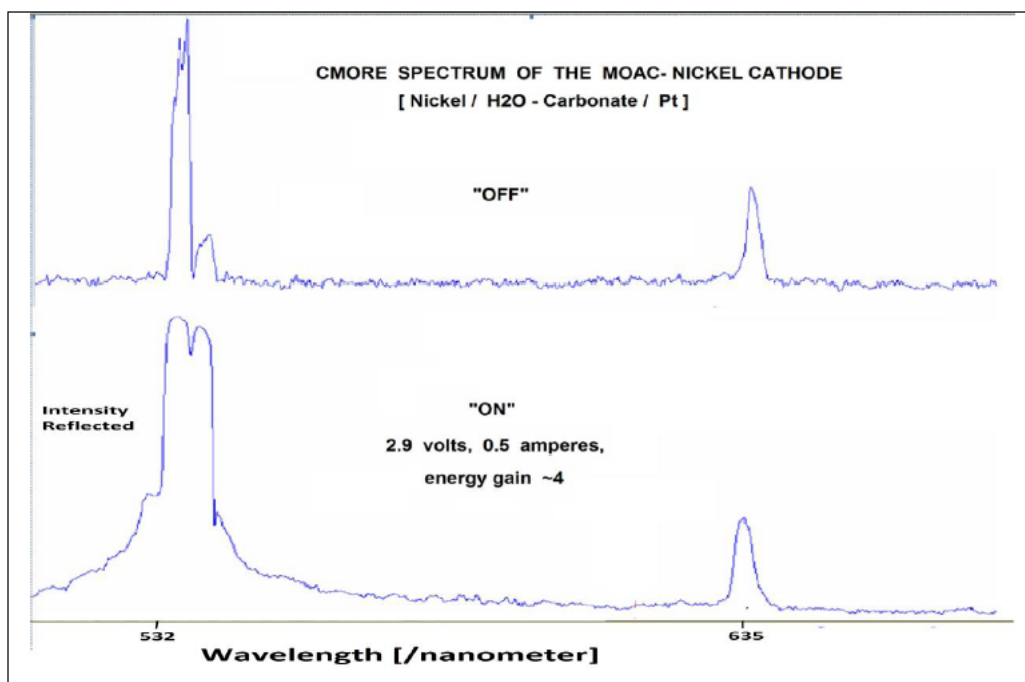
Figure 1. CMORE spectra of an aqueous Nickel/H_2O/Pt system. These are two CMORE spectra of a CF/LANR aqueous Nickel/H_2O/Pt system in two electrical states; "off" (*top*), and active XSH mode (*bottom*). Shown are the reflected optical intensities as a function of wavelength (increasing to the right-hand side).

2. Background

2.1. Successful LANR requires considerable engineering

LANR success is rewarded by "excess heat", which means that the energy producing reactions have generated de novo helium into the lattice ($\sim10^{12}$ for every molecules/J [3]). There are also other reactions, but most are unwanted and many quench the desired reactions and pathways. The LANR method which Fleischmann and Pons first taught in March 1989 (aqueous, low impedance, Pd/D_2O/Pt) had problems, including inefficiency and non-reproducibility. This created havoc for those inexperienced in metallurgy, electrochemistry, and physics. Many "negative" results are due to a failure to operate the system at the optimal operating point, which is an optimum peak in the excess heat and power gain curves as a function of input electrical power [3–5].

2.2. Dry NANOR®-type CF/LANR preloaded components

Dry preloaded NANOR®-type LANR (lattice assisted nuclear reaction) components have been described in the literature [6,7]. The NANOR®-type components have been used to investigate material science [1,2,6–12] and radiation physics [1,2,10,11] of their active LANR systems. Several reports demonstrated that several electrical transconduction states exist, but that only one is active, desired, and capable of producing "excess heat" [1,2,12].

2.3. Optical Raman, and coherent Raman, scattering

Classic Raman spectroscopy involves the inelastic scattering of light which generates new frequencies which result from the interaction of light the irradiated matter [13]. Raman Stokes scattering transfers some of the energy from the incident light to excited states in the irradiated material, and thus some of the reflected wavelengths are red-shifted. Raman anti-Stokes scattering results when the irradiated material already contains excited states, and the reflected photons are blue-shifted by the difference in energy between the excited states returning to their ground state.

The major problem of the Raman effect is that it produces very weak signals because the photon conversion efficiencies are less than 10^{-18}. As Sir Chandrasekhara Raman stated, the effect has "excessive feebleness" [13]. These very small signals result because the proportionality constant $\chi(3)$, known as the "third-order susceptibility", is only linearly proportional to the local oscillator density.

However, that is not the case when irradiation is made using coherent lasers which yield a much larger signal because with coherent illumination there results phase-matching conditions and quadratic dependence on the number of local oscillators. Thus, even with the same selection rules, the coherent irradiation Raman effect yields a much greater signal intensity (circa 10^6 times greater) [14,15]. Maker and Terhune [16] first reported on Coherent Anti-Stokes Raman Scattering (CARS [17]) using a pulsed ruby laser and a Raman generated frequency-shifted beam to examine benzene. The CARS has since produced a new imaging modality for biomedicine [18,19]. Similarly, coherent anti-Stokes Raman scattering in CF/LANR (CMORE spectroscopy) has yielded a new imaging modality for excited energy states which only appear in working active CF/LANR systems [1,2].

2.4. CMORE coherent Raman scattering of CF/LANR materials

In Fig. 2, shown are the CMORE spectra which were obtained from a ZrO_2 preloaded active nanomaterial demonstrating power gain. As in Fig. 1, the spectra in Fig. 2 show reflected optical intensity as a function of wavelength, initially from two incident coherent optical beams but then reflected by backscatter along with the initial optical beams from the nanomaterial. The CMORE spectra reveal different types of activity states from the same sample, observed by the same diagnostic. Specifically, Fig. 2 shows this for the same NANOR®-type component electrically driven in three states. One state is the unwanted electrical avalanche mode [12]. The other state is the desired optimal operational state (the active excess heat (XSH) mode), where excess energy is being released. The third state is the state where the electrical drive is "off".

Note the apparent diversity in outcome of the spectra for the same input. Anti-Stokes peaks appear when the electrical drive generates excess heat but differ in energy, amount, and in what stimulates their appearance. When driven in the avalanche mode, the anti-Stokes peaks differ considerably from those which appear during the excess heat-producing or desired mode.

2.5. Dry NANOR®-type CF/LANR preloaded components

Dry preloaded NANOR®-type LANR (lattice assisted nuclear reaction) components have been described in the literature [6,7]. The NANOR®-type components have been used to investigate material science [1,2,6–12] and radiation physics [1,2,10,11] of their active LANR systems. Several reports demonstrated that several electrical transconduction states exist, but that only one is active, desired, and capable of producing "excess heat" [1,2,12].
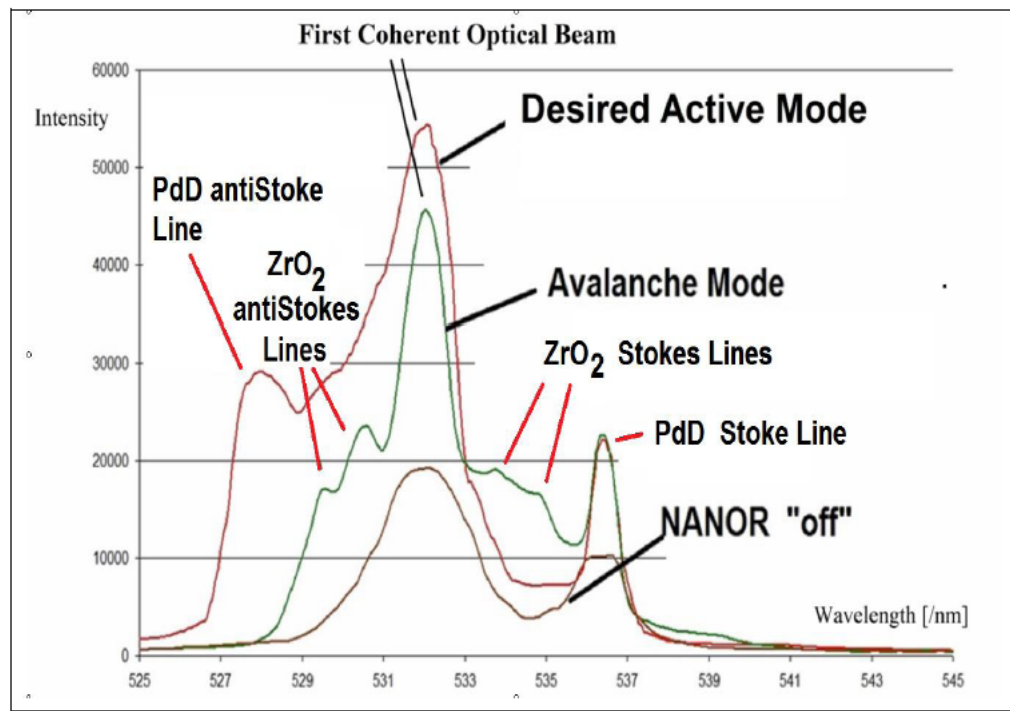
In Fig. 2, the CMORE spectra were obtained from a ZrO_2 preloaded active nanomaterial demonstrating power gain. As with Fig. 1, the spectra in Fig. 2 show reflected optical intensity as a function of wavelength, initially from two incident coherent optical beams but then reflected by backscatter along with the initial optical beams from the nanomaterial.

Figure 2. CMORE spectra of ZrO$_2$PdD NANOR®-type CF/LANR. These are the overlaid spectra of the three different electronic states optical signatures for the same preloaded ZrO$_2$PdD NANOR®-type CF/LANR component in three different electrical drive modes. Shown are spectra of the same NANOR®-type CF/LANR component (Nanor® 7,6) in three different electronic states, resolved by dual wavelength coherent electric-driven volume-enhanced reflection spectroscopy. Labelled are the assignments of the anti-Stokes peaks to zirconia and PdD.

The CMORE spectra reveal different types of activity states from the same sample, observed by the same diagnostic. Specifically, Fig. 2 shows this for the same NANOR®-type component electrically driven in two states (the unwanted electrical avalanche mode [12] and the optimal operational state, the desired, active XSH mode, where excess energy is being released), and "off". There is diversity and distinguishing spectra in outcome.

Anti-Stokes peaks appear when the electrical drive generates excess heat but differ in energy, amount, and in what stimulates their appearance. When driven in the avalanche mode, the anti-Stokes peaks differ considerably from those which appear during the excess heat-producing or desired mode.

3. Experimental

3.1. Materials – MOAC cell and system

The aqueous cell system used for this report is a Ni/H$_2$O/Pt system which was designed to have a large electrode area [20]. The cathode weighs 4.7 pounds, and was made from #46 hard drawn smooth nickel wire (0.00399 cm diameter, with an area of ~240,000 cm^2). The anode was five folded platinized sheets of titanium with an area of ~3200 cm^2, for a surface area ratio of cathode to anode of 75:1. The electrolyte was a dilute carbonate solution (K$_2$CO$_3$); ~0.1 M in distilled water of natural deuteron abundance. Two internal ohmic controls were used. Figure 3 shows the LANR cell
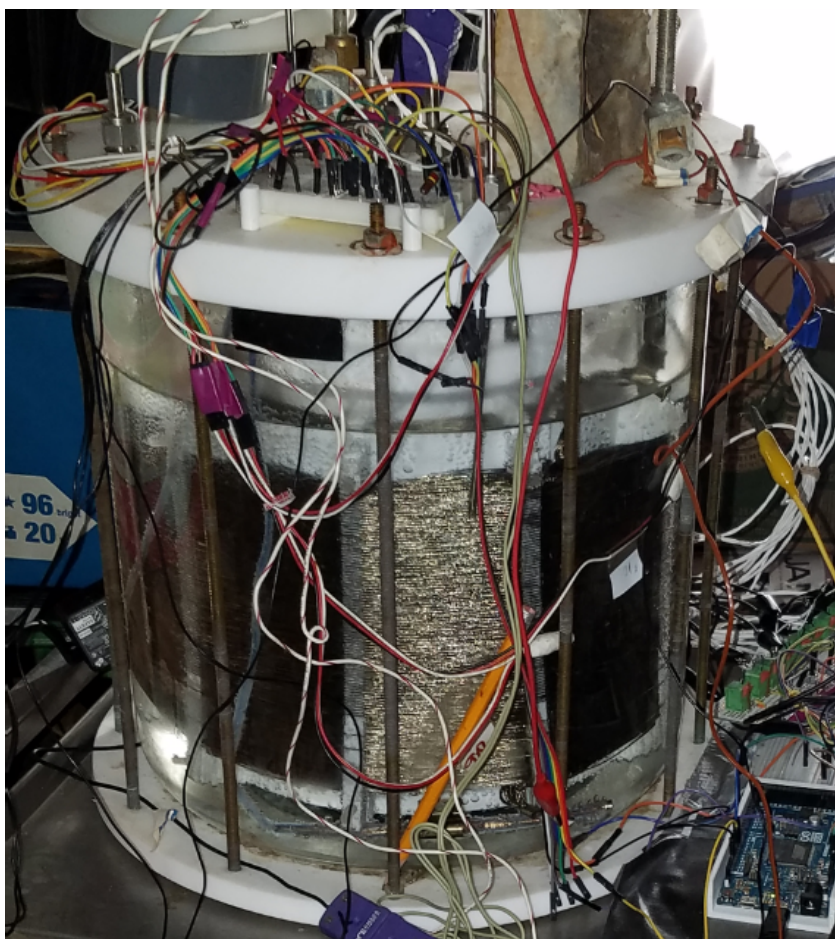
Figure 3.   The LANR MOAC electrolytic cell. This figure shows the electrolytic cell used (3 l). Acquisition of the cathode surface by the CMORE spectrophotometer's incident coherent optical beam was to a small area of the very large cathode.

used. It has a 3 l capacity when filled; here unfilled, not connected to the power supply, thermistor monitoring system, or the gas venting actually used.

3.2. Methods – Signal pickup by CMORE spectroscopy

In this study, a 532 nm laser was used to elicit the Raman spectra, and a weaker 635 nm laser was used for calibration [1,2]. The green laser (532 nm peak) had a power output level of about 150 mW. The red orange laser (635 nm peak) had a power output level of about ~2 mW for energy calibration. The sample surface illuminated was the cathode.

3.3. Methods – Electrical driving components

The cell was electrical driven, or not, by a steady direct current electrical drive [2.9 V, 0.50 A; with a measured energy gain of ~4.0 using $V \times I$ as the electrical input) while it was irradiated by the two lasers while physically maintained

in position. The component was electrically activated and controlled, and was designed to include and use several controls. Using several ohmic (thermal) and other controls, the anti-Stokes to Stokes (aS/S) ratio was determined when the materials were examined in both the "off" condition and where the desired cold fusion reactions occur [1,2].

4. Results

In Fig. 1, the curves are from dual wavelength coherent electric-driven volume-enhanced reflection spectroscopy of aqueous Nickel/H_2O/Pt system with power gain – and when "off". CMORE spectra show reflected optical intensity as a function of wavelength, initially from two incident coherent optical beams but then reflected by backscatter along with the initial optical beams from a small area of the electrically driven (or not) cathode.

In Fig. 1, the functional, desired "Excess Heat" (XSH) Mode is indicated by a unique signature using dual wavelength electric-driven volume-enhanced reflection spectroscopy. One can easily see the distinguishing optical output in the desired correctly driven active "state" as revealed by the new diagnostic technology.

The reflected optical backscatter along with the reflected optical beams from the component in its desired "excess heat" state has an XSH-related anti-Stokes peak which is singular and at higher energy. This distinguishing, higher energy, single, anti-Stokes peak (which also heralds phonon gain) is not seen in the "off" state.

5. Conclusions

5.1. Anti-Stokes peaks of the electrically driven Ni/H_2O–D_2O/Pt system reveals the desired "excess heat" state

The CMORE spectroscopy heralds the "desired mode" or "excess heat production mode", as demonstrated again in this report. Active aqueous Nickel/H_2O/Pt CF/LANR systems with power gain have diagnostic CMORE spectroscopic signatures. There is an XSH-related anti-Stokes peak which is singular and at higher energy. This distinguishing, higher energy, single, anti-Stokes peak (which also heralds phonon gain) is not seen in the "off" state.

From a materials point of view, it appears that acoustic phonons result from, or are required for, an active cold fusion process producing energy gain in its "excess heat" (XSH) mode in both this aqueous system and nanomaterial CF/LANR systems.

5.2. Implications for improvement of LANR systems

There are important implications to this new finding. CMORE spectroscopy is capable of rapidly differentiating the inactive or quenched states from the active excess heat (XSH) producing state in CF/LANR electrodes, nanomaterials, and systems. Successful cold fusion systems indicate their activity by a large increase in the aS/S ratio for BOTH active aqueous and nanomaterial CF/LANR systems.

Therefore, CMORE spectroscopy is a useful diagnostic which can generate spectra in real time and is able to illuminate, visualize, and help identify different states for a CF/LANR material or component, before the appearance of measurable excess heat for the first time. The system can determine which state the material or component is in, in real time, even as it is electrically driven, and may be able to determine time constants for changes between levels.

Most importantly, CMORE spectroscopy can saliently detect the desired reactions just as products begin to appear and accumulate (e.g. heat). Therefore, it has great use because it reveals both the desired, and undesired, reactions and states and may enable better control, and possible detection of other states of operation – and therefore reactions and products. For example, by observing the presence and perhaps width of the anti-Stokes peak, it may be possible to better tune CF/LANR systems away from undesired inactive modes and quenching reactions (such as the unwanted avalanche mode in CF/LANR nanomaterials).

Acknowledgments

References

[1] M.R. Swartz and P.L. Hagelstein, Increased PdD anti-Stokes peaks are correlated with excess heat mode, *J. Condensed Matter Nucl. Sci.* **24** (2017) 130–145.

[2] M.R. Swartz, Optical detection of phonon gain distinguishes an active cold fusion/LANR component, *J. Condensed Matter Nucl. Sci.* **20** (2016) 29–53.

[3] M.R. Swartz, Survey of the observed excess energy and emissions in lattice assisted nuclear reactions, *J. Sci. Exploration* **23** (4) (2009) 419–436.

[4] M.R. Swartz, Excess power gain using high impedance and codepositional lanr devices monitored by calorimetry, heat flow, and paired stirling engines, *Proc. ICCF14* **1** (2008) 123; ISBN: 978-0-578-06694-3, 123, (2010); www.iscmns.org/iccf14/ProcICCF14a.pdf.

[5] M.R. Swartz and G. Verner, Excess heat from low electrical conductivity heavy water spiral-wound Pd/D_2O/Pt and Pd/D_2O-PdCl$_2$/Pt devices, *Condensed Matter Nucl. Sci. Proc.ICCF-10*, World Scientific, Singapore, ISBN 981-256-564-6, 29-44; 45-54 (2006).

[6] [6] M.R. Swartz, G. Verner, J. Tolleson and P.L. Hagelstein, Dry, preloaded NANOR®-type CF/LANR components, *Current Science* **108** (4) (2015) 595.

[7] M.R. Swartz, G. Verner and J. Tolleson, Energy gain from preloaded ZrO_2–PdNi–D nanostructured CF/LANR quantum electronic components, *J. Condensed Matter Nucl. Sci.* **13** (2014) 528; www.iscmns.org/CMNS/JCMNS-Vol13.pdf.

[8] M.R. Swartz and P.L. Hagelstein, Demonstration of energy gain from a gain using fractionated magnetic fields on ZrO_2–PdD nanostructured preloaded ZrO_2–PdD nanostructured CF/LANR quantum electronic device at MIT, *J. Condensed Matter Nucl. Sci.* **13** (2014) 516; www.iscmns.org/CMNS/JCMNS-Vol13.pdf.

[9] M.R. Swartz, G. Verner, J. Tolleson, L. Wright, R. Goldbaum and P.L. Hagelstein, Amplification and restoration of energy components, *J. Condensed Matter Nucl. Sci.* **15**(2015) 66; www.iscmns.org/CMNS/JCMNS-Vol15.pdf.

[10] M.R. Swartz, Incremental high energy emission from a ZrO_2–PdD nanostructured quantum electronic component CF/LANR, *J. Condensed Matter Nucl. Sci.* **15**(2015) 92; www.iscmns.org/CMNS/JCMNS-Vol15.pdf.

[11] M.R. Swartz, G. Verner J. Tolleson, L. Wright, R. Goldbaum, P. Mosier-Boss and P.L. Hagelstein, Imaging of an Active NANOR®-type LANR component using CR-39, *J. Condensed Matter Nucl. Sci.* **15** (2015) 81; www.iscmns.org/CMNS/JCMNS-Vol15.pdf.

[12] M.R. Swartz, P.L. Hagelstein and G. Verner, Impact of electrical avalanche through a ZrO_2–NiD nanostructured CF/LANR component on its incremental excess power gain, ICCF-19, *J. Condensed Matter Nucl. Sci.* **19** (2016) 1–11.

[13] C.V. Raman, Scientific papers of C.V. Raman, S. Ramaseshan (Ed.), Vol. 1, India, *The Scattering of Light*, Indian Academy of Sciences, Bangalore, India, 1988.

[14] Ji-xin Cheng, Eric O. Potma and X. Sunney Xie, Coherent anti-Stokes Raman scattering correlation spectroscopy: probing dynamical processes with chemical selectivity, *J. Phys. Chem.* A **106** (2002) 8561–8568.

[15] Conor L. Evans and X. Sunney Xie, Coherent anti-Stokes Raman scattering microscopy: chemical imaging for biology and medicine, *Ann. Rev. Anal. Chem.* **1** (2008) 883–909.

[16] P.D. Maker and R.W. Terhune, Study of optical effects due to an induced polarization third order in the electric field strength, *Phy. Rev.* **137** (3A) (1965) 801–818.

[17] R.F. Begley, A.B. Harvey and R.L. Byer, Coherent anti-Stokes Raman spectroscopy, *Appl. Phys. Lett.* **25** (7) (1974) 387–390.

[18] C.L. Evans, E.O. Potma, M. Puoris'haag, D. Cote, C.P. Lin and X.S. Xie, Chemical imaging of tissue in vivo with video-rate coherent anti-Stokes Raman scattering microscopy, *Proc. Natl. Acad. Sci*. USA, **102** (2005) 16807.

[19] C.L. Evans, X. Xu, S. Kesari, X.S. Xie, S.T.C. Wong and G.S. Young, Chemically-selective imaging of brain structures with CARS microscopy, *Opt. Expr.* **15** (2007) 12076.

[20] M.R. Swartz, C. Haldemann, A. Weinberg and B. Ahern, Excess heat is linked to deuterium loss in an aqueous nickel CF/LANR system, Poster ICCF-21, and Proc. ICCF21, to appear.

Research Article

On the Experiment that Could Answer the Question Whether the Like Charged Particles, with Relative Velocity Close to Zero, Repel or Attract?

I.N. Tukaev*

Ulianovsk State University, Ulianovsk 432000, Russia

Abstract

This paper considers the conditions of an experiment with results which could answer unambiguously the following question: do like charged particles repel or attract when the magnitude of their relative velocity is close to zero? The answer to this question will either confirm the validity of Coulomb's law, which states that the like charged particles always repel, or the validity of hypothesis by Gustav Theodor Fechner, which was proposed in 1845, and stated that like charged particles with relative velocity close to zero, attract.

© 2018 ISCMNS. All rights reserved. ISSN 2227-3123

Keywords: Bound pairs of charged particles, Charged particle, Cold fusion, Condensate, Coulomb law

1. Introduction

The main theoretical problem to explaining Cold Fusion is the Coulomb repulsion of the slow particles participating in the process. The major difference between the nuclear fusion which occurs at high temperature and Cold Fusion is the relative velocity of particles participating in the reaction. In plasma nuclear fusion at high temperatures, particles are initially fast, whereas in Cold Fusion they are slow. But as the fast, like-charged particles approach one another, the simultaneous decrease of their relative velocity and of the distance between them occurs along with their Coulomb repulsion. Therefore, both decreased distance between particles and their decreased relative velocity can switch the Coulomb repulsion of protons to nuclear attraction. Separating one process from the other and determining the major reason that forces the protons to attract during the fusion process is not possible.

In mathematics, there are two types of knowledge about the properties of mathematical objects: the first is a hypothesis and the second is a theorem. The hypothesis is a statement of properties of mathematical objects, which is not proved by strict logical statements accepted in the mathematical community. A theorem is a statement of

---

*E-mail: in-t@rambler.ru.

properties of mathematical objects proved by strict logical statements accepted in the mathematical community. There are theorems proved by using those proved before. There are theorems proved in assumption that the hypothesis used for proving is valid. The latter types of theorems are called "candidate theorems", which become theorems after the hypotheses are confirmed.

In physics, as well as in mathematics, there are also two types of knowledge about the properties of physical objects and the processes in which they participate: the first is a hypothesis and the second is a law. The physical hypothesis is a statement about the properties of a physical object or a process in which it participates, that has not been proved experimentally, according to the rules accepted in the physical community. The physical law is a statement about the properties of a physical object or a process in which it participates, proved experimentally, according to the rules accepted in the physics community. The physical law is a statement about the properties of a physical object or a process in which it participates, proved experimentally, according to the rules accepted in the physics community. There are physical theories using physical laws proved before. There are physical theories using hypotheses that assumed valid. The latter types of theories are the physical "candidate laws", which become laws after the hypotheses used in them are proved.

In mathematics, if the practical use of a hypothesis results in a contradiction, it is considered erroneous and does not become a theorem. In physics, there is a different way of using hypotheses in theories. If the practical use of a theory, which previously described the reality properly, results in a contradiction, then the hypothesis on which this theory is based, is not yet considered erroneous. An experiment is required in order to recognize the hypothesis as erroneous, and it must prove the invalidity of hypothesis unambiguously. Whether the required experiment can be performed depends on technological ability. Therefore, in practical physics, scientists use hypotheses which describe reality properly in certain cases and are considered laws. The Coulomb law is that kind of hypothesis.

2. Coulomb's Law and Fechner's Hypothesis

The Coulomb law is a law of interaction between the immobile charges. It was formulated at the end of 18th century while studying the interaction of two electrically charged balls, but not the interaction of two electrically charged elementary particles. When Charles-Augustine de Coulomb proposed the law, immobility was accepted at zero magnitude of relative velocity of bodies. This interaction was investigated, while the motion velocity of elementary particles in these bodies was not considered. The electrically charged substance in electrified bodies was considered immobile. However, today we have enough experimental facts to allow the conclusion that all bodies observable in nature consist of particles, and the particle's dynamic systems form these bodies, and that all particles, both atoms and molecules themselves and free electrons and protons in these dynamic systems, possess different kinetic energies, and hence, different magnitudes of velocities relative to one another, even if the temperature of these systems approaches absolute zero. No experiments confirming the validity of Coulomb's law for two like charged elementary particles, with a magnitude of relative velocity is close to zero, have been carried out. Therefore, Coulomb's law in its current formulation is an experimentally unproved hypothesis. Coulomb's law is applied in many physical theories that are used in the research of fundamental properties of interaction between the electrically charged elementary particles. That is why the experimental validation of Coulomb's law for interaction of elementary charges with relative velocity close to zero is a necessary condition for the practical use of all theories based on the Coulomb law.

When Ampere formulated the law of interaction of electric currents, it became clear that the interaction of electric charges depends on their velocities, and the Coulomb forces underwent modifications. In the second half of the 19th century the theory of interaction of electrically charged particles, which was developed by Wilhelm Eduard Weber on the basis of modified Coulomb forces, depending on the distances between particles and their first and second derivatives with respect to time [1,2], was the most widely accepted interpretation. At that time, Weber assumed that the Coulomb law is valid for charged particles immobile relative to each other. As this theory was criticized, other

attempts to explain interactions of moving electric charges using the modified coulomb forces were undertaken [3,4]. However, in the 20th century the separation of forces acting between the charged elementary particles by two types, the Coulomb and magnetic ones, became generally recognized. All later theories that used Coulomb forces to model dynamic systems of elementary particles, including Weber's theory, assumed that the Coulomb law is valid for charged particles that are immobile relative one another, and no alternative hypotheses were considered.

A hypothesis stating that like charged particles attract in certain conditions, which depends on motion velocities of particles, was advanced by Gustav Theodor Fechner in 1845, before Weber published his theory. Considering the interaction of elements of current, he made the following two assumptions [5]:

(1) Each action of a current element might be considered as a combination of actions of a positive particle and a negative, equal to it in its strength, that simultaneously pass the same element of space in the opposite directions.
(2) According to first assumption, the interaction of two current elements can be presented based on the assumption that similar types of electricity act attractively on one another if they move in the same direction or to the same vertex of an angle, whereas dissimilar ones attract if they move in the opposite directions or if one of them approaches the vertex of an angle while the other one moves away from it.

Pursuing the logic of his hypothesis with respect to the interaction of charged particles of two elements of current, Fechner concluded that "similar particles attract if they move in the same direction and repel if they move in the opposite sides" [5].

As follows from Fechner's reasoning, if magnitudes of velocities of particles relative to immobile parallel elements of current were equal, then the relative velocity of like charged particles, which move in the same direction, equals zero. According to Fechner's hypothesis, the particles will attract. According to Coulomb's law, they will repel. Therefore, Fechner's hypothesis contradicts Coulomb's law for like charged particles immobile relative to one another. As demonstrated above, the Coulomb law in its present wording should be considered a hypothesis until it is verified experimentally. Therefore, today we have two alternative hypotheses, neither of them verified experimentally.

3. Fechner's Hypothesis in Modern Conditions

Physicists of the 19th century had much less experimental data than we have today. Today the level of experimental and theoretical physics allows us to ask the following question:

Do the like charged particles repel or attract if the magnitude of their relative velocity is close to zero?

We can ask this question by analyzing the dynamics of charged particles in the processes that occur:

(1) at low temperatures:

    (a) formation of condensate of bound pairs of electrons in superconductors [6];
    (b) formation of the so-called ionic "crystal beams" when the beam of ions is cooled with the beam of electrons [7];

(2) in atomic nuclei:

    (a) formation of bound pairs of protons, which is confirmed by the kinematics of double-proton decay [8];
    (b) evaporation of nuclear fluid, which is similar to liquid-to-gas phase transition of nuclear and classical fluids in the drop nuclear model [9].

Proceeding from the analysis of these processes, we can conclude the following:

(1) At low temperatures of the substance, and hence, at low magnitudes of their relative velocities, electrons may attract, form the bound pairs and be in the gaseous or liquid state. As the temperature of the substance rises, the magnitudes of relative velocities of electrons increase as well, and electrons begin to repel one another.

(2) At low temperatures, and hence, at low magnitudes of their relative velocities, positive charged particles may attract one another.

(3) In the atomic nuclei, positive charged particles may attract, form bound pairs and be in the gaseous or liquid state. As the temperature of nucleus rises, the magnitudes of positively charged particles' relative velocities increase as well, and positively charged particles begin to repel one another.

Based on these three conclusions, we can reformulate Fechner's hypothesis on the attraction of like charged particles by making the following assumptions:

(1) With magnitudes of relative velocities close to zero:

- electrons attract one another,
- protons attract one another.

(2) With magnitudes of relative velocities that increase starting from certain values:

- electrons repel one another according to Coulomb law,
- protons repel one another according to Coulomb law.

These assumptions contradict Coulomb's law as a law of interaction of two like charged elementary particles, where the magnitude of relative velocity equals to zero.

4. On the Conditions and Feasibility of the Experiment

In order to either confirm or deny the assumptions made in the previous chapter, an experiment that could clearly answer the following question is required:

Do the like charged particles repel or attract if the magnitude of their relative velocity is close to zero?

Answering this question, we should observe the interaction of like charged particles under the following conditions:

(1) It should be possible to slow down the relative velocities of particles to the values close to zero.
(2) Particles should be localized in the vacuum.
(3) It should be possible to change the distances between the interacting particles.
(4) The velocity of particles relative to surveillance instruments should be much less than the speed of light in the vacuum.

The first condition is the most important part of the proposed experiment. The second is required to eliminate the influence of other elements on the interaction of like charged particles if the presence of these elements might explain the attraction of particles (e.g., the influence of atoms of superconductor crystal lattice during the formation of electron condensate). The third condition is necessary in order to exclude the possible explanation of particles' attraction by the distance between them reduced to certain values (for instance, the nuclear forces might be such explanation). The fourth condition is required in order to eliminate the possible explanation of particles' attraction by relativistic effects (e.g., a self-focusing of a beam of relativistic particles).

In theory, all these conditions can be fulfilled. The results of analytical and numerical studies of charged particles' motion trajectories during their interaction with two coaxial charged circles located at some distance from one another were performed in the paper [10], and reveal the following possibilities:

- the continuous localization and accumulation of like charged particles, which initial conditions of motion relative to the charged circles are strictly determined, in the vacuum between the charged circles at the strictly defined circular trajectories without changing the electrostatic field of circles if the charge of particles is of the same sign as that of circles;
- keeping the like charged particles localized for a long period of time;
- shortening the distances between the neighboring particles localized at the same circular trajectory and the reduction of magnitudes of their relative velocities by increasing the number of particles localized at this trajectory.

Observing the dynamics of a certain number of like charged particles localized at the certain circular trajectory, one could verify either the Coulomb law or Fechner's hypothesis by answering the following question:

Do the like charged particles repel or attract if the magnitude of their relative velocity is close to zero?

If the particles repel, then no anomalies in particles dynamics that would contradict the Coulomb law will be observed. If particles attract, then the formation of bound pairs of like charged particles and a condensate of these pairs will probably be observed, just like it occurs with electrons in superconductors or protons in atomic nuclei.

5. Conclusion

If the experiment confirms Fechner's hypothesis on the attraction of like charged elementary particles if the magnitude of their relative velocity approaches zero, then this fact may become a starting point not only for the theoretical explanation of Cold Fusion phenomena but also for the description of many other physical phenomena. In this case, the electrostatic trap, which theory is presented in [10], the nuclei of various elements will probably be synthesized from the same nuclei, for example, those of helium. A radioactive element, from which alpha particles are emitted with the same in moduli velocities, may be the source of helium nuclei. The less the initial velocity of particles, the smaller can be the dimensions of the electrostatic trap. Obviously, this experiment will not be simple or easy-to-do. It will require knowledge and experience of similar experiments. However, the cost of performing it may be not so high since there is no need for a particle accelerator and a trap that should hold the particles possessing high kinetic energies.

If the experiment confirms Fechner's hypothesis, then this fact will allow for the following assumptions:

- the switching from the Coulomb repulsion of protons to their nuclear attraction is the result of reduction of their relative velocity, not the distance between them;
- the protons of the atomic nucleus, as well as those of the proton condensate, are slow, and the increase of their relative velocity causes the decay of the nucleus, or the evaporation of the proton condensate, when the attraction of protons switches to their Coulomb repulsion while their relative velocity increases.

The process of mass evaporation of the proton condensate will be a Coulomb explosion of protons, which are located very close to one another. The technology of proton condensation will allow to accumulate the kinetic energy of protons. The energy of proton expansion during the evaporation of condensate will depend on the distance, at which the protons are in the condensate. As soon as the protons, which velocity relative to the condensate is higher than the critical value, appear in the surface layer of the proton condensate, they will repel from the whole volume of condensate according to the Coulomb law and pass their kinetic energy to the substance surrounding the condensate. If we launch this technology to the near-Earth space and condensate the protons of solar wind, we could use the proton condensate both as a source of energy and as a raw material for the synthesis of nuclei of various chemical elements.

I believe that people in the electric power industry, and researchers studying nuclear synthesis who have the necessary experience and material resources should try to answer this question:

Do like charged particles repel or attract if the magnitude of their relative velocity is close to zero?

References

[1] W. Weber, Electrodynamisce maassbestimmungen, *Prince Jablonowski Society*, Leipzig, 211–378, 1846.

[2] W. Weber, Electrodynamisce maassbestimmungen, *Annalen der Physik und Chemie*, Leipzig, 193–240, 1848.

[3] E.T. Whittaker, *A history of the theories of aether and electricity: from the age of Descartes to the close of the nineteenth century*, London, New York, Longmans, Green [etc.], 1910.

[4] F. Rosenberger, *Die Geschichte der Physik in Grundzugen; mit synchronistischen Tabellen der Mathematik, der Chemie und beschreibenden Naturwissenschaften sowie der allgemeinen Geschichte*, Braunschweig, F. Vieweg und Sohn, 1882–1890.

[5] G.T. Fechner, Uber die Verknupfung der Faradayschen Inductions–Erscheinungen mit den Ampereschen electro-dynamischen Erscheinungen, *Annalen der Physik und Chemie*, Leipzig **64** (1845) 337–345.

[6] V.L. Ginzburg, Superconductivity and superfluidity (what was done and what was not), *Physics-Uspekhi.* **40** (1997) 407–432.

[7] V.V. Parkhomchuk and A.N. Skrinskii, Electron cooling: 35 years of development, *Physics-Uspekhi.* **43** (2000) 433–452.

[8] G. Raciti, G. Cardella, M. De Napoli, E. Rapisarda, F. Amorini and C. Sfienti, Experimental evidence of ^{2}He decay from ^{18}Ne excited states, *Phys. Rev. Lett.* **100** (2008) 192503.1–192503.4.

[9] V.A. Karnaukhov, H. Oeschler, S.P. Avdeyev, E.V. Duginova, V.K. Rodlonov, A. Budzanowskic, W. Karczc, O.V. Bochkarev, E.A. Kuzmin, L.V. Chulkov, E. Norbecke and A.S. Botvina, Thermal multifragmentation, nuclear fog and critical temperature for the liquid–gas phase transition, *Particles and Nuclei, Letters* **4** (2002) 5–13.

[10] I. Tukaev, Electrostatic trap for localisation and confinement of likely charged particles, *Prog. Electromagnetics Res. M* **67** (2018) 21–33.
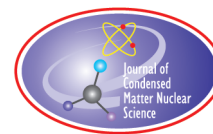
Research Article

Analysis of Martian Nuclear Spacecraft Powered by Low Energy Nuclear Reactions (LENRs)

Tae Ho Woo*

Department of Mechanical and Control Engineering, The Cyber University of Korea, 106 Bukchon-ro, Jongno-gu, Seoul 03051, Republic of Korea

Abstract

This paper presents a model to determine the optimum power source for a manned spacecraft to Mars; that is to say, the most economical and reliable power source. Low energy nuclear reactions (LENR) is evaluated for application to several areas including space travel, in which the vacuum of space cannot provide any propellant or other materials. It is assumed that LENR may become a practical source of useable energy. Several things must be considered for a successful journey from Earth to Mars, including the trip rout, the type of rocket, energy source, and the spacecraft speed. These are discussed for space travel using LENR. The velocity of the rocket increases as the mass flow rate decreases. The shortest route of a trip to Mars is selected to reduce cost.
© 2018 ISCMNS. All rights reserved. ISSN 2227-3123

Keywords: Energy, Low energy nuclear reactions (LENRs), Mars, Spacecraft

1. Introduction

I propose to find a power source for a spacecraft to Mars that is optimized to be economical and reliable. Conventional chemical energy is not strong enough compared to things like nuclear fusion. However, it would require a gigantic motor to produce fusion reactions in a spaceship that does from Earth to Mars. LENR is investigated, with the assumption that the vacuum of space cannot provide any propellant or other materials. The astronauts will have only the limited amount of materials they bring from Earth. It is assumed that LENR may become a practical source of useable energy.

Unmanned interplanetary missions from Earth to Mars were first attempted in 1960, when a USSR spacecraft failed to launch. The most recent mission is the InSight rocket, planned in 2016 and launched in 2018 [1]. Several robots and vehicles have operated on Mars. Most have performed detection and measurements of the planet surface. Atmospheric and seismic investigations have also been performed. The goal of many investigations has bene to look for biological substances which could be used to construct and support human colony in the near future. The search for evidence for water is one of the most important tasks. according to a recent report there is evidence for flowing rivulets of salty water in the summer [2].

---

*E-mail: thwoo@cuk.edu, thw@snu.ac.kr, Tel.: +82 2 6361 1924, Fax: +82 2 6361 1800.

The average distance from Earth to Mars is 55,000,000 km. Several things must be considered for a successful journey from Earth to Mars, including the trip rout, the type of rocket, energy source, and the spacecraft speed. These are discussed for space travel using LENR. From its introduction in 1989, LENR has been interesting because it is a very abundant, clean and green energy source. Although there have been many studies of LENR, it still needs to be developed for practical or realistic applications. It would be especially effective for comparatively low power applications.

Several propulsion methods for deep-space rockets have been developed [3]. Most spacecraft use chemical fuel, in which the hot reaction mass is expelled from the vehicle [3]. Until now, this has made journeys to Mars vary from 150 to 300 days; Viking 1 (1976) took 335 days, and the Curiosity lander (2012) took 253 days [4]. Charles Bolden of NASA said that in the future, the proposed Variable Specific Impulse Magnetoplasma Rocket (VASIMR) could reach Mars within five months. With this method, radio waves are used to ionize and heat propellant, and magnetic fields would accelerate the plasma to generate thrust [5,6]. In 2009, an experiment was done with a VASIMR in the International Space Station (ISS) with a full operational capacity of 200 kW [7].

In the search for other power sources for interplanetary missions, the LENR catalysis-based nuclear reaction is investigated in this paper. In 1989 Dr. Martin Fleischmann and Dr. Stanley Pons announced success in generating nuclear reactions in laboratory experiments at the University of Utah [8]. This effect is also called Chemically Assisted Nuclear Reactions (CANR), because the nuclear behavior is apparently caused by metallic catalyzed reactions [9]. In the conventional description of nuclear fusion reactions, the electromagnetic force causes the nuclear reaction by fusing the nuclei. In contrast, with lender (or see ANR) it is assumed the nuclear reactions occur in the space of some lattices such as palladium where the vacuum exists with all huge area given the scale of nanoscopic molecules of hydrogen. The area is relatively huge because there is "plenty of space at the bottom" as Richard Feynman put it in his famous lecture [10]. According to Miley [11–21], a highly dense molecular structures of palladium could produce abundant heat, with proton-deuterium interactions occurring at a level of 10^{24} atoms per centimeter. The heat can be converted to electrical energy. The expected energy production is estimated and it is proposed as a strategy for interplanetary travel. Section 2 explains the methods used in this study. Section 3 describes the results of the study. Some conclusions are drawn in Section 4.

2. Method

There are several issues to consider in a journey to Mars, such as route, and the layout of the spacecraft. The velocity of the spacecraft is related to the quality of the trip, and velocity depends upon the energy source. Furthermore, the combinational functions of these issues are important because the failure of a journey could be caused by an accident.

2.1. The route of journey

The distance to Mars is a key issue, and varies depending on the positions of Earth and Mars. The two planets are seldom within the shortest possible distance. The path is not in two-dimensional space, but within the sun's polar coordinate system. Figure 1 shows a diagram of the Mars journey where the orbits of Earth and Mars are plotted. Choosing the shortest distance is very important to reduce the travel duration, the orbits are one of the most important considerations. The target position is predicted. The effect of both Earth and Mars orbits are used to calculate the path. In some cases, a flyby can be used to accelerate the spacecraft. The velocity of the rocket is increased by a factor of two compared to the flyby planet speed. Hence, the flyby is a method of gravity assisted operation [22].
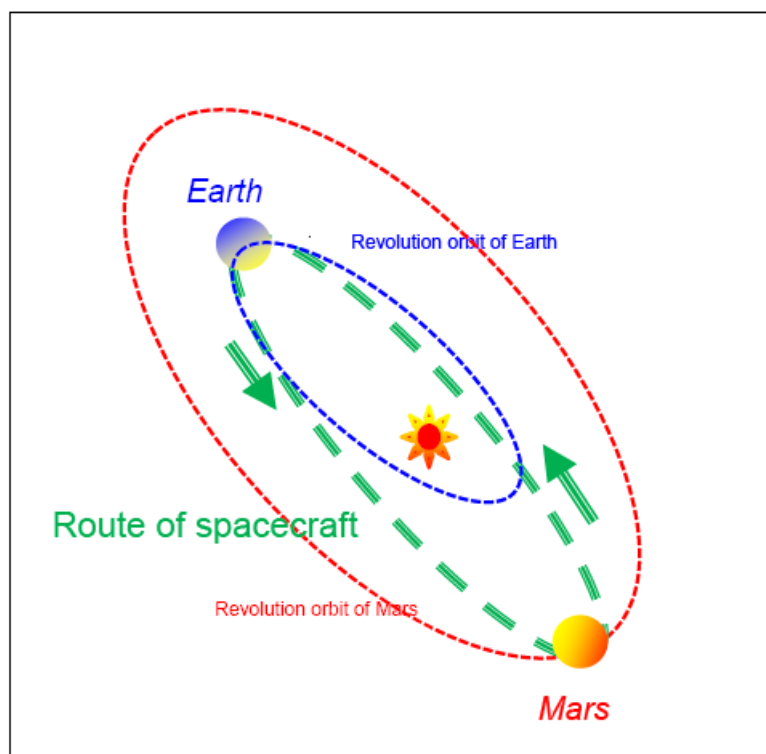
Figure 1. Diagram of the route to Mars journey.

2.2. The design of the spacecraft

In the design of a spacecraft suitable for a man to trip to Mars, there must be a well-protected crew cabin, as shown in Fig. 2. This section of the spacecraft includes a rotating cabin to produce artificial gravity. Even if the gravity is not the same as Earth's, it should be enough to allow humans to stand up and walk. The radiation shielding of the crew cabin is a critical matter to preserve health of the crew during the trip. The ratio of the power produced by the rocket engine and the design energy and velocity of the spacecraft can be calculated.

2.3. The source of energy

The spacecraft would include a heat-driven electric generator. Figure 3 shows the configuration of the LENR in a palladium Face Centered Cubic (FCC) lattice. The LENR heat source produces the combined energy of all of the individual LENR battery units. The heat is produced by D_2 (or H_2) gas reactions with the palladium. In Fig. 4, the heat is converted to electricity which is supplied to the relevant systems of the spacecraft. Figure 5 shows graphs of proton and palladium interactions as the transvers view of collisions, ion ranges, and collision events at 20 keV proton injection into the palladium.
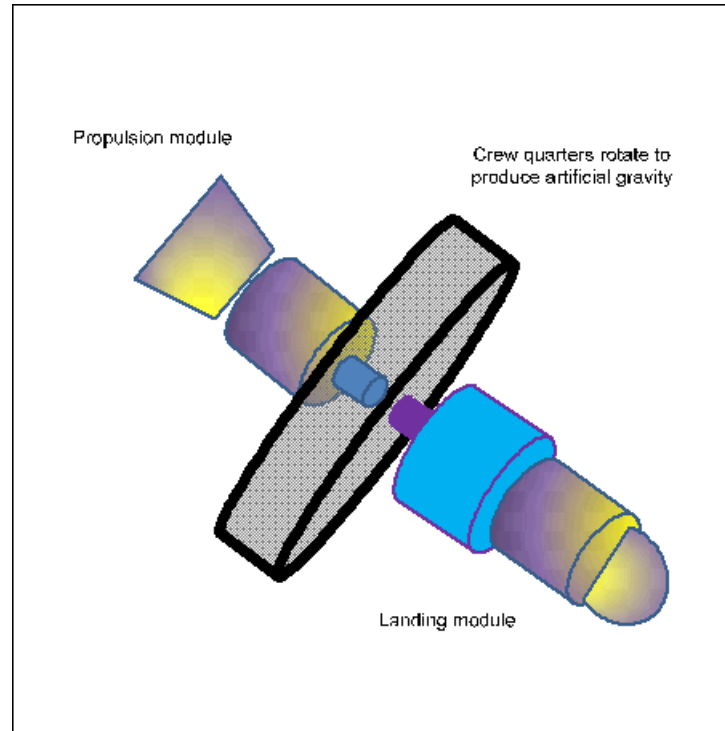
Figure 2. Simplified configuration of Martian spacecraft.

2.4. The speed of spacecraft

Currently, the speed of a Martian rocket is 20,000 km/h (=5.556 km/s) and the duration of the trip averages 114.58 days (about 3 months 25 days) [4]. The relation of power, force, and speed is as follows [23]:

$$P = F\frac{d}{t},\tag{1}$$

where P is power (kW), F the force (N), d the distance (m), and t is time (s). Using this equation, one can estimate the effects of different power sources. Table 1 shows the relationship between energy and speed of spacecraft [24]. Using Eq. (1), the thrust is 0.5 N in Table 1. So, the velocity of LENR is 2.8 km/s. So, for the source from LENUCO, LLC, the speed is obtained as follows where the power is 1.5 kW [25]:

Table 1. Relationship between energy and speed of spacecraft.

	Min. power/thrust (kW/N)	Effective exhaust velocity(km/s)
Soil fuel rocket	0.5	1
Bipropellant rocket	2.5	5
LENR rocket	1.4	?
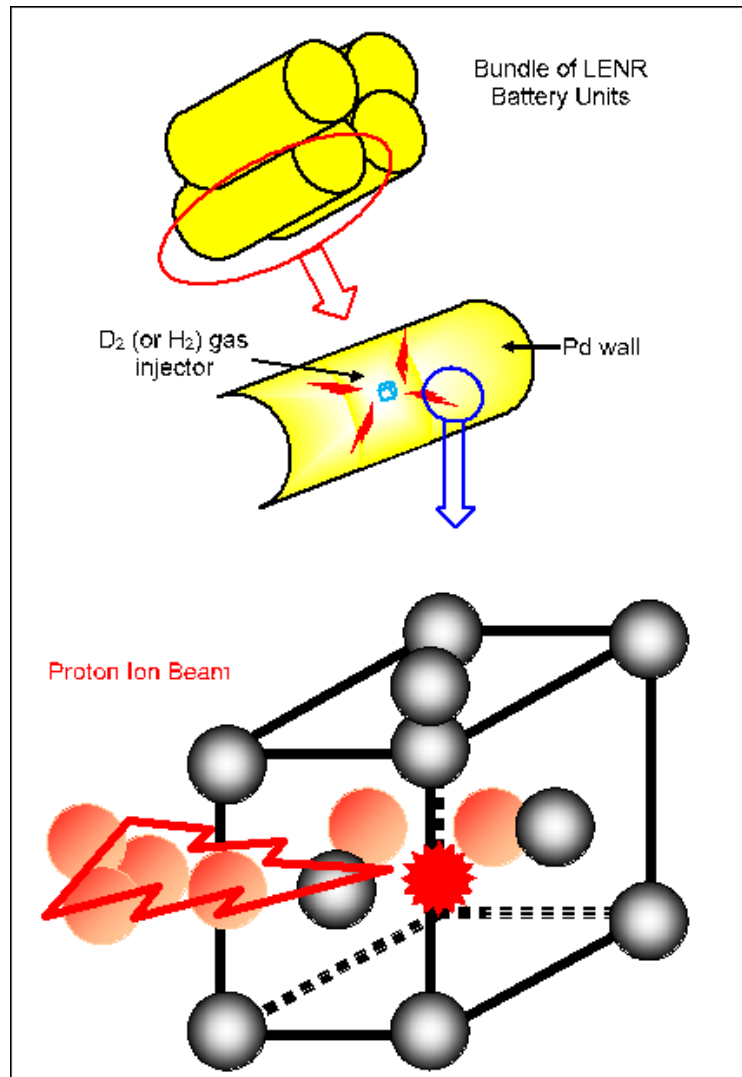
Figure 3.   Configuration of the LENR in the palladium's FCC lattice.

$$\frac{d}{t} = \frac{1.5\,\text{kW}}{0.5\,\text{N}} = 3\,\text{km/s}. \tag{2}$$

For the stacked form with 30 kW [25]:

$$\frac{d}{t} = \frac{30\,\text{kW}}{0.5\,\text{N}} = 60\,\text{km/s}. \tag{3}$$
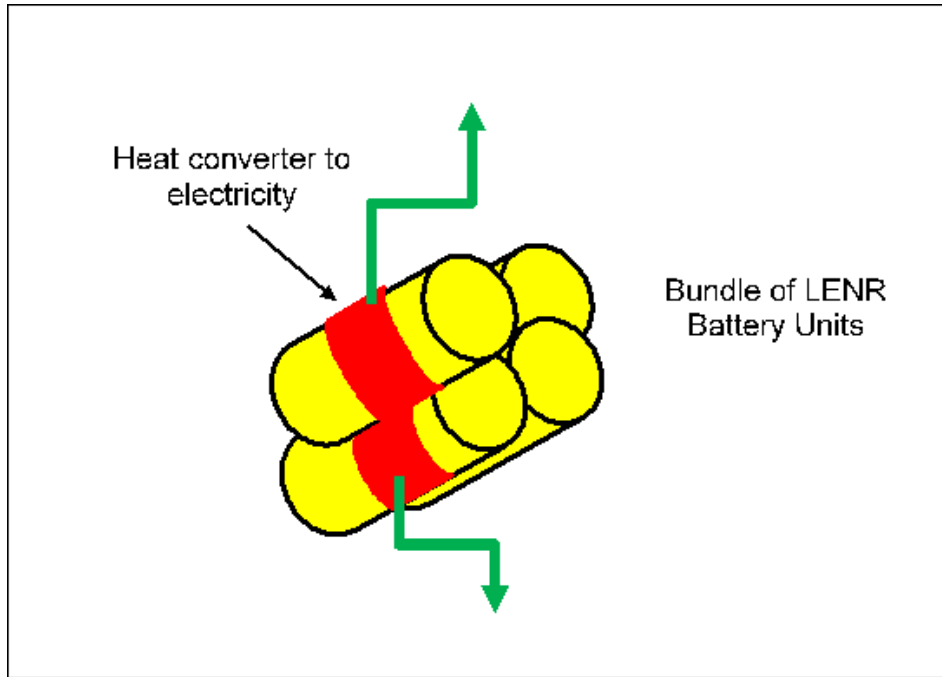
Figure 4.   Electric production by the heat coils.

Hence, the period is reduced from 114.58 to 10.61 days:

$$\frac{114.58 \, \text{days}}{60 \, \text{km per s}/5.556 \, \text{km per s}} = 10.610 \, \text{days}. \tag{4}$$

In another relation, the thrust is [26]:

$$F = \dot{m}(v_2 - v_1), \tag{5}$$

where $\dot{m}$ is mass flow rate (kg/s), v_1 the inlet velocity, and v_2 is the outlet velocity. Assuming $v_1 = 0$ and using Eq. (1) we get:

$$P = (\dot{m}v_2)\,\frac{d}{t} = \dot{m}v_2^2. \tag{6}$$

Then,

$$\sqrt{\frac{P}{\dot{m}}} = v_2. \tag{7}$$

The velocity is obtained from the mass and power.
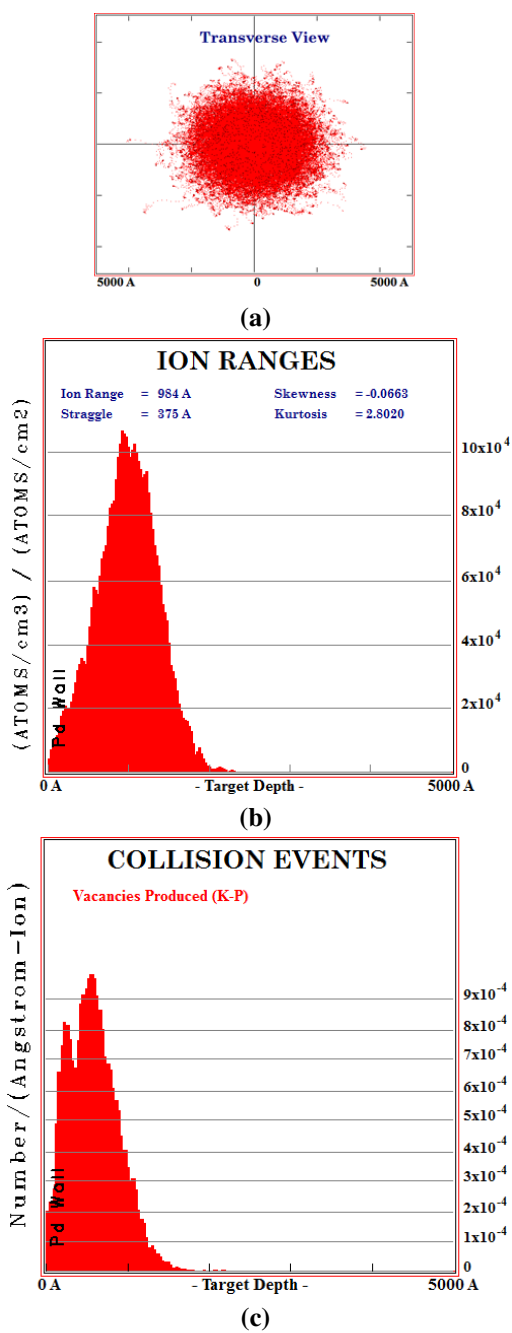
Figure 5. Graphs of proton and palladium interactions. (a) Transverse view of collisions, (b) ion ranges, and (c) collision events (20 keV).
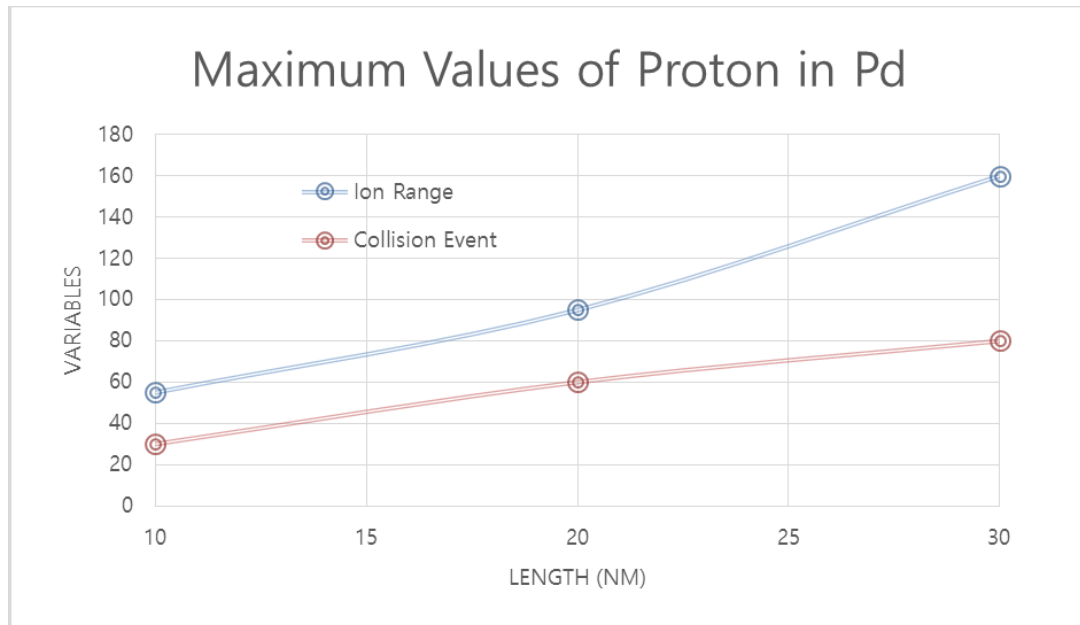
Figure 6. Maximum values of the proton in palladium as ion range and collision event.
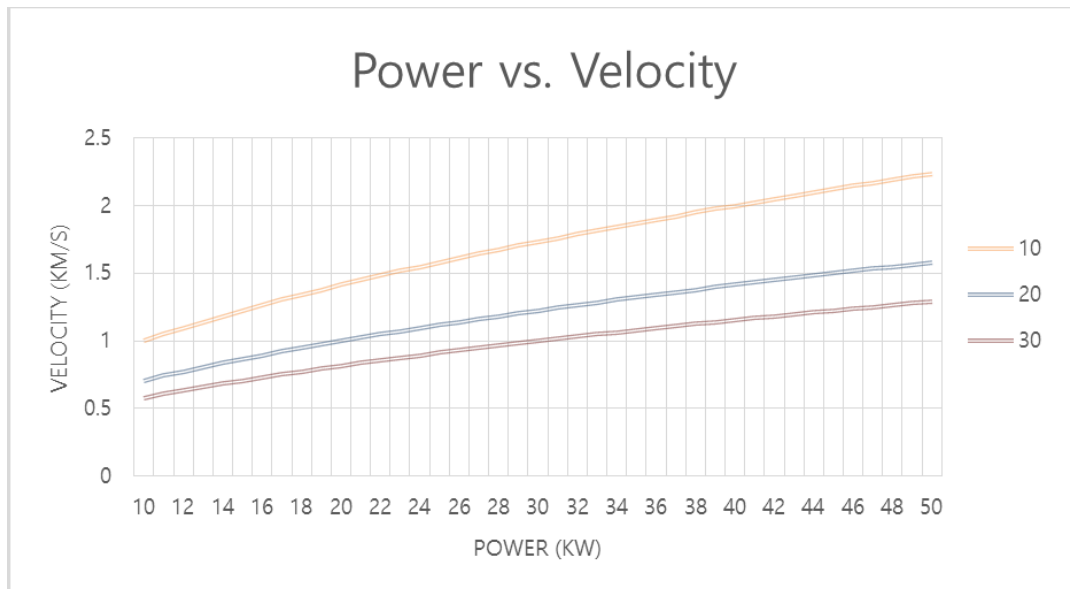
Figure 7. Relation of power and velocity in mass flow rate of 10, 20 and 30 kg/s.

3. Results

Simulations of the energy productions by LENR and the relevant velocity are estimated. Figure 6 is the maximum values of the proton in palladium as ion range and collision event. In Fig. 7, the relation of power and velocity in mass flow rate of 10, 20, and 30 kg/s is seen. The velocity of the rocket increases as the mass flow rate decreases in which the reasonable velocity of spacecraft could be obtained. Regarding the route of the spacecraft, the shortest route of the Martian trip could be selected to reduce the cost of travel.

4. Conclusions

The concept of building a human colony on another planet can be considered. Travel to the other planet is the first step, and then the next step is the building a city including industries like those on the Earth. Here are some findings in this work

- The new kind of power source is investigated.
- LENR might be applied to the spacecraft.
- The effect on a trip to Mars is analyzed.
- Given the large reduction in the duration of the trip, a successful colony on Mars could be established in near future.

An LENR propulsion system would be better, more economical and safer. Conventional power sources such as chemical or solar energy are difficult to make, and a trip using them is of long duration. Therefore, the LENR concept would be an important and attractive perspective energy source. An LENR powered rocket could be considered as one of the best power sources for a trip to Mars. Especially, heavy manned spacecraft systems need a compact and cheap system for the general facility where human and living spaces must be harmonized for the long duration of the trip. Reducing the duration of the trip is a very important matter for interplanetary travel. Especially, for traveling beyond Mars, the current power sources cannot be used for manned exploration because it would take too long.

Using VASIMR power, lunar and Martian missions and deep space travel may be possible at a greatly reduced cost. A high power density source will be needed for destinations or beyond Mars. For the crews, this will be needed to overcome problems such as health and psychological factors. Radiation in the outer parts of the solar system is an extreme hazard to humans. Spacecraft will need to be equipped with strong shielding material. New kinds of alloy metal might be developed for this purpose. For commercial traffic systems, safety is as important as economic factors would be. The radiation shielding will have to be installed on the spaceship surface. Furthermore, very long journeys might cause considerable psychological problems.

International cooperation in developing Martian rocket travel might be a better system than the current individual nations based Mars exploration strategy. If the United Nations (UN) were to take a major role in assembling the exploration systems, the construction would be done effectively. Considering the natural and social structure of the world, it is reasonable to prepare for a future colony on Mars for a new society and industry could be established. This colony might eventually initiate trade between Mars and Earth. The oars from Mars might be shipped to earth by specially designed spacecraft. Once this kind of industry is launched, social relations would be set up and a flourishing space industry would be born.

References

[1] W.B. Banerdt, S. Smrekar, L. Alkalai, T. Hoffman, R. Warwick, K. Hurst, W. Folkner, P. Lognonné, T. Spohn, S. Asmar, D. Banfield, L. Boschi, U. Christensen, V. Dehant, D. Giardini, W. Goetz, M. Golombek, M. Grott, T. Hudson, C. Johnson, G. Kargl, N. Kobayashi, J. Maki, D. Mimoun, A. Mocquet, P. Morgan, M. Panning, W.T. Pike, J. Tromp, T. van Zoest, R. Weber

and M. Wieczorek, The insight team, insight: an integrated exploration of the interior of mars, *43rd Lunar and Planetary Science Conference*, March 19–23, 2012, The Woodlands, TX, USA.

[2] AP, Life on Mars? NASA says planet appears to have flowing water, Associated Press (AP), Young Broadcasting of Knoxville Inc., A Media General Company (2015). http://wate.com/2015/09/28/life-on-mars-nasa-says-planet-appears-to-have-flowing-water/>.

[3] Science Daily, Spacecraft propulsion, Rockville, MD, USA (2015) <http://http://www.sciencedaily.com/terms/spacecraft_propulsion.htm>.

[4] F. Cain, Universe Today (2013) <http://www.universetoday.com/14841/how-long-does-it-take-to-get-to-mars/>

[5] F. Morring, Commercial route. *Avi. Week & Space Technol.* **172**(6) (2010) 20–23.

[6] N. Stapinsky, Nautel's space oddity (RF generator for Ad Astra), Plant Magazine, May. 13, 2010, Toronto, Canada, <http://www.plant.ca/production/nautels-space-oddity-473/>.

[7] As Astra Rocket Company, VASIMR®VX-200 reaches 200 kW power, Milestone, Webster, TX, USA (2009) <http://www.adastrarocket.com/Release_200kW_01Oct2009Final.pdf>.

[8] E-Cat World, What is LENR? (2015) <http://www.e-catworld.com/what-is-lenr/)>.

[9] LENR-CANR.org, Home, Chamblee, GA, USA (2015). <http://lenr-canr.org/wordpress/>.

[10] E. Drexler, *There's Plenty of Room at the Bottom,* Richard Feynman, Pasadena, 29 December 1959) (2009). <http://metamodern.com/2009/12/29/theres-plenty-of-room-at-the-bottom%E2%80%9D-feynman-1959/>.

[11] L. Holmlid, H. Hora, G. Miley and X. Yang, Ultra high-density deuterium of rydberg matter clusters for inertial confinement fusion targets, *Las. and Part Bea.* **27** (2009) 529.

[12] A.B. Karabut, A.G. Lipson and A.S. Roussetsky, Correct measurement of D–D reaction yield and in high current pulse-periodic deuterium glow discharge operating at 0.85–1.20 keV voltage applied, *Proc. 8th Int. Conf. of Cold Fusion*, Italy, 2000, p. 335.

[13] A. Lipson, B.J. Heuser, C. Castano, G.H. Miley, B. Lyakhov and A. Mitin, Transport and magnetic anomalies below 70 K in a hydrogen-cycled Pd foil with a thermally grown oxide, *Phys. Rev. B.* **72** (2005) 212507.

[14] A.G. Lipson, B.J. Heuser, and C.H. Castano, Celik-Aktas A, observation of a low-field diamagnetic contribution to the magnetic susceptibility of deformed single crystal PdH$x(x \simeq 4.0 \times 10^{-4})$, *Phys. Lett. A.* **339** (2005) 414.

[15] A.G. Lipson, A.S. Rusetskii, A.B. Karabut and G.H. Miley, D–D reaction enhancement and X-ray generation in a high-current pulsed glow discharge in deuterium with titanium cathode at 0.8–2.45 kV, *J. Exp. Theoret. Phys.* **100**(6) (2005) 1175.

[16] G.H. Miley, Product Characteristics and Energetics in thin-film electrolysis experiments, *Proc. Int. Conf. on Cold Fusion*, Vancouver, Canada, 1998, pp. 241–246.

[17] G.H. Miley and J.A. Patterson, Nuclear transmutations in thin-film nickel coatings undergoing electrolysis, *J. New Energy.* **1**(3) (1996) 5.

[18] G.H. Miley, G. Narne, M.J. Williams, J.A. Patterson, J. Nix, D. Cravens and H. Hora, Multilayer thin-film microspheres after electrolysis, *Proc. Int. Conf. on Cold Fusion*, Vol. 2, edited by New Energy and Industrial Tech. Dev. Org., Japan, 1996,. p. 529.

[19] G.H. Miley and X. Yang, Deuterium cluster target for ultra-high density, *18th Topical Meeting on the Technology of Fusion Energy,* San Francisco, CA, USA, 2009.

[20] G.H. Miley, X. Yang and H.A. Hora, A potentially game changing "green" power source based on low energy nuclear reactions (LENRs), Nuclear and Emerging Technologies for Space 2012, The Woodlands, TX, USA, March 19–23, 2012.

[21] G.H. Miley, N. Luo, A.G. Lipson and A.B. Karabut, A unique plasma discharge driven solid-state X-ray laser, SPIE Ablation, Taos, NM, USA, 2004.

[22] NASA, Basics of Space Flight, 2015, Sec. 1, Ch. 4, NASA (National Aeronautics and Space Administration) Jet Propulsion Laboratory.

[23] J. Yoon, Convert thrust to horsepower (2004). <http://www.aerospaceweb.org/question/propulsion/q0195.shtml>.

[24] Wikipedia, Spacecraft propulsion (2015). <https://en.wikipedia.org/wiki/Spacecraft_propulsion>.

[25] G.H. Miley, J.J. Kim, E. Ziehm, T. Patel and B. Stunkard, Progress in development of an LENR power cell for space, *Proc. of Nuclear & Emerging Technologies for Space* (NETS), 2015, Albuquerque, NM, USA, February 23–26, 2015.

[26] C.E. Dole, *Flight Theory and Aerodynamics*, Wiley, New York, NY, USA, 1981.
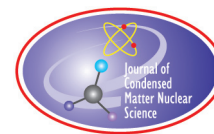
Research Article

Observation of Non-exponential Decay in X-ray and γ Emission Lines from Co-57

Florian Metzler, Peter Hagelstein*and Siyuan Lu

Massachusetts Institute of Technology, Cambridge, MA, USA

Abstract

On May 20, 2017, we started a series of experiments with the goal of observing vibrationally induced excitation transfer of the 14.4 keV nuclear state from excited Fe-57 to ground state Fe-57 nuclei. A steel plate with a Co-57 substrate on the front surface was vibrated by a piezoelectric transducer near 2.21 MHz; and emission in the X-ray region was recorded with an Amptek X-123 detector on the front side, a scintillator/photomultiplier detector on the back side, and a Geiger counter on the back side. The experiments provided a negative result for the originally sought ultrasonically induced excitation transfer effect, but instead showed non-exponential time histories for photon counts on all three detectors. Specifically, increased emission of the 14.4 keV gamma, Fe K_α and K_β X-rays was observed at early time. This enhancement was present at the start of the experiments at about 19% above expected levels for the 14.4 keV gamma, and about 17% for the Fe K-alpha, with the enhancement decaying away with a time constant of about 2.5 days. Emission on the Sn K_α was consistent with the expected exponential decay of Co-57 at the 1% level. Non-exponential decay with an enhancement at early time was also seen for the weak Fe K_α escape peak, and in the back-side Geiger counter data; and a reduction at early times was seen on the higher energy channels of the scintillator/photomultiplier detector counter both looking at the back side. The observed non-exponential decay is connected with the tightening of bolts on wooden clamps on the corners of the steel plate, which apply mechanical stress to the sample. Candidate interpretations are considered, in which the stress induced in the steel results in scattering and generation of THz phonons by dislocations, and in which phonon–nuclear coupling mediated by THz phonons leads to the transfer of nuclear excitation to other nuclei ("excitation transfer"), which can cause spatial delocalization of the source and angular anisotropy of the photon emission.
© 2018 ISCMNS. All rights reserved. ISSN 2227-3123

Keywords: Anomaly, Co-57, Excitation transfer, Non-exponential decay, Phonon–nuclear coupling

1. Introduction

The announcement of the excess heat effect in an electrochemical experiment with Pd in heavy water by Fleischmann and Pons in 1989 [1,2] was met with great skepticism, especially among physicists, in part because the effect was unexpected and seemingly impossible to reconcile with known nuclear physics and solid state physics. The many subsequent observations of the effect [3] support the contention that the excess heat effect is real, but more than 28

years later, there is no accepted explanation as to why it might occur. Under normal conditions when a nuclear reaction produces energy, the resulting energy is carried off as energetic nuclear radiation. The absence of energetic nuclear radiation commensurate with the energy produced in the Fleischmann–Pons experiment provides reason for skepticism, and also provides a barrier to understanding the reaction mechanism [4]. For example, in an incoherent deuteron-deuteron fusion reaction it is possible to observe p+t and n+^{3}He to confirm the existence of the two dominant reaction pathways, and to measure the particle momenta and energies in order to shed light on the reaction kinematics. With no energetic reaction products associated with energy production in the Fleischmann–Pons experiment, a similar approach cannot be used to study the reaction mechanism. Because of this, it has been impossible to clarify unambiguously what nuclei are involved in Fleischmann–Pons experiments and derivative experiments, or how the reaction works (other than to say that it does not work like a conventional incoherent nuclear reaction).

Over the years there have been several hundred papers published describing a wide range of theoretical ideas as to how an excess heat effect might occur. Some of the proposals are in conflict with experiment as they predict energetic radiation. For those proposals which do not predict energetic radiation it is difficult to make an unambiguous connection with the Fleischmann–Pons experiment since they tend to involve mechanisms which have not been experimentally tested. Without independent experimental confirmation of at least some of the intermediate parts it is difficult to develop much confidence that any such model is correct. For example, we are currently interested in models based on a relativistic phonon–nuclear interaction [5], in which the absence of energetic nuclear radiation in Fleischmann–Pons type experiments is accounted for through the subdivision of 24 MeV quanta (the mass difference between D_2 and ^{4}He) to lower nuclear transitions, and eventually to down-conversion of the nuclear excitation into a commensurate number of phonons [6,7]. While the theoretical arguments seem strong, an unambiguous experimental confirmation of the underlying phonon–nuclear interaction and the resulting down-conversion effect is required.

Based on experience gained from the interaction of theory and experiment over the years since 1989, it seems clear that there will not be agreement on mechanism based on interpretations of results from Fleischmann–Pons type experiments alone. What is needed are different but related experiments, in which the same mechanisms are involved, but which permit an unambiguous interpretation [8]. We have previously advocated for up-conversion experiments, in which vibrations are up-converted to produce nuclear excitation, and we have interpreted collimated X-ray emission in the experiments of Karabut [9–17], and of Kornilova and coworkers [18–22], as due to the up-conversion of a commensurate number of vibrational quanta i.e. phonons.

Theory suggests that for phonon–nuclear coupling to be strong enough to show observable effects, the frequency of a vibrational mode ought to be as high as possible. However, suitable commercial sources for THz vibration excitation have not been available to us at the time of the reported experiments. Collimated X-ray emission in the Karabut experiment and in the Kornilova experiment suggest that observable effects may also occur at lower frequency vibrations. Cardone and coworkers have reported a variety of anomalies in experiments in which a steel bar is subject to vibrations at 20 kHz; including neutron emission [24–29] alpha emission [25,26,30–32], and elemental and isotopic anomalies [33–35] (see the reviews [36,37]). We interpret the observations of Cardone and coworkers as possibly resulting from up-conversion mechanisms at play. All of this suggested the possibility of observing effects from up-conversion in experiments with vibrations well below the THz regime.

Over recent years, we have been working toward experiments to experimentally investigate phonon–nuclear coupling and expected mechanisms and effects resulting from it. We tried earlier to make use of MHz vibrations to drive up-conversion in steel plates and excite ground state iron nuclei. In these up-conversion experiments, we sought – but did not find – collimated X-ray emission [38,39]. We have been able to drive metal plates up to 10 MHz. One set of up-conversion experiments involved high power piezoelectric transducers that have resonances near 2.2 MHz and could deliver over 100 W of vibrational energy to the plate [40]. We have also acquired and developed radiation detectors as diagnostics for changes in photon emission resulting from up-conversion and excitation transfer experiments. Moreover, in many of these experiments, compressional wooden clamps were applied to the edges of the sample plates,

so as to provide damping to the vibrations. This measure was motivated by the theoretical models suggesting that the presence of such damping could facilitate observable effects [61]. None of our conducted up-conversion experiments showed effects indicative of phonon–nuclear coupling at play. Consequently, we explored ways of increasing the chances of generating observable effects if they exist.

We have recently proposed an excitation transfer experiment, where phonon exchange with a highly excited vibrational mode transfers the excitation from excited nuclei to identical ground state nuclei located elsewhere [23]. Nuclear excited states in such an experiment originate from the decay of radioactive nuclei. Whereas an up-conversion experiment would require a high phonon–nuclear coupling strength to show observable effects, the newly proposed excitation transfer experiment would require a comparatively lower phonon–nuclear coupling strength and relatively minimal energy exchange with vibrations. Consequently, conditions for an excitation transfer experiment with observable effects are expected to be more easily and more likely created compared to conditions for an up-conversion experiment with observable effects.

In the Spring of 2017, we began the first set of excitation transfer experiments. In practice, these experiments differed from the earlier up-conversion experiments in that now the experimental setup included a constant source of short-lived iron nuclei in excited states. This was the case because of the presence, on the surface of the steel plate, of radioactive Co-57 which decays into excited Fe-57. The goal then was to look for effects resulting from the transfer of such given excitation to other nuclei (originally in ground state) during vibrational stimulation. The first series of experiments employed the above mentioned 2.2 MHz piezoelectric transducer for inducing vibrations. Each experiment lasted several hours. Compressional wooden clamps had been applied to the sample plate once at the beginning of the series of experiments and left in place. When considering the data of each of these experiments, the results appeared negative: We did not notice changes in photon emission correlated with vibrational stimulation.

However, when analyzing the entirety of acquired data across the full series of these early experiments, i.e. across several days, we did notice something unexpected: from the beginning of the series onward, the photon emission from the Fe-57 nuclear transition at 14.4 keV showed a non-exponential time history, as did the Fe K_α and K_β X-rays. We initially suspected a problem with the Amptek X-123 X-ray detector, but after further analysis we gained confidence that the X-123 detector functioned properly during the experiment (for example, the Sn K_α time history was consistent with normal exponential decay of the Co-57 at the percent level, and different detectors reported non-exponential time histories simultaneously).

After becoming aware of the unexpected observations across the series of shorter experiments from May 20-31, we began to consider the data across this period as representing a single exploratory experiment which we now refer to as the May 20 experiment. No physical change was made to the experimental setup of said May 20 experiment after applying the compressional clamps and placing the sample in front of detectors on May 20, 2017.

As a result of the unexpected observations, we were faced with an array of issues. Foremost among them: Is the effect real, or an artifact of the detectors or of the experiment? Also important is the interpretation of the observed effect: Why should there be a non-exponential time history, and what is the associated physical effect? Another question concerns the cause of the anomaly: The anomaly was present at the beginning of the experiment, which suggests that the cause was something that happened prior. This needed to be clarified, and many runs have since been carried out which help shed light on the experiment and effects observed. In such subsequent runs, the effect has been consistently observed (albeit comparatively weaker than in the first experiment) and these runs will be described in more detail in future reports.

In this initial paper, our focus will be primarily on the first observation of the anomaly, in part because it represents a critical milestone in this experimental campaign, and in part because much effort has gone into the analysis of the data. What follows is a detailed description of the experimental setup and resulting observations. At the end of this paper, we consider possible interpretations as well.
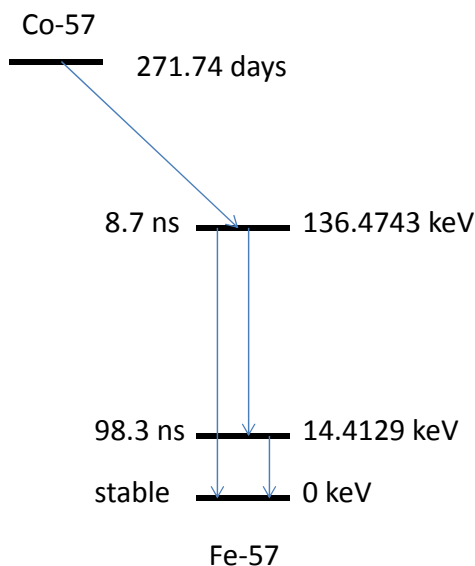
Figure 1. Simplified version of the nuclear decay scheme for Co-57; energy levels and half-life times are from the NUDAT2 online database of Brookhaven National Lab.

2. Beta Decay of Co-57, and Fe-57 Nuclear Levels

In the excitation transfer experiments introduced above, we use Co-57 to produce excited nuclear states of Fe-57. Excitation transfer effects are considered to affect the lowest two excited states of Fe-57 which are described in the following section. A brief review of some of the theoretical ideas associated with phonon–nuclear coupling, excitation transfer, and other mechanisms which motivate these experimental design choices is provided in Appendix A.

2.1. Co-57 beta decay scheme

A simplified version of the nuclear decay scheme of Co-57 [41–44] is illustrated in Fig. 1. Co-57 beta decays through electron capture, resulting 99.80% of the time [45] in the excited state of Fe-57 at 136.47 keV . A small fraction of the time, there is decay to higher energy Fe-57 states [46,47], which we will not concern ourselves with in what follows. The dominant gammas that result are the 14.4129 keV transition (which is widely used in Mössbauer studies), and two harder gamma transitions at 122.0614 keV and at 136.4743 keV.

2.2. Phonon exchange effects under consideration

We were most interested in the possibility of an excitation transfer effect involving the Fe-57 14.4 keV state, since the half-life is reasonably long (98.3 ns) and the transition energy reasonably low. An excitation transfer effect might manifest as delocalization through a decrease in the 14.4 keV gamma emission measured in the vicinity of the Co-57 source coinciding with an increase of such gamma emission elsewhere, or perhaps through collimation of the 14.4 keV gamma. Also possible might be an excitation transfer effect for the 136.5 keV state, but excitation transfer involving this state should be weaker compared to the lower state since the half-life is shorter (8.7 ns) and the transition energy is higher.
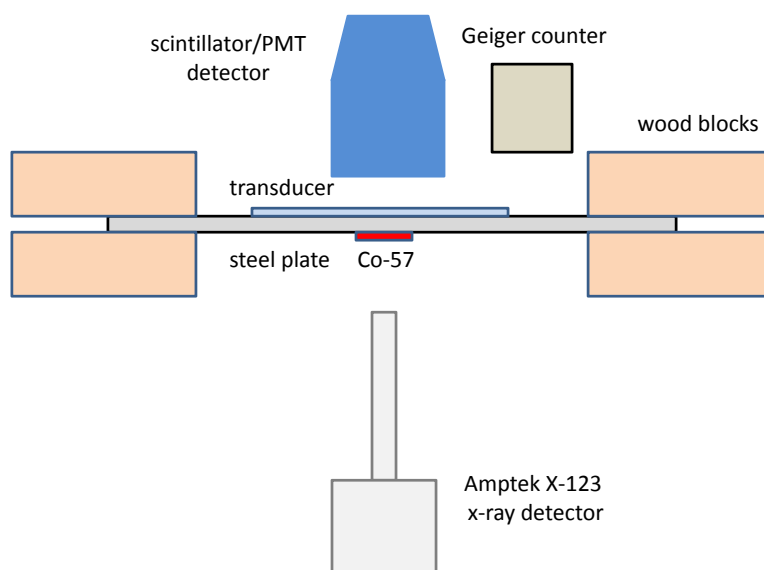
Figure 2. An idealized schematic of the experiment. The transducer is on top of the steel plate, with the Co-57 underneath. Wood blocks are clamped onto opposite corners (here idealized as sides) of the steel plate to add loss. The Amptek X-123 X-ray detector views the Co-57 from below; the scintillator/PMT detector views the sample from above, and the Geiger counter views the top side of the steel plate near a corner away from the Co-57.

3. Experimental Details, May 20 Experiment

As mentioned above, the initial goal of the experiment was to look for evidence of excitation transfer induced by vibrations near 2.21 MHz, generated with a piezoelectric transducer. The plan was to create a sample with excited state Fe-57 resulting from from the decay of Co-57, apply vibrations, and to look for a loss of the strength of the 14.4 keV nuclear transition at the site of the Co-57 when vibrations are present.

3.1. Experimental setup

A simplified schematic of the experiment is shown in Fig. 2, indicating the primary elements of the experimental configuration (details concerning individual elements follow below). Four pieces of plywood were bolted down on opposite corners of the steel plate to provide loss [40]. Three holes were drilled in each piece of plywood for bolts, and nuts were screwed on with a torque wrench, resulting in compressional stress on the plate of approximately 2000 lbsf. As described below, Co-57 was placed on the front side of the steel plate through evaporation of an acid solution, with the front side facing down in the figure, above a coarse aluminum protective mesh (not shown in the schematic), with the Amptek X-123 X-ray detector below. The scintillator/PMT detector looks down on the back side, off to the side of the transducer. The Geiger counter also views the back side of the steel from above, oriented over a free corner away from the Co-57. A side-view photograph of the steel plate, wood clamps, and detectors is shown in Fig. 3.
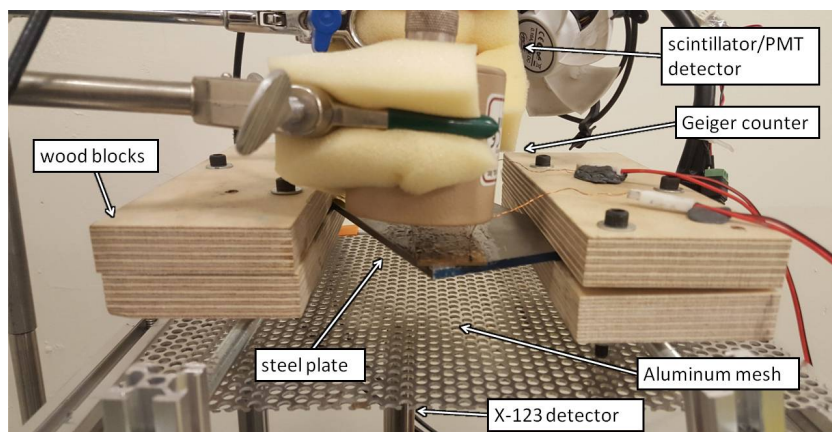
Figure 3. Experimental setup. Four plywood clamps are tightly bolted onto the steel plate, which rests on a rigid rack for support. Below is a protective coarse aluminum mesh which rests on an aluminum frame. Below the aluminum mesh is the Amptek X-123 X-ray detector, which rests on foam (not shown) to minimize vibrational coupling. Above the steel plate on top of the corner of the steel plate is the Geiger counter in a holder with foam. Behind the Geiger counter is a scintillator/PMT X-ray detector.

3.2. Steel plate

We used a 3"×6"×5/32" steel plate made of low-carbon steel (McMaster-Carr part number 1388K546) shown in Fig. 4. The uppermost peak of the $n = 3$ fundamental resonance for this (loaded) plate is observed around 2.22 MHz (Fig. 5), slightly below the transducer resonance (the resonance of this transducer is a bit higher than for the one discussed in Ref. [40]). The corresponding longitudinal sound speed of steel estimated from this frequency is 5.870×10^5 cm/s with an uncertainly on the order of 1% due to variations present in the thickness of the plate.
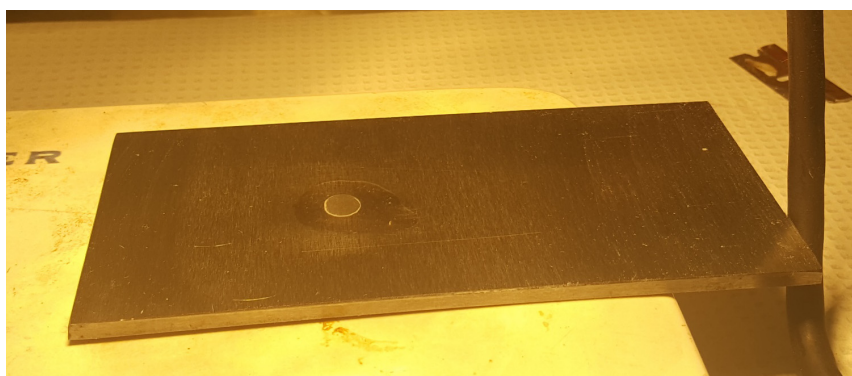
Figure 4. Steel plate sample with 200 μCi of evaporated Co-57.

3.3. Co-57

We obtained 1000 μCi of ^{57}CoCl$_2$ from Eckert & Ziegler, in 0.1 M HCl, which came as 0.15 ml of solution in a 0.3 ml vial in November 2016. Roughly 1/3 was evaporated onto the steel (which involved using a micropipette to move some of the solution from the vial to the steel plate, and then waiting on the order of an hour for evaporation in air). The half-life of Co-57 is 271.74 days, so by the time of the May 20 experiment there was roughly 200 μCi remaining on the plate. The evaporated solution was covered by epoxy (J-B Weld 50112 Clear 25 ml ClearWeld Quick-Setting Epoxy Syringe) in order to prevent flaking off or physical loss of Co-57 activity. A ring-shaped residue is present at the end of the evaporation. The size of the evaporated region can be seen in Fig. 4 as the small whitish region approximately 1 cm in diameter, and the epoxy covering can be seen as the clear layer approximately 3 cm in diameter over and surrounding the evaporated region.

3.4. Transducer and gel

Ultrasonic vibrations were driven by a high-power 1"×6.5" piezoelectric transducer rated for 1.95–2.07 MHz from PCT Systems Inc. For unloaded low power operation at room temperature on Styrofoam, and for operation on steel, the transducer's resonance was found to be slightly higher than rated (approximately 2.26 MHz). For mechanical coupling of the transducer to the steel we used VersaSonic multipurpose high temperature ultrasonic couplant from ECHO Ultrasonics. The piezo crystal was driven by an E&I A150 Broadband Power Amplifier through an Amplifier Research DC2600A dual directional coupler. When the transducer was driven we made use of a 20% duty cycle to avoid high temperature in the piezo crystal. The electrical power reported in Fig. 5, and later on in the paper, refers to the peak (and not average) power.
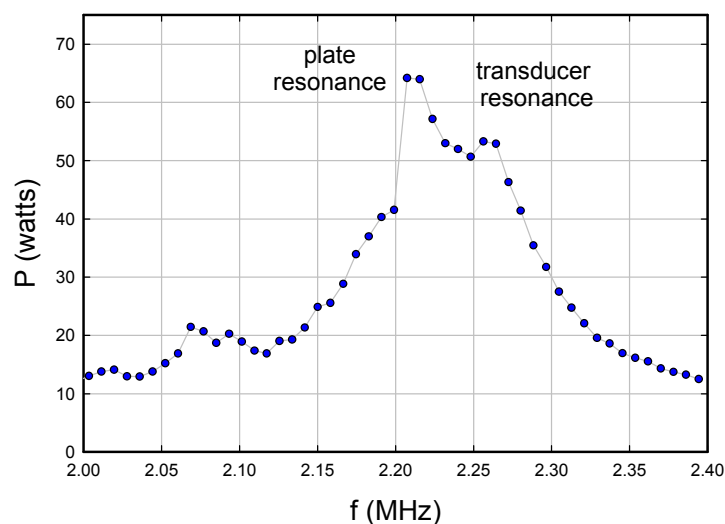
Figure 5. Electrical power to the transducer as a function of frequency for one of the transducer drive periods for the May 20 experiment.
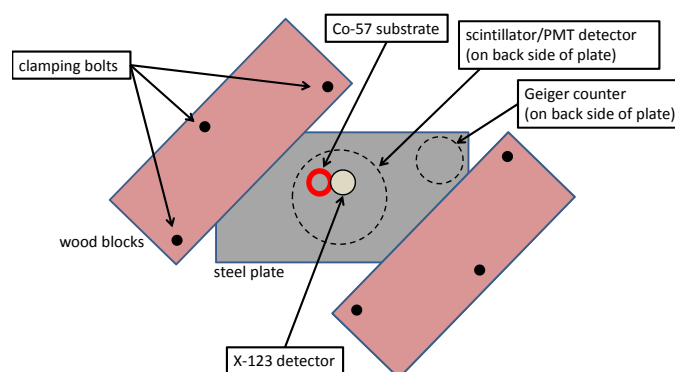
Figure 6. Steel plate (*light gray*); plywood clamps (*brown*); locations of bolts (*black*); there was one location for the evaporated Co-57, with four positions possible indicated by the red circles.

3.5. Clamps on steel plate

An effort was made after the May 20 experiment to determine the arrangement of the plywood clamps on the steel plate. From this reconstruction a layout was drawn to provide an approximate indication (see Fig. 6). The position of the plywood clamps on the steel could be determined from the residual indentations in the wood, and the locations of the bolt holes are available from photographs; these are indicated in the figure. The Co-57 evaporation is off-center, and the closest distance between the Co-57 and the nearest clamp edge is 1.22 in.

3.6. Aluminum mesh

There was a coarse aluminum mesh between the steel plate and the Amptek X-123 detector which we installed in order to provide protection for the thin Be window of the detector. This mesh is sold by McMaster-Carr (part number 9232T191) as Aluminum Perforated Sheet, 0.063″ thick with 0.1875″ diameter holes and 51% open area. It is made out of 3003 aluminum.

3.7. X-123 X-ray detector

For X-ray and gamma detection on the front side of the plate (facing the radioactive source) we used a 500 μm Amptek X-123 Si-PIN detector with a 0.5 mil Be window and 6 mm^2 area. For the data discussed in this paper we used spectra recorded every minute and logged with a time stamp. We used 2048 bins up to a maximum energy near 28 keV.

For data analysis, the energy band time history data presented later in the paper consists of summed up counts over 40 bins (525 eV) for the Fe K$_\alpha$ and Fe K$_\beta$ lines, and 60 bins (788 eV) for the Fe-57 14.4 keV line. For the Sn K$_\alpha$ line 69 bins (906 eV) were used, and for the Sb K$_\alpha$ line 43 bins (564 eV) were used.

3.8. Scintillator/PMT X-ray detector

On the back side of the plate (not facing the radioactive source) we used a scintillator/photomultiplier detector for X-ray and gamma detection. This detector uses a 250 μm ZnS scintillator (normally used for alpha detection) and a Hamamatsu 3″ photomultiplier tube (PMT), model R6233, with a thin radfilm cover to block visible light. This

detector was built by iRad Inc in Florida. The PMT was operated with a GS-2000-PRO driver from Bee Research. The analog output went into a Focusrite 192 kHz low-noise USB audio interface and was analyzed with open source Theremino MCA software. The 2048 channel spectrum was recorded once every minute with a time and date stamp.

3.9. Geiger counter

We made use of a Ludlum Geiger counter with a Model 44-88 Alpha Beta Gamma detector probe, and with a Ludlum 2350-1 Data Logger, to detect radiation on the back side. The Ludlum system develops an estimate for the count rate per minute roughly each half second, and the rate was logged roughly once each second with a time and date stamp.

3.10. Neutron detector

A Wendi-2 neutron detector from Thermo Fisher was placed next to the experimental assembly to monitor for possible neutron emission during the experiment.

4. Experimental results: shorter runs with MHz Vibrations

As mentioned in the introduction, the goal of the experiment was to test whether vibrations induced by the piezoelectric transducer could cause excitation transfer of the Fe-57 14.4 keV excited state population. We began with runs driving the transducer at high power (approximately 150 Watt); however, we were concerned that the detectors might be seeing noise due to the high current level used to power the transducer, so in later runs we reduced the transducer power and
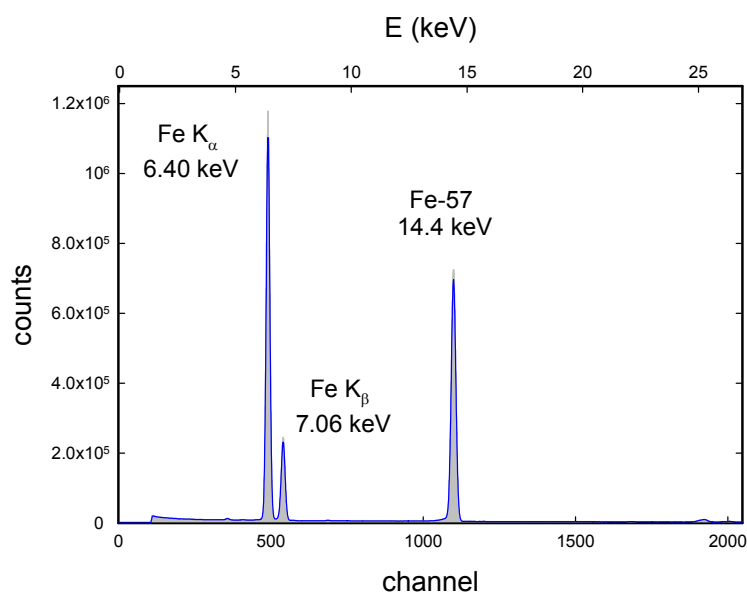
Figure 7. Time-integrated spectrum for first part of the experiment (20–23 May); raw counts per channel (*grey histogram*); averaged spectrum (*blue line*).

increased the duty cycle at which the transducer was driven (to 25% and 30%). Results from the low power run are considered in this section. Results for the entire period covering all runs, i.e. what we now refer to collectively as the May 20 experiment, are discussed from Section 5 onward.

4.1. Time-integrated X-ray spectrum

The primary diagnostic in this experiment is the Amptek X-123 detector, so we begin by considering the X-ray and gamma lines from this detector. The X-123 spectrum integrated over the first few days (5/20/17 14:48 to 5/23/17 06:50) of the experiment is shown in Fig. 7. A discussion of the calibration of the X-123 spectrum is given in Appendix B, along with line identifications in the spectra.

The 14.4 keV gamma line shows up clearly in the middle of the spectrum; and at lower energy, the lines resulting from the Fe K_α and Fe K_β transitions are very strong. There is the possibility of Fe K_α or Fe K_β radiative decay following the initial electron capture by Co-57; subsequently, there is a substantial probability of Fe K_α or Fe K_β radiative decay following the nonradiative decay of the 14.4 keV state by internal conversion [48–50].

4.2. Excitation transfer test with moderate transducer power

The test for excitation transfer – as initially envisioned – involved the prediction of a prompt reduction in the 14.4 keV gamma line while ultrasonic vibrations were generated via the piezoelectric transducer. In Fig. 8 we show the time history of counts per hour for the 14.4 keV line along with the peak transducer power. To construct this plot we summed the counts taken and logged each minute to develop one hour totals, which are plotted at the time of the last minute of the accumulation, relative to the start of the first day of the May 20 experiment. In this plot, as well as in other plots in this paper, no background subtraction is applied.

The figure suggests that there is no significant dip in the emission when the transducer is driven, as had been considered. If there is a more general response of the emission strength to the vibrations, it is not particularly obvious from this data set; however, we will revisit this question in connection with higher power operation later on in Section 7.

5. Experimental results: entire May 20 experiment, Amptek X-123 data

When considering the entirety of the May 20-31 period – as opposed to the shorter runs considered in the previous section – we observed non-exponential decay for the principal emission lines most clearly in the Amptek data. Before we examine time histories for lines with non-exponential time dependence below, we first consider observations of some weaker high energy lines that are consistent with exponential decay.

5.1. Weaker lines in the spectrum

In Fig. 7 we focused on the strong lines normally seen from the beta decay of Co-57, and now we are interested in the weaker lines in the spectrum. A logarithmic version of the time-integrated spectrum is shown in Fig. 9 in which we can see several weaker lines. We have marked the Fe K_α escape peak at 4.51 keV, as well as the Sn K_α at 25.2 keV. Above the Sn K_α there is a line (unmarked) at 26.3 keV which is the Sb K_α. Just below the 14.4 keV gamma is an escape peak for the 14.4 keV gamma.

5.2. Decay of the Sn K_α X-ray line

The steel plate contains a small amount of Sn, as we verified by X-ray fluorescence (XRF) measurements of an equivalent steel plate ordered from the same supplier. This line is relevant since it is present as a result of ionization
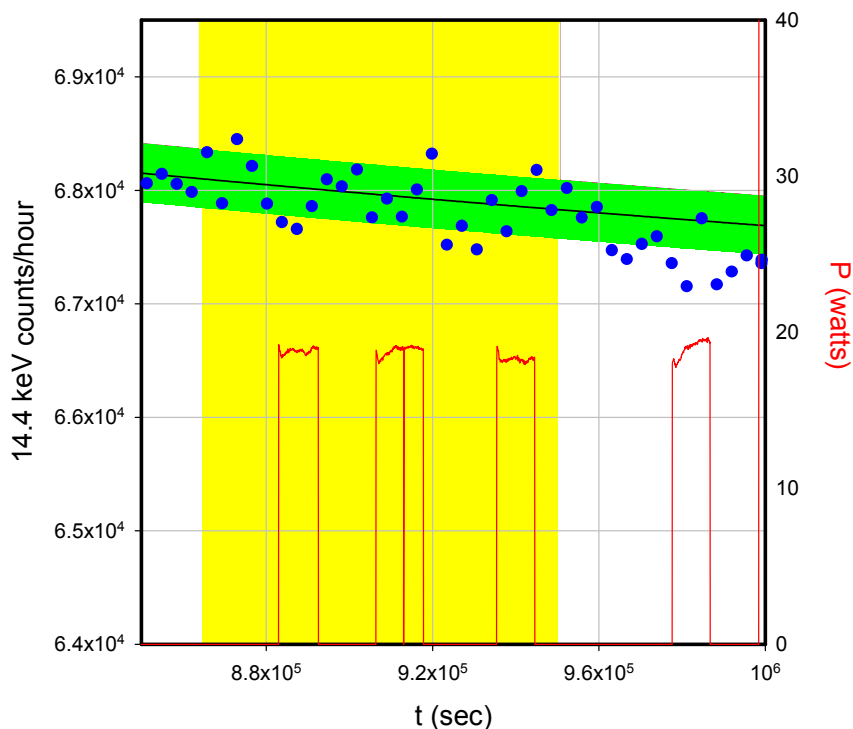
Figure 8. Counts on the Fe-57 nuclear transition at 14.4 keV as a function of time (*blue*); global empirical model (described in the following section) fit to the data (*black*); $\pm 1\sigma$ region determined by the square root of counts based on empirical model (*green area*); transducer power (*red*). Time in seconds indicated at the bottom; days between 5/29 and 5/31 indicated by the yellow and white background (each color band marks one day).

due to the harder 122.1 and 136.5 keV gammas of the 136.5 keV state initially populated by the decay of Co-57. Because of this, we can learn something frm the Sn K_α line about the dynamics of the 136.5 keV state indirectly, since in this experiment we do not have direct measurements of the harder gammas. The results are shown in Fig. 10. We see that the time history is consistent with the 271.74 day half-life exponential decay at the level of about 1%.

The arrival of counts during an accumulation time is governed by Poisson statistics, so that the standard deviation is the square root of the number of counts. While we have available spectra taken once per minute, the scatter of the resulting time history is sufficiently large as to be uninteresting. We have summed over 6 h of these one minute spectra (with the total plotted at the end of the 6-hour period in each case) in order to reduce the scatter.

5.3. Decay of the Sb K_α X-ray line

As mentioned above, there is a weak X-ray line above the Sn K_α that we identify as the Sb K_α (see Appendix B). From the same steel XRF measurements mentioned in Section 5.2 for Sn, we found also that Sb is present. We would expect to see a similar decay on this line as for the Sn K_α, since both the Sn and Sb K_α lines result from photoionization due
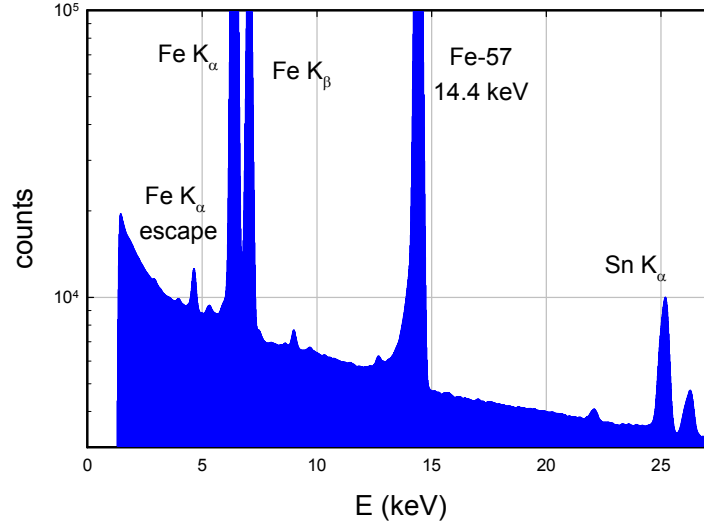
Figure 9. Time-integrated spectrum for first part (20–23 May) part of the run; raw counts (*blue histogram*).

to the harder gammas. In Fig. 11 is shown the time history, and we see that the decay on this line is consistent with 271.74 day half-life exponential decay at the level of about 1.5%. Note that in this case, there are more counts due to the "background" than due to Sb K_α X-rays (see Fig. 9); however, since the "background" in this case is due to the detector response to the harder gammas, we would expect a similar time history for both contributions. The spread is a bit larger compared to the Sn K_α since the signal is weaker.

5.4. Non-exponential decay of the 14.4 keV gamma line

The 14.4 keV gamma line in this experiment shows a non-exponential decay (see Fig. 12). This result was not expected, and has been the source of astonishment and much discussion. We interpret the faster-than-exponential decay observation to be due to an enhancement of the signal at early time, instead of due to accelerated decay of Co-57 (which would be inconsistent with the Sn K_α and Sb K_α time histories present in the sections above).

For this plot, and for those that follow, we made use of an empirical model given by

$$\ln I(t) \; = \; -\frac{t}{\tau} + a + b\,\mathrm{e}^{-t/\tau_0} \tag{1}$$

with $\tau = 271.74/\ln 2$ days from the NUDAT2 database. From this model we can estimate the intensity expected if no anomaly were present from

$$\ln I_0(t) \; = \; -\frac{t}{\tau} + a. \tag{2}$$

From a least squares fitting of the model parameters to the data we find

$$\tau_0 \; = \; 2.18 \times 10^5 \ \mathrm{s}, \tag{3}$$
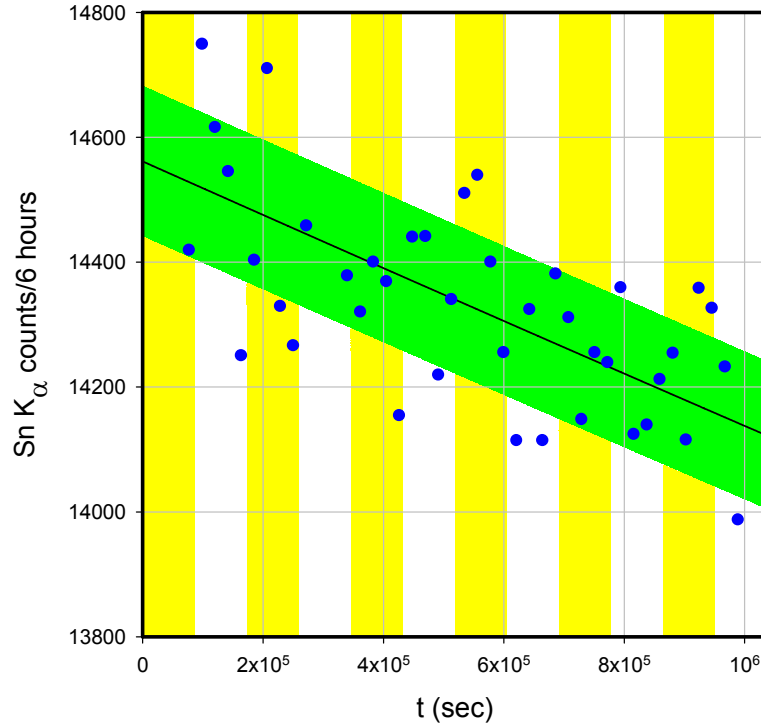
Figure 10. Time history of the of the Sn K$_\alpha$ transition (*blue circles*); exponential decay with 271.74 days half-life (*black*); $\pm 1\sigma$ error bars determined by the square root of the average number of counts (*light green solid region*). The bottom time axis is in seconds; the alternating yellow and white background show the duration of each day between 5/20 and 5/31.

which is a time constant associated with the physical configuration of the experiment, and not with any fundamental nuclear process. We see in Fig. 12 that this empirical model provides a good fit to the data.

5.5. Spectrum near the 14.4 keV gamma line as a function of time

If the enhancement of 14.4 keV excited states of Fe-57 were created through some new process, there might be the possibility of a modification in the line shape. Note that since the line is instrument broadened (FWHM of 220 eV for this line with the Amptek X-123 detector), such an effect would need to be very large in order to be seen with this kind of measurement. This provides us with the motivation to examine the spectrum in the vicinity of the 14.4 keV line up close. The spectrum as a function of time is shown in Fig. 13. We summed 30 min of data for each data point used in this plot. We see some data loss near 300 000 s, and we can see clearly that the line is brighter at early times in the experiment. There seems to be a minor drift in the relative channel average (on the order of a few tenths of a channel, or 2–3 eV at 14.4 keV), which may be due in part to a small drift in the detector gain (since the dynamics of the average relative channel is similar for the 14.4 keV X-ray and Fe K$_\alpha$ gamma). There does not appear to be a significant change in the line shape observed with the X-123 at early time in this data.
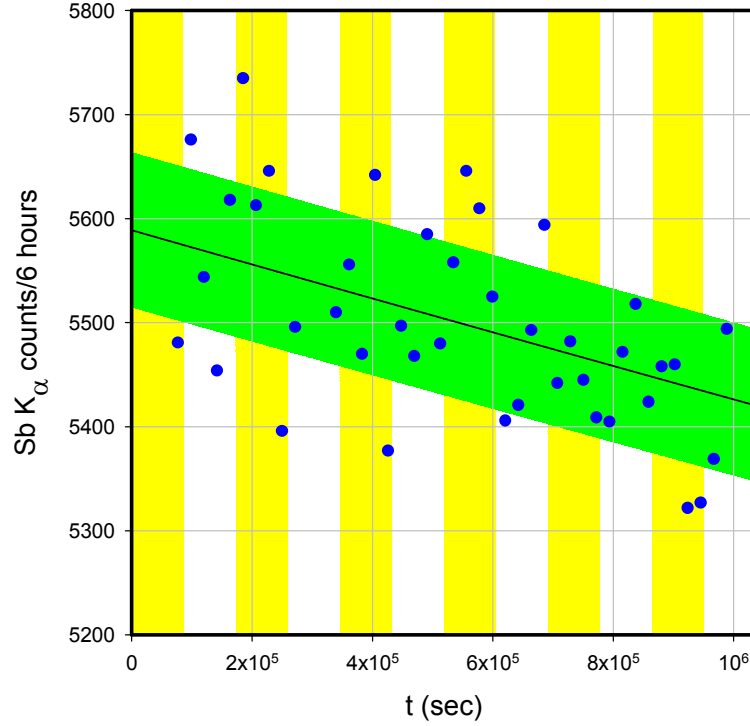
Figure 11. Time history of the of the Sb K_α transition (*blue circles*); exponential decay with 271.74 days half-life (black); $\pm 1\sigma$ error bars determined by the square root of the average number of counts (*light green solid region*). The bottom time axis is in seconds; the alternating yellow and white background show the duration of each day between 5/20 and 5/31.

5.6. Non-exponential decay of the Fe K_α X-ray line

A similar non-exponential decay history is observed also for the Fe K_α X-ray, as shown in Fig. 14. We would expect internal conversion of the 14.4 keV nuclear state to lead to Fe K_α emission, so it does not come as a surprise that we should see a qualitatively similar anomaly in the Fe K_α emission (note that there is also a contribution to the Fe K_α emission following the initial Co-57 capture). We again fit to the empirical model above, with a time constant parameter of

$$\tau_0 = 2.16 \times 10^5 \text{ s}, \tag{4}$$

which is within about 1% of what was found for the 14.4 keV gamma transition above.

5.7. Non-exponential decay of the Fe K_β X-ray

We observe similar dynamics on the Fe K_β transition as shown in Fig. 15 (as expected since the mechanism of Fe K_β emission is very similar to that for Fe K_α). The time constant parameter in this case is similar to the previous cases
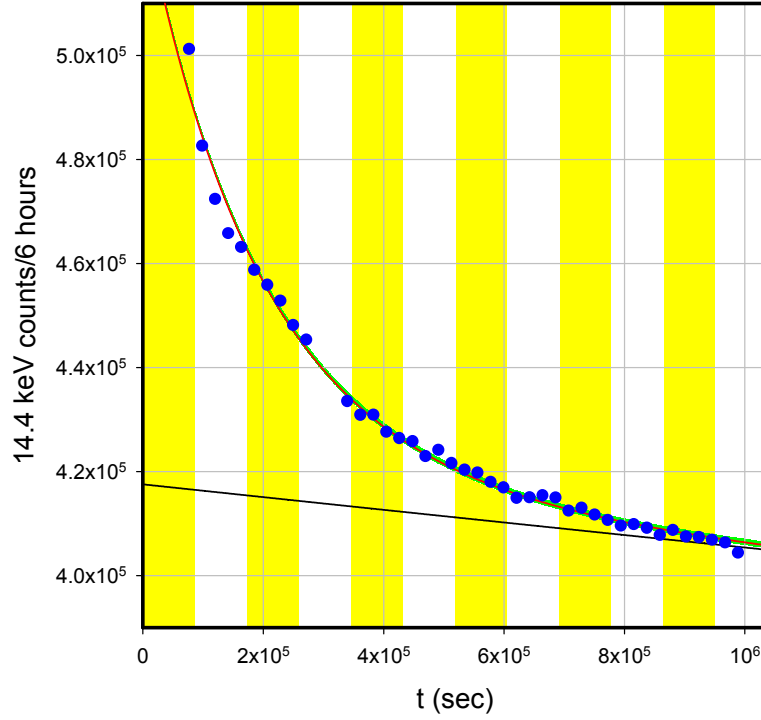
Figure 12. Time history of the of the Fe-57 nuclear transition at 14.4129 keV (*blue circles*); empirical model (*red*); exponential decay with 271.74 day half life consistent with empirical model (*black*); the $\pm 1\sigma$ error bars determined by the square root of the average number of counts (*light green solid region*) is sufficiently narrow to be obscured by the red line of the empirical model. The bottom time axis is in seconds; the alternating yellow and white background show the duration of each day between 5/20 and 5/31.

$$\tau_0 \;=\; 2.23 \times 10^5 \text{ s.} \tag{5}$$

5.8. Non-exponential decay for the Fe K_α escape peak

We would expect to see the same non-exponential decay time history in the Fe K_α escape peak as in the Fe K_α X-ray; however, since the escape peak is much weaker, the competing contribution from the "background" due to the harder gammas (which decay exponentially) leads to a dilution of the effect. We analyzed the dynamics of the emission from this line (see Fig. 16) with the result that there is a non-exponential component that is less pronounced than for Fe K_α. For the model used in Fig. 16 we used $\tau_0 = 2.16 \times 10^5$ s value from the Fe K_α fit. As mentioned above, no background subtraction was done for this line. There again is more relative spread in the data since the count rate is much lower.

The decay of the signal is compatible with the time constant τ_0 of the Fe-57 14.4 keV gamma and Fe K_α and K_β X-ray lines. Due to the weakness of the line, the spread is large, so that the Fe K_α escape data does not provide a strong constraint on τ_0.
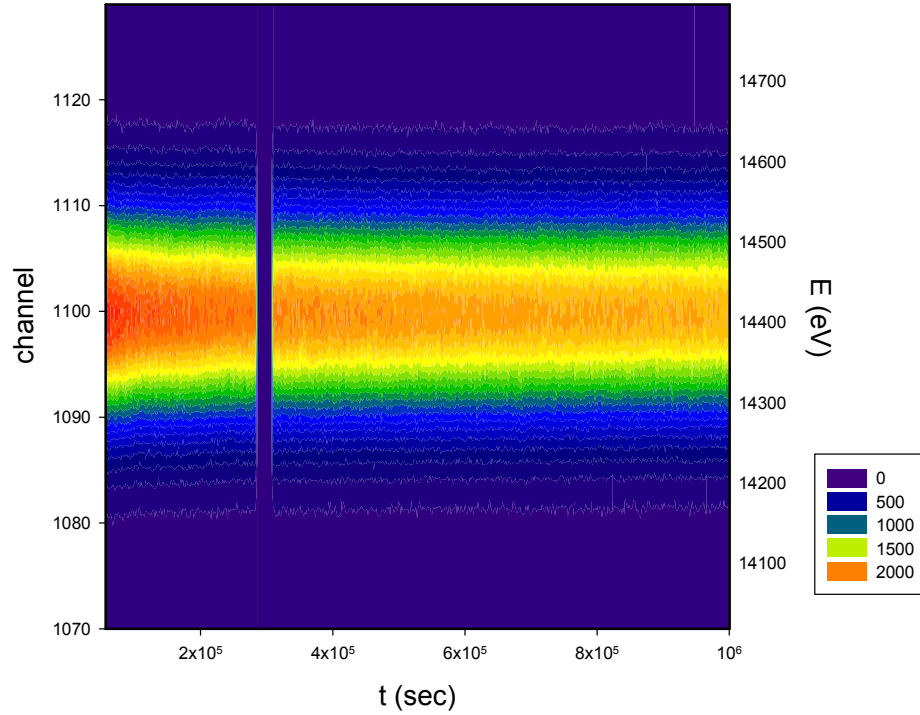
Figure 13. Time history (counts per 30 min) of the spectrum of the Fe-57 nuclear transition at 14.4129 keV; the time axis (*bottom*) is in seconds; the channel number is on the left and the energy is on the right.

6. Experimental results: entire May 20 experiment, data from other detectors

In this section, we are interested in results from the Geiger counter, from the scintillator/PMT detector, and also from the neutron detector. The neutron detector did not exhibit an unexpected dynamical time history, but unexpected non-exponential decays were recorded on the other detectors.

6.1. Non-exponential decay of the Geiger counter signal

The Geiger counter was pointed at the back side of the steel plate, and the plate is sufficiently thick that there is no possibility of the 14.4 keV gamma or the Fe K_α, K_β X-rays from the Co-57 making it through the plate without being absorbed. Consequently, only the harder 122.1 and 136.5 keV gammas (and the much weaker gammas at even higher energy) from the Co-57 make it to the back side. In this experiment the Geiger counter is relatively distant from the Co-57 source, so that the signal strength due to the Co-57 is reduced by a factor of about 50 from what is measured in close proximity. Now, we know from the Sn K_α signal that the time history of the 122.1 and 136.5 keV gammas as determined by the Sn K_α proxy does not show a strong early time enhancement. Consequently, the non-exponential decay of the Geiger counter signal shown in Fig. 17 is providing new information not available from the front side X-123 data.
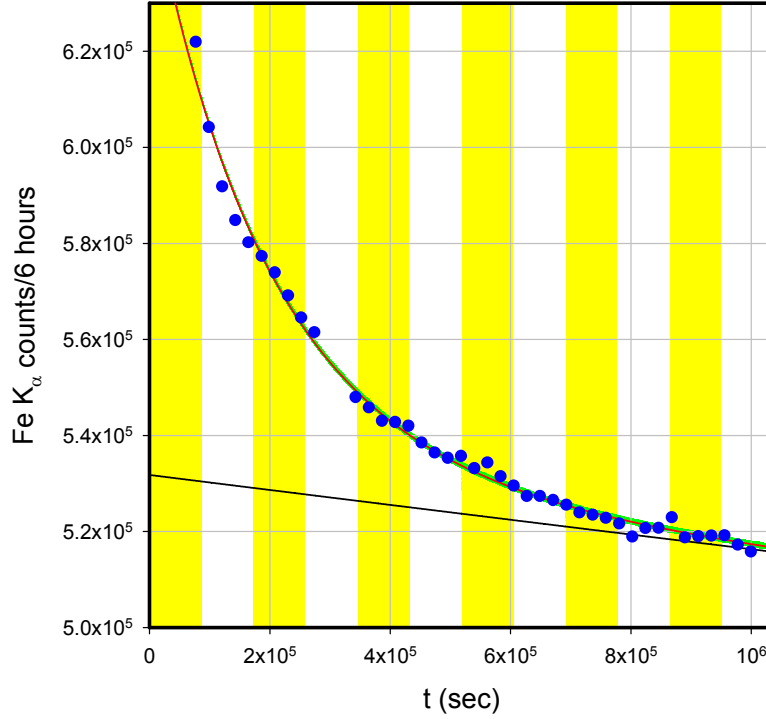
Figure 14. Time history of the of the Fe K_α X-ray (*blue circles*); empirical model (*red*); exponential decay with 271.74 days half-life consistent with empirical model (*black*); the $\pm 1\sigma$ error bars determined by the square root of the average number of counts (*light green solid region*) is sufficiently narrow to be obscured by the black line of the empirical model. The bottom time axis is in seconds; the alternating yellow and white background show the duration of each day between 5/20 and 5/31.

Because the May 20 experiment was not originally conceived as a single experiment but rather as a series of shorter runs, Geiger counter data was not taken throughout the entire May 20-31 period, resulting in a significant gap and fewer data points to work with. Nevertheless, it is clear that the decay in this case is very much non-exponential. We have fit the available data points, accumulated as above, to the empirical model once again. The optimization of the model leads to a value for τ_0 of

$$\tau_0 = 2.930 \times 10^5 \text{ s,} \tag{6}$$

We note that the fluctuations in this case are larger than what would be expected from the total counts per 30 min. One contributing reason for this is that an estimate for the counts per second determined by the Geiger counter system was stored only approximately once per second, instead of twice per second as the system records internally.

Figure 15. Time history of the of the Fe K$_\beta$ X-ray (*blue circles*); empirical model (*red*); exponential decay with 271.74 days half-life consistent with empirical model (*black*); the $\pm 1\sigma$ error bars determined by the square root of the average number of counts (*light green solid region*). The bottom time axis is in seconds; the alternating yellow and white background show the duration of each day between 5/20 and 5/31.

6.2. Results for the scintillator/PMT detector

We recall that the scintillator/PMT detector is also located on the back side (not facing the Co-57 substrate). At the time of the May 20 experiment, the driver of the scintillator/PMT detector was still occasionally plagued by interruptions (with a sudden on and later sudden off time characteristic) during which noise in the form of pulses with a very long decay time was added to the signal. Nevertheless, much of the data from this detector is intact, and in some of the channels there appears to be a distinct non-exponential signal. Here we have chosen to display the data sets (analyzed using accumulation based on the same approach as for the other data) including periods containing obvious interruptions since a unique systematic retrospective separation of the data and interruption noise is not possible.

The most straightforward data set is the summed channels corresponding roughly to the 1–2 keV range. The time history is seen to be consistent with exponential (aside from interruptions) for the 271.74 day beta decay half-life of Co-57, as shown in Fig. 18. The sharp excursions up to the vicinity of 5000 counts per 30 min are interruption noise, as are the excursions down below 4000 counts/30 min. For these channels the aluminum in the radfilm covering the scintillator in strongly absorptive, so that few soft X-rays get through and register. In the presence of lower energy sources this detector gives a spectrum with a shape consistent with Al X-ray fluorescence, where the aluminum in the radfilm may be radiating inefficiently. There may be contributions to the signal also from the harder gammas incident
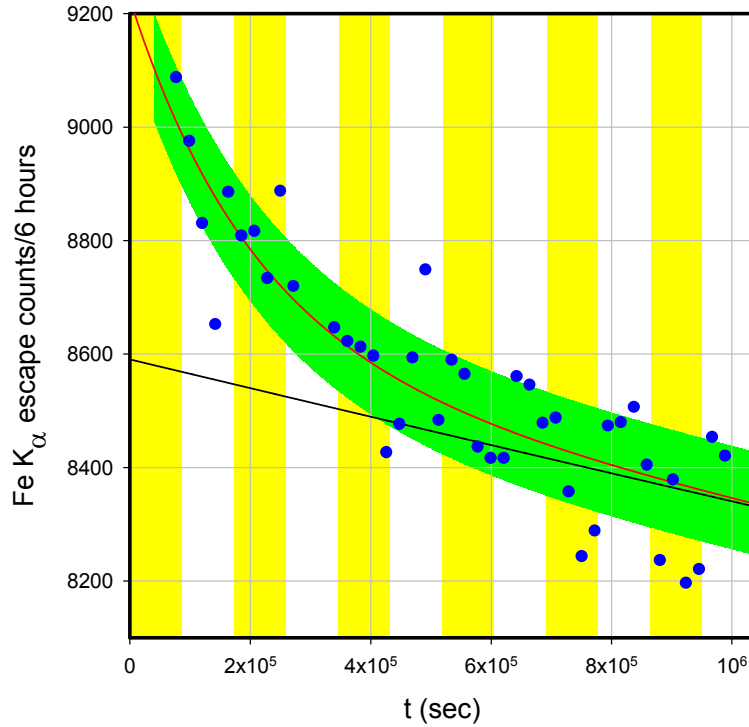
Figure 16. Time history of the of the Fe K$_\alpha$ escape peak (*blue circles*); empirical model (*red*); exponential decay with 271.74 days half-life consistent with empirical model (*black*); the $\pm 1\sigma$ error bars determined by the square root of the average number of counts (*light green solid region*). The bottom time axis is in seconds; the alternating yellow and white background show the duration of each day between 5/20 and 5/31.

in other parts of the detector.

In Fig. 19 we show the time history of the summed channels between 2 and 4 keV, along with a parabolic model curve to guide the eye. Due to the poor energy resolution of the scintillator/PMT detector, we would expect minor contributions from the Fe K$_\alpha$ to appear in these channels. Once again the fast excursions above 140 000 counts/30 min are interruption noise, as are the excursions below 130 000 counts/30 min. We see a non-exponential decay with a qualitatively different dynamics than what was seen on the front side by the Amptek X-123 and on the edge of the back plate by the Geiger counter.

The time history for the summed scintillator/PMT channels between 4 and 10 keV are shown in Fig. 20. These channels were selected to capture the bulk of the Fe K$_\alpha$ and K$_\beta$ lines, should such emission occur keeping in mind that all Fe K$_\alpha$ and K$_\beta$ emission originating from the front side is absorbed by the plate, but there is some XRF due to the harder gammas. We see again a roughly parabolic signal with interruption noise present. The early fast excursions up to 1.1×10^6 counts/30 min and the later excursions down below 9.8×10^5 counts/30 min are due to the interruption noise.

The time history for the summed channels between 10 and 20 keV is shown in Fig. 21, also with a parabolic curve that approximates the signal in the absence of the interruptions. The intent of this set of channels was to capture what
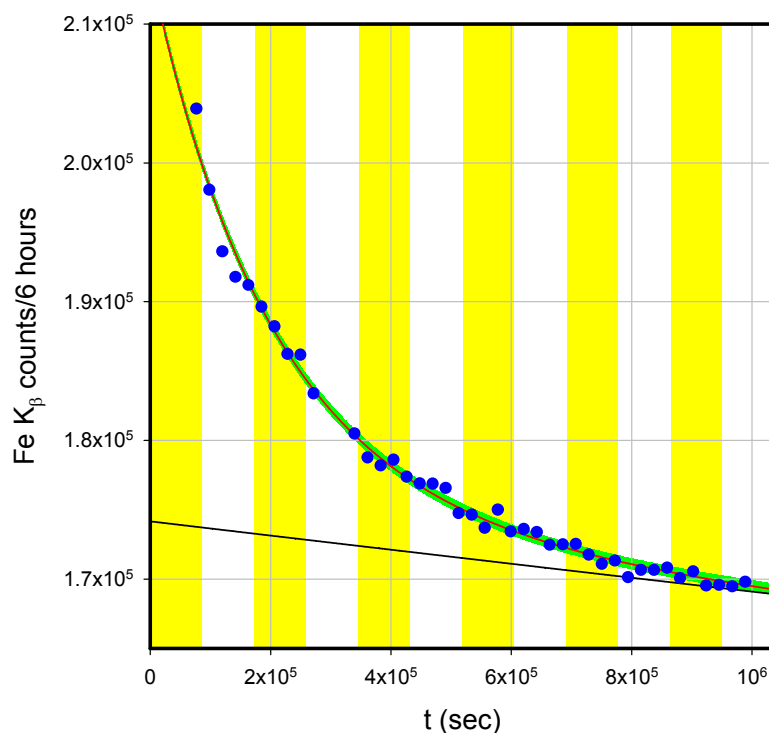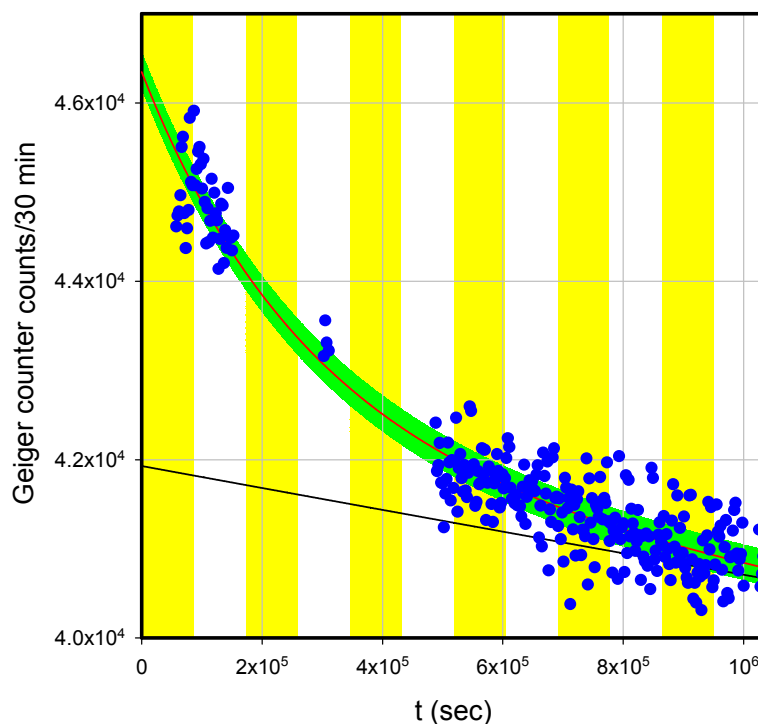
Figure 17. Time history of the of the Geiger counter signal (*blue circles*); empirical model (*red*); exponential decay with 271.74 days half-life consistent with empirical model (*black*); the $\pm 1\sigma$ error bars determined by the square root of the average number of counts (*light green solid region*). The bottom time axis is in seconds; the alternating yellow and white background show the duration of each day between 5/20 and 5/31.

was going on in the general vicinity of the 14.4 keV gamma ray (as yet we have not seen 14.4 keV emission on the back side in other experiments with good spectral resolution). A roughly parabolic response is evident, and the occasional large downward excursions are due to the interruption noise. We note that there are fluctuations present in the data well beyond what would be expected from Poisson statistics.

Finally, the time history for the uppermost channels above 20 keV is shown in Fig. 22, which shows a similar trend to the other channels. We see a parabolic signal with a few sharp downward excursions due to interruption noise.

At the time of writing this text, the occasional interruptions and resulting noise exhibited by this detector have been addressed. Despite the less than ideal condition of the data taken with this detector during the May 20 experiment, we chose to report the data here with the caveats mentioned above.

6.3. Neutron counts

Data from the neutron detector is shown in Fig. 23. We see that the total number of counts per six hours is low, so that the statistical fluctuations are relatively large compared to the average count rate. The average count rate is 64.9 counts per 6 hours which is equivalent to 3.00×10^{-3} counts/s. Given the listed efficiency of the detector which is 0.84 cps/μSv/h, the average background count rate is then 3.6 nSv/h. This data set is consistent with no incremental
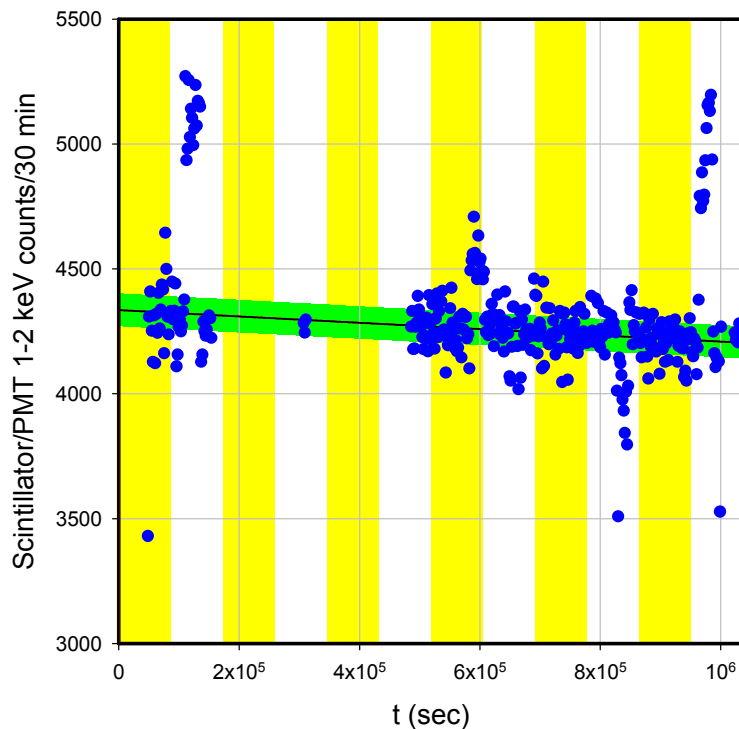
Figure 18. Time history of the of the 1–2 keV channel of the scintillator/PMT detector (*blue circles*); empirical model (*red*); exponential decay with 271.74 days half-life consistent with empirical model (*black*); the $\pm 1\sigma$ error bars determined by the square root of the average number of counts (*light green solid region*). The bottom time axis is in seconds; the alternating yellow and white background show the duration of each day between 5/20 and 5/31.

neutron emission during the experiment with a 1 σ upper limit of 0.44 nSv/h.

7. Basic Considerations

Non-exponential decay observed for the 14.4 keV gamma line, and for the Fe K_{α} and K_{β} X-ray lines, by the front-side Amptek X-123 detector, appears to us to be anomalous. Some support for such an assertion is provided by a similar time history for the back-side Geiger counter away from the Co-57, even though the origin of the back side Geiger counter signal must be different. The scintillator/PMT detector on the back side near the Co-57 reports a different (early reduction instead of enhancement) and slower non-exponential decay.

It could be argued that any interpretation is premature: since the May 20 experiment was the first of its kind; since the effects seen in subsequent experiments were weaker; and since some colleagues may view the results presented in this paper as artifacts. The thought here is that it is appropriate to discuss both possible sources of problems (which should be addressed in subsequent experiments), and also to discuss possible interpretations (which might point to future experiments that might provide clarification and confirmation). In this section we focus on some basic issues. With respect to interpretation, one hypothesis based on delocalization of the nuclear excitation as a result of excitation
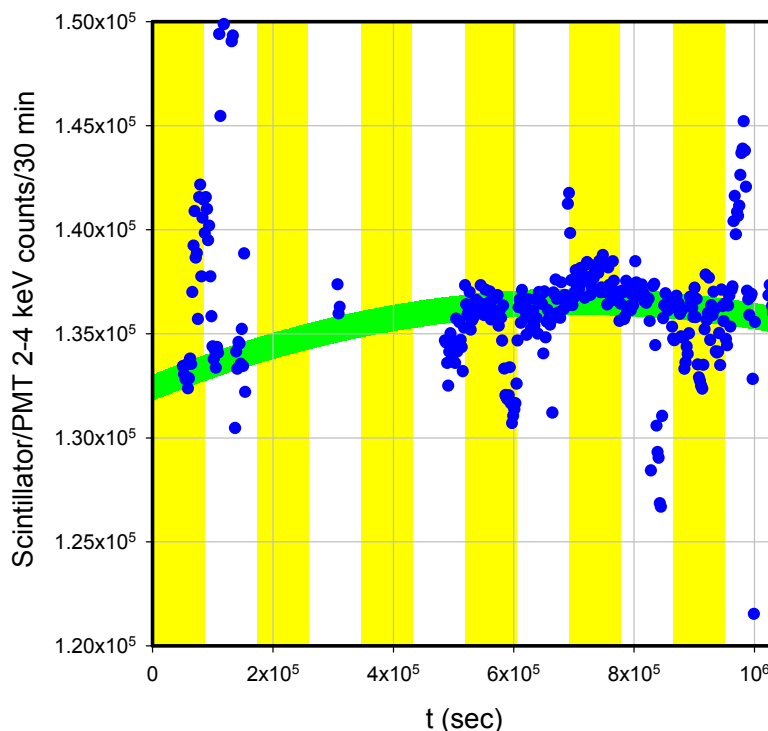
Figure 19. Time history of the of the 2–4 keV channel of the scintillator/PMT detector (*blue circles*); simple parabolic model (*red*); the $\pm 1\sigma$ error bars determined by the square root of the average number of counts (*light green solid region*). The bottom time axis is in seconds; the alternating yellow and white background show the duration of each day between 5/20 and 5/31.

transfer is discussed in Appendix C for the early time non-exponential decay effect observed in the X-123 data.

7.1. Epoxy seal

A reduction of the 14.4 keV gamma and Fe K_α and K_β X-ray intensity would occur if there were a continuous loss of Co-57 from the evaporated region. The epoxy seal was examined following the experiment, and showed no obvious signs of degradation; however, some discoloration is evident (see Fig. 24). No radioactivity was found on collection paper at the bottom of the experiment after the run.

7.2. Amptek X-123 detector operation

The first hypothesis considered was the possibility that the X-123 detector was functioning improperly in some way, perhaps losing counts over time. The Co-57 source strength used is well within the operating range of the detector, so we do not expect to see saturation effects. Measurements made in subsequent experiments with the X-123 detector, and also with other detectors, have shown similar non-exponential decay effects, and control experiments have shown exponential decay as expected.
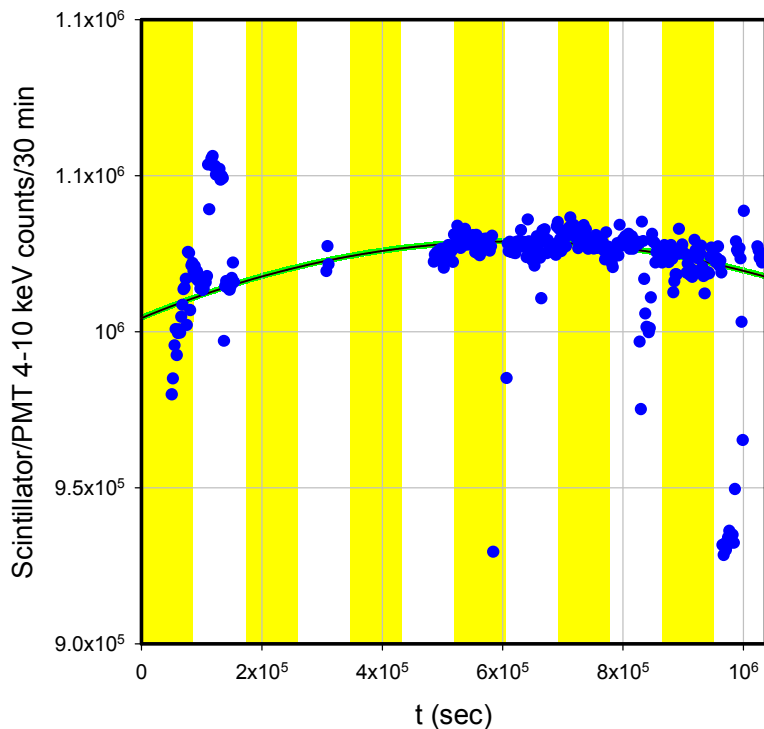
Figure 20. Time history of the of the 4–10 keV channel of the scintillator/PMT detector (*blue circles*); simple parabolic model (*red*); the $\pm 1\sigma$ error bars determined by the square root of the average number of counts (*light green solid region*). The bottom time axis is in seconds; the alternating yellow and white background show the duration of each day between 5/20 and 5/31.

The Sn K_α in this experiment provides for a control – albeit an imperfect one – in that the time history is consistent with exponential decay with the known half-life of 271.74 days to within 1% or so over the length of the experiment. This suggests that during the experiment the detector is able to see time histories which are both exponential at the 1% level, and also non-exponential with enhanced emission at the 17% and 19% level.

Note that in the future we would like to have in the data a time history for a control line, where there is no question as to what the time history should be. One possibility is to field a radioactive source other than Co-57 that would provide a line within the Amptek X-123 detector window. One possibility for this is Sm-151 (90 years half-life), which decays to an excited state in Eu-151 at 21.541 keV that emits a corresponding 21.5 keV gamma that we can see. Another possibility is to make use of another, untreated Co-57 source to photoionize a K-shell (for example in Mo or Pd) to produce a characteristic X-ray in our window. We would want to block such a secondary Co-57 source from the detector to prevent overlap with the treated Co-57 source. The advantage of this approach is that we would then have a control line with a 271.74 day half-life.

It might be that the observed non-exponential decay is associated with lines that have a high count rate. Arguing against this is the non-exponential decay seen in the much weaker Fe K_α escape peak. In future experiments it would make sense to include a proxy for the Fe K_α (such as Ti) and for the 14.4 keV gamma (such as Br), where the K_α would
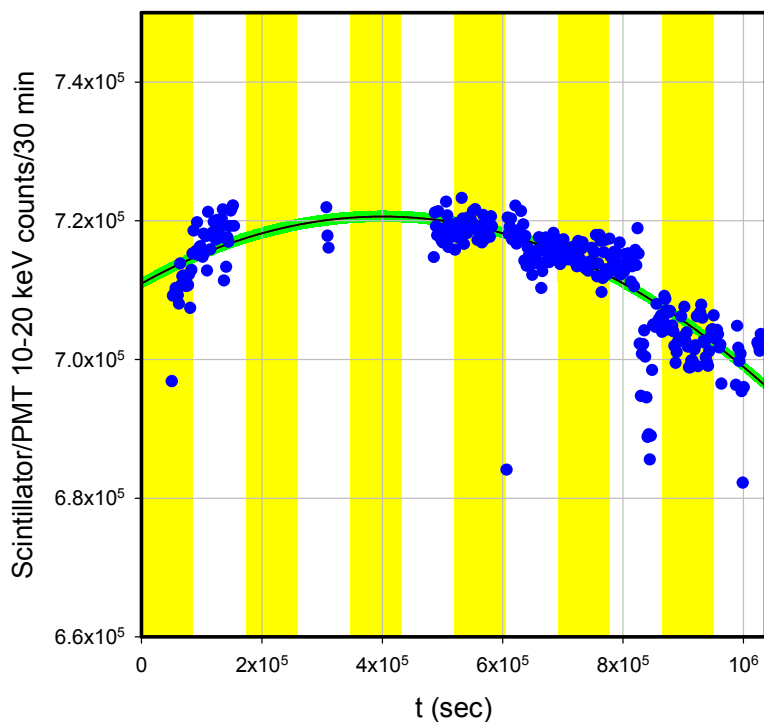
Figure 21.   Time history of the of the 10–20 keV channel of the scintillator/PMT detector (*blue circles*); simple parabolic model (*red*); the $\pm 1\sigma$ error bars determined by the square root of the average number of counts (*light green solid region*). The bottom time axis is in seconds; the alternating yellow and white background show the duration of each day between 5/20 and 5/31.

be produced following photoionization from the strong lines resulting in an independent witness to non-exponential decay.

7.3. Relative motion

Since we are using a protective mesh between the sample and X-123 detector, it is possible for relative motion to produce a change in the absorption (which might lead to either an increase or a decrease in the observed X-ray emission).

Arguing against this is the fact that the X-123 was secured by a sample holder, and the sample and wood blocks rested on a stable rack. A substantial force (not present in the experiment) would be required to move the detector, and a significant force (also not present in the experiment) would have been needed to move the sample. It may be that the steel plate moves some when the transducer is powered. Nevertheless one would not expect a smooth exponential relaxation to appear in the signal as was observed in the experiment. Note that the Geiger counter is on the back side with no partial blocking by the aluminum mesh, and we see a similar non-exponential decay effect.

In future experiments it would seem to be prudent to pay direct attention to the relative motion, and also to monitor it with a camera and a microscope to measure whether significant motion occurs.
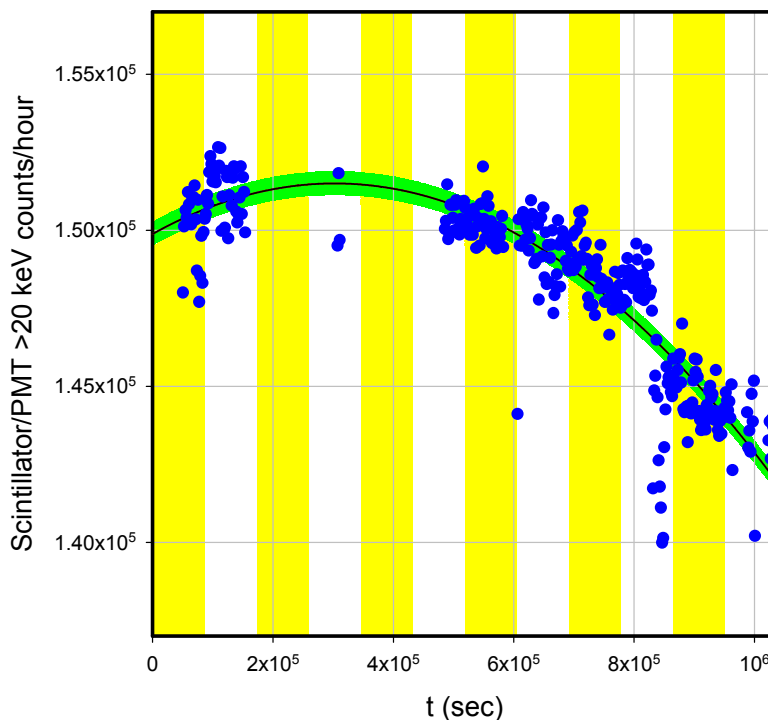
Figure 22. Time history of the of the channels above 20 keV channel of the scintillator/PMT detector (*blue circles*); simple parabolic model (*red*); the $\pm 1\sigma$ error bars determined by the square root of the average number of counts (*light green solid region*). The bottom time axis is in seconds; the alternating yellow and white background show the duration of each day between 5/20 and 5/31.

7.4. Co-57 decay is not accelerated

Other researchers have put forth claims previously for the anomalous accelerated loss of radioactivity in other kinds of experiments (see [51–56]; note that these references represent only a subset of such papers and that there are additional papers in the literature that suggest the existence of such an effect). In part because of this, we entertained the possibility that a loss of activity might be occurring in the May 20 experiment.

Arguing against this is the observed Sn K_α signal with a time history consistent with exponential decay at the 1% level, given the radioactivity present at the beginning of the experiment. This line is produced following photoionization of a K-shell electron by the harder 122.1 and 136.5 keV gammas, so it acts as a proxy in this experiment for the angle-averaged time history of the harder gammas. Since the Fe-57 136.5 keV state is fed from the decay of Co-57 following electron capture, we conclude that the beta decay of Co-57 is consistent with the expected exponential decay (with a 271.74 days half-life) at roughly a level of 1% during the time of the experiment.

An independent argument can be made based on the fact that we would expect the ratio of the intensity of the 14.4 keV gamma line to the Fe K_α line to be constant if produced by a varying beta decay rate. In Fig. 25 we show the ratio of 14.4 keV gamma counts to Fe K_α X-ray counts as a function of time, where a minor decrease in the ratio during the course of the experiment can be seen. This is inconsistent with a loss of Co-57 activity as an explanation
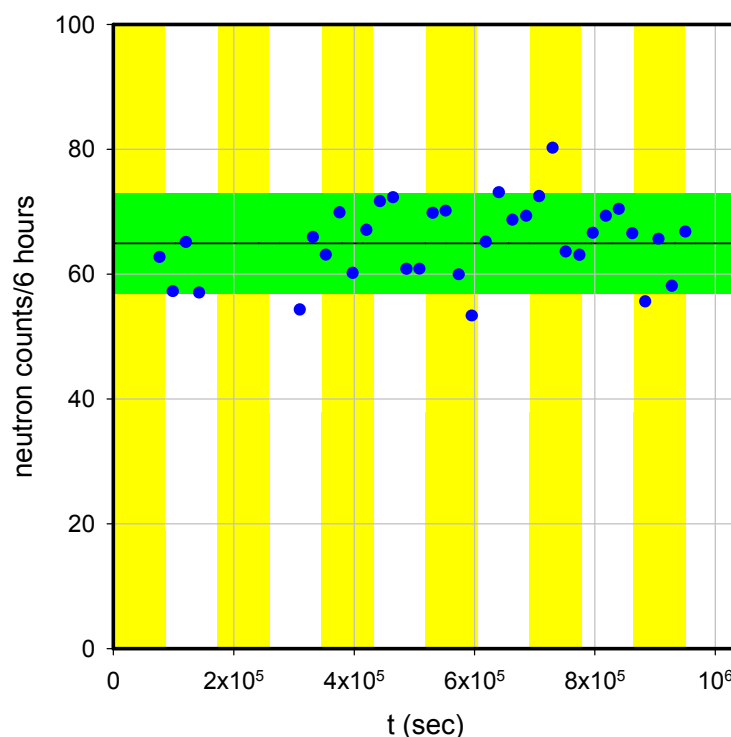
Figure 23. Time history of the neutron counts (*blue circles*); average count rate (*black*); $\pm 1\sigma$ error bars determined by the square root of the average number of counts (*light green solid region*). The bottom time axis is in seconds; the days are marked on top, with the alternating yellow and white background giving the duration of each day.

for the effect.

We interpret the anomalous time-dependence of the emission of the 14.4 keV gamma, and Fe K_α and K_β X-rays as due to an increase in emission at early times, and not due to accelerated decay of Co-57. In subsequent experiments we have observed the emission to increase (weakly) in response to vibrational stimulation, and also in experiments with in situ mechanical stress generated via heat pulses.

7.5. Possibility of up-conversion of 2.21 MHz vibrations

One of the original goals of this experimental effort was to determine whether MHz vibrations can be up-converted to produce nuclear excitation. As discussed briefly above, our results from the May 20 experiments do not support this initial prediction as an explanation for the anomalous observations made (see Fig. 8). In subsequent experiments we have also not seen a prompt response of the X-ray or gamma emission in the Amptek X-123 spectra due to changes in the transducer power.

Figure 24. Photograph of the epoxy covering the HCL and Co-57 taken after the May 20 experiment.

7.6. Impact of 2.21 MHz vibrations on the anomaly

The enhanced gamma and X-ray signals were present from the start of the experiment, which from later experimentation we attribute to having been a result of the tightening of the bolts on the wooden clamps and the resulting mechanical stress. However, it could be asked whether the 2.21 MHz vibrations we imposed had any effect, even if not prompt. To shed light on this, we show in Fig. 26 the Fe K_α signal plotted along with the peak transducer power (with a 20% duty cycle the average power is less by a factor of 5). The emission strength does not seem to increase or decrease much while the transducer is run. During the experiment we noticed a weak response (increase) of the photon emission registered by the detector following some of the transducer pulses, which led us to adopt a lower power drive protocol in case the transducer current was impacting the detectors.

7.7. Cause and effect

In the May 20 experiment, the front-side enhancement of photon emission is present from the start of the experiment, and we only observed the subsequent decay (but not the increase preceding it). It was not obvious at the time of the experiment what caused such an enhancement. We assumed initially that something in the protocol used prior to data collection was responsible, with a focus on tightening the bolts on the wood and sample as perhaps key. In later experiments we found that the enhancement can be produced by tightening clamps, or by applying stress in other configurations, as will be described in future publications. Also, triggering the enhancement and the following decay is evident in experiments in which thermal pulses were used to create mechanical stress in situ, as will be discussed in a following paper.
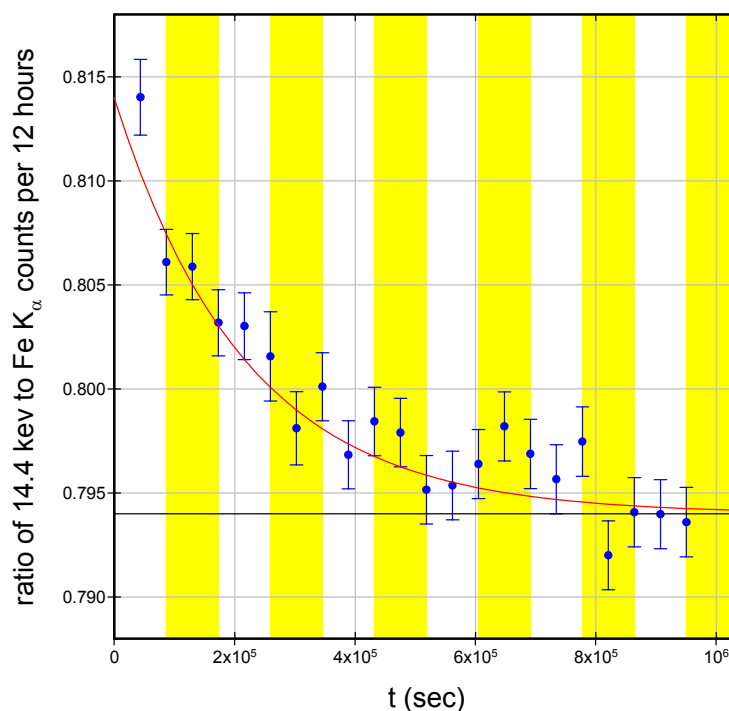
Figure 25. Ratio of counts per 12 h for the 14.4 keV gamma to the counts per 12 h for the Fe K_α X-ray (*blue circles*); simple $a + b \exp(-t/\tau_0)$ fit with $\tau_0 = 2.18 \times 10^5$ s; constant a (*black line*). The bottom time axis is in seconds; the days are marked on top, with the alternating yellow and white background giving the duration of each day.

8. Discussion and Conclusions

The original goal of the runs that now make up the May 20 experiment was to test for excitation transfer of the Fe-57 14.4 keV excited state mediated by strong, piezoelectrically induced vibrations near 2.21 MHz through a (time-correlated) reduction in the 14.4 keV gamma near the source, or an increase from elsewhere in the sample. As discussed above, we saw no evidence for this kind of excitation transfer effect under the conditions of the experiment.

Instead, we saw a different effect. The data shows an enhancement early in the experiment of the 14.4 keV gamma emission, and in the Fe K_α and K_β X-ray emission. This effect can be seen clearly in the data presented above (see Figs. 12, 14 and 15), and was observed with good signal to noise ratio.

Since exponential decay would normally be expected from a radioactive source, the non-exponential decay effect that we saw is anomalous in the sense of being unexpected. As such, the May 20 experiment is in our view potentially an important one.

The May 20 experiment was our first attempt at this kind of excitation transfer experiment. Because of this, we are motivated to consider reproducibility and the possibility of an artifact as issues. The enhancement at early time of
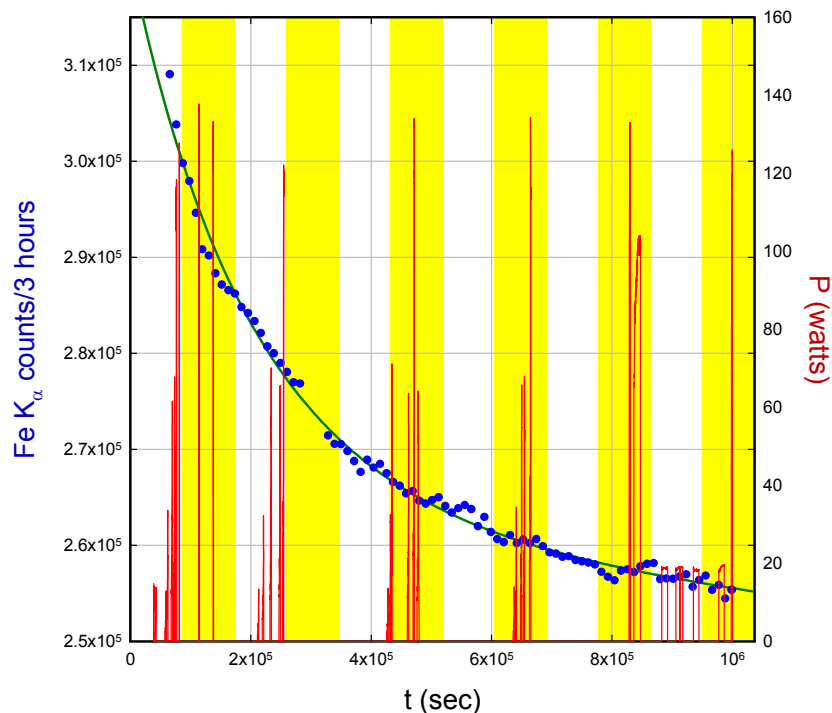
Figure 26. Time history of the Fe K$_\alpha$ signal (*blue circles*); empirical model (*solid green line*); peak transducer power (*solid red line*).

the strong gamma and X-ray lines is reproducible in our experiments, but subsequent observations so far have shown a weaker version of the effect. This indicates that there have been elements of the experiment not under our control (otherwise we would be able to see a large version of the signal each time), and not everything that is important experimentally was fully understood.

The interpretation of the data presents its own set of issues. During the long delay associated with the review process of this paper, there have been many subsequent experiments; and from these experiments some degree of understanding has begun to emerge.

For the early time enhancement of the Fe-57 14.4 keV gamma, and the Fe K$_\alpha$ and K$_\beta$ X-ray emission, one candidate interpretation involves a small degree of delocalization of the excitation among the Fe-57 nuclei in the substrate evaporated with the Co-57. With the Amptek detector being partially blocked by the protective mesh, it may be that even a small amount of delocalization of the excitation across the substrate provides for a substantial increase (or decrease) of the signal registered by the detector when excitation transfer occurs. This interpretation is discussed further in Appendix C.

Delocalization in connection with this hypothesis would require phonon exchange, and theory indicates that the rate for excitation transfer is much higher for THz phonons. So, this motivates us to think about what the source of these THz phonons might be. The enhancement in the Amptek signal appears (from subsequent experiments) to be correlated to the tightening of the bolts which apply stress to the steel plate through the wood clamps. The long (several

days) duration of the effect motivates us to consider creep, which is the (plastic) deformation/relaxation of a stressed viscoelastic medium. In the case of steel, creep occurs in part through the movement of dislocations, and we expect a substantial population of dislocations in the rolled steel used in the plate on which the Co-57 is deposited. Linear dislocations experience a force in a shear stress field, which in the presence of friction results in an average dislocation velocity (with constant stress). Part of the friction is due to phonon scattering and phonon radiation, which provides a possible mechanism for THz phonon generation and for a non-isotropic THz phonon distribution. This hypothesis is the subject of Appendix D.

The interpretation of the Geiger counter signal involves different spectral lines and a different mechanism. The Geiger counter responds more strongly to the harder 122 and 136 keV gammas than to the 14.4 keV gamma or Fe K_α and K_β X-rays (and we have observed this in subsequent experiments). The Geiger counter looks at the back side of the sample (the Co-57 is on the front side), so that there is no contribution from the 14.4 keV line (which is absorbed completely by the steel plate). There are weak Fe K_α and K_β signals on the back side as a result of photoionization by the harder gammas. Consequently, the Geiger counter time history is dominated by the 122 keV and 136 keV signals in the general vicinity of the Geiger counter, which is over a corner of the plate far from the Co-57 source. In this case, the intensity of these harder gammas at the Geiger counter position is enhanced at early time, and one interpretation for this is an anisotropic distribution of the harder gammas as a result of excitation transfer. This is consistent with early time non-exponential decay seen in later experiments with a NaI detector.

The reduction at early time in the higher channels of the scintillator/PMT detector is thought to be a result of an anisotropy of the harder gammas as well. Instead of being more intense at early time, one interpretation is that the harder gammas in the vicinity of the scintillator/PMT detector, which the detector probably responds to indirectly, is reduced at early time. The time history of the lowest channel is not consistent with this and remains not understood at present.

Our results are generally supportive of the observation of collimated X-ray emission reported previously by Karabut; and also by Kornilova and coworkers.

Our results are also (weakly) supportive of the observations of neutrons and alphas in the experiments of Cardone and coworkers, which we might expect to show up in our experiments if higher stress levels are achieved (assuming that greater stress produces a transfer of higher energy quanta). In a similar way our results are (weakly) supportive of the observations of neutron and alpha emission in the fracture experiments of Carpinteri and coworkers [57–59].

A modification of the time history of a gamma line produced by applying stress to a metal has deep and important theoretical implications. Our candidate interpretations at present involve excitation transfer, mediated by phonon–nuclear coupling. If the experimental results are not artifactual, one is tempted to conclude that phonon–nuclear coupling occurs and can be studied experimentally.

One goal of our research is to develop a well defined and well characterized version of the experiment, which would be appropriate to share with others. The May 20 experiment described here is the first version of an excitation transfer test and is followed by subsequent experiments which we will report on in future publications.

Appendix A.   Review of Phonon Exchange and Related Mechanisms

The May 20 experiment was carried out in order to provide experimental feedback on a theoretical proposal for an excitation transfer effect. This motivates us to provide here a brief review of phonon–nuclear coupling and excitation transfer. These mechanisms constitute building blocks for proposed up-conversion, down-conversion and subdivision mechanisms, which have been the focus of theoretical work aimed at shedding light on various anomalies in Condensed Matter Nuclear Science. Some discussion of these mechanisms follows in this Appendix.

Appendix A.1. phonon–nuclear interaction

We can write the phonon–nuclear interaction for a single nucleus in the form [5]

$$\hat{H}_{int} = \hat{\mathbf{a}} \cdot c\hat{\mathbf{P}}, \tag{A.1}$$

where $\hat{\mathbf{a}}$ operates on the internal nuclear degrees of freedom, and where $\hat{\mathbf{P}}$ is the momentum of the nuclear center of mass which depends on the vibrations. We can think of the $\hat{\mathbf{a}}$ operator as causing an internal nuclear transition, and the momentum operator $\hat{\mathbf{P}}$ as either creating or destroying a phonon. If dealing with two specific nuclear states and one highly excited phonon mode it is possible to reduce the interaction to

$$\hat{H}_{\text{int}} \rightarrow V_0(\hat{c}^\dagger + \hat{c})\bigg(\mid\uparrow\rangle\langle\downarrow\mid + \mid\downarrow\rangle\langle\uparrow\mid\bigg), \tag{A.2}$$

where $\hat{c}^\dagger$ and $\hat{c}$ are phonon creation and annihilation operators, and where $\mid\uparrow\rangle\langle\downarrow\mid$ raises the internal nuclear state $\mid\downarrow\rangle\langle\uparrow\mid$ lowers it. For dynamics governed by this kind of interaction, a single phonon exchange (absorption or emission) is coupled with a nuclear transition (raising or lowering).

The coupling of atoms and nuclei with the electromagnetic field is mediated by a similar interaction Hamiltonian, so it would be natural for us to think of a nuclear transition decay associated with phonon emission in connection with this Hamiltonian. While people do study single phonon exchange in connection with nuclear spin splitting in a strong magnetic field, here we are interested in internal nuclear states with energies that differ by keV or more, in which case there is no possibility of nuclear excitation or decay through the exchange of a single phonon. Instead we need to consider higher-order processes in which two or more phonons are exchanged.

Appendix A.2. Excitation transfer

The simplest higher-order process relevant to the discussion is excitation transfer. In the simplest case where two identical nuclei interact with a common excited vibration mode, it is possible to transfer nuclear excitation from one nucleus to the other. Suppose that nucleus A is excited while nucleus B is in the ground state initially. Then the exchange of one phonon can cause nucleus A to de-excite to the ground state, resulting in an (off-resonant) intermediate state where both nuclei are in the ground state. And then the exchange of a second phonon can cause nucleus B undergo a transition to the excited state. If the number of phonons is the same afterward as before, then this excitation transfer process can be resonant. The different pathways possible at lowest order are shown in Fig. 27.

This kind of excitation transfer process is the lowest-order effect that we might hope to see in the experiment (since it involves the exchange of only two phonons). Resonant excitation transfer can produce phase coherence if order is present, which can result in the angular anisotropy thought to be responsible for non-exponential decay effects associated with the harder gammas in the May 20 experiment.

Collimated gamma emission is possible in the case that phase coherence is present over a larger area of the surface, and where the lattice planes are aligned [60]. We had previously considered the presence of collimated X-rays to signify the presence of phonon up-conversion with a uniform vibrational mode. This should be updated to include (as more likely) the presence of resonant excitation transfer at the surface.

Resonant excitation transfer can move excitation from one location to another. In the event that the phonon mode is delocalized, such as for piezoelectrically induced MHz vibrations corresponding to plate resonances, the excitation has the possibility of being transferred from the vicinity of the radioactive source to pretty much anywhere in the plate. This is the effect predicted in the original design of the experiment. In contrast, a single excitation transfer event mediated by high frequency vibrations in the GHz or THz regime will only move the excitation a small distance, since
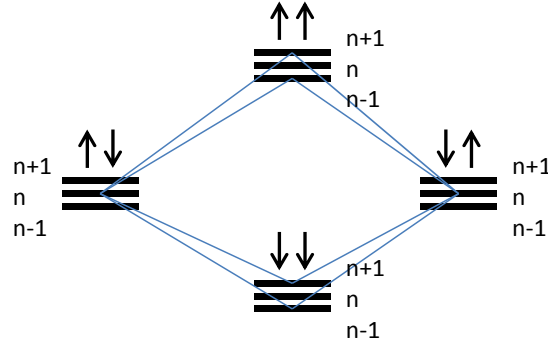
Figure 27. Simplified schematic of excitation transfer between two nuclei with single phonon exchange. The ↑ represents a nucleus in an excited state, and the ↓ represents a nucleus in the ground state.

these modes are very lossy and hence localized. However, many sequential excitation transfers with high frequency vibrations has the potential to lead to an overall transfer to a remote location.

The phonon–nuclear coupling interaction within the discussion above involves E1 symmetry (with only a single phonon exchange associated with each nuclear transition), while the transition from the Fe-57 ground state to the 14.4 keV excited state has M1+E2 symmetry. Consequently, excitation or de-excitation would involve two-phonon exchange and transitions to intermediate states, with excitation transfer involving the exchange of $0, \pm 2, \pm 4$ phonons.

Appendix A.3. Up-conversion

As discussed above our interest in up-conversion comes from an interest in the down-conversion mechanism conjectured to be the explanation for the absence of commensurate nuclear radiation associated with excess heat in the Fleischmann–Pons experiment. Models that we have studied for down-conversion also describe up-conversion on equal footing [61–64].

From the simplest perspective in the up-conversion process under consideration a great many phonons are exchanged to produce nuclear excitation (Fig. 28). These models indicate that up-conversion places more constraints on the requirements for the physical system than excitation transfer, with the most severe requirements coming when the number of quanta up-converted Δn

$$\Delta n = \frac{\Delta E}{\hbar \omega_0} \tag{A.3}$$

is large. Here ΔE is the up-converted energy and $\hbar \omega_0$ is the phonon energy. This consideration favors high frequency phonons in the THz regime. Up-conversion with 2.2 MHz phonons is particularly difficult since the associated phonon energy is very small (9.1 neV). The highest frequency phonons for BCC crystalline iron are near 38 meV [65], which according to the models makes up-conversion to the keV regime much more accessible. Our preference in all cases is to work with higher frequency THz phonons. However, in our initial experimental work, we focused on MHz vibrations in part since the experiments were much easier to be implemented, and since previous experimental work suggested that positive results could be obtained with lower frequency stimulation.
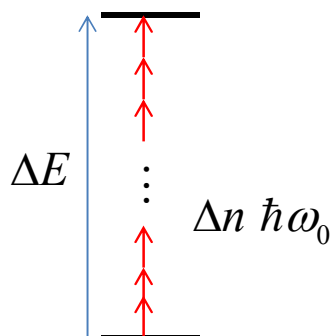
Figure 28. Simplified schematic of up-conversion for nuclear excitation by the conversion of a large number of phonons.

Up-conversion in the models occurs through the energy exchange of a great many single-phonon exchange interactions taking place rapidly before decoherence occurs. Excitation transfer effects might be observable under conditions where only a few phonon exchange interactions occur; however if up-conversion is observed then we know that a very large number of phonon exchange interactions must have occurred.
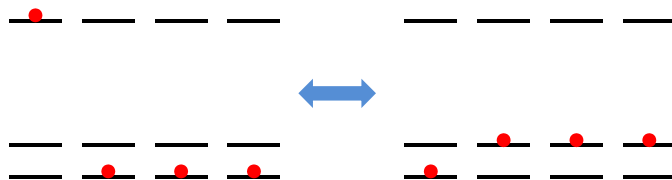
Figure 29. Simplified schematic of subdivision, where a single highly excited nuclear state is exchanged for many nuclear excitations at lower energy.

Appendix A.4. Subdivision

A problem was found when we made use of down-conversion models to reduce the large 24 MeV ΔE value associated with the $D_2/^4$He transition for excess heat in the Fleischmann–Pons experiment, where Δn is very large (on the order of 10^9 or greater), and it seemed difficult to connect theory with experiment. However, if the large 24 MeV quanta is instead exchanged for many lower energy (keV-level) nuclear excitations, then the resulting down-conversion problem becomes much more attractive. This conversion of a high energy nuclear excitation into many smaller nuclear excitations was termed "subdivision" (see Fig. 29), and it requires a modest number of phonon exchange interactions to occur. Typically there will not be a precise resonance available, so the energy mismatch δE will need to be taken up through down-conversion

$$\begin{aligned} \Delta E_1 = \ & \Delta N \Delta E_0 + \delta E \\ = \ & \Delta N \Delta E_0 + \Delta n \hbar \omega_0. \end{aligned} \tag{A.4}$$

A hindrance of the reaction rate can come from either too many excitations ΔN, or more likely from too many up-converted phonons Δn.

Appendix B. X-123 Calibration

The analysis of the data for the May 20 experiment depends in an important way on the calibration of the X-123, which motivates us to consider the calibration briefly in this appendix.

Appendix B.1. Calibration

For calibration, we chose the three strongest lines which result directly from the Co-57 source (the Fe-57 14.4 keV gamma, and the Fe K_α and K_β X-rays), along with two much weaker but clear X-ray lines (the Sn K_α and the Sb K_α). These are listed in Table 1. For the May 20 data set, we summed all available spectral data for the 11 days of the run to a single cumulative spectrum, and used a local Gaussian fit with a sloped baseline

$$f(i) = A \exp \left\{ -\frac{(i - i_0)^2}{\Delta i^2} \right\} + B + Ci \tag{B.1}$$

over channels in the vicinity of the lines, where i is the channel number, and where the other parameters (A, i_0, Δi, B, C) are determined by least squares fitting.

The Amptek X-123 detector settings were not changed after the experiment, and we might expect a minor drift over the following months. Channel averages are given in Table 1 for the May 20 spectra, and also for a spectrum taken subsequently starting on August 6, 2017. There are only minor differences in the average channel values; however, the

Table 1.   Major lines chosen for determination of the calibration parameters.

Line	Energy (eV)	Average channel May 20, 2017	Average channel Aug 6, 2017	FWHM (eV)
Fe K_α	6399.5	490.931	490.795	173.4
Fe K_β	7058.0	540.569	540.405	182.7
Fe-57 γ	14421.9	1099.713	1099.394	222.1
Sn K_α	25192.6	1919.218	1918.422	408.9
Sb K_α	26272.0	2002.277	2000.738	381.1

spectra are sufficiently close that it is possible to make use of calibration spectra taken subsequently to help with the line identifications.

Appendix B.2. Linear calibration

We used least squares fitting for the May 20 data set to develop a linear calibration of the form

$$E(\text{eV}) \;=\; a_0 + a_1 i, \tag{B.2}$$

where E is the energy in eV, and where i is the channel number; with fitting parameters given by

$$a_0 \;=\; -50.2842, \qquad a_1 \;=\; 13.1504. \tag{B.3}$$

The standard deviation associated with this fit is

$$\sigma \;=\; 8.937 \, \text{eV}. \tag{B.4}$$

Appendix B.3. Cubic calibration

Least squares fitting was also used to develop a cubic calibration for the May 20 data set with a lower standard deviation based on

$$E(\text{eV}) \;=\; a_0 + a_1 i + a_3 i^3 \tag{B.5}$$

with fitting parameters

$$a_0 \;=\; -75.413, \qquad a_1 \;=\; 13.1943, \qquad a_3 \;=\; -8.39972 \times 10^{-9}. \tag{B.6}$$

The standard deviation in this case is

$$\sigma \;=\; 4.801 \, \text{eV}. \tag{B.7}$$

This cubic calibration does a little better than a quadratic calibration, for which the standard deviation is 5.122.

Appendix B.4. Peak identifications

Results for the May 20 spectra augmented with calibration runs carried out in August are summarized in Table 2. We see good agreement between known line positions and estimates for the two calibrations. During the runs in August we took XRF calibration spectra in place with Ti, Zn and Sn samples, which confirmed earlier identifications in the case of Zn and Sn. The Ca K_α and K_β lines were much stronger in the August spectra.

We were not expecting to see escape peaks with a Si-PIN detector since the fluorescence yield of the Si K_α is low; however, there are clear escape peaks present associated with the strong Fe-57 gamma and Fe K_α and K_β lines at an energy of

$$E[\text{escape}] \;=\; E_0 - E[\text{Si K}_\alpha] \;=\; E_0 - 1739.8 \, \text{eV}. \tag{B.8}$$

Identifications for the weaker lines in the summed spectra for the May 20 experiment listed in Table 2 are shown in Fig. 30.

Table 2. Average channel numbers for identified and also for unidentified lines from the May 20 data; average channel numbers for lines observed in August runs are in brackets; known energies for the different X-ray transitions and gamma transition are listed, along with energy values from the linear and cubic fits.

Line	Average channel	Energy (eV)	Linear energy (eV)	Cubic energy (eV)
Ca K_α	[284.999]	3690.5	3697.6	3684.8
Ca K_β	[309.090]	4012.7	4014.4	4002.6
Ti K_α	[347.324]	4508.8	4517.2	4506.9
Ti K_β	[378.609]	4931.8	4928.6	4919.6
Fe K_α escape	358.040	4659.5	4658.1	4648.3
Fe K_β escape	408.683	5318.0	5324.1	5316.3
Fe K_α	490.931	6399.5	6405.7	6401.1
Fe K_β	540.569	7058.0	7058.4	7055.7
Zn K_α	[660.381]	8631.1	8634.0	8635.4
?	688.133		8998.9	9001.3
Zn K_β	[732.641]	9572.0	9584.2	9588.0
?	740.924		9693.2	9697.1
Fe-57 γ escape	967.691	12681.9	12675.2	12685.0
Fe-57 γ	1099.713	14421.9	14411.4	14423.4
Zr K_α	1198.711	15746.3	15713.2	15726.3
Ag K_α	1683.961	22103.1	22094.5	22103.2
Sn K_α	1919.218	25192.6	25188.2	25187.9
Sb K_α	2002.277	26272.0	26280.5	26275.8

Appendix B.5. Unidentified peaks at 9.00 and 9.69 keV

There are two weak lines present in the May 20 spectra with energies of 8998.9 and 9693.2 eV based on the linear calibration which have been frustrating to identify. We had initially (prior to the research leading to an accurate calibration) thought that they were Zn K_α and K_β lines; however, in the August spectra we can see the 8998.9 eV line offset from the Zn K_α and K_β. Certainly there are X-ray transitions known near 9.00 keV; in the NIST data base there are Cu KM and KN lines between 8.977 and 8.980 keV, and Hg and Hf LM lines between 9.019 and 9.023 keV, none of which are attractive candidates. Around 9.69 keV there are also lines known; there is a W LM line near 9.673 keV, Tl and Au LM lines listed between 9.701 and 9.713 keV, and Ta and W LN lines predicted between 9.708 and 9.717 keV, none of which are compelling candidates. In all cases one would expect to see other lines with appropriate relative intensities; however, and these other lines are not present in the spectra. We took data with a Ta foil irradiated by Co-57, and the emission pattern looks nothing like the unidentified spectral features.

We considered the possibility that the unidentified lines might be summation peaks according to

$$E[\text{Fe } K_\alpha + \text{Cl } K_\alpha] = E[\text{Fe } K_\alpha] + E[\text{Cl } K_\alpha] = 6399.47 + 2621.87 = 9021.33 \text{ eV}, \tag{B.9}$$

$$E[\text{Fe } K_\beta + \text{Cl } K_\alpha] = E[\text{Fe } K_\beta] + E[\text{Cl } K_\alpha] = 7057.98 + 2621.87 = 9679.85 \text{ eV}. \tag{B.10}$$

Since the HCl volatilizes during the evaporation of the $^{57}\text{CoCl}_2$ in 0.1 M HCl solution on the surface of the steel, we would not expect much chlorine to be present on the surface in amounts more than twice the Co-57. In spectroscopy measurements we do not see a clear Cl K_α line in the Amptek X-123 spectrum, due in part to the high background in the low energy channels, and in part to the weakness of the signal.
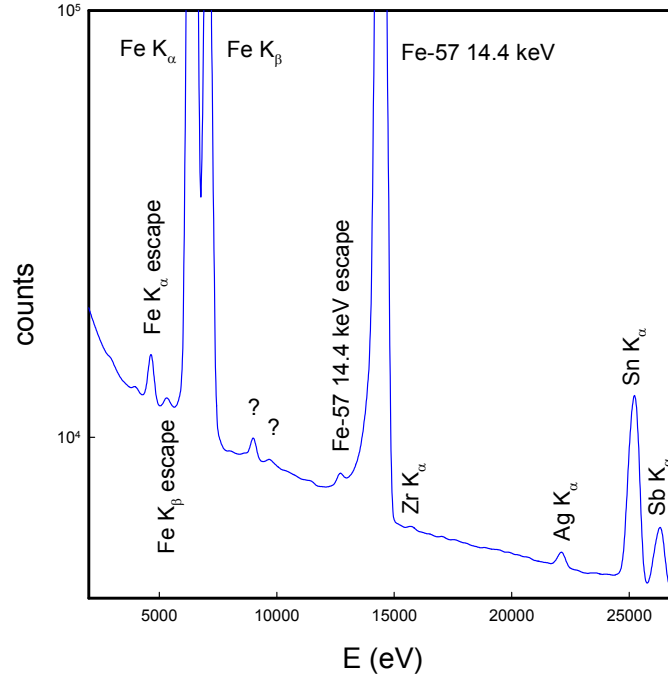
Figure 30. Weak lines in the smoothed time-integrated spectrum for all data from the May 20 experiment including identifications.

We carried out an experiment with graphite sheets to block the low energy lines while passing the Fe K_α in order to clarify the issue. The result was that the 9.00 keV line was not eliminated, which rules out the possibility of the unidentified lines being summation peaks.

One speculative possibility for the 9.00 keV line identification is that it might be an escape peak associated with the 14.4 keV gamma due to a low-level impurity in the Si. We can compute for a Cr impurity

$$E[^{57}\text{Fe } 14.4219 \text{ keV}] - E[\text{Cr } K_\alpha] = 9.007 \text{ keV}. \tag{B.11}$$

This is in good agreement with the observed linear near 9.00 keV.

Appendix B.6. Time-history of the 9.00 keV line

The time history of the 9.00 keV line is non-exponential (see Fig. 31), but shows only a modest version of the early time enhancement (a roughly 2% increase, where we might have expected to see a roughly 20%). This is explainable if only the weak line itself is showing a strong non-exponential decay, with the background decaying much more slowly consistent with the 271.74 day half life. To clarify this it would be useful to separate out the time dependence of the local background from the line itself, which is problematic since the line is weak which leads to statistical issues. Perhaps the most straightforward way to see the relative contributions in this case is to look at the contour plot of
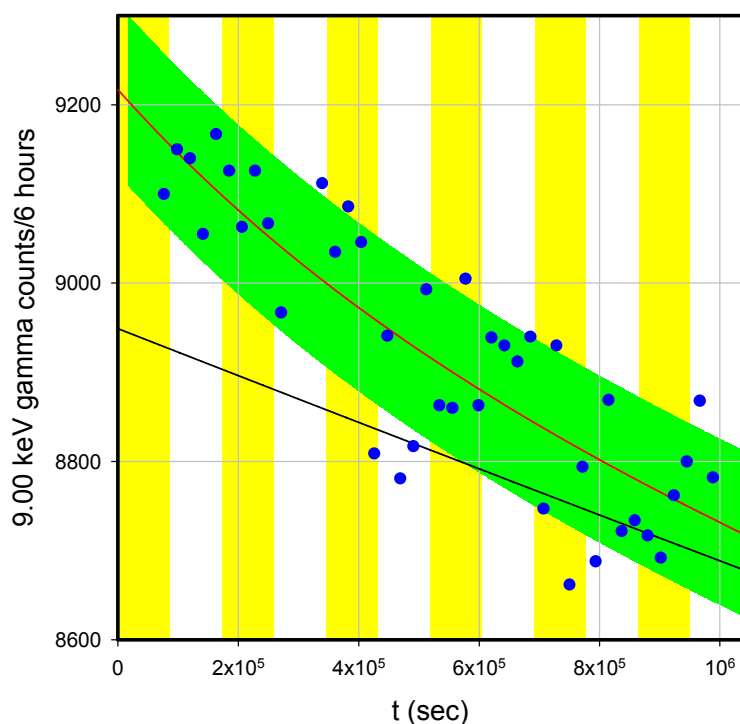
Figure 31. Time history of the of the unidentified 9.00 keV peak (*blue circles*); empirical model (*red*); exponential decay with 271.74 days half-life consistent with empirical model (*black*); the $\pm 1\sigma$ error bars determined by the square root of the average number of counts (light green solid region). The bottom time axis is in seconds; the alternating yellow and white background show the duration of each day between 5/20 and 5/31.

counts per 6 h as a function of time and energy (shown in Fig. 32). We see that the background away from the line is reasonably constant in time, while the line itself shows a noticeable decrease over the duration of the experiment.

Appendix C. Possibility of a Delocalization Effect

Although the May 20 experiment shows an unexpected non-exponential decay effect, the experiment itself does not provide direct information as to how such an effect is produced. In Appendix A, we reviewed briefly some of the effects that we might have predicted to see, but in retrospect our focus has to be on such excitation transfer effects which require the least amount of new physics to give effects in an experiment. As a weak effect, excitation transfer would be expected to be dominated by a resonant version of the effect (in which no net energy is exchanged with phonons), which would produce phase coherence. Phase coherence is potentially observable via dynamic angular anisotropy, which in the May 20 experiment is most likely the reason that we see non-exponential time histories in the Geiger counter (which responds most strongly to the 122 and 136 keV gammas), and perhaps in the scintillator/PMT detector as well.

If the indirect coupling matrix element associated with excitation transfer is strong, then we would expect many excitation transfers to be possible before dephasing occurs, and also that non-resonant excitation transfer events would
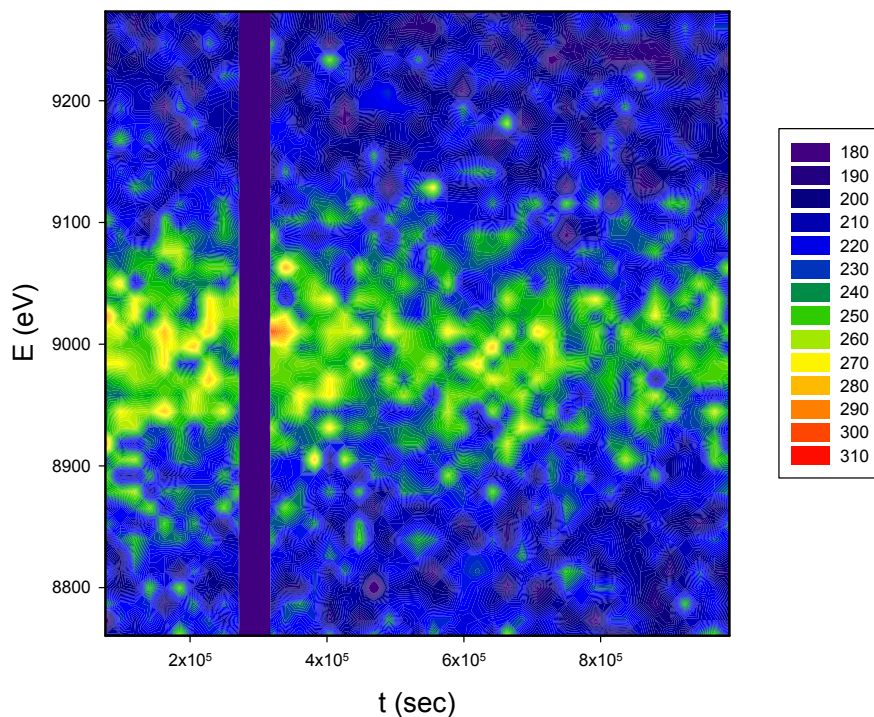
Figure 32. Time history (counts per 6 h) of the spectrum of the unidentified 9.00 keV peak; the time axis (*bottom*) is in seconds; the energy is on the left.

dominate. Due to this latter effect we would not expect phase coherence, which would suggest a lack of angular anisotropy associated with the 14.4 keV gamma. Since the Fe K_α X-ray results from incoherent decay processes, we would not expect to see angular anisotropy effects associated with the strong X-ray transitions. These various theoretical statements appear to be consistent generally with results from the May 20 experiment, and also from subsequent experiments. One might have argued that the non-exponential decay effect in the 14.4 keV gamma was due to angular anisotropy, but in such a scenario the explanation of a very similar non-exponential decay effect in the Fe K_α and K_β X-rays becomes problematic.

The notion of multiple excitation transfers occurring prior to the decay of the 14.4 keV excited state is conceptually straightforward. In an abstract sense we understand that multiple excitation transfers will produce a larger delocalization of excitation in the strong coupling regime compared to the weak coupling regime. We then run into issues associated with the suggestion that enough excitation transfers can occur within the 98.3 ns half-life of the 14.4 keV state to produce delocalization at the hundred micron to millimeter scale, which is what would be required to account for non-exponential time histories observed by the X-123 detector with the coarse aluminum mesh. For example, if excitation transfer were mediated by THz phonon exchange, then we would expect the separation between nuclei for a single excitation transfer to be restricted to on the order of 100 Å. Unless this fast excitation transfer effect were directional, it is hard to imagine that enough isotropic excitation transfer events could move an excitation more than 100 μm across the plate surface.

There are other issues as well. We had evaporated the Co-57 onto a steel plate, in part because the steel has Fe-57 as a constituent at the level of 2.11%. If excitation transfer can delocalize excitation more than 100 μm, then we might expect the excitation to go into the steel, where the emitted low energy radiation would be absorbed. On the face of it, excitation transfer consistent with this picture can lead to a non-exponential effect in which the emission registered above the plate surface is reduced instead of increased.

At this point we take advantage of many subsequent months of thought and contributions from colleagues in order to devise a relevant picture.

The evaporation of a sessile droplet on a flat surface has recently become a topic of interest, as reviewed in Ref. [66]. We are familiar with rings left following the evaporation of coffee, which itself has been studied in some detail (see e.g. [67]. One would expect a similar model to apply for a non-colloidal liquid. Salt crystal formation on various flat insulators was studied in Ref. [68], while the evaporation of various salts on a metal surface was studied in Ref. [69]. We have so far not found studies of the evaporation of $CoCl_2$ in aqueous HCl on steel, but we would expect (and by now have observed) a ring resulting from our evaporation. The ring formed during the evaporation of the solution is a bit larger than 1 cm in diameter, with a width of roughly 0.5 mm.

The amount of radioactive chloride that corresponds to the initial activity is small, and by itself would not constitute enough material to be observable as a ring (as observed by Malcolm Fowler/Los Alamos). Consequently, we know that there must be something else in the residue, and the only question is what. An elemental or isotopic analysis of the solution would have been appropriate to settle this, but we were not able to arrange for such an analysis due to the radioactivity, and the remainder of the solution had already been used for a second evaporation before we understood that this was important. From e-mail exchanges with Eckert & Ziegler we understand that probably there is little other than Co-57 present in the stock which they buy from their suppliers. If the stock was made a long time ago, then it is possible that Fe-57 will have accumulated. Since according to Eckert & Ziegler such stock can be several years old, in the picture we are working with at present it is presumed that most of the residue is daughter Fe-57 from earlier Co-57 decays.

If so, then the residue itself will be preferred for receiving excitation transfer (in comparison to the Fe-57 in the steel plate) due to the ready availability of ground state Fe-57, and we might expect excitation transfer to result in excitation moved from one part of the residue to another. We know that the residue is strongly inhomogeneous (because we can see the ring), and we might expect that excitation would go preferentially to where there is more Fe-57.

Suppose now that the coarse aluminum mesh between the plate and the Amptek X-123 detector blocks emission from where the excitation is originally coming from, and passes emission from where the excitation is transferred to. In this picture we might expect a non-exponential enhancement of registered emission. The enhancement can lead to a non-exponential decay effect, as observed, assuming that more phonons are present early on due to relaxation (of moving dislocations, or viscoelasticity in the epoxy, or rearrangement at interfaces – see section below for details). If so, then we might equally well have seen a non-exponential increase (as has been observed in later experiments) if the mesh were to pass emission from where excitation comes from. It would also have been possible to see a small effect (as has been observed), if on average emission is passed equally from regions where excitation originates from and where excitation ends up. This general picture is consistent as far as we know from much later experiments focusing in localized regions within the substrate.

What is left then is to think about the spatial scale and implications. To account for the magnitude of the non-exponential component, excitation transfer on a spatial scale of a few hundred microns to the millimeter scale is needed. How this happens is not understood at present. There are some candidate hypotheses available. One is that the excitation transfer is sufficiently fast that many small 100 Å steps produce effects at the larger scale. Another hypothesis is that the excitation transfer is directional, perhaps as a result of non-resonant phonon exchange, or perhaps as a consequence of the inhomogeneity of the Fe-57. Another possibility is that in the strong coupling limit highly off-resonant states are occupied which have no decay channels open, resulting in a reduction in the overall decay rate.

Appendix C.1. Al mesh

The mesh is thick (absorbing) for the 14 keV gamma (97%) and Fe K_α and K_β X-rays (100%), so that transmission only occurs through the holes. The sensitive part of the Si PIN detector is a square 6 mm^2 in area. We assume for this discussion that the 6 mm^2 area of the detector is located 10 cm below the source. In between the source and detector is the mesh. We know the size of the holes in the mesh (0.47625 cm diameter), and the average transmission (51%).

Suppose we define r to be the radius of the hole, and b to be the distance between the center of a hole and the nearest neighbor. In this case, the average transmission t is the ratio of the area of the holes in one triangle with neighboring hole centers as vertices divided by the area of the triangle

$$t = \frac{\pi r^2 / 2}{\sqrt{3} b^2 / 4}. \tag{C.1}$$

From this we can write the distance between the holes to be

$$b = \sqrt{\frac{2\pi r^2}{\sqrt{3} t}} = 0.635 \text{ cm}. \tag{C.2}$$

Appendix C.2. Detector alignment

The Amptek X-123 detector area (6 mm^2) is small compared to the hole area (17.8 mm^2), so that whether the X-ray and gamma ray signals make it through the mesh is dependent on whether there is a hole above the detector or not. In the May 20 experiment there was no attempt at optimization of the signal relative to the local mesh position, so that the position of the detector relative to the hole is unknown. This was an uncontrolled random variable in the early experiments.

Appendix C.3. Count rate and mesh transmission

We can make a rough estimate for the mesh transmission from the observed count rate of the Fe-57 14.4 keV gamma. The expected count rate R can be estimated in terms of the source strength S according to

$$\begin{aligned}
R &= \Delta\Omega \times T_{\text{mesh}} \times \eta \times S \\
&= \left(\frac{6 \text{ mm}^2}{4\pi d^2} \right) \times T_{\text{mesh}} \times \eta \times \left(0.091 \times 200 \, \mu\text{Ci} \times 3.7 \times 10^{10} \text{ Bq} \right) \\
&= \left(4.77 \times 10^{-5} \right) \times T_{\text{mesh}} \times \eta \times \left(6.73 \times 10^5 \right) \frac{\text{counts}}{\text{s}},
\end{aligned} \tag{C.3}$$

where $\Delta\Omega$ is the acceptance angle, where T_{mesh} is the (unknown) transmission of the mesh, and where η is the efficiency of the detector. According to [45] there are 9.1 14.4 keV gammas produced per 100 Co-57 disintegrations. From the Amptek website the intrinsic efficiency (Be window and Si absorption) of the detector is about

$$\eta = 0.725. \tag{C.4}$$

The expected count rate is then

$$R = 23.3 \, T_{\text{mesh}} \, \frac{\text{counts}}{\text{s}}. \tag{C.5}$$

The observed count rate in the May 20 experiment for the 14.4 keV gammas is about

$$R = 4.15 \times 10^5 \, \frac{\text{counts}}{6 \, \text{h}} = 19.2 \, \frac{\text{counts}}{\text{s}}. \tag{C.6}$$

These estimates are consistent with a mesh transmission of

$$T_{\text{mesh}} = 0.82 \tag{C.7}$$

with substantial uncertainties at this point in the Co-57 activity, and in the distance d between source and detector. The relatively good agreement between source strength and count rate in this estimate is encouraging; however, it is not possible to develop an accurate estimate for the mesh transmission in this case.

A similar computation for the Fe K_α is not so consistent. The source efficiency is more than 5 times higher, so one might expect to see a much higher count rate. Amptek does not report an absolute efficiency for the X-123 Si PIN detector, but lists an intrinsic efficiency near 95%. Including photoabsorption in air helps to a minor degree to explain why we do not see a 4–5× higher count rate. It is likely that the X-123 has a low absolute efficiency near 6.4 keV. This conclusion is supported by the study of Ref. [70].

Appendix C.4. Discussion

The relative position of the source, mesh and detector are critical parameters which were uncontrolled in the May 20 experiment due to the exploratory nature of this experiment, and which have a big impact on reproducibility. We were not aware of this in the early runs, and as a result there was much variation in the magnitude and sign of the non-exponential decay effect. A consequence of this is that this kind of experiment would be expected to be very sensitive to the relative positions, and changes during the experiment would produce artifacts similar to the effects reported.

The large magnitude of the non-exponential component of the signal in the May 20 experiment indicates delocalization occurring on a spatial scale no less than hundreds of microns, and perhaps more than 1 mm, given the picture outlined above. If so, this would be stunning, and would be an effect well worth studying in detail much further.

Experiments in which Fe-57 (free of Co-57) is placed near the residue are of interest, as we will want to see excitation going into the Fe-57 from regions containing the Co-57 to have confidence that we are seeing this kind of excitation transfer.

Appendix D. Possibility of THz Phonon Generation from Creep

Given the experimental results described above, it is not yet possible to draw any firm conclusions about what is going on in detail in the sample from the data presented. On the other hand, if the enhanced early time emission is real, then it needs an explanation, and we are going to need hypotheses that can be addressed in future experiments and in future theoretical work.

The experiment was set up and run in order to see whether we could induce delocalization of the Fe-57 14.4 keV excited state through phonon exchange by vibrating the steel plate strongly at 2.21 MHz. This did not seem to work as discussed above. The rate for excitation transfer in a molecule in the absence of loss scales as the phonon frequency squared [23], which draws attention to the low 2.21 MHz phonon frequency as an issue, and also focuses attention

on the possibility that THz phonons might be present in the experiment. If so, then we are interested in mechanisms present in the experiment which might generate THz phonons.

Since the early time enhancement was present when we began taking data, our attention is focused on what happened to the sample prior to the experiment. Before the May 20 experiment, the steel plate had been resting on a rack with no wood blocks attached, but with piezoelectric transducer and ultrasonic coupling gel on top, and with earlier sets of transducer pulses applied. In preparation for the experiment the sample was picked up, then one corner was placed between two pieces of wood and bolts tightened, at the equivalent force of about 2000 lbs. This was followed by a similar procedure for the other two pieces of wood. Then the steel plate with wood blocks was placed on the rack as in the photograph (Fig. 3), and data was collected.

Appendix D.1. Ultrasound absorption issues

The stress in the steel is greatest near the wood clamps, with compressional stress between, and shear stress near the edge outside of the steel-wood interface. Phonons generated near the clamps could propagate to the vicinity of the Co-57 substrate only at "low" frequency, since ultrasonic attenuation in steel leads to an absorption length on the order of 1 cm near 10 MHz [71–73]. There is little reason to believe that this will make a difference given that driving the steel plate with over 100 watts near 2.21 MHz does not produce an observable response that can be correlated with the period when the plate is driven.

THz phonons are strongly absorbed in all solids, and we would expect an absorption length on the order of 10 nm or less. This focuses our attention on dislocations, which have a long lifetime, which are present in rolled steel, and which scatter and generate THz phonons locally when they move. THz phonons scattered or radiated then by moving dislocations very close to the nuclear excitation have the potential to produce excitation transfer.

Appendix D.2. Creep and dislocation movement

The early time enhancement of the gamma and X-ray emission seen in the experiment appears to decay away with a relaxation time of about two and a half days. This relaxation time is not connected to the nuclear levels of Fe-57 in an obvious way; however, it may be consistent with creep, since there is the possibility of plastic deformation in the steel [74–77] and wood [78–80]. The plastic deformation associated with creep occurs through the flow of dislocations.

Dislocations experience a force in the presence of stress [81], and plastic deformation in iron is dominated by screw dislocations [82]. The dislocation velocity $v(T)$ increases with temperature [83], in one model according to [84,85]

$$v(T) \;=\; \nu_{\mathrm{D}} \frac{b}{l_{\mathrm{c}}} \frac{L}{l_{\mathrm{c}}} a \exp\left\{ \frac{\Delta G(\sigma)}{k_{\mathrm{B}} T} \right\}, \tag{D.1}$$

where ν_{D} is the Debye frequency, b the distance between two rows of atoms in a slip plane, l_{c} the critical length for kink nucleation, L the length of the linear dislocation, where a is the slip distance for a single activation, and where ΔG is the free energy of activation which is a function of stress σ (edge and screw dislocations experience a force under shear stress).

The rate of plastic deformation is given by what is often referred to as Orowan's equation [86–88]

$$\frac{\partial}{\partial t} \epsilon \;=\; \alpha b \rho \overline{v}, \tag{D.2}$$

where ϵ is the strain, b the Burgers vector, ρ the density of dislocations, $\overline{v}$ the average dislocation velocity, and α is a geometrical factor. It would follow from these arguments that we would might expect the temperature dependence of

creep to obey an Arrhenius law. Consistent with this, Cuddy reported that the observed rate of creep in steel could be fit by a model of the form [75]

$$\frac{\partial}{\partial t}\epsilon \;=\; A\sigma_A^n \exp\left\{-\frac{Q}{RT}\right\},$$

(D.3)

where Q is an activation energy, σ_A the applied stress, n a fitting parameter (5.8 for the measurements fitted), and A is a proportionality constant. If THz phonons from plastic deformation are responsible for the effects observed, then we might expect a version of the experiment run with steel at elevated temperature to show a faster decay.

In future experiments we would like to see whether the anomaly is sensitive exclusively to shear stress, or whether tensile or compressional stresses also can produce anomalies. Such tests would be useful for shedding light on how best to design new experiments, as well as being helpful for theory. Late in the writing of this paper an early paper came to our attention describing the observation of gamma radiation emitted as a result of various materials subjected to very high levels of shear stress [89].

Appendix D.3. Time-dependence and creep

The empirical fitting model that we made use for the intensity of the gamma and X-ray emission is consistent with

$$I(t) \;=\; I_0\; e^{-t/\tau} \exp\left\{b\; e^{-t/\tau_0}\right\} \;\rightarrow\; I_0\; e^{-t/\tau}\left[1 + b\; e^{-t/\tau_0}\right]$$

(D.4)

for small fitting parameter b (the exponential empirical model was used since it produced a lower error). The exponential decay of the anomaly be^{-t/τ_0} is consistent generally with the exponential decay associated with solutions for simple viscoelastic models for initial value problems [90,91], under the assumption that the non-exponential part of the emission is proportional to the (creep) strain rate.

Appendix D.4. Phonon emission by moving dislocations

At high velocity dislocations radiate THz phonons efficiently [92], which perhaps might provide the beginning of a connection with up-conversion models discussed in the Introduction. However, the level of stress present in the May 20 experiment is insufficient to produce dislocation velocities sufficiently fast as to get to the stress regime where high rates of phonon emission occur. At lower dislocation velocity part of the friction is due to interaction with phonons, so that while THz phonon emission is inefficient, there is substantial coupling to and scattering with high-frequency phonon modes [93–95].

Appendix D.5. Creep in steel, and in other materials

Once our focus turned to creep in the experiment, we immediately presumed that creep in the steel in the vicinity of the Co-57 was most important. However, we might expect creep to be present in the wood clamps, epoxy, or ultrasonic coupling gel, where creep can be induced much more readily. THz phonons generated in the epoxy in general are more distant (and less likely to be important), except for the surface layer in contact with the Co-57 residue and steel. Creep in the wood or gel is sufficiently distant that one might expect it to impact the region of the Co-57 only indirectly.

Friction effects generally between the steel, residue and epoxy are likely important in generating very high frequency vibrations that could produce the effects observed.

Appendix E. Possibilities for Future Experimentation

The non-exponential decay observed at early time in the Fe-57 14.4 keV line, and in the Fe K_α and K_β X-rays, if real and if connected with phonon–nuclear coupling, potentially opens the door to a wide range of new experiments. In this appendix we consider some possibilities.

Appendix E.1. Studying excitation transfer

If we are able to delocalize nuclear excitation perhaps at the millimeter scale through excitation transfer with only modest levels of THz phonons from creep, then perhaps delocalization over larger distances is possible with more THz phonons. This could be studied with an energy dispersive X-ray camera.

Over what range can excitation transfer work? For example, suppose we put in a barrier layer of iron that is depleted in Fe-57, could we reduce excitation transfer through it, or stop it completely? The same approach could be used with a barrier layer made of a different material.

Would we get a much stronger version of the effect if we worked with a sample made of Fe-57?

Can the effect be seen using other low energy transitions? One candidate is the 6.237 keV E1 transition in Ta-181, which is longer lived, which should be helpful for the development of coherent effects. Another is the 1.565 keV M1+E2 transition in Hg-201, which has the advantage of a lower energy nuclear transition.

We would expect larger Dicke factors to be associated with excitation transfer in the event that most of the participating nuclei are initialized in the same ground state. This suggests that we might want to work with a strong magnetic field and low temperature, or perhaps a magnetized sample at low temperature.

Excitation transfer can be resonant, or non-resonant, which would make a difference in terms of angular anisotropy or beam formation in a material with aligned crystal planes. Is it possible to control the THz phonons in such a way as to maximize resonant excitation transfer and hence maximize the anisotropy?

Appendix E.2. Possibility of observing subdivision

Excitation transfer requires the least amount of phonon exchange of the relevant mechanisms reviewed in Section 2, which is why we have focused on excitation transfer mechanisms in connection with the May 20 experiment. Subdivision in the models requires coherent energy exchange, which makes it more challenging than excitation transfer, but the amount of energy exchange is less than for up-conversion. The demonstration of a subdivision effect would be extremely important, in that it would show that coherent energy exchange is possible.

Finding good resonances can minimize the energy mismatch and is a key issue for subdivision. A list of candidates relevant to experiments involving a Co-57 source is given in Table 3.

Table 3. Candidates for subdivision driven by a Co-57 source

Initial isotope	Energy (keV)	Final isotope	Energy (keV)	ΔN	Mismatch (keV)
Fe-57	136.4743	Sc-45	12.40	11	0.07
Fe-57	136.4743	Ta-181	136.262	1	0.212
Fe-57	14.4129	Hg-201	1.565	9	0.328
Fe-57	136.4743	Hg-201	1.565	87	0.340
Fe-57	136.4743	Os-186	137.159	1	–0.685
Fe-57	136.4743	Ta-181	6.237	22	–0.74

The lowest mismatch among the candidates is for

$$^{57}\text{Fe}(136.47) + 11\ ^{45}\text{Sc}(0)\quad\leftrightarrow\quad ^{57}\text{Fe}(0) + 11\ ^{45}\text{Sc}(12.40) + 0.07\text{ keV.}$$
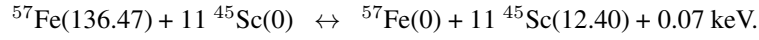
An experiment to demonstrate subdivision might involve the evaporation of radioactive Co-57 solution onto a steel plate, while at the same time evaporating scandium chloride in solution.

Non-resonant excitation transfer from the 136.47 keV state of Fe-57 might be possible to the 136.262 keV of Ta-181 according to

$$^{57}\text{Fe}(136.47) + ^{181}\text{Ta}(0)\quad\leftrightarrow\quad ^{57}\text{Fe}(0) + ^{181}\text{Hg}(136.262) + 0.212\text{ keV.}$$
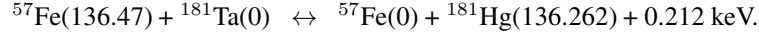
The energy mismatch is 212 eV, which is one of the lower mismatches among the candidates in Table 3. There is also a subdivision possible from the 136.47 keV state of Fe-57 to the 6.237 keV state of Ta-181

$$^{57}\text{Fe}(136.47) + 22\ ^{181}\text{Ta}(0)\quad\leftrightarrow\quad ^{57}\text{Fe}(0) + 22\ ^{181}\text{Hg}(6.237) - 0.74\text{ keV.}$$
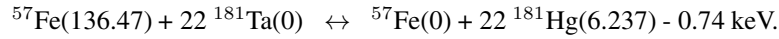
These two could be distinguished since non-resonant excitation transfer would result in Ta K_α X-ray emission; but no Ta K_α emission would be associated with subdivision – instead we would expect to see M-shell emission lines.

Another interesting possibility is to attempt the subdivision of the Fe 14.4 keV state to produce excitation of the 1565 eV state in ^{201}Hg according to

$$^{57}\text{Fe}(14.41) + 9\ ^{201}\text{Hg}(0)\quad\leftrightarrow\quad ^{57}\text{Fe}(0) + 9\ ^{201}\text{Hg}(1.565) + 0.33\text{ keV.}$$
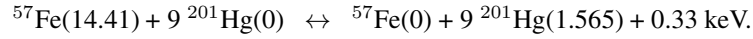
The energy mismatch is about 330 eV, which is again one of the lower mismatches in the table.

We had entertained the possibility that subdivision might account for the enhanced emission at early time in the May 20 experiment. Subdivision of the 136.5 keV state to the 14.4 keV state would be described by

$$^{57}\text{Fe}(136.47) + 9\ ^{57}\text{Fe}(0)\quad\leftrightarrow\quad ^{57}\text{Fe}(0) + 9\ ^{57}\text{Fe}(14.421) + 6.76\text{ keV.}$$
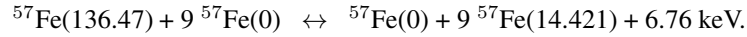
The relatively large energy mismatch, combined with the short (8.7 ns) half-life of the 136.5 keV state, suggests that this process would not be favored in the May 20 experiment. If this process were dominant, we would have seen a reduction in the Sn-K_α proxy for the harder 122 keV and 136 keV along with increased 14.4 keV and Fe K_α emission. Due to the relative absence of a decrease in the Sn K_α signal at early time in the data we consider this subdivision mechanism as unlikely to account for the observations reported in this paper.

Appendix E.3. Issues associated with up-conversion experiments

Our interest in up-conversion and down-conversion come from our interpretation of several anomalies in Condensed Matter Nuclear Science. The excess heat effect in the Fleischmann–Pons experiment would not be anomalous if there were a down-conversion mechanism established consistent with the models we have developed. Collimated X-ray emission in the Karabut experiment would not be anomalous if there were an up-conversion mechanism accepted. As mentioned above, up-conversion and down-conversion are described by the same basic models, so a demonstration of up-conversion implies down-conversion can occur, and vice versa. We are interested in whether the predicted up-conversion and down-conversion mechanisms can be demonstrated experimentally. Note that the experimental demonstration of a subdivision effect would strongly support the notion that up-conversion and down-conversion can work.

One candidate hypothesis for the early time enhancement in the May 20 experiment is up-conversion, which we have considered seriously in connection with the May 20 experiment. According to theory up-conversion would occur as a result of a great many non-resonant excitation transfer events before the transition decoheres. If so, then we would like to see unambiguous evidence for excitation transfer first, which is why our interest focuses on candidate

hypotheses involving excitation transfer first. Arguing against an up-conversion mechanism is that similar experiments carried out with no Co-57 do not show reproducible emission in the scintillator/PMT detector.

For future up-conversion experiments we consider working with a low-energy transition (such as the 1.565 keV transition in Hg-201 or the 6.237 keV transition in Ta-181) [4], and then follow the model which points to the importance of: the number of identical nuclei involved in the ground state; maximization of the number of optical phonons in a mode that is spatially uniform; maximization of the half-life of the upper and lower states; ensuring that loss is present (which is thought to be dealt with in the low-Q resonator modes of optical phonons). These same issues should be relevant for similar reasons for subdivision and for excitation transfer.

Acknowledgments

References

[1] M. Fleischmann and S. Pons, Electrochemically induced nuclear fusion of deuterium, *J. Electroanal. Chem. and Interfacial Electrochem.* **261** (1989) 301–308.

[2] M. Fleischmann, S. Pons, M. W. Anderson, L. J. Li, and M. Hawkins, Calorimetry of the palladium–deuterium–heavy water system, *J. Electroanal. Chem. and Interfacial Electrochem.* **287** (1990) 293–348.

[3] E. Storms, *Science of Low Energy Nuclear Reaction: A Comprehensive Compilation of Evidence and Explanations about Cold Fusion*, World Scientific, New Jersey, USA, 2004.

[4] P.L. Hagelstein, Bird's Eye View of Phonon Models for Excess Heat in the Fleischmann–Pons Experiment, *J. Condensed Matter Nucl. Sci.* **6** (2011) 169.

[5] P.L. Hagelstein, Quantum composites: A review, and new results for models for Condensed Matter Nuclear Science, *J. Condensed Matter Nuclear Science* **20** (2016) 139–225.

[6] P.L. Hagelstein and I.U. Chaudhary. Phonon models for anomalies in condensed matter nuclear science, *Current Science* **108** (2015) 507.

[7] P.L. Hagelstein, Current status of the theory and modeling effort based on fractionation, *J. Condensed Matter Nucl. Sci.* **19** (2016) 98–109.

[8] P.L. Hagelstein, Directional X-ray and gamma emission in experiments in condensed matter nuclear science, *Current Science* **108** (2015) 601.

[9] A.B. Karabut, Research into powerful solid X-ray laser (wave length is 0.8–1.2nm) with excitation of high current glow discharge ions, *Proc. 11th Int. Conf. on Emerging Nuclear Energy Systems*, 29 September–4 October 2002, Albuquerque, New Mexico, USA, pp. 374–381.

[10] A.B. Karabut, Experimental research into characteristics of X-ray emission from solid-state cathode medium of high-current glow discharge, *Proc. 10th Int. Conf. on Cold Fusion*, August 24–29, 2003, Cambridge, MA, USA.

[11] A.B. Karabut, Research into characteristics of X-ray emission laser beams from solid-state cathode medium of high current glow discharge, *Proc. 11th Int. Conf. on Cold Fusion*, 31 October–5 November, 2004, France, pp. 253–257.

[12] A.B. Karabut, Study of energetic and temporal characteristics of X-ray emission from solid state cathode medium of high current glow discharge, *Proc. 12th Int. Conf. on Cold Fusion*, December 2–7, 2006, Japan, pp. 344–350.

[13] A.B. Karabut, E.A. Karabut, Research into energy spectra of X-ray emission from solid cathode medium during the high current glow discharge operation and after the glow discharge current switch off, *Proc. 14th Int. Conf. on Cold Fusion*, August 10–15, 2008, USA.

[14] A.B. Karabut and E.A. Karabut, Study of deuterium loading into Pd cathode samples of glow discharge, *Proc. of 9th Int. Workshop on Anomalies in Hydrogen/Deuterium Gas Loaded Metals*, 6–11 September 2010, Siena, Italy.

[15] A.B. Karabut, E.A. Karabut and P.L. Hagelstein, Spectral and temporal characteristics of X-ray emission from metal electrodes in a high-current glow discharge, *J. Condensed Matter Nucl. Sci.* **6** (2012) 217.

[16] A.B. Karabut and E.A. Karabut, Research into excited 0.6–6.0 keV energy levels in the cathode solid medium of glow discharge by X-ray spectra emission, *J. Condensed Matter Nucl. Sci.* **8** (2012) 159.

[17] A.B. Karabut, Research into excited long lived 0.6–6.0 keV energy levels in the cathode solid medium of glow discharge by x-Ray spectra emission, *J. Materials Sci. Eng. B* **3** (2013) 298.

[18] A.A. Kornilova, V.I. Vysotskii, N.N. Sysoev, N.K. Litvin, V.I. Tomak and A.A. Barzov, Generation of intense X-rays during ejection of a fast water jet from a metal channel to atmosphere, *J. Surface Investigation: X-ray, Synchrotron and Neutron Techniques* **4** (2010) 1008–1017.

[19] A.A. Kornilova, V.I. Vysotskii, N.N. Sysoev, N.K. Litvin, V.I. Tomak and A.A. Barzov, Shock-cavitational mechanism of X-ray generation during fast water stream cavitation, *Moscow University Phys. Bulletin* **65** (2010) 46–50.

[20] V.I. Vysotskii, A.A. Kornilova and A. O. Vasilenko, Observation and investigation of X-ray and thermal effects at cavitation, *Current Science* **108** (2015) 114.

[21] V.I. Vysotskii, A.A. Kornilova, A. O. Vasilenko and V.I. Tomak, Detection and investigation of undamped temperature waves excited under water jet cavitation, *J. Surface Investigation. X-ray, Synchrotron and Neutron Techniques* **8** (2014) 1186–1192.

[22] V.I. Vysotskii, A.A. Kornilova, A. O. Vasilenko, T. B. Krit and M. V. Vysotskyy, The prediction, observation and study of long-distant undamped thermal waves generated in pulse radiative processes, *Nucl. Instr. Meth. Phys. Res. Section B: Beam Interactions with Materials and Atoms* (2017).

[23] P.L. Hagelstein and I.U. Chaudhary, Coupling between the center of mass and relative degrees of freedom in a relativistic quantum composite and applications, *J. Condensed Matter Nucl. Sci.* **24** (2017) 117–122.

[24] F. Cardone, R. Mignani, M. Monti, A. Petrucci and V. Sala, Piezonuclear neutrons from iron, *Modern Phys. Lett. A* **27** (2012) 1250102.

[25] F. Cardone and S. Duro, Anisotropy angle of the DST-emissions, *Modern Phys. Lett. B* **28** (2014) 1450156.

[26] G. Albertini, V. Calbucci and F. Cardone, Statistics of piezonuclear emissions: early results, *Modern Phys. Lett. B* **28** (2014) 1450036.

[27] F. Cardone, G. Cherubini, M. Lammardo, R. Mignani, A. Petrucci, A. Rosada, V. Sala and E. Santoro, Violation of local Lorentz invariance for deformed space–time neutron emission, *Eur. Phys. J. Plus* **130** (2015) 55–65.

[28] F. Cardone and A. Rosada, Energy spectra and fluence of the neutrons produced in deformed space–time conditions, *Modern Phys. Lett. B* **30** (2016) 1650346.

[29] F. Cardone, A. Manuello, R. Mignani, A. Petrucci, E. Santoro, M. Sepielli and A. Carpinteri, Ultrasonic piezonuclear reactions in steel and sintered ferrite bars, *J. Adv. Phys.* **5** (2016) 69–75.

[30] G. Albertini, V. Calbucci, F. Cardone, G. Fattorini, R. Mignani, A. Petrucci, F. Ridolfi and A. Rotili, Evidence of alpha emission from compressed steel bars, *Int. J. Modern Phys. B* **27** (2013) 1350124.

[31] F. Cardone, V. Calbucci and G. Albertini, Possible evidence of piezonuclear alpha emission, *J. Advanced Phys.* **2** (2013) 20–24.

[32] F. Cardone, V. Calbucci and G. Albertini, Deformed space–time of the piezonuclear emissions, *Modern Phys. Lett. B* **28** (2014) 1450012.

[33] F. Cardone, A. Petrucci and A. Rosada, Isotopical changes induced by ultrasounds in iron, *Int. J. Modern Phys. B* **28** (2014) 1450107.

[34] G. Albertini, F. Cardone, M. Lammardo, A. Petrucci, F. Ridolfi, A. Rosada, V. Sala and E. Santoro, Atomic and isotopic changes induced by ultrasounds in iron, *J. Radioanal. Nucl. Chem.* **304** (2015) 955–963.

[35] F. Cardone, M. Lammardo, A. Petrucci, A. Rosada and E. Santoro, Isotopical changes in piezonuclear iron, *J. Adv. Phys.* **5** (2016) 90–96.

[36] G. Albertini, V. Calbucci, F. Cardone and A. Petrucci, Piezonuclear reactions and DST-reactions, *Materials and Processes*

for Energy: Communicating Current Research and Technological Developments, A. Mendez-Vilas (Ed.), 2013, pp. 769–780.

[37] G. Albertini, L. Kostro and F. Cardone, Deformed Space–Time Reactions, *Unified Field Mechanics: Natural Science Beyond the Veil of Spacetime-Proc. IX Symposium Honoring Noted French Mathematical Physicist Jean-Pierre Vigier* R.L. Amoroso et al. (Eds.), World Scientific, NJ, USA, 2016, pp. 157–163.

[38] F.L. Tanzella, P.L. Hagelstein, J. Bao and M.C.H. McKubre, Progress report on an experiment to clarify collimated X-ray emission in Karabutï£¡s experiment, *X-Ray Lasers 2014*, Springer, Berlin, 2016, pp. 115–120.

[39] F.L. Tanzella, J. Bao, M.C.H. McKubre and P.L. Hagelstein, Seeking X-rays and charge emission from a copper foil driven at MHz frequencies, *J. Condensed Matter Nucl. Sci.* **19** (2016) 110–118.

[40] F. Metzler, P.L. Hagelstein and S. Lu, Developing phononï£¡nuclear coupling experiments with vibrating plates and radiation detectors, *J. Condensed Matter Nucl. Sci.* **24** (2017) 98–113.

[41] D.E. Alburger and M.A. Grace, The Disintegration of Cobalt 57, *Proc. Phy. Soc. Section A* **67** (1954) 280–283.

[42] B. Crasemann and D.L. Manley, Radioactivity of Co^{57}, *Phy. Rev.* **98** (1955) 66–68.

[43] J.M. Cork, M.K. Brice and L.C. Schmid, Energies of the radiations from Co^{57} and Co^{58}, *Phy. Rev.* **99** (1955) 703–705.

[44] A.T.G. Ferguson, M.A. Grace and J.O. Newton, The decay of the 136 keV level in Fe^{57}, *Nucl. Phys.* **17** (1960) 9–15.

[45] V.P. Chechev and N.K. Kuzmenko, CEA Table de radiounucléides ^{57}Co, Laboratoire National Henri Becquerel LNE-LNHB/CEA Report (2014).

[46] O.C. Kistner and A.W. Sunyar, Excited states of ^{57}Fe populated in ^{57}Co decay, *Phy. Rev.* **139** (1965) B 295–B 299.

[47] G.D. Sprouse and S.S. Hanna, Gamma ray transitions in ^{57}Fe, *Nucl. Phys.* **74** (1965) 177–183.

[48] S.B. Garfinkel and J.M.R. Hutchinson, The standardization of cobalt-57, *Int. J. Appl. Radiation and Isotopes* **17** (1966) 587–593.

[49] M.E.C. Troughton, The absolute standardization of cobalt-57, *Int. J. Appl. Radiation and Isotopes* **17** (1966) 145–150.

[50] W. Rubinson and K.P. Gopinathan, Conversion coefficients of the Fe^{57} 14.4-keV transition, the K-capture fraction in Co^{57} e^- capture and the K-fluorescence yield of Fe, *Phy. Rev.* **170** (1968) 969.

[51] A.V. Simakin and G.A. Shafeev, Initiation of Nucl. reactions under laser irradiation of Au nanoparticles in the aqueous solution of uranium salt, *Appl. Phys. A* **101** (2010) 199–203.

[52] A.V. Simakin and G.A. Shafeev, Effect of laser irradiation of nanoparticles in aqueous uranium salt solutions on nuclide activity, *Quantum Electron.* **41** (2011) 614.

[53] A.V. Simakin and G.A. Shafeev, Accelerated alpha-decay of uranium isotopes induced by exposure of aqueous solution of uranium salt with gold nanoparticles to laser radiation, *Phys. Wave Phenomena* **21** (2013) 31–37.

[54] E.V. Barmina, I.A. Sukhov, N.M. Lepekhin, Yu S. Priseko, V.G. Filippov, A.V. Simakin and G.A. Shafeev, Application of copper vapour lasers for controlling activity of uranium isotopes, *Quantum Electron.* **43** (2013) 591–596.

[55] E.V. Barmina, A.V. Simakin and G.A. Shafeev, Laser-induced caesium-137 decay, *Quantum Electron.* **44** (2014) 791–792.

[56] S.N. Andreev, The nonlinear quenching of the radioactivity of cesium-137, *All-Russian Scientific Forum of Young Scientists "Science of the future – the young science"*, Kazan, Sept. 20–23, 2016.

[57] A. Carpinteri, F. Cardone and G. Lacidogna, PiezoNucl. neutrons from brittle fracture: early results of mechanical compression tests, *Strain* **45** (2009) 332–339.

[58] A. Carpinteri, F. Cardone and G. Lacidogna, Energy emissions from failure phenomena: mechanical, electromagnetic, nuclear, *Experimental Mechanics* **50** (2010) 1235–1243.

[59] A. Carpinteri, G. Lacidogna, A. Manuello and Oscar Borla, PiezoNucl. fission reactions from earthquakes and brittle rocks failure: evidence of neutron emission and non-radioactive product elements, *Experimental Mechanics* **53** (2013) 345–365.

[60] P.L. Hagelstein, Probabilistic models for beam, spot and line emission for collimated X-ray emission in the Karabut experiment, *J. Condensed Matter Nucl. Sci.* **22** (2017) 53–73.

[61] P.L. Hagelstein and I.U. Chaudhary, Energy exchange in the lossy spin–boson model, *J. Condensed Matter Nucl. Sci.* **5** (2011) 52.

[62] P.L. Hagelstein and I.U. Chaudhary, Second-order formulation and scaling in the lossy spin–boson model, *J. Condensed Matter Nucl. Sci.* **5** (2011) 87.

[63] P.L. Hagelstein and I.U. Chaudhary, Local approximation for the lossy spinï£¡-boson model, *J. Condensed Matter Nucl. Sci.* **5** (2011) 102.

[64] P.L. Hagelstein and I.U. Chaudhary, Coherent energy exchange in the strong coupling limit of the lossy spin–boson model,

J. Condensed Matter Nucl. Sci. **5** (2011) 116.

[65] V.J. Minkiewicz, G. Shirane and R. Nathans, Phonon dispersion relation for iron, *Phy. Rev.* **162** (1967) 528.

[66] H.Y. Erbil, Evaporation of pure liquid sessile and spherical suspended drops: A review, *Adv. Colloid and Interface Sci.* **170** (2012) 67–86.

[67] R.D. Deegan, O. Bakajin, T.F. Dupont, G. Huber, S.R. Nagel and T.A. Witten, Contact line deposits in an evaporating drop, *Phys. Rev. E* **62** (2000) 756–765.

[68] N. Shahidzadeh, M.F.L. Schut, J. Desarnaud, M. Prat and D. Bonn, Salt stains from evaporating droplets, *Scientific Reports* **5** (2015) 10335.

[69] V.E. Nakoryakov, S.Ya. Misyura and S.L. Elistratov, Non-isothermal desorption of droplets of complex composition, *Thermal Sci.* **16** (2012) 997–1004.

[70] D. Pacella, A. Romano, S.H. Lee, F. Causa, L. Gabellieri and W. Choe, Self-consistent calibration of detectors and sources for hard and soft X-ray diagnostics, *Modern Instrumentation* **3** (2014) 13–23.

[71] R.L. Roderick and R. Truell, The measurement of ultrasonic attenuation in solids by the pulse technique and some results in steel, *J. Appl. Phys.* **23** (1952) 267–279.

[72] K. Kamigaki, Ultrasonic attenuation in steel and cast iron, *Science reports of the Research Institutes, Tohoku University. Ser. A, Phys. , Chemistry and Metallurgy* **9** (1957) 48–77.

[73] J.-D. Aussel and J.-P. Monchalin, Measurement of ultrasound attenuation by laser ultrasonics, *J. Appl. Phys.* **65** (1989) 2918–2922.

[74] R.M. Goldhoff, Uniaxial creep-rupture behavior of low-alloy steel under variable loading conditions, *Trans. AMSE, J. Basic Eng.* **87** (1965) 374–378.

[75] L.J. Cuddy, Internal stresses and structures developed during creep, *Metallurgical and Materials Trans. B* **1** (1970) 395–401.

[76] E. Krempl, An experimental study of room-temperature rate-sensitivity, creep and relaxation of AISI type 304 stainless steel, *J. Mechanics Phys. Solids* **27** (1979) 363–375.

[77] L.A. Deibler, Room temperature creep in metals and alloys, *Sandia National Lab Report* No. SAND2014-17935 (2014).

[78] P. Gressel, Untersuchungen ï£¡ber das Zeitstandbiegeverhalten von Holzwerkstoffen in Abhï£¡ngigkeit von Klima und Belastung, it Eur. J. Wood and Wood Products **30** (1972) 347–355.

[79] S.J. Smulski, Creep functions for wood composite materials, *Wood and Fiber Sci.* **21** (1989) 45.

[80] D.E. Lyon and A.P. Schniewind, Prediction of creep in plywood Part I. Prediction models for creep in plywood, *Wood Fiber Sci.* **10** (2007) 28–38.

[81] M. Peach and J.S. Koehler, The forces exerted on dislocations and the stress fields produced by them, *Phy. Rev.* **80** (1950) 436.

[82] D. Caillard, Kinetics of dislocations in pure Fe. Part I. In situ straining experiments at room temperature, *Acta Materialia* **58** (2010) 3493–3503.

[83] A.P.L. Turner and T. Vreeland, The effect of stress and temperature on the velocity of dislocations in pure iron monocrystals, *Acta metallurgica* **18** (1970) 1225–1235.

[84] M.S. Duesbery, The influence of core structure on dislocation mobility, *Phil. Magazine* **19** (1969) 501–526.

[85] F. Louchet, L.P. Kubin and D. Vesely, In situ deformation of bcc crystals at low temperatures in a high-voltage electron microscope dislocation mechanisms and strain-rate equation, *Phil. Magazine A* **39** (1979) 433–454.

[86] E. Orowan, Problems of plastic gliding, *Proc. Phy. Soc.* **52** (1940) 8.

[87] A.S. Krausz, The activation volume associated with the plastic deformation of ice, *Appl. Sci. Res.* **26** (1972) 86–92.

[88] E. Nadgornyi, Dislocation dynamics and mechanical properties of crystals, *Progr. Materials Sci.* **31** (1988) 1–530.

[89] T.Y. Gorazdovskii, Hard radiation from solids failing in shear, *JETP Lett.* **5** (1967) 64–67.

[90] D. Roylance, Engineering viscoelasticity, Course notes, Dept. of Materials Science and Engineering, Massachusetts Institute of Technology, 200, pp. 11–37.

[91] F. Mainardi and G. Spada, Creep, relaxation and viscosity properties for basic fractional models in rheology, *Eur. Phy. J. – Special Topics* **193** (2011) 133–160.

[92] J. Marian and A. Caro, Moving dislocations in disordered alloys: Connecting continuum and discrete models with atomistic simulations, *Phy. Rev. B* **74** (2006) 024113. See Fig. 12.

[93] J. Lothe, Theory of dislocation motion in pure slip, *J. Appl. Phys.* **33** (1962) 2116–2125.

[94] J.D. Eshelby, The interaction of kinks and elastic waves, *Proc. Roy. Soc. (London). Series A, Mathematical and Physical Sciences* **A266** (1962) 222–246.

[95] A. Hikata, R.A. Johnson and C. Elbaum. Interaction of dislocations with electrons and with phonons, *Phy. Rev. B* **2** (1970) 4856–4863.

Phonon-mediated Nuclear Excitation Transfer

Peter L. Hagelstein*

Massachusetts Institute of Technology, Cambridge, MA, USA

Abstract

Excitation transfer has long been of interest in biophysics, where electronic excitation is transferred from one location to another mediated by photon exchange. We are interested in the transfer of nuclear excitation mediated by phonon exchange, which according to our theoretical approach lies at the foundation of many anomalies in Condensed Matter Nuclear Science. The transfer of excitation from one site to another involves coupling to off-resonant intermediate states with either no excitation or double excitation; as such it is a quantum mechanical effect with no classical counterpart. The indirect coupling interaction can be determined from second-order perturbation theory for an electric dipole (E1) interaction, and the resulting interaction is weak due to destructive interference. We present results for resonant phonon-mediated excitation transfer based on the relativistic phonon-nuclear boost interaction identified recently. The analysis is extended to the more complicated case of magnetic dipole (M1) interactions, where fourth-order perturbation theory is needed for the interaction. We find severe destructive interference effects very much weaken the indirect interaction in both cases. Some improvement is possible due to loss; however, the improvement seems insufficient to account for the effects seen in excitation transfer experiments in our lab. To address this issue, we propose here that shifts in the off-resonant basis state energies could lead to much larger indirect interactions. The evaluation of shifts in the basis state energies is a major project, which requires the specification of the nucleon-nucleon interaction off of resonance, and the evaluation of off-resonant binding energies; these are projects to be addressed in the future. The transverse Breit interaction is given off of resonance. The resulting indirect interaction for excitation transfer is consistent with a delocalized transfer effect, and also with cooperative (Dicke) enhancements; we expect shifts in the basis state energies to lead to new models for up-conversion and down-conversion as well. Possible connections between the model and recent experimental results from excitation transfer experiments involving a ^{57}Co source on steel are discussed. We also consider incoherent excitation transfer, where the large excitation associated with the D_2/^{4}He transition is transferred to highly excited unstable states in the nuclei of the host lattice. While the mechanism was proposed many years ago to account for low-level emission of energetic alphas, there has subsequently been no clarification of mechanism associated with these experiments, which provides motivation for us to consider the possibility of confirming or rejecting the mechanism through a systematic study where the ejected particle energy is determined as a function of the nuclear mass of host lattice nuclei. The argument is extended to excitation transfer from the HD/^{3}He transition, where few MeV alpha emission may be a candidate explanation for the observations of Storms and Scanlan, and where proton emission from ^{6}Li may be a candidate explanation for the 0.79 MeV proton signal reported by Lipinski and Lipinski.

---

*Corresponding author. E-mail: plh@mit.edu.

1. Introduction

Motivation for an interest in the problem stems from the search for an explanation for the mechanism involved in excess heat production in the Fleischmann–Pons experiment [1,2]. Since the energy produced does not come out as energetic nuclear radiation, there must be other channels involved, and from early on we have focused on the possible coupling of the nuclear energy directly into vibrations. For this to work there are a host of issues to face, including the specification of an appropriate phonon-nuclear interaction, the identification of a down-conversion mechanism through which the large nuclear quanta can be converted to the low-energy vibrational quanta, and eventually some experimental verification that the models correspond to reality [3]. Relatively recently we have identified a (some-what obscure) relativistic interaction (the boost correction to the nuclear potential) as a candidate to provide for an appropriate phonon-nuclear interaction [4]. This mechanism allows for the exchange of vibrational quanta from the "macroscopic" lattice with nucleons of the "microscopic" internal nuclear system.

Up-conversion and down-conversion can be analyzed in simple models in which two-level systems are coupled to a common oscillator. Unfortunately, destructive interference hinders the rate at which down-conversion occurs in these models, so in order to achieve a fast down-conversion rate one needs to find a way to reduce the destructive interference. We noticed that loss processes which are antisymmetric off of resonance (different for off-resonant basis states with higher energy than for off-resonant bases states with lower energy) can remove the destructive interference, and models for up-conversion and down-conversion were quantified under conditions where the destructive interference is completely eliminated [5–9].

In these models the large energy quantum is down-converted through the sequential emission of phonons, one phonon at a time, in a great many phonon exchange processes (where each one individually involves the raising or lowering of the nuclear state) that need to be completed before coherence is lost. According to the models there are cooperative effects (Dicke enhancement) which can help if the coupling between the nuclei and a highly excited phonon mode is the same for each nucleus. Looked at two interactions at a time, this phonon exchange and nuclear raising and lowering together make up an excitation transfer step.

In recent years we have worked toward the development of new experiments that focus on providing tests of some of the theoretical statements and models in detail. Initially we worked with up-conversion experiments, but had little luck. Last year we moved to experiments focusing on excitation transfer, and observed anomalous effects [10], which have subsequently become the focus of our experimental studies. There has emerged over the last few years a new appreciation of the importance of the excitation transfer mechanism itself; as an important theoretical mechanism in its own right; as a mechanism amenable to experimental study; and with a real prospect of connecting experiment with theory. This year we have continued the experiments, but in addition have continued the theoretical studies hoping to construct models that we might compare in detail with current or with future experiments. This discussion then places excitation transfer studies into context, and provides the motivation for our focus on the problem.

In what follows our first task is to develop an introductory discussion to help bring readers from other areas up to speed with some of the basic issues associated with excitation transfer. Next we present the results of calculations of the indirect interaction associated with phonon-mediated nuclear excitation transfer first for the simplest case of electric dipole (E1) nuclear transitions, and then for the much more complicated case of magnetic dipole (M1) transitions. We have known for years that destructive interference results in a very weak indirect interaction in the E1 case, but it was not clear what the situation would be for M1 transitions. In contrast to our presentation at ICCF21, here we find that destructive interference severely impacts the indirect interaction for the M1 case as well. We have discussed many times the possibility that loss can reduce the destructive interference associated with up-conversion and down-conversion; here the approach is extended to nuclear excitation transfer, with the result that a modest improvement is obtained. This motivates us to seek other mechanisms which might reduce the destructive interference, and in this work we discuss a new mechanism that involves off-resonant shifts in the basis state energies.

Following these discussions, we turn to possible interpretations of effects seen in our excitation transfer experiments in terms of the excitation transfer models.

In the latter part of the paper we consider incoherent excitation transfer mechanisms associated with the transfer of large excitation from the $D_2/^4He$ transition and $HD/^3He$ transition to highly-excited unstable states which decay through disintegration.

Appendix A provides an enumeration of lengthy terms for one of the M1 indirect interactions. In Appendix B we provide details associated with a dynamical model for two driven nuclei in proximity coupled through resonant excitation transfer. And in Appendix C a brief discussion of internal conversion in connection with excitation transfer is given in response to a reviewer's comments.

2. Excitation Transfer

Excitation transfer of electronic excitation as a physical process was considered in the 1930s in connection with photosynthesis. A theory for photon-mediated resonant excitation transfer was given by Förster in 1948 [11], focusing on the lowest-order Coulomb dipole–dipole interaction [12]. In an idealized excitation transfer event, excitation at one site is transferred to another site. In the initial state the excitation can be thought of as being at site 1 with no excitation at site 2; and in the final state the excitation is at site 2 with no excitation remaining at site 1. We might write for an incoherent resonant excitation transfer event

$$A_1^* A_2 \; \rightarrow \; A_1 A_2^*, \tag{1}$$

where A is an excited atom or molecule. A non-resonant excitation transfer event is also possible, in which the excitation in the initial state is at a higher energy than the excitation in the final state, with the energy difference transferred to some other degree of freedom. Non-resonant excitation transfer involving phonon emission could be written as

$$A_1^* B_2 \; \rightarrow \; A_1 B_2^* + \hbar\omega_p \tag{2}$$

in which the atoms or molecules at the different sites are A and B, and where the phonon energy is $\hbar\omega_p$.

2.1. Intermediate states

In the brief discussion above we have taken advantage of a feature of the formalism specific to electromagnetism in the Coulomb gauge, where the Coulomb interaction is modeled as a simple potential, and there is no discussion of the emission or absorption of a virtual photon. However, were we to make use of a different gauge (specifically one in which the Coulomb potential is not used) then our discussion would be more complicated. In this more complicated version of the discussion, a photon would be emitted at one site coupled to a raising or lowering of the atomic or molecular state, and that same photon would be absorbed at the other site coupled to the raising or lowering of the molecular state. In this case Eq. (1) would be replaced by

$$A_1^* A_2 \quad \begin{array}{c} \nearrow \quad A_1^* A_2^* + h\nu \quad \searrow \\[6pt] \searrow \quad A_1 A_2 + h\nu \quad \nearrow \end{array} \quad A_1 A_2^*, \tag{3}$$

where we have used $h\nu$ for the exchanged photon. In this version of the excitation transfer process it becomes clear that the exchange is mediated by photons, and that off-resonant intermediate states are present in which both atoms or molecules are either excited or unexcited at the same time. In this resonant excitation transfer process, the system has sufficient energy to allow one atom/molecule to be excited and one unexcited (the initial and final states work this way, and they would be considered to be on resonance). One of the intermediate states has both atoms/molecules excited, and also has a photon present. The system in this case does not have sufficient energy to be in this state, so we consider it to be off-resonance. It is a virtual state. The system couples to it from both the initial state and final state, so in an excitation transfer it will have finite occupation; but its oscillatory time dependence will be that of the initial state (and/or final state) and not the time dependence it might have if the system had sufficient energy for both to be excited. We emphasize that energy is conserved from the initial state transitioning to the final state in this resonant interaction; however, energy is not conserved for the intermediate states – instead they are just off of resonance. The photon does not take up the mismatch in excitation energy.

2.2. Excitation transfer mediated by phonon exchange

It is possible for atoms and molecules in condensed matter to undergo a change of state in connection with phonon emission or absorption. In this case excitation transfer can be mediated by phonon exchange instead of photon exchange. For phonon-mediated resonant excitation transfer we might write

$$
\mathrm{A}_1^*\mathrm{A}_2 + n\hbar\omega_\mathrm{p}
\begin{array}{c}
\nearrow \; \mathrm{A}_1^*\mathrm{A}_2^* + (n+1)\hbar\omega_\mathrm{p} \\
\nearrow \; \mathrm{A}_1^*\mathrm{A}_2^* + (n-1)\hbar\omega_\mathrm{p} \searrow \\
\\
\searrow \; \mathrm{A}_1\mathrm{A}_2 + (n+1)\hbar\omega_\mathrm{p} \nearrow \\
\searrow \; \mathrm{A}_1\mathrm{A}_2 + (n-1)\hbar\omega_\mathrm{p} \nearrow
\end{array}
\; \mathrm{A}_1\mathrm{A}_2^* + n\hbar\omega_\mathrm{p}.
\tag{4}
$$

Things are a little different in this case since there is the possibility that we have phonons already present in the phonon mode involved in the exchange. A phonon can be created or destroyed in connection with a raising or lowering, so now there are four intermediate states involved (at lowest order).

2.3. Toy model for phonon-mediated excitation transfer

It is possible to develop a toy model for phonon-mediated excitation transfer based on the spin–boson model for which the Hamiltonian is

$$
\hat{H} = \Delta E \frac{\hat{s}_z}{\hbar} + \hbar\omega_0 \hat{a}^\dagger \hat{a} + V(\hat{a} + \hat{a}^\dagger)\frac{2\hat{s}_x}{\hbar},
\tag{5}
$$

where the first term on the right-hand side accounts for the energy of the two-level system with transition energy ΔE, where the second term accounts for the simple harmonic oscillator energy, and where the third term describes a linear coupling between the two systems. In this model a phonon exchange (which can be a creation or annihilation) occurs along with a raising or lowering of the two-level system.

We are interested in a solution of the time-independent Schrödinger equation

$$
E\Psi = \hat{H}\Psi
\tag{6}
$$

that is relevant to excitation transfer. For this we make use of a finite basis approximation in which we take a solution of the form

$$\Psi = c_1 \Phi_1 + \cdot + c_6 \Phi_6, \tag{7}$$

where the individual basis states are taken to be

$$\Phi_1 = |\uparrow, \downarrow, n\rangle, \quad \Phi_2 = |\downarrow, \downarrow, n-1\rangle, \quad \Phi_3 = |\downarrow, \downarrow, n+1\rangle,$$

$$\Phi_4 = |\uparrow, \uparrow, n-1\rangle, \quad \Phi_5 = |\uparrow, \uparrow, n+1\rangle, \quad \Phi_6 = |\downarrow, \uparrow, n\rangle. \tag{8}$$

The notation here works as follows: the first two-level system can be in the ground state ($\downarrow$) or in the excited state ($\uparrow$) as determined by the first entry in the ket; the second two-level system can similarly be in the ground or excited state as determined by the second entry in the ket; the third entry in the ket is the number of phonons in the oscillator.

The eigenvalue equation associated with the finite basis approximation can be written as

$$Ec_1 = n\hbar\omega_0 c_1 + V\sqrt{n}c_2 + V\sqrt{n+1}c_3 + V\sqrt{n}c_4 + V\sqrt{n+1}c_5,$$

$$Ec_2 = \left[-\Delta E + (n-1)\hbar\omega_0 \right] c_2 + V\sqrt{n}c_1 + V\sqrt{n}c_6,$$

$$Ec_3 = \left[-\Delta E + (n+1)\hbar\omega_0 \right] c_3 + V\sqrt{n+1}c_1 + V\sqrt{n+1}c_6,$$

$$Ec_4 = \left[\Delta E + (n-1)\hbar\omega_0 \right] c_4 + V\sqrt{n}c_1 + V\sqrt{n}c_6,$$

$$Ec_5 = \left[\Delta E + (n+1)\hbar\omega_0 \right] c_5 + V\sqrt{n+1}c_1 + V\sqrt{n+1}c_6,$$

$$Ec_6 = n\hbar\omega_0 c_6 + V\sqrt{n}c_2 + V\sqrt{n+1}c_3 + V\sqrt{n}c_4 + V\sqrt{n+1}c_5. \tag{9}$$

It is possible to eliminate the expansion coefficients associated with the off-resonant basis states ($c_2, \ldots, c_5$) algebraically resulting in

$$Ec_1 = n\hbar\omega_0 c_1 + \left(\frac{V^2 n}{E + \Delta E + \hbar\omega_0} + \frac{V^2(n+1)}{E + \Delta E - \hbar\omega_0} + \frac{V^2 n}{E - \Delta E + \hbar\omega_0} + \frac{V^2(n+1)}{E - \Delta E - \hbar\omega_0} \right)(c_1 + c_6),$$

$$Ec_6 = n\hbar\omega_0 c_6 + \left(\frac{V^2 n}{E + \Delta E + \hbar\omega_0} + \frac{V^2(n+1)}{E + \Delta E - \hbar\omega_0} + \frac{V^2 n}{E - \Delta E + \hbar\omega_0} + \frac{V^2(n+1)}{E - \Delta E - \hbar\omega_0} \right)(c_1 + c_6). \tag{10}$$

This can be recast in the form of an equivalent two-level system according to

$$Ec_1 = \left[n\hbar\omega_0 + \Sigma_{11}(E) \right] c_1 + V_{16}(E)c_6,$$

$$Ec_6 = \left[n\hbar\omega_0 + \Sigma_{66}(E) \right] c_6 + V_{61}(E)c_1, \tag{11}$$

where the self-energies are

$$\Sigma_{11}(E) = \Sigma_{66}(E) = \frac{V^2 n}{E + \Delta E - (n-1)\hbar\omega_0} + \frac{V^2(n+1)}{E + \Delta E - (n+1)\hbar\omega_0}$$
$$+ \frac{V^2 n}{E - \Delta E - (n-1)\hbar\omega_0} + \frac{V^2(n+1)}{E - \Delta E - (n+1)\hbar\omega_0} \tag{12}$$

and where the indirect coupling coefficients are

$$V_{16}(E) = V_{61}(E) = \frac{V^2 n}{E + \Delta E - (n-1)\hbar\omega_0} + \frac{V^2(n+1)}{E + \Delta E - (n+1)\hbar\omega_0}$$
$$+ \frac{V^2 n}{E - \Delta E - (n-1)\hbar\omega_0} + \frac{V^2(n+1)}{E - \Delta E - (n+1)\hbar\omega_0}. \tag{13}$$

We see that in this equivalent two-level system model the basis state energies depend on the eigenvalue E, as do the indirect coupling terms. If we assume that the coupling is weak, then the eigenvalue E would be close to the basis state energy of Φ_1 and Φ_6 so that

$$E \rightarrow n\hbar\omega_0. \tag{14}$$

In this case the indirect coupling matrix elements are

$$V_{16} = V_{61} \rightarrow \frac{2V^2\hbar\omega_0}{(\Delta E)^2 - (\hbar\omega_0)^2} \rightarrow \frac{2V^2\hbar\omega_0}{(\Delta E)^2}. \tag{15}$$

We see that destructive interference has led to cancellation effects so that the indirect coupling matrix element is much smaller than the individual terms contributing to it (assuming that the oscillator energy $\hbar\omega_0$ is much smaller than the transition energy ΔE), and that there is no longer any dependence on the degree of excitation of the oscillator. A version of this model is discussed briefly in Lu's thesis [13].

3. Phonon-mediated Nuclear Excitation Transfer

It was recognized that phonon-nuclear interactions can be based on a (known) boost correction for the strong force inside of a moving (and accelerating or oscillating) nucleus [4]. We are motivated in this section to exercise this theory by applying it to excitation transfer. For simplicity in this section we focus on nuclear E1 transitions for which only a single phonon exchange is coupled to a nuclear transition. Some discussion of this problem was given previously in Ref. [14].

3.1. Nuclear and phonon Hamiltonian

To describe the internal nuclear states, the phonon modes, and the phonon-nuclear coupling in general we can make use of the Hamiltonian [15,16]

$$\hat{H} = \sum_j \mathbf{M}_j c^2 + \sum_j \mathbf{a}_j \cdot c\hat{\mathbf{P}}_j + \sum_{\mathbf{k},\sigma} \hbar\omega_{\mathbf{k},\sigma} \hat{a}_{\mathbf{k},\sigma}^\dagger \hat{a}_{\mathbf{k},\sigma}. \tag{16}$$

The first term on the RHS describes the internal nuclear energy in a finite basis approximation, where the mass matrix $\mathbf{M}_j$ for the nucleus at lattice site j is a diagonal matrix with the individual nuclear state masses as entries. The mass energy of a particular nuclear state $|J, m\rangle$ is

$$(E_{Jm})_j = (M_{Jm,Jm} c^2)_j. \tag{17}$$

The last term on the right-hand side describes the vibrational energy in a mode expansion, where $\hbar\omega_{\mathbf{k},\sigma}$ is the energy of a phonon with momentum $\hbar\mathbf{k}$ with polarization denoted by σ. The middle term on the right-hand side accounts for the relativistic phonon-nuclear interaction, where the $\mathbf{a}$ matrix contains off-diagonal entries given by [4]

$$\left(\mathbf{a}_{Jm,J'm'} \cdot c\hat{\mathbf{P}} \right)_j$$
$$= \left\langle J, m \left| \frac{1}{M} \sum_k \beta_k \hat{\mathbf{P}}_j \cdot \hat{\boldsymbol{\pi}}_k + \frac{1}{2Mc} \sum_{k<l} \left[(\beta_k \boldsymbol{\alpha}_k + \beta_l \boldsymbol{\alpha}_l) \cdot \hat{\mathbf{P}}_j, \hat{V}_{kl} \right] \right| J', m' \right\rangle \tag{18}$$

for a two-particle nuclear potential model, following the derivation and notation of Ref. [4]. M in this formula is the nuclear mass, where the difference in mass between the two states is presumed small relative to the total mass. The momentum operator $\hat{\mathbf{P}}_j$ for a monatomic lattice is

$$\hat{\mathbf{P}}_j = \sum_{\mathbf{k},\sigma} \mathbf{u}_{\mathbf{k},\sigma} \sqrt{\frac{M\hbar\omega_{\mathbf{k},\sigma}}{2N}} \left(\frac{\hat{a}_{\mathbf{k},\sigma} e^{i\mathbf{k}\cdot\mathbf{R}_j^{(0)}} - \hat{a}_{\mathbf{k},\sigma}^\dagger e^{-i\mathbf{k}\cdot\mathbf{R}_j^{(0)}}}{i} \right). \tag{19}$$

The equilibrium position of the center of mass for a nucleus at site j is $\mathbf{R}_j^{(0)}$.

3.2. Reduced Hamiltonian

Since the phonon-nuclear interaction has E1 symmetry for the nuclear transition, only a single nuclear transition is needed at each of the two sites in order to complete an excitation transfer. Consequently we only need to keep track of these two nuclear states, which allows for a significant reduction of the Hamiltonian. Unfortunately we cannot make use of the standard two-level system machinery, since each of the nuclear states will have a number of degenerate levels which need to be accounted for. The resulting reduced Hamiltonian can be written as

$$\hat{H} = \sum_k \hbar\omega_k \hat{a}_k^\dagger \hat{a}_k + \sum_j \sum_{m_0} (|J_0 m_0\rangle M_0 c^2 \langle J_0 m_0|)_j + \sum_j \sum_{m_1} (|J_1 m_1\rangle M_1 c^2 \langle J_1 m_1|)_j$$
$$+ \sum_j \sum_{m_0} \sum_{m_1} \left(|J_0 m_0\rangle\langle J_0 m_0|\mathbf{a}_j|J_1 m_1\rangle\langle J_1 m_1| + |J_1 m_1\rangle\langle J_1 m_1|\mathbf{a}_j|J_0 m_0\rangle\langle J_0 m_0| \right)$$
$$\cdot c \sum_{\mathbf{k},\sigma} \mathbf{u}_{\mathbf{k},\sigma} \sqrt{\frac{\hbar M\omega_{\mathbf{k},\sigma}}{2N}} \left(\frac{\hat{a}_{\mathbf{k},\sigma} e^{i\mathbf{k}\cdot\mathbf{R}_j^{(0)}} - \hat{a}_{\mathbf{k},\sigma}^\dagger e^{-i\mathbf{k}\cdot\mathbf{R}_j^{(0)}}}{i} \right), \tag{20}$$

where we focus on the ground state $|J_0, m_0\rangle$ and an excited state $|J_1, m_1\rangle$.

3.3. Phonon-nuclear interaction as a perturbation

The reduced Hamiltonian in the previous section can be recast as

$$\hat{H} = \hat{H}_0 + \hat{V}, \tag{21}$$

where $\hat{H}_0$ describes the unperturbed system

$$\hat{H}_0 = \sum_k \hbar\omega_k \hat{a}_k^\dagger \hat{a}_k + \sum_j \sum_{m_0} (|J_0 m_0\rangle M_0 c^2 \langle J_0 m_0|)_j + \sum_j \sum_{m_1} (|J_1 m_1\rangle M_1 c^2 \langle J_1 m_1|)_j \tag{22}$$

and where $\hat{V}$ describes the perturbation

$$\hat{V} = \sum_j \sum_{m_0} \sum_{m_1} \left(|J_0 m_0\rangle\langle J_0 m_0|\mathbf{a}_j|J_1 m_1\rangle\langle J_1 m_1| + |J_1 m_1\rangle\langle J_1 m_1|\mathbf{a}_j|J_0 m_0\rangle\langle J_0 m_0| \right)$$

$$\cdot c \sum_{\mathbf{k},\sigma} \mathbf{u}_{\mathbf{k},\sigma} \sqrt{\frac{\hbar M \omega_{\mathbf{k},\sigma}}{2N}} \left(\frac{\hat{a}_{\mathbf{k},\sigma} e^{i\mathbf{k}\cdot\mathbf{R}_j^{(0)}} - \hat{a}_{\mathbf{k},\sigma}^\dagger e^{-i\mathbf{k}\cdot\mathbf{R}_j^{(0)}}}{i} \right). \tag{23}$$

3.4. Formal second-order interaction

A nice feature of this formalism is that we are able to develop operators that describe the second-order as well as higher-order interactions within the perturbation theory explicitly. At second-order we can write

$$\hat{V}_2 = \hat{V}(E - \hat{H}_0)^{-1}\hat{V}. \tag{24}$$

Excitation transfer at second-order is described by this operator (along with other effects). We can think of the $\hat{V}$ at the right of the right-hand side when it operates on an initial state as either raising or lower the nuclear state at a site while creating or destroying a phonon. The intermediate state that results is off of resonance, and the off-resonant denominator keeps track of how far and in which direction off of resonance intermediate states are. The $\hat{V}$ operator on the left of the right-hand side then raises or lowers the nuclear state at possibly a different site, also while creating or destroying a phonon.

3.5. Resonant second-order interaction

After a significant computation and taking into account that the Brillouin zone is symmetric it is possible to isolate the resonant part of the second-order interaction relevant to excitation transfer; we can write

$$\left(\hat{V}(E - \hat{H}_0)^{-1}\hat{V} \right)_{\text{resonant}} \rightarrow \frac{Mc^2}{(\Delta E)^2} \sum_{j<j'} \sum_{m_0} \sum_{m_1} \sum_{m_0'} \sum_{m_1'} \left(|J_0 m_0\rangle\langle J_1 m_1| \right)_j \left(|J_1 m_1'\rangle\langle J_0 m_0'| \right)_{j'}$$

$$\langle J_0 m_0 | \mathbf{a}_j | J_1 m_1 \rangle \cdot \left[\frac{1}{N} \sum_{\mathbf{k},\sigma} (\hbar \omega_{\mathbf{k},\sigma})^2 \mathbf{u}_{\mathbf{k},\sigma} \mathbf{u}_{\mathbf{k},\sigma} \cos \left(\mathbf{k} \cdot (\mathbf{R}_{j'}^{(0)} - \mathbf{R}_j^{(0)}) \right) \right] \cdot \langle J_1 m_1' | \mathbf{a}_{j'} | J_0 m_0' \rangle$$

$$+ \frac{Mc^2}{(\Delta E)^2} \sum_{j<j'} \sum_{m_0} \sum_{m_1} \sum_{m_0'} \sum_{m_1'} \left(|J_1 m_1\rangle \langle J_0 m_0| \right)_j \left(|J_0 m_0'\rangle \langle J_1 m_1'| \right)_{j'}$$

$$\langle J_1 m_1 | \mathbf{a}_j | J_0 m_0 \rangle \cdot \left[\frac{1}{N} \sum_{\mathbf{k},\sigma} (\hbar \omega_{\mathbf{k},\sigma})^2 \mathbf{u}_{\mathbf{k},\sigma} \mathbf{u}_{\mathbf{k},\sigma} \cos \left(\mathbf{k} \cdot (\mathbf{R}_{j'}^{(0)} - \mathbf{R}_j^{(0)}) \right) \right] \cdot \langle J_0 m_0' | \mathbf{a}_{j'} | J_1 m_1' \rangle \Bigg\}. \tag{25}$$

We see in this expression a similar degree of cancellation as we found in the toy model considered above. Destructive interference has led to the cancellation of all lowest-order terms, and there does not remain any dependence on the number of phonons in the different phonon modes. Contributions from high-frequency phonon modes dominates this interaction.

3.6. Discussion

There exist many stable isotopes with E1 transitions from the ground state, for which this kind of model might apply. A list of the low energy transitions is presented in Table 1. For both the toy model and for the resonant second-order interaction above one finds the transition energy in the denominator, which would suggest our focus should be on nuclei with the lowest energy transitions from the ground state. In this case the 6.237 keV transition in ^{181}Ta is favored.

We have evaluated the contribution to the $\hat{\mathbf{a}}$-matrix element for the 6.237 keV transition of ^{181}Ta from the boosted spin–orbit interaction, making use of a single proton model in a deformed potential model. The result we obtained that the magnitude is on the order of 10^{-6} – a result which indicates that this contribution is weak.

One approach to testing for this kind of excitation transfer effect might be to look for angular anisotropy in the gamma emission from excited state ^{181}Ta(6237 keV) in crystalline Ta. A computation of the summation over the different phonon modes indicates that we would expect a weak excitation transfer dominated by transfer to the nearest neighbors. Making use of the indirect coupling formula given above and our estimate for the indirect matrix element, we might expect it possible to see a deviation from the isotropic case on the order of 10^{-3}. Given the relative weakness of emission of the 6.237 keV gamma, such an experiment would be expected to be technically challenging.

Table 1. Low-energy electric dipole (E1) transitions from the ground state of stable nuclei, from the BNL Nudat2 database. The internal conversion coefficient is α.

Isotope	E(keV)	$T_{1/2}$	Multipolarity	α
Ta-181	6.237	6.05 μsec	E1	70.5
Dy-161	25.65135	29.1 ns	E1	2.29
Gd-157	63.929	0.46 μsec	E1	0.961
Dy-161	74.56668	3.14 ns	E1	0.672
Gd-155	86.5479	6.50 ns	E1	0.434
Eu-153	97.43100	0.198 ns	E1	0.307
Dy-161	103.062	0.60 ns	E1	0.285
Gd-155	105.3083	1.16 ns	E1	0.256
F-19	109.9	0.591 ns	E1	
Dy-161	131.8	0.145 ns	[E1]	0.1475
Eu-153	151.6245	0.36 ns	E1	0.092
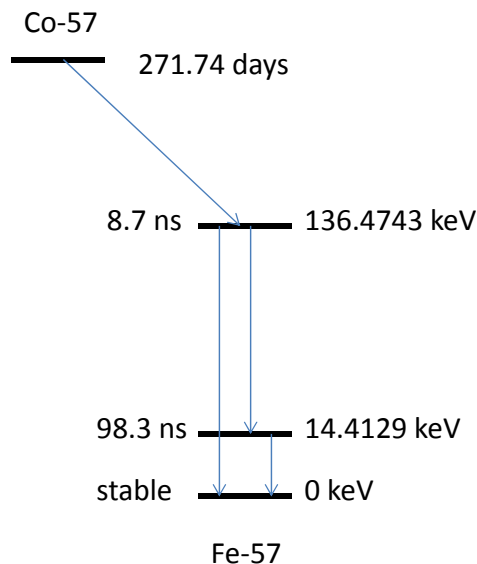
Figure 1. Simplified version of the nuclear decay scheme for Co-57; energy levels and half-life times are from the Nudat2 online data base of Brookhaven National Lab.

4. Excitation Transfer for M1 and E2 Transitions

The development of an excitation transfer experiment in ^{181}Ta based on the production of excited state nuclei from the decay of a radioactive source is problematic due to difficulties acquiring radioactive ^{181}W. Consequently in our lab we have focused on experiments involving excited states of ^{57}Fe that are populated from the decay of the more readily available radioactive ^{57}Co [10,13]. The primary decay path following electron capture associated with the beta decay of the ^{57}Co nucleus is shown in Fig. 1. Transitions from the ground state to the 14.4 keV state and 136.5 keV state are M1+E2, with the magnetic dipole (M1) contribution dominant, and the electric quadrupole (E2) contribution much weaker.

Since the phonon–nuclear interaction of the boost correction involves an E1 nuclear transition, in order to couple between the ground state and lowest excited states in ^{57}Fe we will need two phonon exchanges and intermediate states that couple through individual single phonon E1 transitions. A model for excitation transfer in this case will be more complicated since the lowest-order contribution will involve the exchange of four phonons.

This provides a new problem on which we might exercise the new phonon-nuclear theory. We are encouraged in that we appear to be seeing changes in X-ray and gamma emission consistent with the presence of excitation transfer in experiments. However, it is discouraging that the lowest-order interaction in the E1 version of the problem leads to such a weak indirect interaction.

At ICCF21 we described some preliminary results suggesting that destructive interference was not as bad in the M1 problem than in the E1 problem described in the previous section. The issue here is that since the models and calculations are new, with essentially no relevant previous work done on them, it is not obvious at the outset whether excitation in the M1 transition will be qualitatively different. A detailed and debugged version of the calculation is needed to provide clarification. Months after the conference a new set of calculations have been carried out, with the result that destructive interference indeed results in very weak indirect interactions. In this section we will provide a

brief review of the issues and associated calculations. The conclusion to be drawn is that the most straightforward and simplest application of the theory does not lead to predictions consistent with experiment. This will motivate us to consider modifications of the model in subsequent sections.

4.1. Simple classification of the interactions

Excitation transfer in the E1 case is particularly simple in that there is only a single transition and a single phonon mode involved for any specific contributing term at second order in perturbation theory. However, for the M1 and E2 cases, two different transitions are involved for each nucleus, and phonon exchange can occur with one phonon mode, two phonon modes, or three different phonon modes. We have carried out calculations systematically for all cases, and find that each case has its own technical issues and peculiarities in the computations, and leads to different expected behavior at the end. In what follows we summarize the essential results for the different cases.

4.2. Reduced version of the Hamiltonian

We make use of the same phonon–nuclear Hamiltonian as before in Equation (16), but this time we make use of an expanded subset given by

$$
\begin{aligned}
\hat{H} = {} & \sum_k \hbar\omega_k \hat{a}_k^\dagger \hat{a}_k + \sum_j \sum_{m_0} (|J_0 m_0\rangle M_0 c^2 \langle J_0 m_0|)_j \\
& + \sum_j \sum_{m_1} (|J_1 m_1\rangle M_1 c^2 \langle J_1 m_1|)_j + \sum_j \sum_{J_2} \sum_{m_2} (|J_2 m_2\rangle M_2 c^2 \langle J_2 m_2|)_j \\
& + \sum_j \sum_{m_0} \sum_{J_2} \sum_{m_2} \Big(|J_0 m_0\rangle \langle J_0 m_0|\mathbf{a}_j|J_2 m_2\rangle \langle J_2 m_2| + |J_2 m_2\rangle \langle J_2 m_2|\mathbf{a}_j|J_0 m_0\rangle \langle J_0 m_0| \Big) \\
& \quad \cdot c \sum_{\mathbf{k},\sigma} \mathbf{u}_{\mathbf{k},\sigma} \sqrt{\frac{\hbar M \omega_{\mathbf{k},\sigma}}{2N}} \left(\frac{\hat{a}_{\mathbf{k},\sigma} e^{i\mathbf{k}\cdot\mathbf{R}_j^{(0)}} - \hat{a}_{\mathbf{k},\sigma}^\dagger e^{-i\mathbf{k}\cdot\mathbf{R}_j^{(0)}}}{i} \right) \\
& + \sum_j \sum_{m_1} \sum_{J_2} \sum_{m_2} \Big(|J_1 m_1\rangle \langle J_1 m_1|\mathbf{a}_j|J_2 m_2\rangle \langle J_2 m_2| + |J_2 m_2\rangle \langle J_2 m_2|\mathbf{a}_j|J_1 m_1\rangle \langle J_1 m_1| \Big) \\
& \quad \cdot c \sum_{\mathbf{k},\sigma} \mathbf{u}_{\mathbf{k},\sigma} \sqrt{\frac{\hbar M \omega_{\mathbf{k},\sigma}}{2N}} \left(\frac{\hat{a}_{\mathbf{k},\sigma} e^{i\mathbf{k}\cdot\mathbf{R}_j^{(0)}} - \hat{a}_{\mathbf{k},\sigma}^\dagger e^{-i\mathbf{k}\cdot\mathbf{R}_j^{(0)}}}{i} \right).
\end{aligned}
\tag{26}
$$

The nuclear ground state is denoted by $|J_0, m_0\rangle$, the (relatively low-energy) nuclear excited state is denoted by $|J_1, m_1\rangle$, and (much higher energy) nuclear intermediate states are denoted by $|J_2, m_2\rangle$. Included in this restricted Hamiltonian are transitions between the ground state, and the low-energy excited state, to high-energy intermediate states; but no transitions directly between the ground state and low-energy excited state.

4.3. Interaction in the case of one phonon mode

In this case we make use of fourth-order perturbation theory and assume that the phonon energy is small compared to the nuclear transition energy. A great many terms are involved, and we made use of the symbolic algebra program

Mathematica for all of the algebra. We wrote a computer code that put together an input file for Mathematica which enumerated all states, couplings, and contributing pathways.

The resonant part of the fourth-order interaction involving a single phonon mode which has a non-trivial spatial dependence can be written as

$$\left(\hat{V}(E - \hat{H}_0)^{-1} \hat{V}(E - \hat{H}_0)^{-1} \hat{V}(E - \hat{H}_0)^{-1} \hat{V} \right)_{\text{resonant}} \rightarrow$$

$$\frac{(Mc^2)^2}{4N} \sum_{J_2} \sum_{J_2'} \frac{\left(\begin{array}{c} (E_1 - E_0)^2 - 3(E_1 - E_0)[(E_2 - E_0) + (E_2' - E_0)] \\ +2[(E_2 - E_0)^2 + (E_2 - E_0)(E_2' - E_0) + (E_2' - E_0)^2] \end{array} \right)}{(E_2 - E_0)(E_2' - E_0)(E_1 - E_2)(E_1 - E_2')(E_2 + E_2' - E_0 - E_1)}$$

$$\sum_j \sum_{j'} \sum_{m_0} \sum_{m_1} \sum_{m_2} \sum_{m_0'} \sum_{m_1'} \sum_{m_2'} \left(|J_0 m_0\rangle\langle J_1 m_1| \right)_j \left(|J_1 m_1'\rangle\langle J_0 m_0'| \right)_{j'}$$

$$\sum_\alpha \sum_\beta \sum_\gamma \sum_\delta (\langle J_0 m_0 | \mathbf{a}_j | J_2 m_2\rangle)_\alpha (\langle J_2 m_2 | \mathbf{a}_j | J_1 m_1\rangle)_\beta (\langle J_1 m_1' | \mathbf{a}_{j'} | J_2' m_2'\rangle)_\gamma (\langle J_2' m_2' | \mathbf{a}_{j'} | J_0 m_0'\rangle)_\delta$$

$$\left[\frac{1}{N} \sum_{\mathbf{k},\sigma} (\hbar\omega_{\mathbf{k},\sigma})^2 (\mathbf{u}_{\mathbf{k},\sigma})_\alpha (\mathbf{u}_{\mathbf{k},\sigma})_\beta (\mathbf{u}_{\mathbf{k},\sigma})_\gamma (\mathbf{u}_{\mathbf{k},\sigma})_\delta \cos\left(2\mathbf{k}(\mathbf{R}_{j'}^{(0)} - \mathbf{R}_j^{(0)}) \right) \right]$$

$$+ i \frac{(Mc^2)^2}{2N} \sum_{J_2} \sum_{J_2'} \frac{(2E_2 - E_0 - E_1)(2E_2' - E_0 - E_1)}{(E_1 - E_0)(E_2 - E_0)(E_2' - E_0)(E_2 - E_1)(E_2' - E_1)}$$

$$\sum_j \sum_{j'} \sum_{m_0} \sum_{m_1} \sum_{m_2} \sum_{m_0'} \sum_{m_1'} \sum_{m_2'} \left(|J_0 m_0\rangle\langle J_1 m_1| \right)_j \left(|J_1 m_1'\rangle\langle J_0 m_0'| \right)_{j'}$$

$$\sum_\alpha \sum_\beta \sum_\gamma \sum_\delta (\langle J_0 m_0 | \mathbf{a}_j | J_2 m_2\rangle)_\alpha (\langle J_2 m_2 | \mathbf{a}_j | J_1 m_1\rangle)_\beta (\langle J_1 m_1' | \mathbf{a}_{j'} | J_2' m_2'\rangle)_\gamma (\langle J_2' m_2' | \mathbf{a}_{j'} | J_0 m_0'\rangle)_\delta$$

$$\left[\frac{1}{N} \sum_{\mathbf{k},\sigma} (\hbar\omega_{\mathbf{k},\sigma})^2 (\mathbf{u}_{\mathbf{k},\sigma})_\alpha (\mathbf{u}_{\mathbf{k},\sigma})_\beta (\mathbf{u}_{\mathbf{k},\sigma})_\gamma (\mathbf{u}_{\mathbf{k},\sigma})_\delta \hat{n}_{\mathbf{k},\sigma} \sin\left(2\mathbf{k}(\mathbf{R}_{j'}^{(0)} - \mathbf{R}_j^{(0)}) \right) \right]. \tag{27}$$

We see two basic terms. The first describes a weak interaction that is independent of the number of phonons is a mode, and which is localized to nearest neighbors. The second term describes a weak interaction that is linear in the number of phonons in a mode, and which contributes as long as the phonon occupation is asymmetric with the wave vector $\mathbf{k}$. Since the phonon distribution appears in the summation over the phonon modes, it is possible in this case for excitation transfer to involve nuclei considerably more distant than nearest neighbors. We note that a quantitative evaluation of this formula will require in principle summations over all intermediate E1-coupled states.

These terms are much smaller than those appearing in the case of second-order E1 excitation transfer, due in part to the destructive interference, and in part to the effect occurring at higher-order in perturbation theory.

4.4. Interaction in the case of two phonon modes

In the case of excitation transfer where phonon exchange with two different phonon modes occurs, we require that each mode exchange a phonon with both nuclei. In this case the resonant contribution at fourth order is calculated to be

$$\left(\hat{V}(E - \hat{H}_0)^{-1} \hat{V}(E - \hat{H}_0)^{-1} \hat{V}(E - \hat{H}_0)^{-1} \hat{V} \right)_{\text{resonant}} \rightarrow T_1 + T_2 + T_3 + T_4, \tag{28}$$

where

$$T_1 = \frac{(Mc^2)^2}{4} \sum_{J_2} \sum_{J_2'} \frac{2}{(E_1 - E_0)^2 (E_2 - E_0)(E_2' - E_1)}$$

$$\sum_j \sum_{j'} \sum_{m_0} \sum_{m_1} \sum_{m_2} \sum_{m_0'} \sum_{m_1'} \sum_{m_2'} \left(|J_0 m_0\rangle\langle J_1 m_1| \right)_j \left(|J_1 m_1'\rangle\langle J_0 m_0'| \right)_{j'}$$

$$\langle J_0 m_0 | \mathbf{a}_j | J_2 m_2 \rangle \cdot \left[\frac{1}{N} \sum_{\mathbf{k},\sigma} \hbar\omega_{\mathbf{k},\sigma} \mathbf{u}_{\mathbf{k},\sigma} \mathbf{u}_{\mathbf{k},\sigma} (2\hat{n}_{\mathbf{k},\sigma} + 1) \cos\left(\mathbf{k} \cdot (\mathbf{R}_{j'}^{(0)} - \mathbf{R}_j^{(0)}) \right) \right] \cdot \langle J_1 m_1' | \mathbf{a}_{j'} | J_2' m_2' \rangle$$

$$\langle J_2 m_2 | \mathbf{a}_j | J_1 m_1 \rangle \cdot \left[\frac{1}{N} \sum_{\mathbf{k}',\sigma'} (\hbar\omega_{\mathbf{k}',\sigma'})^2 \mathbf{u}_{\mathbf{k}',\sigma'} \mathbf{u}_{\mathbf{k}',\sigma'} \cos\left(\mathbf{k}' \cdot (\mathbf{R}_{j'}^{(0)} - \mathbf{R}_j^{(0)}) \right) \right] \cdot \langle J_2' m_2' | \mathbf{a}_{j'} | J_0 m_0' \rangle \qquad (29)$$

$$T_2 = \frac{(Mc^2)^2}{4} \sum_{J_2} \sum_{J_2'} \frac{2}{(E_1 - E_0)^2 (E_2' - E_0)(E_2 - E_1)}$$

$$\sum_j \sum_{j'} \sum_{m_0} \sum_{m_1} \sum_{m_2} \sum_{m_0'} \sum_{m_1'} \sum_{m_2'} \left(|J_0 m_0\rangle\langle J_1 m_1| \right)_j \left(|J_1 m_1'\rangle\langle J_0 m_0'| \right)_{j'}$$

$$\langle J_0 m_0 | \mathbf{a}_j | J_2 m_2 \rangle \cdot \left[\frac{1}{N} \sum_{\mathbf{k},\sigma} (\hbar\omega_{\mathbf{k},\sigma})^2 \mathbf{u}_{\mathbf{k},\sigma} \mathbf{u}_{\mathbf{k},\sigma} \cos\left(\mathbf{k} \cdot (\mathbf{R}_{j'}^{(0)} - \mathbf{R}_j^{(0)}) \right) \right] \cdot \langle J_1 m_1' | \mathbf{a}_{j'} | J_2' m_2' \rangle$$

$$\langle J_2 m_2 | \mathbf{a}_j | J_1 m_1 \rangle \cdot \left[\frac{1}{N} \sum_{\mathbf{k}',\sigma'} \hbar\omega_{\mathbf{k}',\sigma'} \mathbf{u}_{\mathbf{k}',\sigma'} \mathbf{u}_{\mathbf{k}',\sigma'} (2\hat{n}_{\mathbf{k}',\sigma'} + 1) \cos\left(\mathbf{k}' \cdot (\mathbf{R}_{j'}^{(0)} - \mathbf{R}_j^{(0)}) \right) \right] \cdot \langle J_2' m_2' | \mathbf{a}_{j'} | J_0 m_0' \rangle \qquad (30)$$

$$T_3 = \frac{(Mc^2)^2}{4} \sum_{J_2} \sum_{J_2'} \frac{2}{(E_1 - E_0)^2 (E_2 - E_0)(E_2' - E_0)}$$

$$\sum_j \sum_{j'} \sum_{m_0} \sum_{m_1} \sum_{m_2} \sum_{m_0'} \sum_{m_1'} \sum_{m_2'} \left(|J_0 m_0\rangle\langle J_1 m_1| \right)_j \left(|J_1 m_1'\rangle\langle J_0 m_0'| \right)_{j'}$$

$$\langle J_0 m_0 | \mathbf{a}_j | J_2 m_2 \rangle \cdot \left[\frac{1}{N} \sum_{\mathbf{k},\sigma} \hbar\omega_{\mathbf{k},\sigma} \mathbf{u}_{\mathbf{k},\sigma} \mathbf{u}_{\mathbf{k},\sigma} (2\hat{n}_{\mathbf{k},\sigma} + 1) \cos\left(\mathbf{k} \cdot (\mathbf{R}_{j'}^{(0)} - \mathbf{R}_j^{(0)}) \right) \right] \cdot \langle J_2' m_2' | \mathbf{a}_{j'} | J_0 m_0' \rangle$$

$$\langle J_2 m_2 | \mathbf{a}_j | J_1 m_1 \rangle \cdot \left[\frac{1}{N} \sum_{\mathbf{k}',\sigma'} (\hbar\omega_{\mathbf{k}',\sigma'})^2 \mathbf{u}_{\mathbf{k}',\sigma'} \mathbf{u}_{\mathbf{k}',\sigma'} \cos\left(\mathbf{k}' \cdot (\mathbf{R}_{j'}^{(0)} - \mathbf{R}_j^{(0)}) \right) \right] \cdot \langle J_1 m_1' | \mathbf{a}_{j'} | J_2' m_2' \rangle \qquad (31)$$

$$T_4 = \frac{(Mc^2)^2}{4} \sum_{J_2} \sum_{J_2'} \frac{2}{(E_1 - E_0)^2 (E_2 - E_1)(E_2' - E_1)}$$

$$\sum_j \sum_{j'} \sum_{m_0} \sum_{m_1} \sum_{m_2} \sum_{m_0'} \sum_{m_1'} \sum_{m_2'} \left(|J_0 m_0\rangle\langle J_1 m_1| \right)_j \left(|J_1 m_1'\rangle\langle J_0 m_0'| \right)_{j'}$$

$$\langle J_0 m_0 | \mathbf{a}_j | J_2 m_2 \rangle \cdot \left[\frac{1}{N} \sum_{\mathbf{k},\sigma} (\hbar\omega_{\mathbf{k},\sigma})^2 \mathbf{u}_{\mathbf{k},\sigma} \mathbf{u}_{\mathbf{k},\sigma} \cos\left(\mathbf{k} \cdot (\mathbf{R}_{j'}^{(0)} - \mathbf{R}_j^{(0)}) \right) \right] \cdot \langle J_2' m_2' | \mathbf{a}_{j'} | J_0 m_0' \rangle$$

$$\langle J_2 m_2 | \mathbf{a}_j | J_1 m_1 \rangle \cdot \left[\frac{1}{N} \sum_{\mathbf{k}',\sigma'} \hbar\omega_{\mathbf{k}',\sigma'} \mathbf{u}_{\mathbf{k}',\sigma'} \mathbf{u}_{\mathbf{k}',\sigma'} (2\hat{n}_{\mathbf{k}',\sigma'} + 1) \cos\left(\mathbf{k}' \cdot (\mathbf{R}_{j'}^{(0)} - \mathbf{R}_j^{(0)}) \right) \right] \cdot \langle J_1 m_1' | \mathbf{a}_{j'} | J_2' m_2' \rangle. \qquad (32)$$

In this case destructive interference has resulted in a very weak interaction which depends on the symmetric part of the phonon distribution in the different modes. The indirect interaction that results is dominated by coupling to nearest neighbors. Once again it is the high-frequency phonon modes which provide the strongest contributions to the interaction.

4.5. Interaction in the case of three phonon modes

For an excitation transfer process involving three phonon modes, we require one mode to be involved in phonon exchange at both sites, and a single phonon exchange with the other modes, one at one site, and one at the other. We are most interested in resonant excitation transfer, which in the case of three modes is potentially problematic since constraints are imposed on the mode energies. For the specific interaction under consideration here, we focus on interactions in which single phonon creation and annihilation occurs for the first mode; for the second mode we require that the phonon interaction involves the creation of a phonon; and for the third mode we require phonon annihilation. Overall the interaction is resonant if the phonon mode energy is matched for the second and third mode. While not exhaustive, this provides a check to see whether or not destructive interference causes a substantial reduction of the strength of the indirect interaction in one case.

The associated contribution to the resonant indirect interaction can be written as

$$
\left(\hat{V}(E - \hat{H}_0)^{-1}\hat{V}(E - \hat{H}_0)^{-1}\hat{V}(E - \hat{H}_0)^{-1}\hat{V} \right)_{\text{resonant}} \rightarrow T_1' + \cdots + T_8', \tag{33}
$$

where we exhibit the first contribution T_1' explicitly here

$$
T_1' = \frac{(Mc^2)^2}{4} \sum_{J_2} \sum_{J_2'} \frac{2}{(E_1 - E_0)^2(E_2 - E_1)(E_2' - E_1)}
$$

$$
\sum_{j} \sum_{j'} \sum_{m_0} \sum_{m_1} \sum_{m_2} \sum_{m_0'} \sum_{m_1'} \sum_{m_2'} \left(|J_0 m_0\rangle\langle J_1 m_1| \right)_j \left(|J_1 m_1'\rangle\langle J_0 m_0'| \right)_{j'}
$$

$$
\langle J_0 m_0 | \mathbf{a}_j | J_2 m_2 \rangle \cdot \left[\frac{1}{N} \sum_{\mathbf{k},\sigma} (\hbar\omega_{\mathbf{k},\sigma})^2 \mathbf{u}_{\mathbf{k},\sigma} \mathbf{u}_{\mathbf{k},\sigma} \cos\left(\mathbf{k} \cdot (\mathbf{R}_{j'}^{(0)} - \mathbf{R}_j^{(0)}) \right) \right] \cdot \langle J_2' m_2' | \mathbf{a}_{j'} | J_0 m_0' \rangle
$$

$$
\langle J_2 m_2 | \mathbf{a}_j | J_1 m_1 \rangle \cdot \left[\sum_{\mathbf{k}',\sigma'} \sqrt{\hbar\omega_{\mathbf{k}',\sigma'}} \mathbf{u}_{\mathbf{k}',\sigma'} \sqrt{\hat{n}_{\mathbf{k}',\sigma'} + 1} e^{-i\mathbf{k}'\cdot\mathbf{R}_j^{(0)}} \right]
$$

$$
\langle J_1 m_1' | \mathbf{a}_{j'} | J_2' m_2' \rangle \cdot \left[\sum_{\mathbf{k}'',\sigma''} \sqrt{\hbar\omega_{\mathbf{k}'',\sigma''}} \mathbf{u}_{\mathbf{k}'',\sigma''} \sqrt{\hat{n}_{\mathbf{k}'',\sigma''}} e^{i\mathbf{k}''\cdot\mathbf{R}_{j'}^{(0)}} \right] \tag{34}
$$

with the remaining terms listed in Appendix A. The resulting interaction is very weak, and localized to nearest neighbors.

4.6. Discussion

The low energy M1 transitions are of interest to us since we appear to be seeing anomalies associated with excitation transfer in experiments. A list of nuclei with low energy M1 and M1+E2 transitions is presented in Table 2. In connection with this list we draw attention to the special case of the low-energy M1+E2 transition in ^{201}Hg at 1.565 keV,

Table 2. Low-energy M1 and M1+E2 transitions from the ground state of stable nuclei, from the BNL Nudat2 database. The internal conversion coefficient is α.

Isotope	E(keV)	$T_{1/2}$	Multipolarity	α
Hg-201	1.5648	81 ns	M1+E2	4.7×10^4
Tm-169	8.41017	4.09 ns	M1+E2	263
Kr-83	9.4057	156.8 ns	M1+E2	17.09
Os-187	9.756	2.38 ns	M1(+E2)	280
U-235	13.0336	0.50 ns	(M1+E2)	497
Fe-57	14.4129	98.3 ns	M1+E2	8.56
Eu-151	21.541	9.6 ns	M1+E2	27.6
Sm-149	22.507	7.33 ns	M1+E2	29.2
Sn-119	23.870	18.03 ns	M1+E2	5.06
Hg-201	26.272	630 ps	M1+E2	71.6
K-40	29.8299	4.25 ns	M1	0.298
Hg-201	32.145	60 ps	M1+E2	39.6
Te-125	35.4925	1.482 ns	M1+E2	13.69
Os-189	36.17	0.52 ns	M1+E2	20.2
Sb-121	37.1298	3.46 ns	M1+E2	10.88
Xe-129	39.5774	0.97 ns	M1+E2	12.03
Dy-161	43.8201	0.83 ns	M1+E2	7.6
U-235	46.103	14 ps	M1+E2	50
W-183	46.4838	0.185 ns	M1+E2	8.4

which we have discussed previous in discussions of collimated X-ray emission. We note also the low-energy M1+E2 transition in ^{57}Fe at 14.4129 keV of interest in our excitation transfer experiments with radioactive ^{57}Co.

The calculation in the fourth-order indirect interactions discussed in this section involved a substantial effort, as on the order of a hundred pathways needed to be included, and as the resulting indirect coupling is extremely sensitive to any errors in the calculation. We had hoped that destructive interference effects might have been avoided for this model, but from the results we obtained it is clear that destructive interference very much impacts the indirect coupling leading to a very weak indirect interaction.

Even though there seems to be no hope accounting for the experimental results quantitatively with this model, there are some features of the model that are consistent qualitatively. In particular, we see excitation transfer dependent on the number of phonons present to nearest neighbors (in the case of phonon exchange with two phonon modes) which seems to be the kind of mechanism that would be relevant to observations of angular anisotropy. In addition we also see excitation transfer dependent on the number of phonons present potentially to distant neighbors (in the case of phonon exchange with one phonon mode) which seems to be what would be needed to account for delocalization effects observed in the experiments.

5. Loss

We found that loss can reduce the destructive interference that hinders the indirect coupling coefficient in the case of up-conversion and down-conversion [5,6]. Loss has the potential to similarly reduce the destructive interference in the case of excitation transfer. It was proposed a decade ago that the local environment can increase the excitation transfer rate in biophysics [17,18]. For phonon-mediated nuclear excitation transfer we have considered the simpler problem of the potential enhancement of the rate due to a difference in the loss for the different intermediate states.

5.1. Indirect coupling for lossy E1 excitation transfer

In the event that loss terms dominate the indirect coupling matrix element for E1 transitions we can write

$$\left(\hat{V}(E - \hat{H}_0)^{-1}\hat{V}\right)_{\text{resonant}} \rightarrow$$

$$-i\frac{\hbar}{2}(\gamma_{00} + \gamma_{11} - \gamma_{01} - \gamma_{10})\frac{Mc^2}{2(\Delta E)^2}\sum_{j<j'}\sum_{m_0}\sum_{m_1}\sum_{m_0'}\sum_{m_1'}\left(|J_0 m_0\rangle\langle J_1 m_1|\right)_j\left(|J_1 m_1'\rangle\langle J_0 m_0'|\right)_{j'}$$

$$\langle J_0 m_0|\mathbf{a}_j|J_1 m_1\rangle \cdot \left[\frac{1}{N}\sum_{\mathbf{k},\sigma}(\hbar\omega_{\mathbf{k},\sigma})^2\mathbf{u}_{\mathbf{k},\sigma}\mathbf{u}_{\mathbf{k},\sigma}(2\hat{n}_{\mathbf{k},\sigma} + 1)\cos\left(\mathbf{k}\cdot(\mathbf{R}_{j'}^{(0)} - \mathbf{R}_j^{(0)})\right)\right] \cdot \langle J_1 m_1'|\mathbf{a}_{j'}|J_0 m_0'\rangle$$

$$-i\frac{\hbar}{2}(\gamma_{00} + \gamma_{11} - \gamma_{01} - \gamma_{10})\frac{Mc^2}{2(\Delta E)^2}\sum_{j<j'}\sum_{m_0}\sum_{m_1}\sum_{m_0'}\sum_{m_1'}\left(|J_1 m_1\rangle\langle J_0 m_0|\right)_j\left(|J_0 m_0'\rangle\langle J_1 m_1'|\right)_{j'}$$

$$\langle J_1 m_1|\mathbf{a}_j|J_0 m_0\rangle \cdot \left[\frac{1}{N}\sum_{\mathbf{k},\sigma}(\hbar\omega_{\mathbf{k},\sigma})^2\mathbf{u}_{\mathbf{k},\sigma}\mathbf{u}_{\mathbf{k},\sigma}(2\hat{n}_{\mathbf{k},\sigma} + 1)\cos\left(\mathbf{k}\cdot(\mathbf{R}_{j'}^{(0)} - \mathbf{R}_j^{(0)})\right)\right] \cdot \langle J_0 m_0'|\mathbf{a}_{j'}|J_1 m_1'\rangle\bigg\}. \tag{35}$$

We have used a notation for the loss in which intermediate states where both nuclei in the ground state are assigned a loss of γ_{00}, intermediate states where both nuclei are in the excited state are assigned a loss of γ_{11}, and where the initial and final states are assigned a loss of γ_{10} and γ_{01} respectively. In the event that a small number of (delocalized) high-frequency phonon modes are very highly excited this version of the indirect interaction can be larger than the lossless contribution, and can be delocalized. This is interesting.

5.2. Loss for M1 transitions with two phonon modes

Instead of a recitation of all of the different terms for all of the different cases for nuclear excitation transfer for M1 transitions, we focus on one example. In the event that the loss terms dominate the resonant indirect interaction we can write

$$\left(\hat{V}(E - \hat{H}_0)^{-1}\hat{V}(E - \hat{H}_0)^{-1}\hat{V}(E - \hat{H}_0)^{-1}\hat{V}\right)_{\text{resonant}} \rightarrow T_a + T_b \tag{36}$$

with

$$T_a = -i\frac{\hbar}{2}\frac{(Mc^2)^2}{4}\sum_{J_2}\sum_{J_2'}\left\{\frac{\gamma_{01} - \gamma_{02'} - \gamma_{11} + \gamma_{12'}}{(E_1 - E_0)(E_2' - E_0)(E_2 - E_1)(E_2' - E_1)}\right.$$

$$+\frac{\gamma_{00} - 2\gamma_{01} + \gamma_{11}}{(E_1 - E_0)^2(E_2 - E_1)(E_2' - E_1)} + \frac{\gamma_{11} - \gamma_{12} - \gamma_{12'} + \gamma_{22'}}{(E_2 - E_0)(E_2' - E_0)(E_2 - E_1)(E_2' - E_1)}$$

$$\left.+\frac{\gamma_{01} - \gamma_{02} - \gamma_{11} + \gamma_{12}}{(E_1 - E_0)(E_2 - E_0)(E_2 - E_1)(E_2' - E_1)}\right\}$$

$$\sum_j\sum_{j'}\sum_{m_0}\sum_{m_1}\sum_{m_2}\sum_{m_0'}\sum_{m_1'}\sum_{m_2'}\left(|J_0 m_0\rangle\langle J_1 m_1|\right)_j\left(|J_1 m_1'\rangle\langle J_0 m_0'|\right)_{j'}$$

$$\langle J_0 m_0|\mathbf{a}_j|J_2 m_2\rangle \cdot \left[\frac{1}{N}\sum_{\mathbf{k},\sigma}\hbar\omega_{\mathbf{k},\sigma}\mathbf{u}_{\mathbf{k},\sigma}\mathbf{u}_{\mathbf{k},\sigma}(2\hat{n}_{\mathbf{k},\sigma} + 1)\cos\left(\mathbf{k}\cdot(\mathbf{R}_{j'}^{(0)} - \mathbf{R}_j^{(0)})\right)\right] \cdot \langle J_1 m_1'|\mathbf{a}_{j'}|J_2' m_2'\rangle$$

$$\langle J_2 m_2 | \mathbf{a}_j | J_1 m_1 \rangle \cdot \left[\frac{1}{N} \sum_{\mathbf{k}',\sigma'} \hbar \omega_{\mathbf{k}',\sigma'} \mathbf{u}_{\mathbf{k}',\sigma'} \mathbf{u}_{\mathbf{k}',\sigma'} (2\hat{n}_{\mathbf{k}',\sigma} + 1) \cos \left(\mathbf{k}' \cdot (\mathbf{R}_{j'}^{(0)} - \mathbf{R}_j^{(0)}) \right) \right] \cdot \langle J_2' m_2' | \mathbf{a}_{j'} | J_0 m_0' \rangle \tag{37}$$

$$T_b = -i \frac{\hbar}{2} \frac{(Mc^2)^2}{4} \sum_{J_2} \sum_{J_2'} \left\{ \frac{\gamma_{01} - \gamma_{02'} - \gamma_{11} + \gamma_{12'}}{(E_1 - E_0)(E_2' - E_0)(E_2 - E_1)(E_2' - E_1)} \right.$$

$$+ \frac{\gamma_{00} - 2\gamma_{01} + \gamma_{11}}{(E_1 - E_0)^2 (E_2 - E_1)(E_2' - E_1)} + \frac{\gamma_{11} - \gamma_{12} - \gamma_{12'} + \gamma_{22'}}{(E_2 - E_0)(E_2' - E_0)(E_2 - E_1)(E_2' - E_1)}$$

$$\left. + \frac{\gamma_{01} - \gamma_{02} - \gamma_{11} + \gamma_{12}}{(E_1 - E_0)(E_2 - E_0)(E_2 - E_1)(E_2' - E_1)} \right\}$$

$$\sum_j \sum_{j'} \sum_{m_0} \sum_{m_1} \sum_{m_2} \sum_{m_0'} \sum_{m_1'} \sum_{m_2'} \left(|J_0 m_0\rangle \langle J_1 m_1| \right)_j \left(|J_1 m_1'\rangle \langle J_0 m_0'| \right)_{j'}$$

$$\langle J_0 m_0 | \mathbf{a}_j | J_2 m_2 \rangle \cdot \left[\frac{1}{N} \sum_{\mathbf{k},\sigma} \hbar \omega_{\mathbf{k},\sigma} \mathbf{u}_{\mathbf{k},\sigma} \mathbf{u}_{\mathbf{k},\sigma} (2\hat{n}_{\mathbf{k},\sigma} + 1) \cos \left(\mathbf{k} \cdot (\mathbf{R}_{j'}^{(0)} - \mathbf{R}_j^{(0)}) \right) \right] \cdot \langle J_2' m_2' | \mathbf{a}_{j'} | J_0 m_0' \rangle$$

$$\langle J_2 m_2 | \mathbf{a}_j | J_1 m_1 \rangle \cdot \left[\frac{1}{N} \sum_{\mathbf{k}',\sigma'} \hbar \omega_{\mathbf{k}',\sigma'} \mathbf{u}_{\mathbf{k}',\sigma'} \mathbf{u}_{\mathbf{k}',\sigma'} (2\hat{n}_{\mathbf{k}',\sigma} + 1) \cos \left(\mathbf{k}' \cdot (\mathbf{R}_{j'}^{(0)} - \mathbf{R}_j^{(0)}) \right) \right] \cdot \langle J_1 m_1' | \mathbf{a}_{j'} | J_2' m_2' \rangle \tag{38}$$

In writing this we have used the notation that the loss associated with basis states with two nuclei in the ground state is γ_{00}, the loss for basis states with one nucleus in the ground state and one in the first excited state is γ_{01}, and so forth.

Note that it is possible for contributions of this kind to be delocalized given a suitable distribution of phonons, and that that excitation can potentially be transferred to a great many nearby ground state nuclei.

5.3. Discussion

In order for loss to have a significant impact on the indirect coupling matrix element in the case of up-conversion and down-conversion there only needs to be a minor contribution associated with each phonon exchange, since a large number of phonon exchange interactions are involved. The situation is different in the case of excitation transfer. Since only a few phonon exchanges occur, the loss needs to be substantial in each case to have a significant impact on the overall indirect interaction.

Loss has the potential to greatly enhance excitation transfer based on the results discussed in this section. The indirect coupling coefficient are smaller than contributions from individual pathways by factors on the order of a differential decay rate times $\hbar$ divided by a relevant nuclear transition energy, which means that the terms are "small". However, if the number of phonons is large in a phonon mode that is delocalized, then the coupling from one site can be to a great many sites, which can increase the total coherent rate by a Dicke factor which is on the order of the square root of the number of possible final state sites.

It is possible that the excitation transfer effects we see in experiments with ^{57}Co are a result of loss-enhanced excitation transfer, but we would expect the differential decay rates not to be particularly large which argues against this. Nevertheless, in such a scenario we would only expect to see excitation transfer effects due to the presence of very highly-excited delocalized THz phonon modes.

6. Off-resonant Shift of the Basis State Energies

Although we found that loss could make a difference in the indirect interaction for excitation transfer in the previous section, the resulting indirect interaction seems too weak to account for the experimental results obtained so far.

Consequently, we are motivated to seek other effects that might impact the indirect interaction. One possibility which we discuss in this section is that the basis state energies may shift off of resonance, which could spoil the destructive interference if the shifts are sufficiently large.

That such an effect is possible in principle can be seen from the equivalent two-level system model of Eq. (11), where the basis state energies acquire a self-energy shift

$$E_n \ \rightarrow \ E_n + \Sigma(E), \tag{39}$$

where the self-energy $\Sigma(E)$ depends explicitly on the energy eigenvalue. If the self-energy depends on the energy eigenvalue, then its contribution would be different on resonance as compared to off-resonance.

We will argue in this section that there could well be a substantial shift in the basis state energies off of resonance. The main argument for this is that the nuclear force itself is due to the exchange of mesons, and since this exchange involves virtual states, the nuclear force is expected to depend on the energy eigenvalue. We would expect the binding energy of a nucleus to be different on resonance compared to off-resonance. In the literature there appears discussions in the 1960s and 1970s that the nucleon-nucleon interaction changes off of resonance, and that this would impact the calculation of various matrix elements contribute off of resonance, providing a constraint on nuclear potential models [19,20]. It would follow that the binding energy itself should differ off of resonance; however, there are no calculations of how the binding energy varies with the amount of energy off of resonance (most relevant may be the calculations discussed in Ref. [21]).

6.1. Brillouin–Wigner theory approach

We are interested in this subsection in applying Brillouin–Wigner theory to the problem of the off-resonant energy shift to a develop formalism to describe the effect. We consider a formal model given by

$$\hat{H} = \hat{H}_0 + \hat{U} + \hat{V}, \tag{40}$$

where $\hat{U}$ describes nuclear state raising and lowering associated with phonon exchange, and where $\hat{V}$ creates or destroys mesons in connection with the strong force.

We consider a sector expansion of the form

$$\begin{aligned} \Psi = &\Psi_{m,0} + \Psi_{m,1} + \cdots \\ &+ \Psi_{m-1,0} + \Psi_{m-1,1} + \cdots \\ &+ \Psi_{m+1,0} + \Psi_{m+1,1} + \cdots \\ &+ \cdots, \end{aligned} \tag{41}$$

where the first index m keeps track of the number of excited nuclei present as a result of phonon exchange, and the second index is the number of mesons present associated with the nucleon-nucleon interaction. Keep in mind that we are considering the phonon exchange to be associated with phonon-nuclear coupling, so that a single phonon exchange is associated with the raising or lowering of the nuclear state. We plug in to the time-independent Schrödinger equation

$$E\Psi = \hat{H}\Psi \tag{42}$$

to obtain coupled eigenvalue equations given by

$$E\Psi_{m,0} = \hat{H}_0\Psi_{m,0} + \hat{U}_+\Psi_{m-1,0} + \hat{U}_-\Psi_{m+1,0} + \hat{V}_-\Psi_{m,1},$$

$$E\Psi_{m,1} = \hat{H}_0\Psi_{m,1} + \hat{U}_+\Psi_{m-1,1} + \hat{U}_-\Psi_{m+1,1} + \hat{V}_-\Psi_{m,2} + \hat{V}_+\Psi_{m,0},$$

$$E\Psi_{m-1,0} = \hat{H}_0\Psi_{m-1,0} + \hat{U}_+\Psi_{m-2,0} + \hat{U}_-\Psi_{m,0} + \hat{V}_-\Psi_{m-1,1},$$

$$E\Psi_{m-1,1} = \hat{H}_0\Psi_{m-1,1} + \hat{U}_+\Psi_{m-2,1} + \hat{U}_-\Psi_{m,1} + \hat{V}_-\Psi_{m-1,2} + \hat{V}_+\Psi_{m-1,0},$$

$$E\Psi_{m+1,0} = \hat{H}_0\Psi_{m+1,0} + \hat{U}_+\Psi_{m,0} + \hat{U}_-\Psi_{m+2,0} + \hat{V}_-\Psi_{m+1,1},$$

$$E\Psi_{m+1,1} = \hat{H}_0\Psi_{m+1,1} + \hat{U}_+\Psi_{m,1} + \hat{U}_-\Psi_{m+2,1} + \hat{V}_-\Psi_{m+1,2} + \hat{V}_+\Psi_{m+1,0},$$

$$\cdots \tag{43}$$

where we have made us of $\pm$ subscripts to keep track of raising or lowering.

For simplicity we would like to eliminate all sectors containing mesons in order to develop sector equations in terms of nuclear potential models. For simplicity our focus will be on single meson exchange, so that we need to eliminate all $\Psi_{m',1}$. To do this we first need to solve for these sector wave functions in terms of other sector wave functions according to

$$\Psi_{m,1} = (E - \hat{H}_0)^{-1}\left(\hat{U}_+\Psi_{m-1,1} + \hat{U}_-\Psi_{m+1,1} + \hat{V}_-\Psi_{m,2} + \hat{V}_+\Psi_{m,0}\right),$$

$$\Psi_{m-1,1} = (E - \hat{H}_0)^{-1}\left(\hat{U}_+\Psi_{m-2,1} + \hat{U}_-\Psi_{m,1} + \hat{V}_-\Psi_{m-1,2} + \hat{V}_+\Psi_{m-1,0}\right),$$

$$\Psi_{m+1,1} = (E - \hat{H}_0)^{-1}\left(\hat{U}_+\Psi_{m,1} + \hat{U}_-\Psi_{m+2,1} + \hat{V}_-\Psi_{m+1,2} + \hat{V}_+\Psi_{m+1,0}\right). \tag{44}$$

We plug in and retain only lowest order terms to obtain

$$E\Psi_{m,0} = \left(\hat{H}_0 + \hat{V}_-(E - \hat{H}_0)^{-1}\hat{V}_+\right)\Psi_{m,0} + \hat{U}_+\Psi_{m-1,0} + \hat{U}_-\Psi_{m+1,0},$$

$$E\Psi_{m-1,0} = \left(\hat{H}_0 + \hat{V}_-(E - \hat{H}_0)^{-1}\hat{V}_+\right)\Psi_{m-1,0} + \hat{U}_+\Psi_{m-2,0} + \hat{U}_-\Psi_{m,0},$$

$$E\Psi_{m+1,0} = \left(\hat{H}_0 + \hat{V}_-(E - \hat{H}_0)^{-1}\hat{V}_+\right)\Psi_{m+1,0} + \hat{U}_+\Psi_{m,0} + \hat{U}_-\Psi_{m+2,0},$$

$$\cdots \tag{45}$$

The single meson exchange contribution to the nucleon-nucleon potential on resonance in this simple model comes about through second-order terms of the form

$$\hat{V}_-(E - \hat{H}_0)^{-1}\hat{V}_+$$

$$\rightarrow \sum_{j<k} \frac{1}{3}\frac{g^2}{\hbar c}m_\pi c^2(\boldsymbol{\tau}_j \cdot \boldsymbol{\tau}_k)\left[\boldsymbol{\sigma}_j \cdot \boldsymbol{\sigma}_k + \left(1 + \frac{3\hbar}{m_\pi c r_{jk}} + \frac{3\hbar^2}{m_\pi^2 c^2 r_{jk}^2}\right)S_{12}\right]\mathrm{e}^{-m_\pi c r_{jk}/\hbar}, \tag{46}$$

where we have selected here the one pion exchange potential from Ref. [22] for the resulting contribution to the nuclear potential. Note that in these older models that heavier meson exchange terms are included, and two-meson exchange terms are needed in order to develop a realistic potential model.

The key issue in this discussion is whether there is a shift in the binding energy due to a modification of the nucleon–nucleon potential off of resonance. To proceed, we first focus on the resonant sector where the energy eigenvalue is determined approximately from the solution of the formal eigenvalue equation

$$E\Psi_{m,0} = \left(\hat{H}_0 + \hat{V}_-(E - \hat{H}_0)^{-1}\hat{V}_+\right)\Psi_{m,0}, \tag{47}$$

where the energy E in this equation appears both as the eigenvalue on the left-hand side and as part of the denominator on the right-hand side.

Consider next a similar calculation for the basis state energy in one of the off-resonant sectors. In this case we could work with the eigenvalue problem

$$E'\Psi_{m+1,0} = \left(\hat{H}_0 + \hat{V}_-(E - \hat{H}_0)^{-1}\hat{V}_+\right)\Psi_{m+1,0}, \tag{48}$$

where E' is the associated eigenvalue, different from E by about one unit of excitation energy ΔE (since we consider $m+1$ instead of m). Suppose that for the purpose of sorting out the denominator on the right-hand side we approximate

$$E' \rightarrow E + \Delta E, \tag{49}$$

then we can write the eigenvalue equation for this off-resonant sector approximately as

$$E'\Psi_{m+1,0} = \left(\hat{H}_0 + \hat{V}_-(E' - \Delta E - \hat{H}_0)^{-1}\hat{V}_+\right)\Psi_{m+1,0}. \tag{50}$$

The nuclear potential off of resonance will then be different than on resonance.

We can make use of a Taylor series expansion to determine the different in the nuclear potential at lowest order. We can write

$$(E' - \Delta E - \hat{H}_0)^{-1} = (E' - \hat{H}_0)^{-1} + \Delta E(E' - \hat{H}_0)^{-2} + \cdots \tag{51}$$

The off-resonance eigenvalue equation can be written approximately as

$$E'\Psi_{m+1,0} = \left(\hat{H}_0 + \hat{V}_-(E' - \hat{H}_0)^{-1}\hat{V}_+ + \Delta E\hat{V}_-(E' - \hat{H}_0)^{-2}\hat{V}_+\right)\Psi_{m+1,0}. \tag{52}$$

To lowest order we would expect a shift in the binding energy linear in the offset energy

$$E' \rightarrow E + \Delta E + \Delta E \langle \hat{V}_- (E' - \hat{H}_0)^{-2} \hat{V}_+ \rangle. \tag{53}$$

Our conclusion from this brief discussion is that we would expect the nuclear binding energy to shift off of resonance. Also, if the nucleon–nucleon interaction changes off of resonance, we would also expect that the nuclear states themselves would be changed.

6.2. Breit interaction off of resonance

The arguments above apply as well to the electromagnetic interaction which is simpler and more familiar, so we were motivated to develop a calculation of the electromagnetic potential off of resonance. This is technically simplest in the Coulomb gauge, where the contribution from transverse photon exchange gives rise to the Breit interaction.

Single transverse photon exchange leads to an interaction that can be split into two components according to

$$\hat{V}_{12} = \hat{V}_{\mathrm{I}} + \hat{V}_{\mathrm{II}}, \tag{54}$$

where the initial evaluation of the second-order interaction leads to

$$\hat{V}_{\mathrm{I}} = q_1 q_2 \sum_{\mathbf{k}} \frac{\hbar c^2}{2\omega_{\mathbf{k}} \epsilon_0 L^3} \frac{(\boldsymbol{\alpha}_1 \cdot \boldsymbol{\alpha}_2)}{(E_{\mathrm{off}} - \hbar\omega_{\mathbf{k}})} + q_1 q_2 \sum_{\mathbf{k}} \frac{\hbar c^2}{2\omega_{\mathbf{k}} \epsilon_0 L^3} \frac{(\boldsymbol{\alpha}_2 \cdot \boldsymbol{\alpha}_1)}{(E_{\mathrm{off}} - \hbar\omega_{\mathbf{k}})} e^{i\mathbf{k}\cdot(\mathbf{r}_2 - \mathbf{r}_1)}, \tag{55}$$

$$\hat{V}_{\mathrm{II}} = -q_1 q_2 \sum_{\mathbf{k}} \frac{\hbar c^2}{2\omega_{\mathbf{k}} \epsilon_0 L^3} \frac{(\boldsymbol{\alpha}_1 \cdot \hat{\mathbf{i}}_{\mathbf{k}})(\boldsymbol{\alpha}_2 \cdot \hat{\mathbf{i}}_{\mathbf{k}})}{(E_{\mathrm{off}} - \hbar\omega_{\mathbf{k}})} e^{-i\mathbf{k}\cdot(\mathbf{r}_2 - \mathbf{r}_1)} - q_1 q_2 \sum_{\mathbf{k}} \frac{\hbar c^2}{2\omega_{\mathbf{k}} \epsilon_0 L^3} \frac{(\boldsymbol{\alpha}_2 \cdot \hat{\mathbf{i}}_{\mathbf{k}})(\boldsymbol{\alpha}_1 \cdot \hat{\mathbf{i}}_{\mathbf{k}})}{(E_{\mathrm{off}} - \hbar\omega_{\mathbf{k}})} e^{i\mathbf{k}\cdot(\mathbf{r}_2 - \mathbf{r}_1)}, \tag{56}$$

where E_{off} is the off-resonant shift in energy (for the off-resonant sector focused on in the previous section with one extra excited nucleus, $E_{\mathrm{off}} = -\Delta E$). These can be reduced in the continuum limit to give

$$\hat{V}_{\mathrm{I}} = -\frac{q_1 q_2}{4\pi\epsilon_0 |\mathbf{r}_2 - \mathbf{r}_1|} (\boldsymbol{\alpha}_1 \cdot \boldsymbol{\alpha}_2) \frac{2}{\pi} \int_0^\infty \frac{\sin(k|\mathbf{r}_2 - \mathbf{r}_1|)}{(k - E_{\mathrm{off}}/\hbar c)} \mathrm{d}k, \tag{57}$$

$$\begin{aligned}
\hat{V}_{\mathrm{II}} = {} & \frac{q_1 q_2}{4\pi\epsilon_0} \frac{\boldsymbol{\alpha}_1 \cdot \boldsymbol{\alpha}_2}{3} \frac{2}{\pi} \int_0^\infty \frac{k j_0(k|\mathbf{r}_2 - \mathbf{r}_1|)}{(k - E_{\mathrm{off}}/\hbar c)} \mathrm{d}k \\
& - \frac{q_1 q_2}{4\pi\epsilon_0} \left((\boldsymbol{\alpha}_1 \cdot \hat{\mathbf{i}}_{\mathbf{r}_2 - \mathbf{r}_1})(\boldsymbol{\alpha}_2 \cdot \hat{\mathbf{i}}_{\mathbf{r}_2 - \mathbf{r}_1}) - \frac{\boldsymbol{\alpha}_1 \cdot \boldsymbol{\alpha}_2}{3} \right) \frac{2}{\pi} \int_0^\infty \frac{k j_2(k|\mathbf{r}_2 - \mathbf{r}_1|)}{(k - E_{\mathrm{off}}/\hbar c)} \mathrm{d}k.
\end{aligned} \tag{58}$$

On resonance these reduce to

$$\begin{aligned}
\hat{V}_{\mathrm{I}} + \hat{V}_{\mathrm{II}} = {} & -\frac{q_1 q_2}{4\pi\epsilon_0 |\mathbf{r}_2 - \mathbf{r}_1|} (\boldsymbol{\alpha}_1 \cdot \boldsymbol{\alpha}_2) \\
& + \frac{q_1 q_2}{4\pi\epsilon_0 |\mathbf{r}_2 - \mathbf{r}_1|} \frac{\boldsymbol{\alpha}_1 \cdot \boldsymbol{\alpha}_2}{3} - \frac{q_1 q_2}{4\pi\epsilon_0 |\mathbf{r}_2 - \mathbf{r}_1|} \frac{1}{2} \left((\boldsymbol{\alpha}_1 \cdot \hat{\mathbf{i}}_{\mathbf{r}_2 - \mathbf{r}_1})(\boldsymbol{\alpha}_2 \cdot \hat{\mathbf{i}}_{\mathbf{r}_2 - \mathbf{r}_1}) - \frac{\boldsymbol{\alpha}_1 \cdot \boldsymbol{\alpha}_2}{3} \right) \\
= {} & -\frac{1}{2} \frac{q_1 q_2}{4\pi\epsilon_0 |\mathbf{r}_2 - \mathbf{r}_1|} \left[(\boldsymbol{\alpha}_1 \cdot \boldsymbol{\alpha}_2) + (\boldsymbol{\alpha}_1 \cdot \hat{\mathbf{i}}_{\mathbf{r}_2 - \mathbf{r}_1})(\boldsymbol{\alpha}_2 \cdot \hat{\mathbf{i}}_{\mathbf{r}_2 - \mathbf{r}_1}) \right]
\end{aligned} \tag{59}$$

consistent with the Breit interaction found in the literature.

6.3. Pole on the integration contour

In the event that E_{off} is positive (so that the energy eigenvalue is larger than the basis state energy) then the integrals in k contain a pole on the k-axis in the range of integration. We can write [23]

$$\int_0^\infty \frac{\sin(k|\mathbf{r}_2 - \mathbf{r}_1|)}{(k - k_0)}\mathrm{d}k$$

$$= -\sin(k_0|\mathbf{r}_2 - \mathbf{r}_1|)\mathrm{ci}(k_0|\mathbf{r}_2 - \mathbf{r}_1|) + \cos(k_0|\mathbf{r}_2 - \mathbf{r}_1|)[\mathrm{si}(k_0|\mathbf{r}_2 - \mathbf{r}_1|) + \pi], \tag{60}$$

where

$$k_0 = \frac{E_{off}}{\hbar c}, \tag{61}$$

$$\mathrm{si}(a) = -\int_1^\infty \frac{\sin(ax)}{x}\mathrm{d}x,$$

$$\mathrm{ci}(a) = -\int_1^\infty \frac{\cos(ax)}{x}\,\mathrm{d}x. \tag{62}$$

The pole on the k-axis in this case does not lead to an imaginary contribution, so we would not expect a new radiative decay channel off of resonance resulting from this contribution.

For the other off-resonant integral

$$\int_0^\infty \frac{k}{k - k_0} j_2(k|\mathbf{r}_2 - \mathbf{r}_1|)\mathrm{d}k, \tag{63}$$

we can express the result in terms of the Meijer G-function when $k_0 < 0$. At present we do not have a result for the extension to $k_0 > 0$, so we do not know whether an imaginary part is generated.

6.4. Indirect interaction for E1 transitions

Under conditions where basis state energy shifts provide the dominant contribution to the indirect second order interaction for excitation transfer associated with E1 transitions we can write for the resonant interaction

$$\left(\hat{V}(E - \hat{H}_0)^{-1}\hat{V}\right)_{\text{resonant}}$$

$$\to \sum_j \sum_{j'} \sum_{m_0} \sum_{m_1} \sum_{m_0'} \sum_{m_1'} \sum_{\mathbf{k},\sigma} \frac{Mc^2\hbar\omega_{\mathbf{k},\sigma}}{2N}$$

$$\left\{ |J_0 m_0\rangle\langle J_0 m_0|\mathbf{u}_{\mathbf{k},\sigma}\cdot\mathbf{a}_j|J_1 m_1\rangle\langle J_1 m_1||J_1 m_1'\rangle\langle J_1 m_1'|\mathbf{u}_{\mathbf{k},\sigma}\cdot\mathbf{a}_{j'}|J_0 m_0'\rangle\langle J_0 m_0'| \right.$$

$$\frac{E_{00} + E_{11} - 2E_{10}}{(E_{10} - E_{00})(E_{11} - E_{10})}(2\hat{n}_{\mathbf{k},\sigma} + 1)\cos[\mathbf{k}\cdot(\mathbf{R}_{j'}^{(0)} - \mathbf{R}_j^{(0)})]$$

$$+ |J_1 m_1\rangle\langle J_1 m_1|\mathbf{u}_{\mathbf{k},\sigma}\cdot\mathbf{a}_j|J_0 m_0\rangle\langle J_0 m_0||J_0 m_0'\rangle\langle J_0 m_0'|\mathbf{u}_{\mathbf{k},\sigma}\cdot\mathbf{a}_{j'}|J_1 m_1'\rangle\langle J_1 m_1'|$$

$$\left. \frac{E_{00} + E_{11} - 2E_{10}}{(E_{10} - E_{00})(E_{11} - E_{10})}(2\hat{n}_{\mathbf{k},\sigma} + 1)\cos[\mathbf{k}\cdot(\mathbf{R}_{j'}^{(0)} - \mathbf{R}_j^{(0)})] \right\}, \tag{64}$$

where E_{00} is the (shifted) basis state energy with both nuclei in the ground state, where E_{11} is the (shifted) basis state energy with both nuclei in the excited state, and where $E_{10} = E_{01}$ is the (unshifted) basis state energy with one nucleus excited and one in the ground state.

6.5. Indirect interaction for one-mode M1 transitions

The indirect interaction for resonant excitation transfer for an M1 transition involving exchange with a single phonon mode can be written as

$$\left(\hat{V}(E - \hat{H}_0)^{-1}\hat{V}(E - \hat{H}_0)^{-1}\hat{V}(E - \hat{H}_0)^{-1}\hat{V} \right)_{\text{resonant}} \rightarrow T_{c0} + T_{c1} + T_{c2} + T_{s1}, \tag{65}$$

where

$$
\begin{aligned}
T_{c0} = &\frac{(Mc^2)^2}{4N} \sum_{J_2} \sum_{J_2'} \left(\frac{2}{(E_{10} - E_{00})(E_{10} - E_{20})(E_{10} - E_{2'0})} + \frac{2}{(E_{10} - E_{11})(E_{10} - E_{21})(E_{10} - E_{2'1})} \right. \\
&+ \frac{1}{(E_{10} - E_{20})(E_{10} - E_{2'0})(E_{10} - E_{2'2})} + \left. \frac{1}{(E_{10} - E_{21})(E_{10} - E_{2'1})(E_{10} - E_{2'2})} \right) \\
&\sum_{j} \sum_{j'} \sum_{m_0} \sum_{m_1} \sum_{m_2} \sum_{m_0'} \sum_{m_1'} \sum_{m_2'} \left(|J_0 m_0\rangle\langle J_1 m_1| \right)_j \left(|J_1 m_1'\rangle\langle J_0 m_0'| \right)_{j'} \\
&\sum_{\alpha} \sum_{\beta} \sum_{\gamma} \sum_{\delta} (\langle J_0 m_0 | \mathbf{a}_j | J_2 m_2 \rangle)_\alpha (\langle J_2 m_2 | \mathbf{a}_j | J_1 m_1 \rangle)_\beta (\langle J_1 m_1' | \mathbf{a}_{j'} | J_2' m_2' \rangle)_\gamma (\langle J_2' m_2' | \mathbf{a}_{j'} | J_0 m_0' \rangle)_\delta \\
&\left[\frac{1}{N} \sum_{\mathbf{k},\sigma} (\hbar\omega_{\mathbf{k},\sigma})^2 (\mathbf{u}_{\mathbf{k},\sigma})_\alpha (\mathbf{u}_{\mathbf{k},\sigma})_\beta (\mathbf{u}_{\mathbf{k},\sigma})_\gamma (\mathbf{u}_{\mathbf{k},\sigma})_\delta \cos\left(2\mathbf{k}(\mathbf{R}_{j'}^{(0)} - \mathbf{R}_j^{(0)}) \right) \right]
\end{aligned}
\tag{66}
$$

$$
\begin{aligned}
T_{c1} = &\frac{(Mc^2)^2}{4N} \sum_{J_2} \sum_{J_2'} \left(\frac{2}{(E_{10} - E_{00})(E_{10} - E_{20})(E_{10} - E_{2'0})} + \frac{2}{(E_{10} - E_{11})(E_{10} - E_{21})(E_{10} - E_{2'1})} \right. \\
&+ \frac{2}{(E_{10} - E_{20})(E_{10} - E_{21})(E_{10} - E_{2'2})} + \frac{2}{(E_{10} - E_{20})(E_{10} - E_{2'0})(E_{10} - E_{2'2})} \\
&+ \frac{2}{(E_{10} - E_{21})(E_{10} - E_{2'0})(E_{10} - E_{2'2})} + \left. \frac{2}{(E_{10} - E_{2'0})(E_{10} - E_{2'1})(E_{10} - E_{2'2})} \right) \\
&\sum_{j} \sum_{j'} \sum_{m_0} \sum_{m_1} \sum_{m_2} \sum_{m_0'} \sum_{m_1'} \sum_{m_2'} \left(|J_0 m_0\rangle\langle J_1 m_1| \right)_j \left(|J_1 m_1'\rangle\langle J_0 m_0'| \right)_{j'} \\
&\sum_{\alpha} \sum_{\beta} \sum_{\gamma} \sum_{\delta} (\langle J_0 m_0 | \mathbf{a}_j | J_2 m_2 \rangle)_\alpha (\langle J_2 m_2 | \mathbf{a}_j | J_1 m_1 \rangle)_\beta (\langle J_1 m_1' | \mathbf{a}_{j'} | J_2' m_2' \rangle)_\gamma (\langle J_2' m_2' | \mathbf{a}_{j'} | J_0 m_0' \rangle)_\delta \\
&\left[\frac{1}{N} \sum_{\mathbf{k},\sigma} (\hbar\omega_{\mathbf{k},\sigma})^2 (\mathbf{u}_{\mathbf{k},\sigma})_\alpha (\mathbf{u}_{\mathbf{k},\sigma})_\beta (\mathbf{u}_{\mathbf{k},\sigma})_\gamma (\mathbf{u}_{\mathbf{k},\sigma})_\delta \hat{n}_{\mathbf{k},\sigma} \cos\left(2\mathbf{k}(\mathbf{R}_{j'}^{(0)} - \mathbf{R}_j^{(0)}) \right) \right]
\end{aligned}
\tag{67}
$$

$$
\begin{aligned}
T_{c2} = {} & \frac{(Mc^2)^2}{4N} \sum_{J_2} \sum_{J'_2} \Bigg(\frac{2}{(E_{10}-E_{00})(E_{10}-E_{20})(E_{10}-E_{2'0})} + \frac{2}{(E_{10}-E_{11})(E_{10}-E_{21})(E_{10}-E_{2'1})} \\
& + \frac{2}{(E_{10}-E_{20})(E_{10}-E_{21})(E_{10}-E_{2'2})} + \frac{2}{(E_{10}-E_{20})(E_{10}-E_{2'0})(E_{10}-E_{2'2})} \\
& + \frac{2}{(E_{10}-E_{21})(E_{10}-E_{2'1})(E_{10}-E_{2'2})} + \frac{2}{(E_{10}-E_{2'0})(E_{10}-E_{2'1})(E_{10}-E_{2'2})} \Bigg) \\
& \sum_j \sum_{j'} \sum_{m_0} \sum_{m_1} \sum_{m_2} \sum_{m'_0} \sum_{m'_1} \sum_{m'_2} \Big(|J_0 m_0\rangle\langle J_1 m_1| \Big)_j \Big(|J_1 m'_1\rangle\langle J_0 m'_0| \Big)_{j'} \\
& \sum_\alpha \sum_\beta \sum_\gamma \sum_\delta (\langle J_0 m_0|\mathbf{a}_j|J_2 m_2\rangle)_\alpha (\langle J_2 m_2|\mathbf{a}_j|J_1 m_1\rangle)_\beta (\langle J_1 m'_1|\mathbf{a}_{j'}|J'_2 m'_2\rangle)_\gamma (\langle J'_2 m'_2|\mathbf{a}_{j'}|J_0 m'_0\rangle)_\delta \\
& \left[\frac{1}{N} \sum_{\mathbf{k},\sigma} (\hbar\omega_{\mathbf{k},\sigma})^2 (\mathbf{u}_{\mathbf{k},\sigma})_\alpha (\mathbf{u}_{\mathbf{k},\sigma})_\beta (\mathbf{u}_{\mathbf{k},\sigma})_\gamma (\mathbf{u}_{\mathbf{k},\sigma})_\delta \, \hat{n}^2_{\mathbf{k},\sigma} \cos\left(2\mathbf{k}(\mathbf{R}^{(0)}_{j'} - \mathbf{R}^{(0)}_j) \right) \right],
\end{aligned}
\tag{68}
$$

$$
\begin{aligned}
T_{s1} = {} & i\frac{(Mc^2)^2}{4N} \sum_{J_2} \sum_{J'_2} \Bigg(\frac{2}{(E_{10}-\mathrm{Eaa})(E_{10}-\mathrm{Eca})(E_{10}-\mathrm{Eda})} - \frac{2}{(E_{10}-\mathrm{Ebb})(E_{10}-\mathrm{Ecb})(E_{10}-\mathrm{Edb})} \\
& + \frac{1}{(E_{10}-\mathrm{Eca})(E_{10}-\mathrm{Eda})(E_{10}-\mathrm{Edc})} - \frac{1}{(E_{10}-\mathrm{Ecb})(E_{10}-\mathrm{Edb})(E_{10}-\mathrm{Edc})} \Bigg) \\
& \sum_j \sum_{j'} \sum_{m_0} \sum_{m_1} \sum_{m_2} \sum_{m'_0} \sum_{m'_1} \sum_{m'_2} \Big(|J_0 m_0\rangle\langle J_1 m_1| \Big)_j \Big(|J_1 m'_1\rangle\langle J_0 m'_0| \Big)_{j'} \\
& \sum_\alpha \sum_\beta \sum_\gamma \sum_\delta (\langle J_0 m_0|\mathbf{a}_j|J_2 m_2\rangle)_\alpha (\langle J_2 m_2|\mathbf{a}_j|J_1 m_1\rangle)_\beta (\langle J_1 m'_1|\mathbf{a}_{j'}|J'_2 m'_2\rangle)_\gamma (\langle J'_2 m'_2|\mathbf{a}_{j'}|J_0 m'_0\rangle)_\delta \\
& \left[\frac{1}{N} \sum_{\mathbf{k},\sigma} (\hbar\omega_{\mathbf{k},\sigma})^2 (\mathbf{u}_{\mathbf{k},\sigma})_\alpha (\mathbf{u}_{\mathbf{k},\sigma})_\beta (\mathbf{u}_{\mathbf{k},\sigma})_\gamma (\mathbf{u}_{\mathbf{k},\sigma})_\delta \, \hat{n}_{\mathbf{k},\sigma} \sin\left(2\mathbf{k}(\mathbf{R}^{(0)}_{j'} - \mathbf{R}^{(0)}_j) \right) \right].
\end{aligned}
\tag{69}
$$

In this case the only destructive interference comes from the symmetry of the Brillouin zone for a term proportional to $\sin\left(2\mathbf{k}(\mathbf{R}^{(0)}_{j'} - \mathbf{R}^{(0)}_j) \right)$ that is independent of the number of phonons present. In this model we have a candidate mechanism with a good chance of connecting with our experiments, as long as the off resonant shift of the basis state energies is substantial.

6.6. Discussion

We have as yet not worked out off-resonant nuclear potential models, although this is currently at the top of our list of projects to address. Were we to focus on the older meson exchange models (Hamada–Johnston potential [24], Reid potential [25], Argonne potential [26], etc.), then it might be possible to develop off-resonant extensions of individual terms that appear in the models based on arguments about the interactions involved and the number of mesons exchanged. However, since the older models are empirical this kind of extension comes with issues associated with the extension. If we focus on the newer chiral effective field theory models [27,28], then the proposed extension is much simpler (at least at low order) and better defined since the chiral effective field theory model itself is simpler.

It would be possible to augment our relativistic Dirac–Fock code to evaluate electronic shifts off of resonance based on the off-resonant version of the Breit interaction in this section.

The indirect interactions for models with off-resonant shifts of the basis state energies are impacted by destructive interference effects much less if the shifts are large (much greater than the maximum phonon energy). We have given the interaction for the M1

single mode case, and the other cases with two modes and three modes behave similarly. These models have the best chance of being able to account for our experimental results, and will be the focus of our studies in the near future.

Note that a shift of the basis state energies off of resonance would have the potential to greatly increase the indirect coupling matrix element associated with up-conversion and down-conversion.

7. Issues Raised in the ^{57}Co Experiments

As mentioned above in May 2017 we observed non-exponential decay effects in experiments where radioactive ^{57}Co was evaporated on a steel sample and mechanical stress was applied [10]. In subsequent experiments we have sought to develop an understanding, and in the process a number of issues have emerged. In this section we focus on a subset of the issues.

7.1. Angular anisotropy

We see in Fig. 1 that following the beta decay of ^{57}Co that the 136.5 keV state of ^{57}Fe is populated, resulting in energetic gammas at 136.5 keV and at 122.1 keV. We have seen non-exponential decay effects associated with these lines [10,13], which we have interpreted as due to a (dynamic) angular anisotropy resulting from resonant excitation transfer.

In the simplest possible relevant excitation transfer model, we consider an excited state ^{57}Fe nucleus in a local BCC lattice made up of ^{57}Fe nuclei (corresponding to a simplistic picture of the residue on the surface of the steel). In a model with excitation transfer only to the eight nearest neighbors, the maximum probability amplitude c_{max} at the nearest neighbors satisfies

$$\sqrt{8}|c_{max}| = \sqrt{8}\frac{2|V_{indirect}|}{\hbar\gamma}, \tag{70}$$

where $V_{indirect}$ is the indirect coupling matrix element from the initial excited ^{57}Fe nucleus to a nearest neighbor, and where γ is the decay rate of the excitation. A dynamical model for the simpler two-site case is described in Appendix B. To be consistent with the experimental results, we would need for $\sqrt{8}|c_{max}|$ to be on the order of 0.1 or so, from which we might estimate the indirect coupling matrix element to be on the order of

$$|V_{indirect}| \rightarrow \frac{1}{2}\,0.1\,\hbar\gamma = 1.6\times 10^{-8}\text{ eV}. \tag{71}$$

The associated theoretical problem is that generally the estimates from the models described in the previous sections lead to indirect coupling matrix elements that are much smaller than this. The thought is that models based on the shift in basis state energies off of resonance probably have the best chance of achieving consistency, but much work remains to develop a reliable estimate from the models.

7.2. Variation of the incremental 14.4 keV gamma to Fe K_α ratio

In the first observation of non-exponential decay effects in May 2017 we saw a roughly 19% increase in the 14.4 keV emission, and a roughly 17% increase in the Fe K_α emission [10]. In subsequent experiments we have seen different incremental ratios: in some cases the incremental 14.4 keV gamma intensity was greater than 19/17 times the incremental Fe K_α X-ray intensity, and in other cases the incremental Fe K_α intensity was more than twice the incremental 14.4 keV gamma intensity. Air absorption causes a reduction the lower energy Fe K_α X-ray intensity, and when using a thermal pulse for stimulation the air absorption is reduced a small amount, which complicates the analysis of the data. Nevertheless, it appears that this incremental ratio is showing an unexpected variation in our experiments, and that this effect may be important.

One potential route toward an explanation is to note that in perturbation theory there are new decay channels available in which the energy from one 14.4 keV excitation can be dissipated at two sites through two internal conversion processes in some of the off-resonant states producing two K-shell holes instead of one. This can lead to an increase in the incremental Fe K_α intensity relative to the incremental 14.4 keV gamma intensity. Some discussion of internal conversion in connection with excitation transfer is given in Appendix C.

7.3. Changes in the 14.4 keV gamma intensity

In January 2018 an experiment was done with our Sample 2 in which a thermal pulse was used to create incremental mechanical stress, and an X-ray detector monitored emission from all of the evaporated region with no mesh blocking the signal. In this case we saw a decrease in the 14.4 keV intensity. This observation permits an interpretation that some of the excitation is transferring into the steel so that the subsequent gamma emission is absorbed.

In late Spring 2018 we carried out a version of this experiment with our Sample 1, hoping to see a similar result. Instead we saw an increase in the 14.4 keV gamma intensity [13]. The difference in the results tells us that the two samples behave very differently, a conclusion that is consistent with many other experiments (our Sample 2 in general tends not to do very much for us). In other experiments where a mesh or pinhole was used, we had been thinking that a delocalization of the excitation could account for an increase or decrease in intensity. However, for these experiments no mesh or pinhole was used.

It might be argued that angular anisotropy might play some role for the 14.4 keV transition; however, in other experiments we have not seen much evidence for angular anisotropy on this line. In both cases there is a qualitatively similar response of the Fe K_α, which cannot show angular anisotropy.

In upcoming experiments we need to use the HPGe detector to monitor the harder gammas at the same time as the 14.4 keV line to clarify whether we might be seeing a subdivision effect (in which the excitation of the 136.5 keV state is divided between several 14.4 keV states, with the dissipation of the left over energy).

7.4. Coincidence measurements

In previous years when we were studying models for up-conversion and for down-conversion, we found that the coupled quantum system seemed to avoid the occupation of states which decayed rapidly, and seemed to favor states with no open decay channels. The conclusion was that in this kind of system one would expect a net reduction in the decay rate over what might be expected if this effect did not occur. In these models we assumed that decay channels would generally be closed for basis states far off of resonance where the basis state energy exceeded the energy eigenvalue.

If we are seeing changes in the incremental 14.4 keV to Fe K_α ratio, then it is possible that this indicates significant occupation of off-resonance states. If so, then it may be that the decay channels are closed for some of the off-resonant states. Consequently we are motivated to consider coincidence experiments in which we monitor to see whether the 14.4 keV gamma arrives within a window of 100 ns or so following the initial beta decay of the ^{57}Co. A coincidence experiment with a properly set acceptance window has the potential to address this issue.

The beta decay of the ^{57}Co occurs with the absorption of a K-shell electron, leaving a K-shell hole in the newly formed ^{57}Fe daughter. Consequently, some of the time we will get a prompt Fe K_α that could be used to trigger the start of an acceptance window in time. The half-life of the 136.5 keV state is 8.7 ns, so that we could instead make use of the 122.1 keV gamma for triggering. In either case a time window near 100 ns would get most of the 14.4 keV emission (the half-life of the 14.4 keV state is 98.3 ns). If the rate of 14.4 keV gammas detected in this window were to drop with mechanical stimulation, and if the rate of 14.4 keV gammas arriving later were to correspondingly increase, then this could indicate that the half-life of the 14.4 keV state was increased. We are considering an experiment of this kind in the coming months.

7.5. Delocalization

Lu took pinhole camera images of the ^{57}Co residue, which showed that the emission was strongest in a ring around the edge of the residue with a "hot spot" evident where the ^{57}Co had collected preferentially [13]. In subsequent experiments with a pinhole and Amptek SDD X-ray detector, the time history of different parts of the ring and hot spot were monitored during thermal stimulation under stress. In the vicinity of the "hot spot" we saw the largest increase in intensity for the 14.4 keV gamma and for the Fe K_α X-ray. In other places we saw lesser increases, and in one location distant from the "hot spot" we saw a decrease in emission. These observations permit an interpretation of a delocalization of the excitation in the residue [13]. In connection with these experiments we have proposed that our radioactive ^{57}Co source contains much ^{57}Fe, and that the residue observed in optical photographs is primarily ^{57}Fe on the surface of the steel (this was suggested by Malcolm Fowler).

This observation focuses our attention on fourth-order indirect interactions for excitation transfer where the interaction can be delocalized.

8. Possibility of E1 Excitation Transfer Experiments

As discussed above, excitation transfer for E1 transitions is accounted for in perturbation theory through a second-order interaction, while excitation transfer for M1 transitions appears as a fourth-order interaction. Note that we would expect a fourth-order interaction in general to be much weaker than a second-order interaction when the coupling is weak. In our excitation transfer experiments with a ^{57}Co source on steel we have seen striking unexpected non-exponential decay effects, involving primarily M1 transitions for the 14.4 keV state and for the 136.5 keV state. This provides motivation for pursuing excitation transfer studies with E1 transitions, which may show a stronger version of the effects.

8.1. Radioactive sources

To develop an analogous excitation transfer experiment for an E1 transition, the big issue has to do with the procurement of a relevant radioactive source. The low energy E1 transitions and potential source isotopes are listed in Table 3. The most interesting candidate E1 transition is the 6.237 keV transition in ^{181}Ta, for which potential sources might be ^{181}Hf and ^{181}W, where ^{181}W is the better choice as it is more efficient in populating the 6.237 keV state. Unfortunately it does not seem possible to obtain ^{181}W from a supplier at this time.

Table 3. Radioactive sources that might be used to produce excited states for E1 transitions.

Isotope	E(keV)	Source (Z-1)	Half-life	Source (Z+1)	Half-life
Ta-181	6.237	Hf-181	42.4 d	W-181	121 d
Dy-161	25.65135	Tb-161	6.90 d	Ho-161	2.48 h
Gd-157	63.929	Eu-157	15.13 h	Tb-157	150 y
Dy-161	74.56668	Tb-161	6.90 d	Ho-161	2.48 h
Gd-155	86.5479	Eu-155	4.9 y	Tb-155	5.3 d
Eu-153	97.43100	Sm-153	46.8 h	Gd-153	241.6 d
Dy-161	103.062	Tb-161	6.90 d	Ho-161	2.48 h
Gd-155	105.3083	Eu-155	4.9 y	Tb-155	5.3 d
F-19	109.9	O-19	26.9 s	Ne-19	17.3 s
Dy-161	131.8	Tb-161	6.90 d	Ho-161	2.48 h
Eu-153	151.6245	Sm-153	46.8 h	Gd-153	241.6 d

The half-life for sources with mass 161 are too short to be useful. At mass 157 we see ^{157}Tb with a long half-life, but when it decays to ^{157}Gd very little (0.34%) population of the 63.9 keV excited state occurs. For mass 155 we see ^{155}Eu with a 4.9 year half-life, which appears to be available as a radioactive source from suppliers. The fraction of the decays that go directly to the 86.5 keV second excited state is 26%, which looks good. At mass 153 ^{153}Gd looks to have a usefully long half-life, the fraction of decays that go to the 97.3 keV state is 37%, and ^{153}Gd appears to be available as a radioactive source.

8.2. Nuclear Bragg scattering with resonant excitation transfer

For low-energy nuclear transitions for which no commercially available radioactive sources are available the question arises as to whether there is some other route to the detection of phonon-induced nuclear excitation transfer. Instead of populating nuclear excited states following beta decay, we might consider exciting them directly with narrow band synchrotron radiation. The use of narrow band radiation from synchrotron sources for applications involving low energy nuclear transitions is reviewed in Refs. [29–31]. A variety of experimental techniques have been pioneered to observe nuclear Bragg scattering, hyperfine effects from oscillations of the scattered signal, phonon interactions, diffusion, and a variety of other effects as well.

The question of interest here is whether resonant excitation transfer might be observed in a nuclear Bragg scattering experiment. Consider a simple model for the vector potential for the scattered wave in the far field which we might write as

$$\hat{A}_z(\mathbf{r}) \;\to\; -i\omega \frac{\mu_0}{4\pi|\mathbf{r}|} \, e^{ikr} \sum_j d_j e^{-i\mathbf{k}\cdot\mathbf{r}_j} \tag{72}$$

with scattered wave vector $\mathbf{k}$, assuming z-polarized incident light with the z-directed dipole moment d_j associated with nucleus j. For simple Bragg diffraction with no phonon exchange and no excitation transfer the induced dipole moments are phase dependent according to

$$d_j = d_0 e^{i\mathbf{k}_0\cdot\mathbf{r}_j} \tag{73}$$

with incident wave vector $\mathbf{k}_0$. We might model resonant excitation transfer as involving a modification in which the nuclear dipole moment acquires contributions from coupling with other sites according to

$$d_j = d_0 e^{i\mathbf{k}_0\cdot\mathbf{r}_j} + \sum_l d_{j,l} \, e^{i\mathbf{k}_0\cdot\mathbf{r}_l}, \tag{74}$$

where $d_{j,l}$ accounts for the contribution to the nuclear dipole moment at site j due to resonant excitation transfer from site l. The phase factors associated with resonant excitation transfer in this model are consistent with the dynamical model discussed in Appendix B. In this case we can write for the ratio of the part of the diffracted intensity due to excitation transfer relative to the unperturbed diffracted intensity

$$\frac{\Delta I}{I} = \frac{\sum_{j,j',l} d_{j',l}^* d_0 e^{i(\mathbf{k}_0-\mathbf{k})\cdot\mathbf{r}_j} e^{-i\mathbf{k}_0\cdot\mathbf{r}_l} e^{i\mathbf{k}\cdot\mathbf{r}_{j'}} + \sum_{j,j',l} d_{j',l} d_0^* e^{-i(\mathbf{k}_0-\mathbf{k})\cdot\mathbf{r}_j} \, e^{i\mathbf{k}_0\cdot\mathbf{r}_l} e^{-i\mathbf{k}\cdot\mathbf{r}_{j'}}}{|d_0|^2 \sum_{j,j'} e^{i(\mathbf{k}_0-\mathbf{k})\cdot(\mathbf{r}_j-\mathbf{r}_{j'})}}. \tag{75}$$

This can be rewritten in the form

$$\frac{\Delta I}{I} = \frac{\left[\sum_j D_j e^{i(\mathbf{k}_0-\mathbf{k})\cdot\mathbf{r}_j}\right]^*}{d_0^* \left[\sum_j e^{i(\mathbf{k}_0-\mathbf{k})\cdot\mathbf{r}_j}\right]^*} + \frac{\left[\sum_j D_j e^{i(\mathbf{k}_0-\mathbf{k})\cdot\mathbf{r}_j}\right]}{d_0 \left[\sum_j e^{i(\mathbf{k}_0-\mathbf{k})\cdot\mathbf{r}_j}\right]}, \tag{76}$$

where we have defined the D_j according to

$$D_j = \sum_l d_{j,l} e^{i\mathbf{k}_0\cdot(\mathbf{r}_l-\mathbf{r}_j)}. \tag{77}$$

The conclusion from this simple model is that resonant excitation transfer may be observable as a change in the intensity of the Bragg peaks.

It seems from the literature that the 14.4 keV transition in ^{57}Fe has been most studied, at least in the early experimental work. Given that our excitation transfer experiments have focused primarily on this transition, it would seem that if experiments as proposed here are pursued, they should probably focus first on establishing the existence of such an effect with the 14.4 keV transition. Afterward, similar experiments on other transitions would be of interest.

One of the most interesting non-iron candidates is the 6.237 keV transition in ^{181}Ta since it is the lowest energy accessible E1 transition, and has the potential to address numerous theoretical issues. The big headache with this transition is that it is normally very weak in Mössbauer experiments since radiative decay is much slower than internal conversion. Nevertheless, this transition has been studied with synchrotron radiation (see Refs. [32–34]). The energy of the line was determined in Ref. [32] to be 6.214 ± 2 keV, which is an improvement over previous determinations. We have used 6.237 keV in this paper consistent with the BNL Nudat2 database energy level, which has not been updated with this revised value.

9. Excitation Transfer from D$_2$/^{4}He and HD/^{3}He

One of our earliest proposals for excitation transfer in connection with experiments in Condensed Matter Nuclear Science [5] concerned a candidate explanation for low-level energetic alpha emission from thin film palladium deuterated through ion bombardment by Chambers et al. [35]. We proposed excitation transfer of a large 24 MeV quantum from the nuclear system D$_2$/^{4}He to a Pd
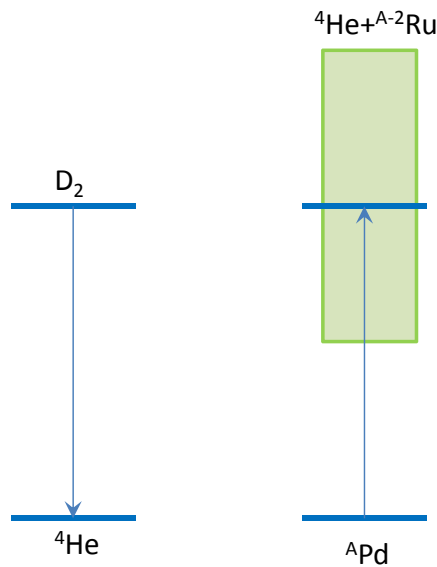
Figure 2. Excitation transfer from a D_2/^{4}He reaction to ionize an alpha particle from a Pd nucleus.

ground state nucleus of the host lattice, as illustrated in Fig. 2. We do not expect a Pd nucleus to have any long-lived excited state in the vicinity of 24 MeV; consequently, this kind of excitation transfer would be an incoherent process.

The initial excitation transfer would create a highly excited compound state [36] which subsequently decays through all available decay channels. Consequently we would expect to see neutron and proton emission as well, and perhaps decays involving heavier products with reduced probabilities. This kind of incoherent excitation transfer process can be described simply within the dynamical model discussed in Appendix B.

Whether this theoretical conjecture concerning excitation transfer is correct or not has at this point not been settled. Unfortunately there has not been a subsequent confirmation of the 21 MeV alpha emission reported in Ref. [35]. On the other hand there have been subsequent reports of energetic alphas (see e.g. [37–41]) as well as energetic neutrons (see Refs. [42,43]). The energetic neutron emission in these latter references is discussed in the context of D+T fusion neutrons; however, as was pointed out earlier the flux of energetic neutrons seems inconsistent with a D+T fusion mechanism [44], which motivates us to consider here an excitation transfer mechanism.

9.1. Alpha energies from D_2/^{4}He excitation transfer

Of interest is whether there might be some way to prove whether excitation transfer is responsible for energetic alpha emission. One possibility might be to test whether the emitted alpha energy for excitation transfer involving different host lattices matches theory. In Fig. 3 we show the reaction energy and ejected alpha energy including recoil as a function of the nuclear mass A. We see that the ejected alpha energy does depend on the host lattice, and that clarification could be obtained if it were possible to establish a relation between the ejected alpha energy and the nuclear mass of the host lattice.

9.2. Neutron energies from D_2/^{4}He excitation transfer

Making the case above based on the observation of alpha particles suffers from the complication that alphas created inside a cathode lose energy before making it out of the cathode. Neutrons resulting from incoherent excitation transfer would not be expected to
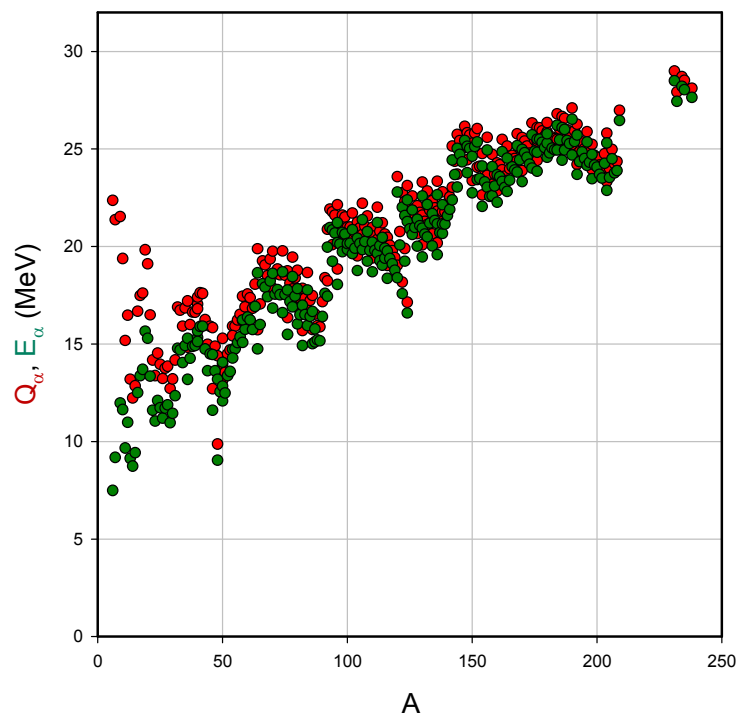
Figure 3. Overall reaction energy (*red*) and ejected alpha energy E_α (*green*) as a function of the initial nuclear mass number A.

lose much energy, and could therefore provide a potentially more faithful diagnostic. The reaction and neutron ejection energy as a function of nuclear mass is shown in Fig. 4.

Plastic track detectors have proven useful for the detection of low-level alpha emission, since they time integrate the signal and are free of electrical noise. These same detectors have been used for low-level neutron emission; however, in this case they suffer from a very low yield, and as yet there does not seem to be a reliable energy calibration in use within our field. Likely a new experiment will be needed with a more standard energy-resolving neutron detector and a source with a higher neutron emission rate.
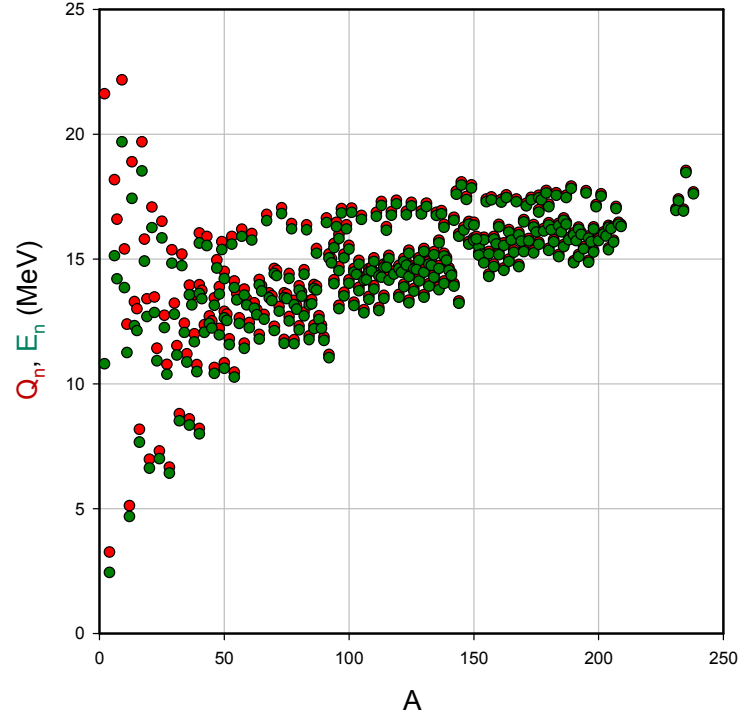
9.3. Alpha energies from HD/^{3}He excitation transfer

It has long been speculated that HD/^{3}He transitions are responsible for excess heat in the light water experiments; however, at this point there has not been reported any measurements correlating ^{3}He with the energy produced. If HD/^{3}He transitions occur, we might expect to see low-level nuclear emissions resulting from incoherent excitation transfer reactions. In this subsection we consider this possibility.

In Fig. 5 we show the reaction energy and expected alpha energy resulting from excitation transfer as a function of the nuclear mass number A. We see some low energy alphas for nuclei with A on the order of 20 or less, then a gap, and then an increasing alpha energy above mass 60. Not included in this figure are estimates of the associated tunneling factors for the ejected alpha through the Coulomb barrier, which if included would lead to vanishingly low ejection probabilities for all points shown above mass 60.

We draw attention to the low-level alpha emission reported by Storms and Scanlan [45] as perhaps being a result of incoherent excitation transfer from the HD/^{3}He transition to low mass nuclei impurities in the host copper metal (which could account for

Figure 4. Overall reaction energy (*red*) and ejected neutron energy (*green*) as a function of the initial nuclear mass number *A*.

alpha emission at a few MeV, but not by itself for the energy shifts reported).

9.4. Neutron energies from HD/^{3}He excitation transfer

Neutron emission resulting from excitation transfer in the case of the HD/^{3}He transition offers the possibility of both gaining evidence for the existence of an excitation transfer effect, and for the possibility that HD/^{3}He transitions can occur. The reaction energy and the ejected neutron energy is shown in Fig. 6 as a function of the nuclear mass number *A*.

9.5. Proton energies from HD/^{3}He excitation transfer

We conclude this brief discussion by considering proton energies expected in the case of incoherent excitation transfer from HD/^{3}He. The reaction energies and ejected proton energies are shown as a function the nuclear mass number *A* in Fig. 7. We note that because the HD/^{3}He transition energy (5.49 MeV) is not so large, and generally the proton binding energy tends to be larger, there are only a few nuclei from which one would expect proton ejection. In the figure we see one isotope (^{6}Li) at low mass number and a few at higher mass number, the latter of which have negligible probability of transmission through the Coulomb barrier.

Consequently, our interest in this discussion is focused on the singular case of proton emission for ^{6}Li based on an excitation transfer reaction which we might write as

$$\left[\text{H+D} \; \rightarrow \; {}^3\text{He} + 5.49 \text{ MeV} \right] + \left[{}^6\text{Li} \; \rightarrow \; \text{p} + {}^5\text{He} - 4.43 \text{ MeV} \right] \; + \; 1.06 \text{ MeV}$$
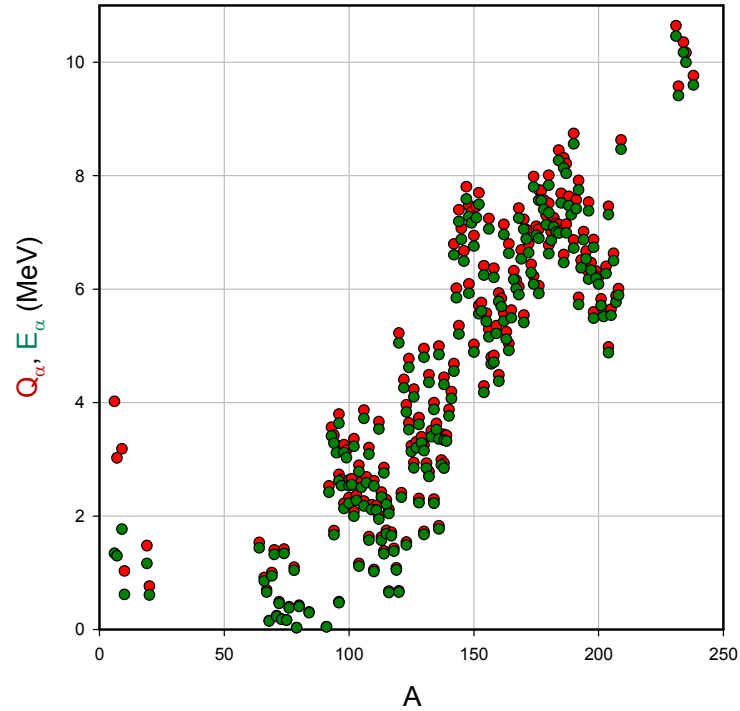
Figure 5. Overall reaction energy (*red*) and ejected alpha energy (*green*) as a function of the initial nuclear mass number A.

leading to an ejected proton energy of 0.88 MeV. We conclude that the observation of proton emission at 0.88 MeV from a lithium sample with H and D present could be argued to support the existence of the corresponding excitation transfer reaction.
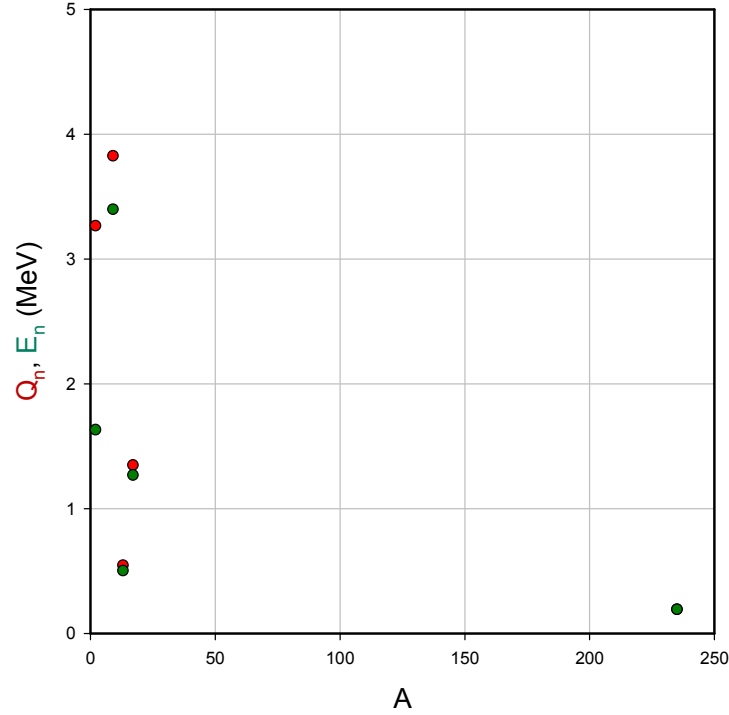
9.6. Proton emission in the Lipinski experiment

Many years of experimentation with proton beams on lithium targets, and on glow discharge experiments with hydrogen gas and lithium present, have been documented in Refs. [46,47]. In [47] an experiment is described in which a proton gun is used to irradiate a lithium foil at an energy of a few hundred eV, and that a strong proton signal (identified as "backscattered" protons) is observed at an energy of 0.79 MeV. The data shown in [47] is redrawn in Fig. 8.

Note that the loss of a proton from ^{6}Li would produce a ^{5}He daughter which decays immediately according to

$$^5\text{He} \ \rightarrow \ \text{n}(0.59 \text{ MeV}) + {}^4\text{He}(0.15 \text{ MeV}).$$

If these protons are due to excitation transfer, then we might expect to see additional lower energy neutrons and alphas. Note that in the documentation of [47] a brief discussion of neutron detection is given, with the conclusion that no neutrons are detected in connection with the experiment (it is not clear from the documentation whether the neutron detection used would have been sensitive to 0.59 MeV neutrons).

Figure 6.   Overall reaction energy (*red*) and ejected neutron energy as a function of the initial nuclear mass number *A*.

9.7. Alpha emission in the Lipinski experiment

In the same experiment where the proton signal mentioned above was observed, it was reported that energetic alphas were seen near 8.5 MeV. The reported spectrum is redrawn in Fig. 9.

The authors attribute the energetic alpha signal to the H(^{7}Li,α)α reaction (due to a greatly enhanced fusion cross section at the few hundred eV of the incident proton beam). We might write this reaction as

$$H + {}^7Li \; \rightarrow \; {}^4He \; (8.67 \; MeV) + {}^4He \; (8.67 \; MeV)$$

from which it is clear that the alpha energy that results could be consistent with the data of Fig. 9.

We contemplated the possibility of H(^{7}Li,α)α reactions due to the 0.79 MeV protons measured above, but the associated fusion cross section is too low to obtain quantitative agreement.

This motivated us to consider an excitation transfer reaction based on the D$_2$/^{4}He transition to ^{7}Li, which we might denote according to

$$\left[D+D \; \rightarrow \; {}^4He + 23.85 \; MeV \right] + \left[{}^7Li \; \rightarrow \; T + {}^4He - 2.47 \; MeV \right] + 21.38 \; MeV.$$

The alpha energy including recoil for this excitation transfer reaction comes out to 9.19 MeV, which is a bit higher than the reported peak energy. Note however that the emission is broad, with an upper end point above 9 MeV. It would be possible to obtain consistency under the assumption that some energy loss in the lithium occurs. The ratio of the energetic alpha emission to proton
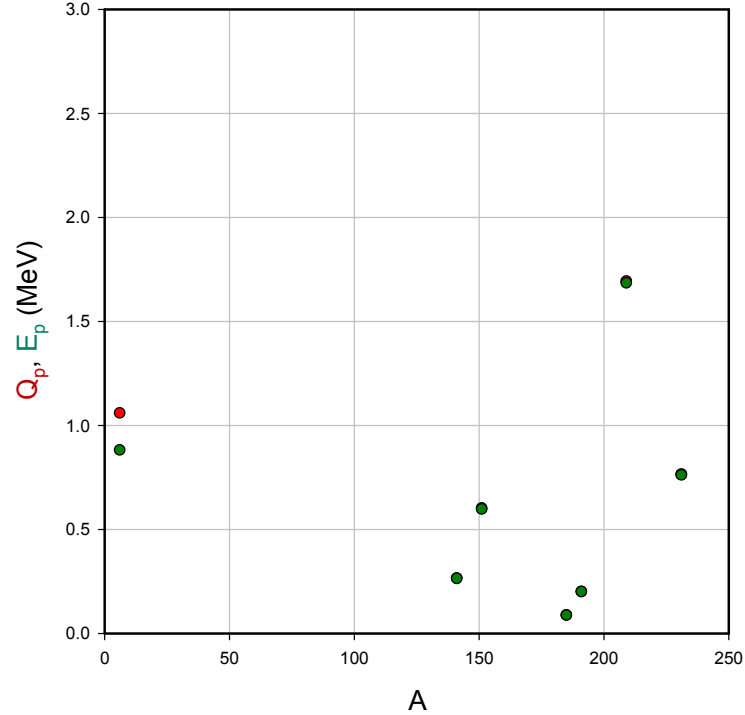
Figure 7. Overall reaction energy (*red*) and ejected proton energy (*green*) as a function of the initial nuclear mass number *A*.

emission is not too far from the natural isotopic ratio of D to H, as would be expected for this mechanism. According to this excitation transfer reaction proposal we would expect to see energetic tritons at higher energy. There is no mention of such higher energy signals in [47], and the upper energy cut-off of the charged particle detector is too low to see them.

10. Discussion

As we discussed in the Introduction, excitation transfer plays a central role in the phonon-based theory that we have pursued for many years, and is implicated in unexpected non-exponential decay that we have seen in experiments with ^{57}Co in our lab. A major goal of our current research is to work toward the development of theoretical models that can be used to compare directly with experiment, or at least as much as possible. Here we report on recent theoretical results based on the relativistic phonon-nuclear coupling interaction that we identified a few years ago.

We discussed the indirect interaction for resonant excitation transfer in the case of E1 and M1 transitions, from second-order and from fourth-order perturbation theory. This kind of calculation corresponds to the most straightforward application of perturbation theory to the models, based on the relativistic phonon-nuclear interaction. We knew beforehand that destructive interference leads to a small effect for the E1 case which we had analyzed previously. Prior to this study it was unclear whether destructive interference would similarly impact the M1 case – the supposition was that it should, but an erroneous preliminary result suggested that there was some hope that this case might avoid some or most of the destructive interference. From the results of substantial calculations briefly summarized above, we now know that the resonant contribution to the fourth-order interaction relevant to excitation transfer is strongly reduced by destructive interference. The resulting interaction is much too small to connect meaningfully with our
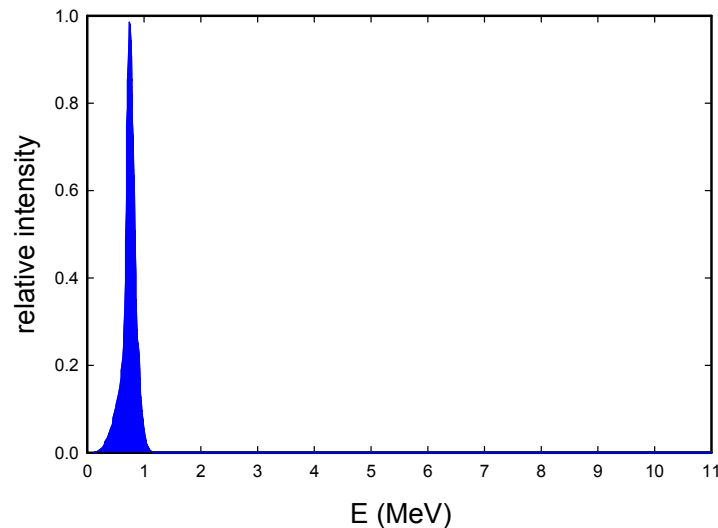
Figure 8.   Proton spectrum from experiment #13 from the second Lipinski patent application. The peak location is given as 790 keV, and the peak area is given as 4.2×10^7 counts. The associated count rate is 4.46×10^5 cps.

experimental results.

Destructive interference similarly hinders up-conversion and down-conversion, and we found in 2002 that in models augmented with loss that the destructive interference could be reduced or eliminated. For this problem loss comes in again and again, and the effects are in this way "amplified"; unlike in the case of excitation transfer where loss has a weaker impact. We discussed briefly above the effect of loss on excitation transfer in both E1 and M1 cases, and it is clear that when a relevant THz phonon mode is highly-excited the indirect interaction can be greatly increased. However, it seems unlikely that the indirect interaction that results can be sufficiently large to account for the experimental results. If the experimental results are a result of excitation transfer, then there must be some new additional effect that we have not considered previously.

In the course of writing this paper it became clear that a possible solution to the problem might lie in the variation of the basis state energies that would be expected off of resonance. Developing expressions for the indirect interaction for this kind of model is completely straightforward; however, the quantification of the resulting interactions depends critically on how large the basis state energy shifts are off of resonance. It is possible to make a good argument for the existence of the effect. In the discussion above we outlined a simple argument for it based on the sector decomposition associated with Brillouin-Wigner perturbation theory. In this approach the nucleon-nucleon interaction itself changes off of resonance. To compute the needed energy shifts, one needs to specify the off-resonant extension of the nucleon-nucleon interaction, and then make use of it for nuclear structure calculations. All in all, a big project which we hope to address in the future.

We have evaluated the off-resonant extension of the Breit interaction associated with transverse photon exchange in the Coulomb gauge, which can be used to evaluate the electronic energy shift for atoms and ions off of resonance. The existence of a pole on the k-axis in the result suggests that there might be an associated radiative decay channel; however, for one of the integrals that we are able to evaluate analytically the contribution of the pole turns out to be real, which rules out such a decay channel for this term. More work is needed to clarify whether the pole in the other integral produces an imaginary contribution.

We also outlined recent thoughts as to how the theoretical models connect with our recent excitation transfer experiments. In the experiments we see an angular anisotropy effect associated with the harder gammas, which could be consistent with excitation transfer to nearby nuclei. Within this interpretation it is possible to develop a rough estimate for the indirect coupling matrix
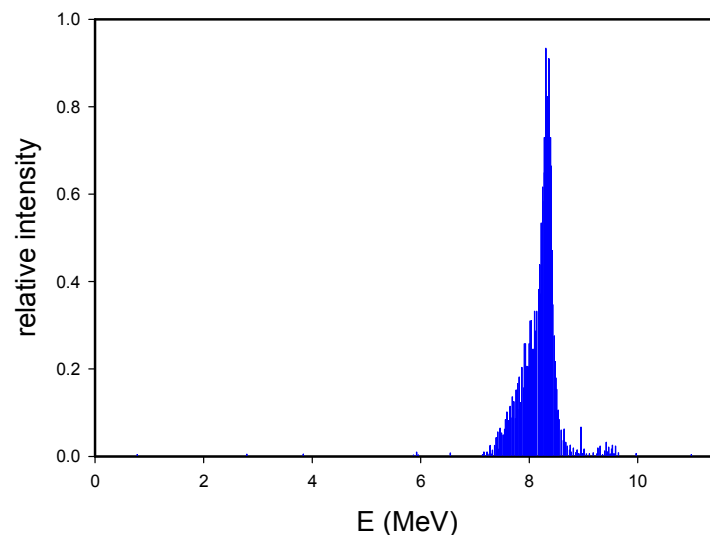
Figure 9. Alphas spectrum from experiment #13 from the second Lipinski patent application. The peak location is given as 8.5 MeV keV (it is closer to 8.3 MeV from the reconstruction in this figure), and the peak area is given as 1.5×10^4 counts. The associated count rate is given as 157 cps.

element. We also see what appears to be a delocalization effect, which may be consistent with the delocalized excitation transfer we see in the models. However, in both cases we are going to need estimates for the off-resonant basis energy shifts to have any hope of quantitative agreement between theory and experiment. Note that what phonon modes are excited, and by how much, is not available in current experiments.

We would very much like to extend the experiments to excitation transfer in E1 transitions. Radioactive sources appear to be available for some higher energy E1 transitions. But what we might learn much more from are excitation transfer experiments with the 6.237 keV transition in ^{181}Ta, for which the relevant radioactive source ^{181}W is currently unavailable from suppliers. This has motivated us to consider new experiments in which excitation transfer might be observed through a modification of the relative Bragg peak intensities in experiments with narrow band synchrotron radiation. Given the large expense associated with synchrotron experiments, such experiments may not be possible any time soon; nevertheless, it seems worthwhile to contemplate such experiments at this time. Note that if such experiments are pursued, it would make sense to demonstrate excitation transfer on the 14.4 keV transition in ^{57}Fe first, since this transition is easier to work with and better studied.

A brief discussion of incoherent excitation transfer reactions based on $D_2/^4$He transitions and HD/^{3}He transitions was given. The idea is that some of the low-level nuclear emissions observed in experiments with PdD may be a result of excitation transfer. Even though the theoretical proposal was put forth in 2000, eighteen years later there has been no confirmation or rejection of this conjecture. One way to sort this out might be to seek a correlation between the emitted particle energy and the masses of the host lattice nuclei. Although we have been thinking about similar emissions driven by the HD/^{3}He transition, it was only recently that we understood that the low-level few MeV alpha emission reported by Storms and Scanlan might be a result of incoherent excitation transfer from the HD/^{3}He transition.

The interesting observations reported by Lipinski and Lipinski have attracted the attention of X. Z. Li in recent years [48]. During the past year it has become clear that incoherent excitation transfer reactions might be involved in the case of the 0.79 MeV proton signal and 8.5 MeV alpha signal reported.

Appendix A. Indirect Interaction for Three Modes

We would generally expect a three-mode interaction to be associated with phonon scattering, rather than with resonant excitation transfer. However, there are conditions under which the three-mode interaction can mediate resonant excitation transfer; for example, when there are three distinct very highly excited modes with surrounding modes unexcited.

As discussed in the text we focused on a particular example in which a phonon from one mode $(\mathbf{k}, \sigma)$ is created by one nucleus and absorbed by the other, where a phonon from another mode $(\mathbf{k}', \sigma')$ is created, and where a phonon from a third mode $(\mathbf{k}'', \sigma'')$ is destroyed. The indirect interaction is resonant if the frequencies of the latter two modes are the same.

As discussed in the main text the contribution to the resonant indirect interaction is

$$\left(\hat{V}(E - \hat{H}_0)^{-1}\hat{V}(E - \hat{H}_0)^{-1}\hat{V}(E - \hat{H}_0)^{-1}\hat{V} \right)_{\text{resonant}} \rightarrow T_1' + \cdots + T_8'. \tag{A.1}$$

The different contributions $T_1' \cdots T_8'$ are given by

$$T_1' = \frac{(Mc^2)^2}{4} \sum_{J_2} \sum_{J_2'} \frac{2}{(E_1 - E_0)^2(E_2 - E_1)(E_2' - E_1)}$$

$$\sum_{j} \sum_{j'} \sum_{m_0} \sum_{m_1} \sum_{m_2} \sum_{m_0'} \sum_{m_1'} \sum_{m_2'} \left(|J_0 m_0\rangle \langle J_1 m_1| \right)_j \left(|J_1 m_1'\rangle \langle J_0 m_0'| \right)_{j'}$$

$$\langle J_0 m_0 | \mathbf{a}_j | J_2 m_2 \rangle \cdot \left[\frac{1}{N} \sum_{\mathbf{k},\sigma} (\hbar\omega_{\mathbf{k},\sigma})^2 \mathbf{u}_{\mathbf{k},\sigma} \mathbf{u}_{\mathbf{k},\sigma} \cos\left(\mathbf{k} \cdot (\mathbf{R}_{j'}^{(0)} - \mathbf{R}_j^{(0)}) \right) \right] \cdot \langle J_2' m_2' | \mathbf{a}_{j'} | J_0 m_0' \rangle$$

$$\langle J_2 m_2 | \mathbf{a}_j | J_1 m_1 \rangle \cdot \left[\sum_{\mathbf{k}',\sigma'} \sqrt{\hbar\omega_{\mathbf{k}',\sigma'}} \mathbf{u}_{\mathbf{k}',\sigma'} \sqrt{\hat{n}_{\mathbf{k}',\sigma'} + 1} e^{-i\mathbf{k}'\cdot\mathbf{R}_j^{(0)}} \right]$$

$$\langle J_1 m_1' | \mathbf{a}_{j'} | J_2' m_2' \rangle \cdot \left[\sum_{\mathbf{k}'',\sigma''} \sqrt{\hbar\omega_{\mathbf{k}'',\sigma''}} \mathbf{u}_{\mathbf{k}'',\sigma''} \sqrt{\hat{n}_{\mathbf{k}'',\sigma''}} e^{i\mathbf{k}''\cdot\mathbf{R}_{j'}^{(0)}} \right], \tag{A.2}$$

$$T_2' = \frac{(Mc^2)^2}{4} \sum_{J_2} \sum_{J_2'} \frac{2}{(E_1 - E_0)^2(E_2 - E_1)(E_2' - E_0)}$$

$$\sum_{j} \sum_{j'} \sum_{m_0} \sum_{m_1} \sum_{m_2} \sum_{m_0'} \sum_{m_1'} \sum_{m_2'} \left(|J_0 m_0\rangle \langle J_1 m_1| \right)_j \left(|J_1 m_1'\rangle \langle J_0 m_0'| \right)_{j'}$$

$$\langle J_0 m_0 | \mathbf{a}_j | J_2 m_2 \rangle \cdot \left[\frac{1}{N} \sum_{\mathbf{k},\sigma} (\hbar\omega_{\mathbf{k},\sigma})^2 \mathbf{u}_{\mathbf{k},\sigma} \mathbf{u}_{\mathbf{k},\sigma} \cos\left(\mathbf{k} \cdot (\mathbf{R}_{j'}^{(0)} - \mathbf{R}_j^{(0)}) \right) \right] \cdot \langle J_1 m_1' | \mathbf{a}_{j'} | J_2' m_2' \rangle$$

$$\langle J_2 m_2 | \mathbf{a}_j | J_1 m_1 \rangle \cdot \left[\sum_{\mathbf{k}',\sigma'} \sqrt{\hbar\omega_{\mathbf{k}',\sigma'}} \mathbf{u}_{\mathbf{k}',\sigma'} \sqrt{\hat{n}_{\mathbf{k}',\sigma'} + 1} e^{-i\mathbf{k}'\cdot\mathbf{R}_j^{(0)}} \right]$$

$$\langle J_2' m_2' | \mathbf{a}_{j'} | J_0 m_0' \rangle \cdot \left[\sum_{\mathbf{k}'',\sigma''} \sqrt{\hbar\omega_{\mathbf{k}'',\sigma''}} \mathbf{u}_{\mathbf{k}'',\sigma''} \sqrt{\hat{n}_{\mathbf{k}'',\sigma''}} e^{i\mathbf{k}''\cdot\mathbf{R}_{j'}^{(0)}} \right], \tag{A.3}$$

$$T_3' = \frac{(Mc^2)^2}{4} \sum_{J_2} \sum_{J_2'} \frac{2}{(E_1 - E_0)^2 (E_2 - E_1)(E_2' - E_1)}$$

$$\sum_j \sum_{j'} \sum_{m_0} \sum_{m_1} \sum_{m_2} \sum_{m_0'} \sum_{m_1'} \sum_{m_2'} \left(|J_0 m_0\rangle\langle J_1 m_1| \right)_j \left(|J_1 m_1'\rangle\langle J_0 m_0'| \right)_{j'}$$

$$\langle J_2 m_2 | \mathbf{a}_j | J_1 m_1 \rangle \cdot \left[\frac{1}{N} \sum_{\mathbf{k},\sigma} (\hbar\omega_{\mathbf{k},\sigma})^2 \mathbf{u}_{\mathbf{k},\sigma} \mathbf{u}_{\mathbf{k},\sigma} \cos\left(\mathbf{k} \cdot (\mathbf{R}_{j'}^{(0)} - \mathbf{R}_j^{(0)}) \right) \right] \cdot \langle J_2' m_2' | \mathbf{a}_{j'} | J_0 m_0' \rangle$$

$$\langle J_0 m_0 | \mathbf{a}_j | J_2 m_2 \rangle \cdot \left[\sum_{\mathbf{k}',\sigma'} \sqrt{\hbar\omega_{\mathbf{k}',\sigma'}} \mathbf{u}_{\mathbf{k}',\sigma'} \sqrt{\hat{n}_{\mathbf{k}',\sigma'} + 1} e^{-i\mathbf{k}'\cdot\mathbf{R}_j^{(0)}} \right]$$

$$\langle J_1 m_1' | \mathbf{a}_{j'} | J_2' m_2' \rangle \cdot \left[\sum_{\mathbf{k}'',\sigma''} \sqrt{\hbar\omega_{\mathbf{k}'',\sigma''}} \mathbf{u}_{\mathbf{k}'',\sigma''} \sqrt{\hat{n}_{\mathbf{k}'',\sigma''}} e^{i\mathbf{k}''\cdot\mathbf{R}_{j'}^{(0)}} \right], \tag{A.4}$$

$$T_4' = \frac{(Mc^2)^2}{4} \sum_{J_2} \sum_{J_2'} \frac{2}{(E_1 - E_0)^2 (E_2 - E_0)(E_2' - E_0)}$$

$$\sum_j \sum_{j'} \sum_{m_0} \sum_{m_1} \sum_{m_2} \sum_{m_0'} \sum_{m_1'} \sum_{m_2'} \left(|J_0 m_0\rangle\langle J_1 m_1| \right)_j \left(|J_1 m_1'\rangle\langle J_0 m_0'| \right)_{j'}$$

$$\langle J_2 m_2 | \mathbf{a}_j | J_1 m_1 \rangle \cdot \left[\frac{1}{N} \sum_{\mathbf{k},\sigma} (\hbar\omega_{\mathbf{k},\sigma})^2 \mathbf{u}_{\mathbf{k},\sigma} \mathbf{u}_{\mathbf{k},\sigma} \cos\left(\mathbf{k} \cdot (\mathbf{R}_{j'}^{(0)} - \mathbf{R}_j^{(0)}) \right) \right] \cdot \langle J_1 m_1' | \mathbf{a}_{j'} | J_2' m_2' \rangle$$

$$\langle J_0 m_0 | \mathbf{a}_j | J_2 m_2 \rangle \cdot \left[\sum_{\mathbf{k}',\sigma'} \sqrt{\hbar\omega_{\mathbf{k}',\sigma'}} \mathbf{u}_{\mathbf{k}',\sigma'} \sqrt{\hat{n}_{\mathbf{k}',\sigma'} + 1} e^{-i\mathbf{k}'\cdot\mathbf{R}_j^{(0)}} \right]$$

$$\langle J_2' m_2' | \mathbf{a}_{j'} | J_0 m_0' \rangle \cdot \left[\sum_{\mathbf{k}'',\sigma''} \sqrt{\hbar\omega_{\mathbf{k}'',\sigma''}} \mathbf{u}_{\mathbf{k}'',\sigma''} \sqrt{\hat{n}_{\mathbf{k}'',\sigma''}} e^{i\mathbf{k}''\cdot\mathbf{R}_{j'}^{(0)}} \right], \tag{A.5}$$

$$T_5' = \frac{(Mc^2)^2}{4} \sum_{J_2} \sum_{J_2'} \frac{2}{(E_1 - E_0)^2 (E_2 - E_1)(E_2' - E_1)}$$

$$\sum_j \sum_{j'} \sum_{m_0} \sum_{m_1} \sum_{m_2} \sum_{m_0'} \sum_{m_1'} \sum_{m_2'} \Big(|J_0 m_0\rangle \langle J_1 m_1| \Big)_j \Big(|J_1 m_1'\rangle \langle J_0 m_0'| \Big)_{j'}$$

$$\langle J_0 m_0 |\mathbf{a}_j| J_2 m_2 \rangle \cdot \left[\frac{1}{N} \sum_{\mathbf{k},\sigma} (\hbar \omega_{\mathbf{k},\sigma})^2 \mathbf{u}_{\mathbf{k},\sigma} \mathbf{u}_{\mathbf{k},\sigma} \cos\Big(\mathbf{k} \cdot (\mathbf{R}_{j'}^{(0)} - \mathbf{R}_j^{(0)}) \Big) \right] \cdot \langle J_2' m_2' |\mathbf{a}_{j'}| J_0 m_0' \rangle$$

$$\langle J_1 m_1' |\mathbf{a}_{j'}| J_2' m_2' \rangle \cdot \left[\sum_{\mathbf{k}',\sigma'} \sqrt{\hbar \omega_{\mathbf{k}',\sigma'}} \mathbf{u}_{\mathbf{k}',\sigma'} \sqrt{\hat{n}_{\mathbf{k}',\sigma'} + 1} \, \mathrm{e}^{-i\mathbf{k}' \cdot \mathbf{R}_{j'}^{(0)}} \right]$$

$$\langle J_2 m_2 |\mathbf{a}_j| J_1 m_1 \rangle \cdot \left[\sum_{\mathbf{k}'',\sigma''} \sqrt{\hbar \omega_{\mathbf{k}'',\sigma''}} \mathbf{u}_{\mathbf{k}'',\sigma''} \sqrt{\hat{n}_{\mathbf{k}'',\sigma''}} \, \mathrm{e}^{i\mathbf{k}'' \cdot \mathbf{R}_j^{(0)}} \right], \tag{A.6}$$

$$T_6' = \frac{(Mc^2)^2}{4} \sum_{J_2} \sum_{J_2'} \frac{2}{(E_1 - E_0)^2 (E_2 - E_1)(E_2' - E_0)}$$

$$\sum_j \sum_{j'} \sum_{m_0} \sum_{m_1} \sum_{m_2} \sum_{m_0'} \sum_{m_1'} \sum_{m_2'} \Big(|J_0 m_0\rangle \langle J_1 m_1| \Big)_j \Big(|J_1 m_1'\rangle \langle J_0 m_0'| \Big)_{j'}$$

$$\langle J_0 m_0 |\mathbf{a}_j| J_2 m_2 \rangle \cdot \left[\frac{1}{N} \sum_{\mathbf{k},\sigma} (\hbar \omega_{\mathbf{k},\sigma})^2 \mathbf{u}_{\mathbf{k},\sigma} \mathbf{u}_{\mathbf{k},\sigma} \cos\Big(\mathbf{k} \cdot (\mathbf{R}_{j'}^{(0)} - \mathbf{R}_j^{(0)}) \Big) \right] \cdot \langle J_1 m_1' |\mathbf{a}_{j'}| J_2' m_2' \rangle$$

$$\langle J_2' m_2' |\mathbf{a}_{j'}| J_0 m_0' \rangle \cdot \left[\sum_{\mathbf{k}',\sigma'} \sqrt{\hbar \omega_{\mathbf{k}',\sigma'}} \mathbf{u}_{\mathbf{k}',\sigma'} \sqrt{\hat{n}_{\mathbf{k}',\sigma'} + 1} \, \mathrm{e}^{-i\mathbf{k}' \cdot \mathbf{R}_{j'}^{(0)}} \right]$$

$$\langle J_2 m_2 |\mathbf{a}_j| J_1 m_1 \rangle \cdot \left[\sum_{\mathbf{k}'',\sigma''} \sqrt{\hbar \omega_{\mathbf{k}'',\sigma''}} \mathbf{u}_{\mathbf{k}'',\sigma''} \sqrt{\hat{n}_{\mathbf{k}'',\sigma''}} \, \mathrm{e}^{i\mathbf{k}'' \cdot \mathbf{R}_j^{(0)}} \right], \tag{A.7}$$

$$T_7' = \frac{(Mc^2)^2}{4} \sum_{J_2} \sum_{J_2'} \frac{2}{(E_1 - E_0)^2 (E_2 - E_0)(E_2' - E_1)}$$

$$\sum_j \sum_{j'} \sum_{m_0} \sum_{m_1} \sum_{m_2} \sum_{m_0'} \sum_{m_1'} \sum_{m_2'} \left(|J_0 m_0\rangle\langle J_1 m_1| \right)_j \left(|J_1 m_1'\rangle\langle J_0 m_0'| \right)_{j'}$$

$$\langle J_2 m_2 | \mathbf{a}_j | J_1 m_1 \rangle \cdot \left[\frac{1}{N} \sum_{\mathbf{k},\sigma} (\hbar\omega_{\mathbf{k},\sigma})^2 \mathbf{u}_{\mathbf{k},\sigma} \mathbf{u}_{\mathbf{k},\sigma} \cos\left(\mathbf{k} \cdot (\mathbf{R}_{j'}^{(0)} - \mathbf{R}_j^{(0)}) \right) \right] \cdot \langle J_2' m_2' | \mathbf{a}_{j'} | J_0 m_0' \rangle$$

$$\langle J_1 m_1' | \mathbf{a}_{j'} | J_2' m_2' \rangle \cdot \left[\sum_{\mathbf{k}',\sigma'} \sqrt{\hbar\omega_{\mathbf{k}',\sigma'}} \mathbf{u}_{\mathbf{k}',\sigma'} \sqrt{\hat{n}_{\mathbf{k}',\sigma'} + 1} \, \mathrm{e}^{-i\mathbf{k}'\cdot\mathbf{R}_{j'}^{(0)}} \right]$$

$$\langle J_0 m_0 | \mathbf{a}_j | J_2 m_2 \rangle \cdot \left[\sum_{\mathbf{k}'',\sigma''} \sqrt{\hbar\omega_{\mathbf{k}'',\sigma''}} \mathbf{u}_{\mathbf{k}'',\sigma''} \sqrt{\hat{n}_{\mathbf{k}'',\sigma''}} \, \mathrm{e}^{i\mathbf{k}''\cdot\mathbf{R}_j^{(0)}} \right], \tag{A.8}$$

$$T_8' = \frac{(Mc^2)^2}{4} \sum_{J_2} \sum_{J_2'} \frac{2}{(E_1 - E_0)^2 (E_2 - E_0)(E_2' - E_0)}$$

$$\sum_j \sum_{j'} \sum_{m_0} \sum_{m_1} \sum_{m_2} \sum_{m_0'} \sum_{m_1'} \sum_{m_2'} \left(|J_0 m_0\rangle\langle J_1 m_1| \right)_j \left(|J_1 m_1'\rangle\langle J_0 m_0'| \right)_{j'}$$

$$\langle J_2 m_2 | \mathbf{a}_j | J_1 m_1 \rangle \cdot \left[\frac{1}{N} \sum_{\mathbf{k},\sigma} (\hbar\omega_{\mathbf{k},\sigma})^2 \mathbf{u}_{\mathbf{k},\sigma} \mathbf{u}_{\mathbf{k},\sigma} \cos\left(\mathbf{k} \cdot (\mathbf{R}_{j'}^{(0)} - \mathbf{R}_j^{(0)}) \right) \right] \cdot \langle J_1 m_1' | \mathbf{a}_{j'} | J_2' m_2' \rangle$$

$$\langle J_2' m_2' | \mathbf{a}_{j'} | J_0 m_0' \rangle \cdot \left[\sum_{\mathbf{k}',\sigma'} \sqrt{\hbar\omega_{\mathbf{k}',\sigma'}} \mathbf{u}_{\mathbf{k}',\sigma'} \sqrt{\hat{n}_{\mathbf{k}',\sigma'} + 1} \, \mathrm{e}^{-i\mathbf{k}'\cdot\mathbf{R}_{j'}^{(0)}} \right]$$

$$\langle J_0 m_0 | \mathbf{a}_j | J_2 m_2 \rangle \cdot \left[\sum_{\mathbf{k}'',\sigma''} \sqrt{\hbar\omega_{\mathbf{k}'',\sigma''}} \mathbf{u}_{\mathbf{k}'',\sigma''} \sqrt{\hat{n}_{\mathbf{k}'',\sigma''}} \, \mathrm{e}^{i\mathbf{k}''\cdot\mathbf{R}_j^{(0)}} \right]. \tag{A.9}$$

Destructive interference has greatly reduced the total indirect interaction in this case from the strength of contributions from individual pathways.

Appendix B. Dynamical Model for Resonant Excitation Transfer

We are interested in the dynamics associated with excitation transfer between two sites in the presence of an oscillatory driving term. The basic idea is to make use of two two-level systems which are coupled together via excitation transfer, and then develop evolution equations using Ehrenfest's theorem.

Appendix B.1. Idealized model

We can describe a simplified version of the model based on a Hamiltonian of the form

$$\hat{H} = -\frac{1}{2}\Delta E \begin{bmatrix} 1 & 0 & 0 & 0 \\ 0 & -1 & 0 & 0 \\ 0 & 0 & 1 & 0 \\ 0 & 0 & 0 & -1 \end{bmatrix} + V_0 e^{-i\omega t} \begin{bmatrix} 0 & e^{i\mathbf{k}\cdot\mathbf{r}_1} & 0 & 0 \\ e^{i\mathbf{k}\cdot\mathbf{r}_1} & 0 & 0 & 0 \\ 0 & 0 & 0 & e^{i\mathbf{k}\cdot\mathbf{r}_2} \\ 0 & 0 & e^{i\mathbf{k}\cdot\mathbf{r}_2} & 0 \end{bmatrix} + U_0 \begin{bmatrix} 0 & 0 & 1 & 0 \\ 0 & 0 & 0 & 1 \\ 1 & 0 & 0 & 0 \\ 0 & 1 & 0 & 0 \end{bmatrix}. \tag{B.1}$$

The first term on the right-hand side describes a pair of two-level systems both with a transition energy ΔE; the second term describes an oscillatory driving term at frequency ω with position phase factors such as would be produced by X-rays from a synchrotron source; and the third term describes coupling via resonant excitation transfer.

Appendix B.2. Evolution equations

We can make use of Ehrenfest's theorem to develop evolution equations according to

$$\frac{\mathrm{d}}{\mathrm{d}t}\langle\hat{Q}\rangle = \left\langle\frac{\partial\hat{Q}}{\partial t}\right\rangle + \frac{1}{i\hbar}\langle[\hat{Q},\hat{H}]\rangle. \tag{B.2}$$

Following the approach used for the dynamics of the two-level system we can define equivalent two-level system operators within the context of this four level system according to

$$\hat{\sigma}_x^{(1)} = \begin{bmatrix} 0 & 1 & 0 & 0 \\ 1 & 0 & 0 & 0 \\ 0 & 0 & 0 & 0 \\ 0 & 0 & 0 & 0 \end{bmatrix}, \quad \hat{\sigma}_y^{(1)} = \begin{bmatrix} 0 & -i & 0 & 0 \\ i & 0 & 0 & 0 \\ 0 & 0 & 0 & 0 \\ 0 & 0 & 0 & 0 \end{bmatrix}, \quad \hat{\sigma}_z^{(1)} = \begin{bmatrix} 1 & 0 & 0 & 0 \\ 0 & -1 & 0 & 0 \\ 0 & 0 & 0 & 0 \\ 0 & 0 & 0 & 0 \end{bmatrix},$$

$$\hat{\sigma}_x^{(2)} = \begin{bmatrix} 0 & 0 & 0 & 0 \\ 0 & 0 & 0 & 0 \\ 0 & 0 & 0 & 1 \\ 0 & 0 & 1 & 0 \end{bmatrix}, \quad \hat{\sigma}_y^{(1)} = \begin{bmatrix} 0 & 0 & 0 & 0 \\ 0 & 0 & 0 & 0 \\ 0 & 0 & 0 & -i \\ 0 & 0 & i & 0 \end{bmatrix}, \quad \hat{\sigma}_z^{(2)} = \begin{bmatrix} 0 & 0 & 0 & 0 \\ 0 & 0 & 0 & 0 \\ 0 & 0 & 1 & 0 \\ 0 & 0 & 0 & -1 \end{bmatrix}. \tag{B.3}$$

Evolution equations for the expectation values of these operators are

$$\frac{\mathrm{d}}{\mathrm{d}t}\langle\hat{\sigma}_x^{(1)}\rangle = \frac{\Delta E}{\hbar}\langle\hat{\sigma}_y^{(1)}\rangle + \frac{U_0}{\hbar}\langle\hat{A}\rangle, \tag{B.4}$$

$$\frac{\mathrm{d}}{\mathrm{d}t}\langle\hat{\sigma}_x^{(2)}\rangle = \frac{\Delta E}{\hbar}\langle\hat{\sigma}_y^{(2)}\rangle - \frac{U_0}{\hbar}\langle\hat{A}\rangle, \tag{B.5}$$

$$\frac{\mathrm{d}}{\mathrm{d}t}\langle\hat{\sigma}_y^{(1)}\rangle = -\frac{\Delta E}{\hbar}\langle\hat{\sigma}_x^{(1)}\rangle - \frac{2V_0}{\hbar}e^{i\mathbf{k}\cdot\mathbf{r}_1}e^{-i\omega t}\langle\hat{\sigma}_z^{(1)}\rangle + \frac{U_0}{\hbar}\langle\hat{B}\rangle, \tag{B.6}$$

$$\frac{\mathrm{d}}{\mathrm{d}t}\langle\hat{\sigma}_y^{(2)}\rangle = -\frac{\Delta E}{\hbar}\langle\hat{\sigma}_x^{(2)}\rangle - \frac{2V_0}{\hbar}e^{i\mathbf{k}\cdot\mathbf{r}_2}e^{-i\omega t}\langle\hat{\sigma}_z^{(2)}\rangle - \frac{U_0}{\hbar}\langle\hat{B}\rangle, \tag{B.7}$$

$$\frac{\mathrm{d}}{\mathrm{d}t}\langle\hat{\sigma}_z^{(1)}\rangle = -\frac{2V_0}{\hbar}e^{i\mathbf{k}\cdot\mathbf{r}_1}e^{-i\omega t}\langle\hat{\sigma}_y^{(1)}\rangle - \frac{U_0}{\hbar}\langle\hat{D}\rangle, \tag{B.8}$$

$$\frac{\mathrm{d}}{\mathrm{d}t}\langle\hat{\sigma}_z^{(2)}\rangle = -\frac{2V_0}{\hbar}e^{i\mathbf{k}\cdot\mathbf{r}_2}e^{-i\omega t}\langle\hat{\sigma}_y^{(2)}\rangle + \frac{U_0}{\hbar}\langle\hat{D}\rangle, \tag{B.9}$$

where we define new operators according to

$$\hat{A} = \begin{bmatrix} 0 & 0 & 0 & -i \\ 0 & 0 & -i & 0 \\ 0 & i & 0 & 0 \\ i & 0 & 0 & 0 \end{bmatrix}, \quad \hat{B} = \begin{bmatrix} 0 & 0 & 0 & -1 \\ 0 & 0 & 1 & 0 \\ 0 & 1 & 0 & 0 \\ -1 & 0 & 0 & 0 \end{bmatrix},$$

$$\hat{C} = \begin{bmatrix} 0 & 0 & 1 & 0 \\ 0 & 0 & 0 & 1 \\ 1 & 0 & 0 & 0 \\ 0 & 1 & 0 & 0 \end{bmatrix}, \quad \hat{D} = \begin{bmatrix} 0 & 0 & i & 0 \\ 0 & 0 & 0 & -i \\ -i & 0 & 0 & 0 \\ 0 & i & 0 & 0 \end{bmatrix}. \tag{B.10}$$

Evolution equations associated with these operators are

$$\frac{\mathrm{d}}{\mathrm{d}t}\langle\hat{A}\rangle = \frac{\Delta E}{\hbar}\langle\hat{B}\rangle + \frac{2V_0}{\hbar}\mathrm{e}^{i\mathbf{k}\cdot\mathbf{r}_1}\mathrm{e}^{-i\omega t}\langle\hat{C}\rangle - \frac{2V_0}{\hbar}\mathrm{e}^{i\mathbf{k}\cdot\mathbf{r}_2}\mathrm{e}^{-i\omega t}\langle\hat{C}\rangle - \frac{2U_0}{\hbar}\langle\hat{\sigma}_x^{(1)} - \hat{\sigma}_x^{(2)}\rangle, \tag{B.11}$$

$$\frac{\mathrm{d}}{\mathrm{d}t}\langle\hat{B}\rangle = -\frac{\Delta E}{\hbar}\langle\hat{A}\rangle + \frac{2V_0}{\hbar}\mathrm{e}^{i\mathbf{k}\cdot\mathbf{r}_1}\mathrm{e}^{-i\omega t}\langle\hat{D}\rangle + \frac{2V_0}{\hbar}\mathrm{e}^{i\mathbf{k}\cdot\mathbf{r}_2}\mathrm{e}^{-i\omega t}\langle\hat{D}\rangle - \frac{2U_0}{\hbar}\langle\hat{\sigma}_y^{(1)} - \hat{\sigma}_y^{(2)}\rangle, \tag{B.12}$$

$$\frac{\mathrm{d}}{\mathrm{d}t}\langle\hat{C}\rangle = -\frac{2V_0}{\hbar}\mathrm{e}^{i\mathbf{k}\cdot\mathbf{r}_1}\mathrm{e}^{-i\omega t}\langle\hat{A}\rangle + \frac{2V_0}{\hbar}\mathrm{e}^{i\mathbf{k}\cdot\mathbf{r}_2}\mathrm{e}^{-i\omega t}\langle\hat{A}\rangle, \tag{B.13}$$

$$\frac{\mathrm{d}}{\mathrm{d}t}\langle\hat{D}\rangle = -\frac{2V_0}{\hbar}\mathrm{e}^{i\mathbf{k}\cdot\mathbf{r}_1}\mathrm{e}^{-i\omega t}\langle\hat{B}\rangle - \frac{2V_0}{\hbar}\mathrm{e}^{i\mathbf{k}\cdot\mathbf{r}_2}\mathrm{e}^{-i\omega t}\langle\hat{B}\rangle + \frac{2U_0}{\hbar}\langle\hat{\sigma}_z^{(1)} - \hat{\sigma}_z^{(2)}\rangle. \tag{B.14}$$

Due to the relative simplicity of this model we are able to describe the dynamics of the associated expectation values with only 10 first-order equations.

Appendix B.3. Empirical loss

For the two-level system model the associated Bloch equations can be augmented with an empirical loss model. Given the similarity with the model here, we propose the generalization

$$\left(\frac{\mathrm{d}}{\mathrm{d}t} + \frac{1}{T_2}\right)\langle\hat{\sigma}_x^{(1)}\rangle = \frac{\Delta E}{\hbar}\langle\hat{\sigma}_y^{(1)}\rangle + \frac{U_0}{\hbar}\langle\hat{A}\rangle \tag{B.15}$$

$$\left(\frac{\mathrm{d}}{\mathrm{d}t} + \frac{1}{T_2}\right)\langle\hat{\sigma}_x^{(2)}\rangle = \frac{\Delta E}{\hbar}\langle\hat{\sigma}_y^{(2)}\rangle - \frac{U_0}{\hbar}\langle\hat{A}\rangle \tag{B.16}$$

$$\left(\frac{\mathrm{d}}{\mathrm{d}t} + \frac{1}{T_2}\right)\langle\hat{\sigma}_y^{(1)}\rangle = -\frac{\Delta E}{\hbar}\langle\hat{\sigma}_x^{(1)}\rangle - \frac{2V_0}{\hbar}\mathrm{e}^{i\mathbf{k}\cdot\mathbf{r}_1}\mathrm{e}^{-i\omega t}\langle\hat{\sigma}_z^{(1)}\rangle + \frac{U_0}{\hbar}\langle\hat{B}\rangle, \tag{B.17}$$

$$\left(\frac{\mathrm{d}}{\mathrm{d}t} + \frac{1}{T_2}\right)\langle\hat{\sigma}_y^{(2)}\rangle = -\frac{\Delta E}{\hbar}\langle\hat{\sigma}_x^{(2)}\rangle - \frac{2V_0}{\hbar}\mathrm{e}^{i\mathbf{k}\cdot\mathbf{r}_2}\mathrm{e}^{-i\omega t}\langle\hat{\sigma}_z^{(2)}\rangle - \frac{U_0}{\hbar}\langle\hat{B}\rangle, \tag{B.18}$$

$$\frac{\mathrm{d}}{\mathrm{d}t}\langle\hat{\sigma}_z^{(1)}\rangle + \frac{\langle\hat{\sigma}_z^{(1)}\rangle - \sigma_{z0}^{(1)}}{T_1} = -\frac{2V_0}{\hbar}\mathrm{e}^{i\mathbf{k}\cdot\mathbf{r}_1}\mathrm{e}^{-i\omega t}\langle\hat{\sigma}_y^{(1)}\rangle - \frac{U_0}{\hbar}\langle\hat{D}\rangle, \tag{B.19}$$

$$\frac{\mathrm{d}}{\mathrm{d}t}\langle\hat{\sigma}_z^{(2)}\rangle + \frac{\langle\hat{\sigma}_z^{(2)}\rangle - \sigma_{z0}^{(2)}}{T_1} = -\frac{2V_0}{\hbar}\mathrm{e}^{i\mathbf{k}\cdot\mathbf{r}_2}\mathrm{e}^{-i\omega t}\langle\hat{\sigma}_y^{(2)}\rangle + \frac{U_0}{\hbar}\langle\hat{D}\rangle, \tag{B.20}$$

$$\left(\frac{\mathrm{d}}{\mathrm{d}t} + \frac{1}{T_{X2}}\right)\langle\hat{A}\rangle = \frac{\Delta E}{\hbar}\langle\hat{B}\rangle + \frac{2V_0}{\hbar}\mathrm{e}^{i\mathbf{k}\cdot\mathbf{r}_1}\mathrm{e}^{-i\omega t}\langle\hat{C}\rangle - \frac{2V_0}{\hbar}\mathrm{e}^{i\mathbf{k}\cdot\mathbf{r}_2}\mathrm{e}^{-i\omega t}\langle\hat{C}\rangle - \frac{2U_0}{\hbar}\langle\hat{\sigma}_x^{(1)} - \hat{\sigma}_x^{(2)}\rangle, \tag{B.21}$$

$$\left(\frac{\mathrm{d}}{\mathrm{d}t} + \frac{1}{T_{X2}}\right)\langle\hat{B}\rangle = -\frac{\Delta E}{\hbar}\langle\hat{A}\rangle + \frac{2V_0}{\hbar}e^{i\mathbf{k}\cdot\mathbf{r}_1}\mathrm{e}^{-i\omega t}\langle\hat{D}\rangle + \frac{2V_0}{\hbar}\mathrm{e}^{i\mathbf{k}\cdot\mathbf{r}_2}\mathrm{e}^{-i\omega t}\langle\hat{D}\rangle - \frac{2U_0}{\hbar}\langle\hat{\sigma}_y^{(1)} - \hat{\sigma}_y^{(2)}\rangle, \tag{B.22}$$

$$\left(\frac{\mathrm{d}}{\mathrm{d}t} + \frac{1}{T_{X1}}\right)\langle\hat{C}\rangle = -\frac{2V_0}{\hbar}\mathrm{e}^{i\mathbf{k}\cdot\mathbf{r}_1}\mathrm{e}^{-i\omega t}\langle\hat{A}\rangle + \frac{2V_0}{\hbar}\mathrm{e}^{i\mathbf{k}\cdot\mathbf{r}_2}\mathrm{e}^{-i\omega t}\langle\hat{A}\rangle, \tag{B.23}$$

$$\left(\frac{d}{dt} + \frac{1}{T_{X1}}\right)\langle\hat{D}\rangle = -\frac{2V_0}{\hbar}e^{i\mathbf{k}\cdot\mathbf{r}_1}e^{-i\omega t}\langle\hat{B}\rangle - \frac{2V_0}{\hbar}e^{i\mathbf{k}\cdot\mathbf{r}_2}e^{-i\omega t}\langle\hat{B}\rangle + \frac{2U_0}{\hbar}\langle\hat{\sigma}_z^{(1)} - \hat{\sigma}_z^{(2)}\rangle \tag{B.24}$$

with T_{X1} and T_{X2} providing direct extensions of T_1 and T_2 for relaxation times associated with excitation transfer related population and polarization operators.

Appendix B.4. Simple solution with no driving term

Suppose that we have two idealized equivalent nuclei in proximity with resonant excitation transfer and no X-ray driving term. If we assume that the T_{X1} relaxation time associated with excitation transfer is the same as the two-level relaxation time T_1, then we can write

$$\left(\frac{d}{dt} + \frac{1}{T_1}\right)\langle\hat{\sigma}_z^{(1)} - \hat{\sigma}_z^{(2)}\rangle = -\frac{2U_0}{\hbar}\langle\hat{D}\rangle, \tag{B.25}$$

$$\left(\frac{d}{dt} + \frac{1}{T_1}\right)\langle\hat{D}\rangle = \frac{2U_0}{\hbar}\langle\hat{\sigma}_z^{(1)} - \hat{\sigma}_z^{(2)}\rangle. \tag{B.26}$$

A relevant solution to these equations is

$$\langle\hat{\sigma}_z^{(1)} - \hat{\sigma}_z^{(2)}\rangle = 2e^{-t/T_1}\cos\left(\frac{2U_0}{\hbar}t\right). \tag{B.27}$$

In this model the occupation probability oscillates back and forth, decaying with the expected decay constant for an excited state.

Appendix B.5. Excitation transfer to an unstable final state

Suppose that we start with a nuclear system in a stable excited state in proximity to a nucleus in a stable ground state, where excitation transfer couples to a final state where the upper state of the newly promoted excited nucleus is very unstable. In this case we can develop a simplified description according to

$$\frac{d}{dt}\langle\hat{\sigma}_z^{(1)}\rangle = -\frac{U_0}{\hbar}\langle\hat{D}\rangle, \tag{B.28}$$

$$\frac{d}{dt}\langle\hat{\sigma}_z^{(2)}\rangle + \frac{\langle\hat{\sigma}_z^{(2)}\rangle - \sigma_{z0}^{(2)}}{T_1} = \frac{U_0}{\hbar}\langle\hat{D}\rangle, \tag{B.29}$$

$$\left(\frac{d}{dt} + \frac{1}{T_1}\right)\langle\hat{D}\rangle = \frac{2U_0}{\hbar}\langle\hat{\sigma}_z^{(1)} - \hat{\sigma}_z^{(2)}\rangle, \tag{B.30}$$

where we have assumed that the destruction of the excitation transfer term is dominated by the decay rate of the unstable excited state. We can solve approximately for $\langle\hat{D}\rangle$ to get

$$\langle\hat{D}\rangle = \frac{2U_0}{\hbar}T_1\langle\hat{\sigma}_z^{(1)} - \hat{\sigma}_z^{(2)}\rangle. \tag{B.31}$$

We can make use of this to develop an estimate for the loss of the initial excitation

$$\frac{d}{dt}\langle\hat{\sigma}_z^{(1)}\rangle = -2\left(\frac{U_0}{\hbar}\right)^2 T_1\langle\hat{\sigma}_z^{(1)} - \hat{\sigma}_z^{(2)}\rangle. \tag{B.32}$$

Appendix C. Impact on Internal Conversion

A reviewer has noted that we do not appear to consider the impact of internal conversion on the model, and on the excitation transfer process, and encouraged us to provide some discussion.

We note that an excited nuclear state can decay radiatively, and generally can also decay through internal conversion wherein the nucleus is de-excited with the excitation energy split between the electron removal energy and kinetic energy. In our experiments we can see gammas at 14.4 keV associated with the radiative decay of the 14.4 keV excited state of ^{57}Fe, and also the Fe K$_\alpha$ results from K-shell holes created via the absorption of a K-shell electron by the ^{57}Co nucleus during beta decay as well as from the internal conversion of the 14.4 keV state. Internal conversion of the highly-excited 136.5 keV state is much weaker, resulting in only a minor contribution to the creation of K-shell holes [49].

In general, a high internal conversion coefficient means that the efficiency of gamma emission is reduced, which generally makes it technically more difficult to carry out an experiment. For example, there are no Mossbauer experiments with the 1.565 keV transition in ^{201}Hg which has a very high internal conversion coefficient.

We would not expect phonon exchange and excitation transfer to have much effect on the internal conversion rate for states that are on resonance, primarily since it is so difficult to have much of an impact on the structure of an excited nuclear state, on a K-shell electronic orbital, or on the energy available for internal conversion. The reviewer has argued that in the presence of a highly-excited phonon mode that it is possible for the electron orbitals to be modified, resulting in changes to the rate for internal conversion. This may be true for the small contribution to internal conversion from the outer electron orbitals that could be modified due to strong lattice vibrations, and would require electron spectroscopy to see. We have not found papers in the literature discussing theory or experimental results for this.

In the absence of loss mechanisms we would expect resonant excitation transfer to be efficient in transferring excitation from one nucleus to another. However, loss can greatly reduce the efficiency for resonant excitation transfer, as can be seen in the model discussed briefly in Appendix B. For low energy nuclear transitions we would expect the dominant loss mechanism to be internal conversion, so the internal conversion rate in general will limit how much excitation is transferred. In this case the T_1 and T_{X1} parameters in the model will be dominated by internal conversion.

In a recent free-electron laser experiment the acceleration of the radiative decay of excited nuclei has been observed due to Dicke superradiance [50]. In such an experiment the internal conversion coefficient would be changed since the radiative decay rate is accelerated.

There appear discussions in the literature of possible modifications of the rate of internal conversion due to resonances [51] and an electron bridge [52].

In the main text there is a discussion of the possible acceleration of the rate for excitation transfer due to loss effects, as long as the loss for the different basis states is changed. For the nuclear part of the problem this involves internal conversion for low-energy nuclear transitions.

We have discussed in the text a modification of the incremental ratio of the 14.4 keV intensity relative to the Fe K$_\alpha$ intensity in our excitation transfer experiments. As discussed above we are considering an interpretation of this involving new decay channels opening for off-resonant basis states.

References

[1] M. Fleischmann, S. Pons and M. Hawkins, *J. Electroanal Chem.* **201** (1989) 301; errata, **263** (1990) 187.

[2] M. Fleischmann, S. Pons, M.W. Anderson, L.J. Li and M. Hawkins, *J. Electroanal. Chem.* **287** (1990) 293.

[3] P.L. Hagelstein, Current status of the theory and modeling effort based on fractionation, *J. Condensed Matter Nucl. Sci.* **19** (2016) 98–109.

[4] P.L. Hagelstein, Quantum Composites: A review and new results for condensed matter nuclear science, *J. Condensed Matter Nucl. Sci.* **20** (2016) 139–225.

[5] P.L. Hagelstein, A unified model for anomalies in metal deuterides, *Proc. ICCF9* (2002) 121–134.

[6] P.L. Hagelstein and I.U. Chaudhary, Energy exchange in the lossy spin–boson model, *J. Cond. Mat. Nucl. Sci.* **5** (2011) 52.

[7] P.L. Hagelstein and I.U. Chaudhary, Second-order formulation and scaling in the lossy spin–boson model, *J. Cond. Mat. Nucl. Sci.* **5** (2011) 87.

[8] P.L. Hagelstein and I.U. Chaudhary, Local approximation for the lossy spin–boson model, *J. Cond. Mat. Nucl. Sci.* **5** (2011) 102.

[9] P.L. Hagelstein and I.U. Chaudhary, Coherent energy exchange in the strong coupling limit of the lossy spin–boson model, *J. Cond. Mat. Nucl. Sci.* **5** (2011) 116.

[10] F. Metzler, P.L. Hagelstein and S. Lu, Observation of non-exponential decay in X-ray and γ emission lines from Co-57, *J. Condensed Matter Nucl. Sci.*, to appear.

[11] Th. Förster, Zwischenmolekulare Energiewanderung und Fluoreszenz, *Annalen der Phyzik* **6** (1948) 55–75.

[12] D.L. Andrews and A.A. Demidov, *Resonant Excitation Transfer*, Wiley, New York, 1999.

[13] S. Lu, Exploring possible coupling between phonons and internal nuclear states, *MIT PhD Thesis*, Cambridge, MA, USA, 2018.

[14] P.L. Hagelstein and I.U. Chaudhary, Coupling between the center of mass and relative degrees of freedom in a relativistic quantum composite and applications, *J. Condensed Matter Nucl. Sci.* **19** (2016) 98–109.

[15] P.L. Hagelstein and I.U. Chaudhary, Including nuclear degrees of freedom in a lattice Hamiltonian, *J. Condensed Matter Nucl. Sci.* **7** (2012) 35–50.

[16] P.L. Hagelstein and I.U. Chaudhary, Phonon–nuclear coupling for anomalies in Condensed Matter Nuclear Science, *J. Condensed Matter Nucl. Sci.* **12** (2013) 105–142.

[17] M. Mohseni, P. Rebentrost, S. Lloyd and A. Aspuru-Guzik, Environment-assisted quantum walks in photosynthetic energy transfer, *J. Chem. Phys.* **129** (2008) 174106.

[18] M.B. Plenio and S.F. Huelga, Dephasing-assisted transport: quantum networks and biomolecules, *New J. Phys.* **10** (2008) 113019.

[19] R. Laughlin and B.L. Scott, Off-energy-shell t-matrix elements for local potentials containing hard cores, *Phys. Rev.* **171** (1968) 1196–1201.

[20] M.K. Srivastava and D.W.L. Sprung, Off-shell behavior of the nucleon-nucleon interaction, *Adv. Nucl. Phys.* **8** (1975) 121–218.

[21] O. Zohni, Investigation of off-shell effects in triton binding-energy calculations with nonlocal-core nucleon-nucleon potentials, *Phys. Rev. C* **8** (1973) 1164–1166.

[22] A. deShalit and H. Feshbach, *Theoretical Nuclear Physics*, Volume 1, Nuclear Structure, Wiley, New York, 1974.

[23] I.S. Gradshteyn and I.M. Ryzhik, *Table of Integrals, Series, and Products*, Academic Press, London, 1980.

[24] T Hamada and I.D. Johnston, A potential model representation of two-nucleon data below 315 MeV, *Nucl. Phys.* **34** (1962) 382–403.

[25] R.V. Reid, Local phenomenological nucleon-nucleon potentials, *Ann. Phys.* **50** (1968) 411–448.

[26] R.B. Wiringa, V.G. J. Stoks and R. Schiavilla, Accurate nucleon-nucleon potential with charge-independence breaking, *Phys. Rev. C* **51** (1995) 38–51.

[27] S. Weinberg, Nuclear forces from chiral lagrangians, *Phys. Lett. B* **251** (1990) 288–292.

[28] R. Machleidt and D.R. Entem, Chiral effective field theory and nuclear forces, *Phys. Reports* **503** (2011) 1–75.

[29] W. Sturhahn, Nuclear resonant spectroscopy, *J. Phys.: Condensed Matter* **15** (2004) S497–S530.

[30] R. Rüffer and A.I. Chumakov, Nuclear resonance, *Synchrotron Light Sources and Free Electron Lasers Accelerator Physics, Instrumentation and Science Applications*, Springer, Berlin, 2014, pp. 1–32.

[31] A. Q. R. Baron, Introduction to High-Resolution Inelastic X-Ray Scattering, *arXiv preprint* arXiv:1504.01098 (2015).

[32] A.I. Chumakov, A.Q.R. Baron, J. Arthur, S.L. Ruby, G.S. Brown, G.V. Smirnov, U. van Bürck and G. Wortmann, Nuclear scattering of synchrotron radiation by ^{181}Ta, *Phys. Rev. Lett.* **75** (1995) 549–552.

[33] O. Leupold, A.I. Chumakov, E.E. Alp, W. Sturhahn and A.Q.R. Baron, Noniron isotopes, *Hyperfine Interactions* **123/124** (1999) 611–631.

[34] I. Serdons, R. Callens, R. Coussement, S. Gheysen, J. Ladriere, S. Morimoto, S. Nasu, J. Odeurs, Y. Yoda and G. Wortmann, Stroboscopic detection of the ^{181}Ta–Mössbauer resonance with synchrotron radiation, *Nucl. Instr. Methods Phys. Res. B* **251** (2006) 297–303.

[35] G.P. Chambers, J.E. Eridon, K.S. Grabowski, B.D. Sartwell and D.B. Chrisey, Charged particle spectra of palladium thin films during low energy deuterium ion implantation, *J. Fusion Energy 9* (1990) 281–285.

[36] J.R. Huizenga and L.R. Moretto, Nuclear level densities, *Annual Rev. Nucl. Sci.* **22** (1972) 427–464.

[37] A.G. Lipson, G.H. Miley, A.S. Roussetski and E.I. Saunin, Phenomenon of an energetic charged particle emission from hydrogen/deuterium loaded metals, *Proc. ICCF10* (2003) 539–558.

[38] A.G. Lipson, G.H. Miley, B.F. Lyakhov and A.S. Roussetski, Energetic charged particle emission from hydrogen loaded Pd and Ti cathodes and its enhancement by He-4 implantation, *Proc. ICCF11* (2004) 324–338.

[39] A.S. Roussetski, CR-39 track detectors in cold fusion experiments: Review and perspectives, *Proc. ICCF11* (2004) 274–280.

[40] A.G. Lipson, G.H. Miley, A.S. Roussetski, B.F. Lyakhov and E.I. Saunin, Reproducible nuclear emissions from Pd/PdO:D*x* heterostructure during controlled exothermic deuterium desorption, *Proc. ICCF12* (2005) 293–313.

[41] A.G. Lipson, A. Roussetski and G.H. Miley, Evidence for condensed matter enhanced nuclear reactions in metals with a high hydrogen solubility, *Proc. ICCF13* (2007) 248–268.

[42] P.A. Mosier-Boss, L.P. Forsley, A.S. Roussetski, A.G. Lipson, F. Tanzella, E.I. Saunin, M. McKubre, B. Earle and D. Zhou, Use of CR-39 detectors to determine the branching ratio in Pd/D co-deposition, *Current Science* **108** (2015) 585–588.

[43] P.A. Mosier-Boss, L.P.G. Forsley and P.K. McDaniel, Investigation of nano-nuclear reactions in condensed matter, *Technical Report for DTRA* (2016).

[44] A.S. Roussetski, Application of CR-39 plastic track detector for detection of DD and DT-reaction products in cold fusion experiments, *Proc. ICCF8* (2000) 253–257.

[45] E. Storms and B. Scanlan, Detection of radiation emitted from LENR, *Proc. ICCF14* (2008) 263–287.

[46] S.A. Lipinski and H.U. Lipinski, Hydrogen–lithium fusion device, methods and applications, *United States Patent Application Publication* US 2009/0274256 A1 (2009).

[47] S.A. Lipinski and H.U. Lipinski, Hydrogen–lithium fusion device, *WIPO/PCT Patent Application Publication* WO 2014/189799 A9 (2014).

[48] X.Z. Li, Z.M. Dong, C.L. Liang, Y.P. Fu, B. Liu, G.S. Huang, S.X. Zheng and S. Chen, Hydrogen-lithium low energy resonant electron-capture and BetheŠs solar energy model, *J. Condensed Matter Nucl. Sci.* **25** (2017) 181–192.

[49] V.P. Chechev and N.K. Kuzmenko, CEA Table de radiounucléides ^{57}Co, Laboratoire National Henri Becquerel LNE-LNHB/CEA Report (2014).

[50] A.I. Chumakov, A.Q. R. Baron, I. Sergueev, C. Strohm, O. Leupold, Y. Shvyd'ko, G.V. Smirnov, R. Rüffer, Y. Inubushi, M. Yabashi, K. Tono, T. Kudo and T. Ishikawa, Superradiance of an ensemble of nuclei excited by a free electron laser, it Nature Physics **14** (2018) 261–265.

[51] F.F. Karpeshin, Resonance internal conversion as a way of accelerating nuclear processes, *Phys. Particles and Nuclei* **37** (2006) 284–305.

[52] V.A. Krutov, Internal conversion in the field of an electronic bridge, *JETP Letters* **52** (1990) 584–588.
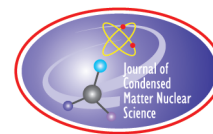
Research Article

Study on the Phenomenon Reported "Neutron Generation at Room Temperature in a Cylinder Packed with Titanium Shavings and Pressurized Deuterium Gas" (4)

Takayoshi Asami*

Research Institute of Innovative Technology for the Earth, 9-2 Kizugawadai, Kizu-cho, Soraku-gun, Kyoto 619-0292, Japan

Abstract

In a previous paper, the Coulomb and nuclear forces between deuteron–deuteron (d–d) particles using the Coulomb formula and the Yukawa formula were calculated and compared. The force of each of them was evaluated in accordance with the distance between them, near the surface of an atomic nucleus. As a result, it was found that there were two regions. One of them is the stronger Coulomb force region and the other is the stronger nuclear force region. At the boundary of these regions, both forces are equal to each other. It appears that if the adsorbed deuterium atom in ligancy 2 and the desorbed free deuteron are placed in a suitable magnetic field, both the electron in the adsorbed deuterium atom in ligancy 2 and the desorbed free deuteron are influenced by the magnetic lines of force. The author deemed that there might be an aperture of the energy barrier. If there is the aperture of such an energy barrier, there must be a possibility for two deuterium nuclei to collide and produce nuclear fusion without being under tremendous high temperatures. To confirm this possibility, the author has studied and evaluated the behavior of the charged particle and calculated the working force under the homogeneous and stable magnetic field. As an example, under this influence in the magnetic field, the working force, the behavior of a deuteron, a co-existing deuteron and an adsorbed deuterium atom in ligancy 2 have been analyzed. However, the working force to the particle, the Lorentz force, is very small compared to the Coulomb force. The motion of the charged particle and the electron orbital plane in an adsorbed deuterium atom in ligancy 2 in the magnetic field is the preferable direction. To analyze the possibility of nuclear fusion at room temperature, it is thought that a more advantageous circumstance than that proposed in this paper should be prepared.
© 2018 ISCMNS. All rights reserved. ISSN 2227-3123

Keywords: Coulomb force, Deuterium, Lorentz force, Magnetic field, Nuclear force

1. Introduction

In the previous paper [1], the Coulomb force and nuclear force between d–d atoms, a deuteron and a deuterium atom in ligancy 2 were calculated. The working force between the deuteron and the deuterium atom in ligancy 2 indicated

---

*Retired. E-mail: takaysami@yahoo.co.jp.

a difference compared to the force between the d–d atoms. This means that the result was caused by circumstantial change.

First of all, when adsorption and/or desorption occurs, the deuterium atoms existence in the Ti shavings brings about a change to the electron orbit, and therefore a loss of the electron in the deuterium atom. As a result, there is a change of the force relation between the deuterium atoms.
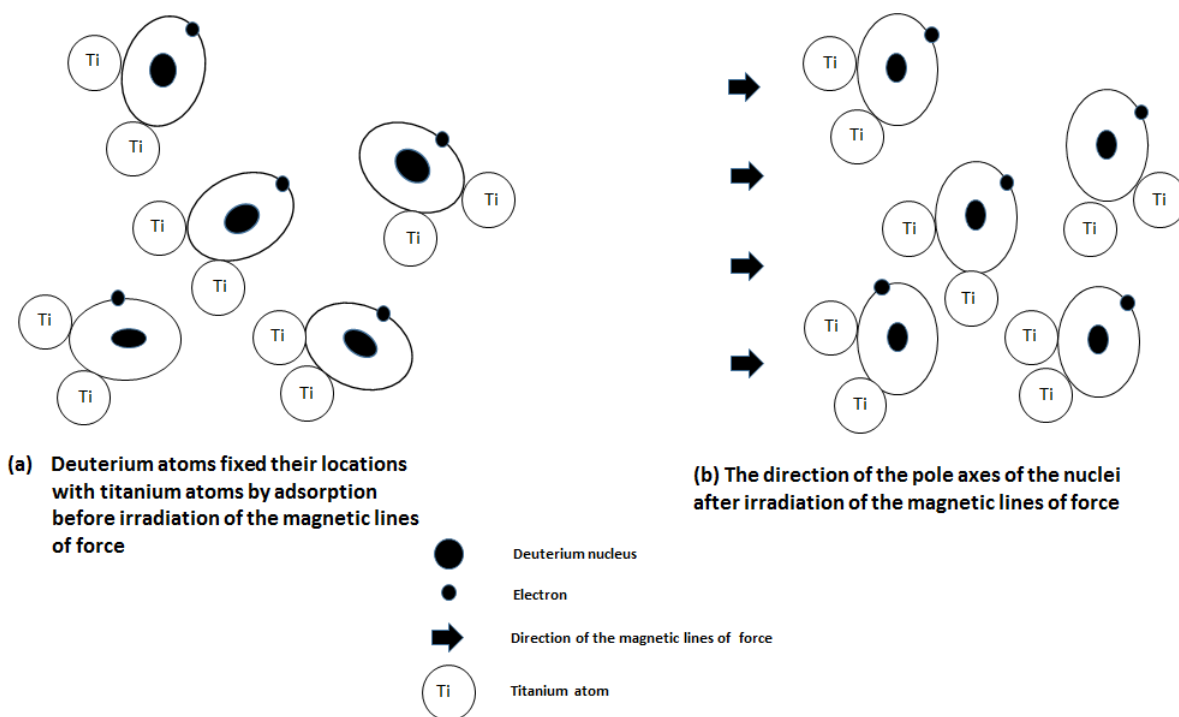
The deuterium atoms in the cylinder packed with Ti shavings are adsorbed by the Ti shavings under the pressurized and cooled conditions and form the specially combined state with Ti atoms [2], that is, the deuterium atom in ligancy 2. After that, it seems that if there is a temperature rise under the pressurization or evacuation, some deuterons desorbed from the Ti shavings produce neutrons.

This paper intends to analyze the behavior, movement and interaction of particles that coexist in the magnetic field and report the movements caused by the magnetic lines of force (MLF), and to determine whether these MLF have the effective influence over the deuterium atom in ligancy 2 and desorbed deuteron and force them to collide with each other.
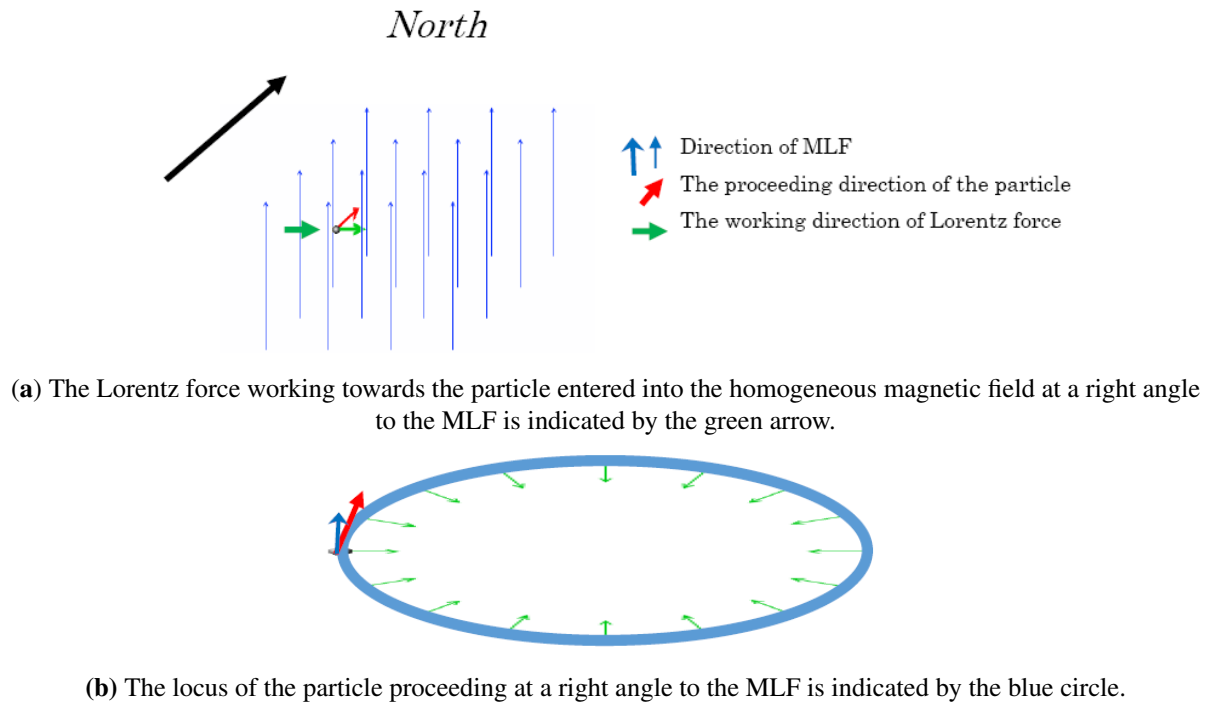
2. Behavior of the Particles in the MLF

2.1. Deuterium atoms in ligancy 2

This analysis is based on a simplified model of the deuterium atoms in ligancy 2. They only combine with two atoms in the Ti crystal cage in Ti shavings [1,2], when placed in a magnetic field. The behavior before and after irradiation

(a) Deuterium atoms fixed their locations with titanium atoms by adsorption before irradiation of the magnetic lines of force

(b) The direction of the pole axes of the nuclei after irradiation of the magnetic lines of force

● Deuterium nucleus

• Electron

➡ Direction of the magnetic lines of force

(Ti) Titanium atom

Figure 1. Behavior of the nucleus and its electron in deuterium atoms in ligancy 2 before and after the irradiation of the MLF in the assumed model.

(**a**) The Lorentz force working towards the particle entered into the homogeneous magnetic field at a right angle to the MLF is indicated by the green arrow.

(**b**) The locus of the particle proceeding at a right angle to the MLF is indicated by the blue circle.

Figure 2.   The motion of a positively charged particle in the homogenous magnetic field at a right angle to the MLF [3].

of the MLF is indicated by the image in Fig. 1 (a) and (b), respectively.

We can say that the model indicated in Fig. 1 simulates, as it were, Fleming's right-hand rule at work on an electron going around the nucleus and entering into the magnetic field, where two Ti atoms with an adsorbed deuterium atom in ligancy 2 are located.

It appears that the motion state of the electrons going around the nucleus are not changed by the Lorentz force because they are stabilized in the magnetic field by being at a right angle to the direction of the MLF and the direction of the nuclear axis. The axis is parallel to the MLF even though the electron orbit is constrained by the Ti atoms.

2.2.   A positively charged particle that has entered into the MLF at a 90° angle

When a charged particle enters into the magnetic field at a right angle to the MLF, Lorentz force works in an easterly direction as indicated by the green arrow in Fig. 2 (a) and (b).

2.3.   A positively charged particle entered into the MLF at the inclined angle θ

If a positively charged particle enters into the MLF with velocity at a right angle, it accepts the Lorentz force and it moves in accordance with the circular motion as indicated in Fig. 2(b). However, if it enters at an inclined angle to the direction of the MLF, it will move in accordance with a spiral locus on the condition of the initial velocity and the inclined angle to the MLF by the Lorentz force. This is indicated by the image in Fig. 3.
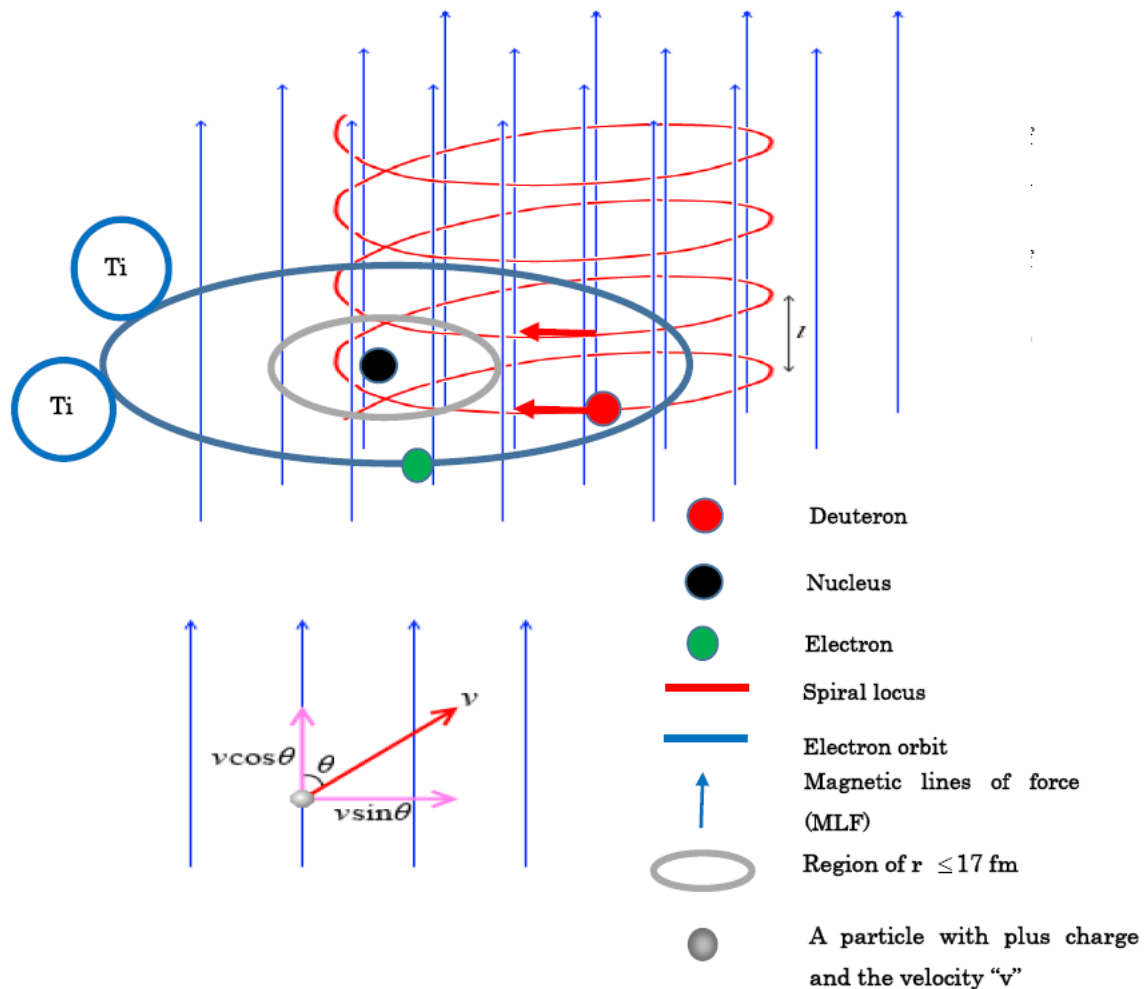
Figure 3. The motion of the example of a positively charged particle proceeding in a northerly direction (N) with an inclined angle, θ to the MLF [3].

It means that the bare deuteron entered with an inclined angle to the magnetic lines of force can enter into the plane including the nucleus and an electron in the deuterium atom in ligancy 2 indicated in Fig. 1. So we can expect that the deuterons will be able to enter into it avoiding the barrier of electrons and approach near the nucleus by specified probability.

Here we assume the following example that the deuteron goes to the north direction (N) with inclined angle θ to the magnetic lines of force indicated in Fig. 3.

It seems that the positively charged particles (or deuterons) entered at an inclined angle θ to the MLF can individually enter onto a plane with a nucleus and an electron (here after referred to as PLANE) in the deuterium atom in ligancy 2 as indicated in Fig. 3.

It appears that positively charged particles will be able to enter into the MLF avoiding the barrier of electrons and approach close to the nucleus under specified conditions.

3. The Influence of the MLF on the Coexistence of Deuterons and Absorbed Deuterium Atoms in Ligancy 2

3.1. Analysis of the movement of a deuteron with velocity, v, in the MLF

In the magnetic field, it appears that the direction of all the nuclear axes of the deuterium atoms in ligancy 2 are parallel to the direction of the MLF as indicated in Fig.1 (b). If a deuteron enters into the circumstance indicated in Fig. 1(b), the locus of its movement will be circular or spiral in accordance with the angle of incidence to the MLF and its velocity, v.

3.2. Behavior of deuterons in the cylinder packed with Ti shavings based on the analysis in Section 3.1

In accordance with the findings in Section 3.1, we can anatomize the behavior of the bare deuterons in the cylinder packed with Ti shavings. In the previous experiment [4], deuterons move in every direction. Two kinds of motions must occur and the possibility of the spiral motion is more probable than the circular motion.

Deuterons that are not moving at a right angle to the MLF, must move in accordance with the spiral locus, and then they will be able to go through the PLANE. Provided they go through the aperture of the Coulomb energy barrier by matching the Lorentz force of each deuteron, and each deuteron accepts the Lorentz force, they will be able to overcome the surrounding influential power.

If this occurs, there is a possibility that some deuterons will enter into the region within the circle with the radius of 17 fm from the center of the nucleus, or the possibility that some of them will collide with the nucleus of a deuterium atom in ligancy 2, as indicated in Fig. 3. This is the region where the nuclear force (F_n) is stronger than the Coulomb force (F_c), hereafter referred to as the "Region of NSTC".

3.3. Presumed actual movement of a particle in the experimental cylinder

The fundamental kinds of movements of a positively charged particle in the magnetic field are explained in Sections 3.1 and 3.2. However, as there are many particles in the cylinder, including deuterium molecules and desorbed deuterons, each of these will collide. It would appear that each particle proceeds, on average, the distance of the mean free path. If the cylinder is not placed under the irradiation of the magnetic lines of force, the locus of each mean free pass of a positively charged particle is a straight line and it would appear that the locus of a particle is composed of the combination of segments of a straight short locus as indicated in Fig. 4 [5].

However, if the cylinder is placed in a magnetic field, the form of each mean free path will be the short part of a circular segment or a spiral segment. The locus of the movement of a deuteron is composed of a combination of these segments.

4. An Example of Motions of a Deuteron with Velocity, v, in the MLF

It should be assumed that the cylinder packed with Ti shavings, containing pressurized deuterium gas, is kept at a cooled state of $-30°$ after being cooled to liquid nitrogen temperature and that this cylinder is in the magnetic field.

Figure 4.   A locus of presumed molecular motion, repeating collision in the gas phase.

The temperature "–30°" was selected because it is the experimental temperature at which neutron emission occurs [4]. Of course, the cylinder should be made of nonmagnetic material.

In the calculation of the mean velocity of a deuteron in the MLF, it is assumed that there is a deuteron which goes through the region of the PLANE in a deuterium atom in ligancy 2. Under the following conditions, the radius of the spiral locus can be calculated.

The angle of incidence to the MLF: 45°. The temperature of a deuteron and deuterium gas in the cylinder after being cooled to liquid nitrogen temperature: –30°. The mean velocity of a deuteron using the following formula and numerical value can be calculated.

$$C = (8RT/\pi M)^{1/2}, \tag{1}$$

where C, R, T and M are mean velocity (cm/s), gas constant ($R = 8.317 \times 10^7$ erg deg^{-1} mol^{-1}), temperature ($T = 243.2$ K) and deuteron mass ($M = 2.014$ g/mol), respectively. Substituting these numerical values to formula (1) $C \fallingdotseq 15.99 \times 10^4$ cm/s. It appears that the deuterons with a plus charge in the cylinder will be influenced by Lorentz force.

The Lorentz force indicated in Fig. 3 is indicated by formula (2)

$$F_{\mathrm{L}} = qvB \sin\theta, \tag{2}$$

where F_{L}, q, v, B and θ denote Lorentz force, N, an electrical charge value, C, velocity of the deuteron (m/s), magnetic flux density, T and an angle between the direction of the MLF and the direction of the velocity of a deuteron (degree), respectively. "v" is indicated by the image in Fig. 3.

Centrifugal force, can be indicated in the following formula (3), providing that there is a right angle between the direction of the proceeding deuteron and the MLF.

$$F = mv^2/r, \tag{3}$$

where F, m, v and r denote centrifugal force, deuteron mass, velocity of the deuteron and the radius of the circular motion of the deuteron, respectively.

When the angle between the proceeding deuteron and the direction of the MLF is θ, the component of the centrifugal force (F_r) at right angles to the MLF is indicated by formula (4).

$$F_r = m(v \sin \theta)^2/r. \tag{4}$$

Using formula (2), the subsequent formula is established.

$$m(v \sin \theta)^2/r = qvB \sin \theta. \tag{5}$$

Substituting the following numerical value, the calculation result is indicated as:
$\theta = 45°$, $m = 3.348 \times 10^{-27}$ kg, $v = 15.99 \times 10^4$ cm/s = 15.99×10^2 m/s (calculated from Eq. (1)), $q = 1.602 \times 10^{-19}$ C and $B = 10$ T, $r = 236.3 \times 10^{-8}$ m.

In this connection, pitch (l) of the spiral locus is as follows.

$$l = v \cos \theta \times (2\pi r/v \sin \theta). \tag{6}$$

Substituting numerical values to formula (6), $l = 1484 \times 10^{-8}$ m.

It appears that the calculated value of the spiral diameter is far larger in this example compared to the electron orbital diameter in the deuterium atom in ligancy 2 [6].

Judging from the calculated value of the radius of the spiral locus under the assumed condition, if the deuteron goes through into the PLANE, the partial short locus of a deuteron near this region is almost a straight line. In the execution of this experiment, a suitable strength of the magnetic field should be predetermined.

The nuclear force at a distance of 17 fm from the nucleus, has an attractive nuclear force (F_n) of 0.00500 MeV/fm ($\fallingdotseq 0.801$ N) as shown in Fig. 5 [7,8]. On the other hand, the Lorentz force is 1.811×10^{-15} N. The Lorentz force is far weaker compared to that of an attractive nuclear force in the region of NSTC where the nuclear force is nearly equal to or stronger than the Coulomb force.

As the moving direction of a free deuteron has a possibility of being any direction in the experimental cylinder, it is possible some free deuterons will enter into the region of NSTC at any angle where the nuclear force is nearly equal
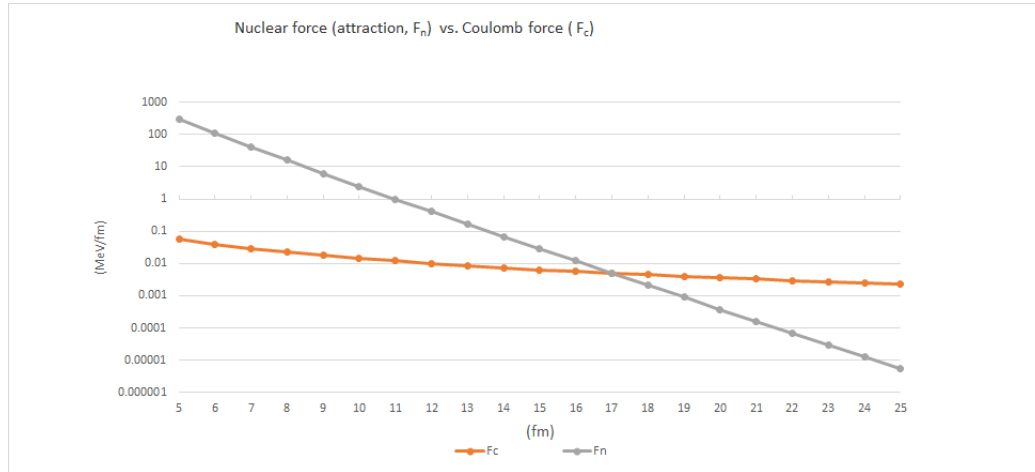
Figure 5. Comparison of Coulomb forces and attractive nuclear force. All the forces are indicated in their absolute values. F_n, nuclear force (attraction), F_c, Coulomb force (repulsion). All the forces are indicated in their absolute values. F_n: nuclear force (attraction), F_c: Coulomb force (repulsion). Pair charge values of each force are F_n: (1 eV, 1 eV) and F_c: (1 eV, 1 eV), respectively.
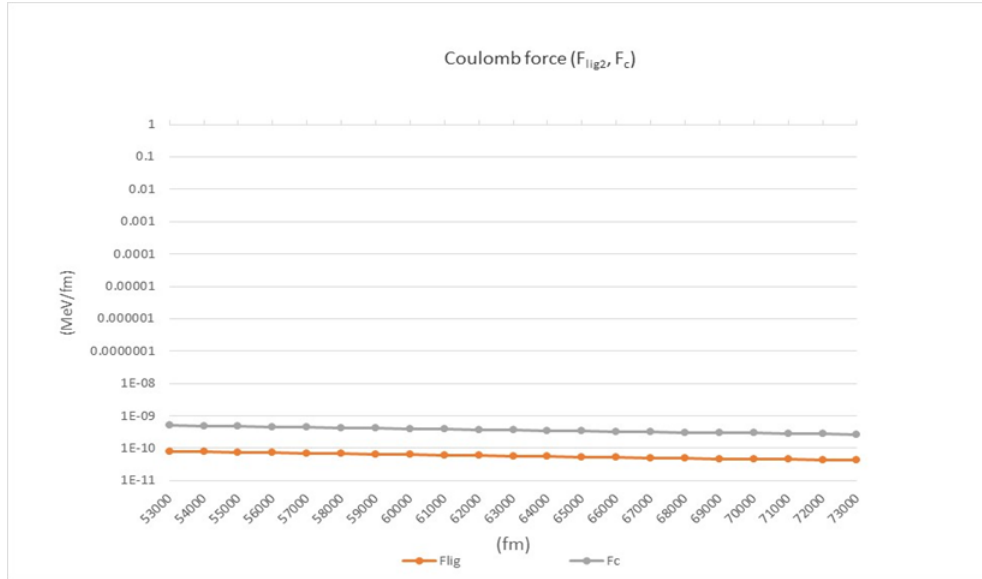
Figure 6. Comparison of Coulomb forces. All the forces are indicated in their absolute values. F_c: Coulomb force (repulsion), F_{lig2}: Coulomb force (attraction). Pair charge values of each force are F_{lig2}: (1 eV, –0.157 eV) and F_c: (1 eV, 1 eV) , respectively.

to or stronger than the Coulomb force. The possibility of entering into the region of NSTC is more important than the magnitude of the Lorentz force in the magnetic field.

The most important condition is that the angle between all the PLANE and the MLF becomes a stable right angle and its condition prepares for the free deuteron to be able to enter into the region of NSTC. For reference, two curves of Coulomb force (F_c) and an attractive nuclear force (F_n) are shown in Fig. 5 [1].

In Fig. 5, the comparison of F_c and F_n is indicated. The line of F_{lig} in Fig. 6 indicates an attractive force between a deuterium atom in ligancy 2 and a deuteron in the range from 0.53 to 0.73 Å. In paper [1], all the lines of force including F_{lig2}, which work between the deuteron and the deuterium atom in ligancy 2 in a range equal to or shorter than 25 fm were shown without any explanation. The paper was, intended to indicate the general comparison and tendency of the magnitude of each force. However, Fig. 5 in paper [1] gives no explanation about the scope of influence of F_{lig2}. So, the revised graphs have been devised in this paper in Figs. 5 and 6 separately.

So, this paper includes Figs.5 and 6 to demonstrate these forces separately.

$$F_n = -g e^{-\kappa r}(1/r^2 + \kappa/r), \tag{7}$$

where g and κ are constants. (Constants g and κ are produced by fitting them with the improved Yukawa formula, $g = -8.501 \times 10^4$, $\kappa = 0.804$.) r is the distance (fm) between two nuclei and F_n is the nuclear force (MeV/fm). We can evaluate the Coulomb force between them by applying Coulomb formula.

$$F_c = (1/4\pi\varepsilon_0)(qq'/r^2), \tag{8}$$

where F_c, ε_0, q, q' and r denote Coulomb force, vacuum dielectric constant, charge (q, q') and the distance between the two charges, respectively.

5. Conclusion

Based on the analyzed results of previous papers [1,2], it has been deemed necessary to prepare the circumstance for a deuteron to be able to approach and collide with a nucleus. It was thought that under such circumstance in the MLF, free deuterons should be able to go through the aperture of the energy barrier. In order to verify this, the related working force to the deuteron in an assumed model was calculated.

Because the force of a deuteron in the MFL under 10 T is too small compared to the Coulomb force in the region, it is difficult for the positively charged particle to have a chance to go through the aperture of the Coulomb energy barrier near the boundary region of NSTC. It appears that the magnetic field effects would not have enough impact on tunneling through the Coulomb barrier as they are too weak, although the detailed calculation is necessary to evaluate the tunnel effect.

A more advantageous circumstance should be prepared to ensure the success of this experiment whereby the desorbed nucleus has a matching force to go through the aperture of the Coulomb energy barrier.

Acknowledgements

References

[1]   T. Asami, G. Giorgi and K. Yamashita and P. Belanzoni, Study on the phenomenon reported "neutron generation at room temperature in a cylinder packed with titanium shavings and pressurized deuterium gas"(3), *J. Condensed Matter Nucl. Sci.* 18 (2016) 24–35.

[2]   T. Asami and N. Sano, Study on the phenomenon reported "neutron generation at room temperature in a cylinder packed with titanium shavings and pressurized deuterium gas"(2) *J. Condensed Matter Nucl. Sci.* 9 (2012) 1–9.

[3]   http://wakariyasui.sakura.ne.jp/p/elec/ro-renn/jibakadenn.html

[4]   H.O. Menlove, M.M. Fowler, E. Garcia, A. Mayer, M.C. Miller, R.R. Ryan and S.E. Jones, Highlights of papers presented at the workshop on cold fusion phenomena, The Measurement of Neutron Emissions from Ti plus D_2 Gas , Santa Fe, New Mexico, May 23–25, 1989, p. 13.

[5]   Mikio Tamura, Physical chemistry (Buturikagaku), Shibundo Co. Ltd., Tokyo, Japan, February 20, 1957, p. 94.

[6]   G. Giorgi, P. Belanzoni, T. Asami and K. Yamashita, Neutron generation via the mechanism adsorption of pressurized deuterium on an electron deficient titanium matrix. An MD-DFT combined analysis on the mechanism of the Ti–D bond formation, *Int. J. Hydrogen Energy* 37 (2012) 18959–18971.

[7]   A. Takahashi, Physics of cold fusion by TSC theory, *J. Phys. Sci. Application* 3(3) (2013) 191–198.

[8]   A. Takahashi, Brief Review of CCF/TSC Theory, Presentation, June 2018, Leading the Japanese Gvt. NEDO project on anomalous heat effect of nano-metal and hydrogen gas interaction. https://www.researchgate.net/project/Leading-the-Japanese-Gvt-NEDO-project-on-anomalous-heat-effect-of-nano-metal-and-hydrogen-gas-interaction.
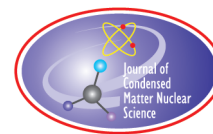
Research Article

Plasmonic Field Enhancement on Planar Metal Surfaces for Condensed Matter Nuclear Fusion

Katsuaki Tanabe*

Department of Chemical Engineering, Kyoto University, Kyoto, Japan

Abstract

The enhancement of electromagnetic field energy density around planar metal/dielectric interfaces has been quantitatively investigated. We have found that a certain degree of enhancement is available for Pd, Ni, and Ti, which are commonly used in the field of condensed-matter nuclear fusion. Our results indicate that this electromagnetic boosting effect may have been unknowingly produced in the experiments reported so far, particularly for the electrolysis-type ones. Importantly, this plasmonic enhancement occurs in the case of an optical-power incidence as well as an electric-bias application. It is therefore important to design and optimize the experimental systems, including the choice of materials, structures, and operating conditions, while accounting for the plasmonic energy enhancement effect around the metal surfaces.

1. Introduction

The power density supplied to deuterium–metal systems may be one of the key factors that activate the condensed-matter nuclear fusion reaction. Free electrons in metals, particularly around metallic surfaces or interfaces with dielectric media, exhibit strong interaction with electromagnetic fields or light in a form of collective oscillation, named *surface plasmons* [1–7]. We previously proposed and analyzed the electromagnetic energy focusing effect around metal nanoparticles and nanoshells that significantly increases the reaction probability [8]. In the present work, we show quantitatively that such plasmonic field enhancement is exerted also on planar metal surfaces.

2. Calculation Methods

We calculate the field enhancement factors, which are the intensity ratios of the fields around the object to those in the absence of the object (metals in this case), or the original incident fields, for planer metals in D_2 (or vacuum) and D_2O. These calculations, which are based on the classical electromagnetic field theory, show quantitatively how much

---

*E-mail: tanabe@cheme.kyoto-u.ac.jp.
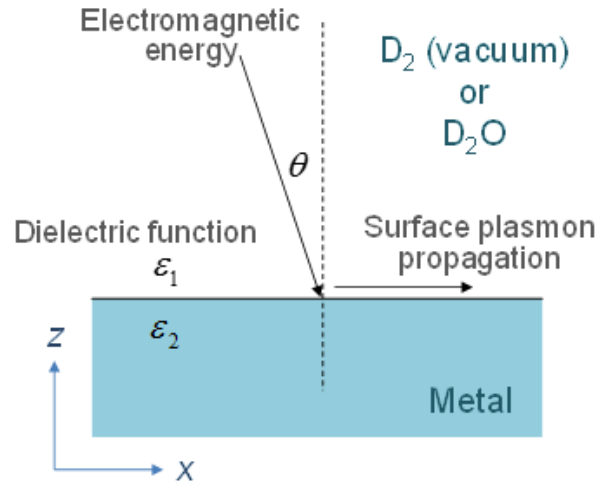
Figure 1. Schematic spatial cross-sectional view of the material system considered in this study for the calculations of field enhancement factors.

energy can be concentrated from the incident optical or electric power. The empirical complex dielectric functions of metals and of the surroundings on frequencies listed in References [9,10] are used for the computation in this paper. The dielectric functions of D_2 (or vacuum) and D_2O were assumed equal to those of the air and H_2O, respectively. We adopted the scheme to derive the maximum field enhancement described in [11]. Removing the noble-metal approximation in [11], as described in detail in the following, we have fully calculated the field enhancement factors for the metals of Pd [12–15], Ni [16–18], and Ti [13,14,19], which are commonly used in the community of condensed-matter fusion.

Figure 1 shows a schematic cross-sectional view of the system under consideration. Let ε_1 and ε_2 be the frequency-dependent complex permittivities or dielectric functions of the surrounding medium and the metal, respectively. θ is the incident angle. We assume an incidence of a p-polarized plane wave as the original electromagnetic field and its coupling into a surface-plasmon mode to determine the maximum field enhancement factors. Following the procedure described in [11], the energy flux towards the x direction per unit length in the y direction (i.e., the Poynting vector) can be formulated as

$$P_{SP} = \frac{c}{8\pi} \int_{-\infty}^{\infty} \mathrm{Re}\left(\vec{E}_{SP} \times \vec{H}_{SP}^*\right) \cdot \hat{x} n \, \mathrm{d}z = \frac{\omega \varepsilon_1}{16\pi} \frac{\left|\vec{E}_{SP}\left(0^+\right)\right|^2}{|q_1|^2 + |k_{SP}|^2} \mathrm{Re}\left\{ \frac{k_{SP}\left(\varepsilon_1 q_1' + \varepsilon_2 q_2'\right)}{\varepsilon_2 q_1' q_2'} \right\}, \tag{1}$$

where c is the speed of light, $\vec{E}_{SP}$ and $\vec{H}_{SP}$ are the electric and magnetic fields of the surface-plasmon mode:

$$\begin{aligned} \vec{H}_{SP} &= H_y \hat{y} \exp\left\{i\left(k_{SP}x - \omega t\right) - q_1 z\right\}, \quad z > 0 \\ &= H_y \hat{y} \exp\left\{i\left(k_{SP}x - \omega t\right) + q_2 z\right\}, \quad z < 0, \end{aligned} \tag{2}$$

$$\begin{aligned} \vec{E}_{SP} &= \frac{c}{\varepsilon_1 \omega} H_y \left(iq_1 \hat{x} - k_{SP}\hat{z}\right) \exp\left\{i\left(k_{SP}x - \omega t\right) - q_1 z\right\}, \quad z > 0 \\ &= \frac{c}{\varepsilon_2 \omega} H_y \left(-iq_2 \hat{x} - k_{SP}\hat{z}\right) \exp\left\{i\left(k_{SP}x - \omega t\right) + q_2 z\right\}, \quad z < 0. \end{aligned} \tag{3}$$

H_y is the amplitude of the magnetic field of the mode. $\vec{E}_{SP}(0^+)$ is the electric field at the metal surface. ω is the frequency of the field. q_1 and q_2 are the complex wave vectors in the z-direction in the surrounding medium and the metal, respectively. k_{SP} is the complex wave vector of the surface-plasmon mode in the x-direction. The wave vectors are calculated by

$$q_j = \frac{\omega}{c}\left(\frac{-\varepsilon_j^2}{\varepsilon_1 + \varepsilon_2}\right)^{1/2} \quad (j = 1, 2), \tag{4}$$

$$k_{SP} = \frac{\omega}{c}\left(\frac{\varepsilon_1 \varepsilon_2}{\varepsilon_1 + \varepsilon_2}\right)^{1/2}. \tag{5}$$

The real and imaginary parts of complex quantities are indicated by primes and double primes, respectively. The energy dissipation flux of the surface plasmon mode is then

$$-\frac{dP_{SP}}{dx} = \alpha P_{SP} = 2k_{SP}" P_{SP} = \frac{\omega \varepsilon_1}{8\pi} k_{SP}" \frac{\left|\vec{E}_{SP}(0^+)\right|^2}{|q_1|^2 + |k_{SP}|^2} \mathrm{Re}\left\{\frac{k_{SP}(\varepsilon_1 q_1' + \varepsilon_2 q_2')}{\varepsilon_2 q_1' q_2'}\right\}, \tag{6}$$

where α is the absorption constant. On the other hand, the energy flux provided into the metal surface by the coupling of the external field into the surface-plasmon mode can be written as

$$\frac{c}{8\pi}\varepsilon_1^{1/2}\cos\theta\left|\vec{E}_0\right|^2(1-R), \tag{7}$$

where $\vec{E}_0$ is the electric field of the incident wave, or namely the external field. R is the reflectivity at the metal surface. In the steady state, those two energy fluxes are equal to each other based on the conservation of energy, and therefore

$$\frac{\omega \varepsilon_1}{8\pi} k_{SP}" \frac{\left|\vec{E}_{SP}(0^+)\right|^2}{|q_1|^2 + |k_{SP}|^2} \mathrm{Re}\left\{\frac{k_{SP}(\varepsilon_1 q_1' + \varepsilon_2 q_2')}{\varepsilon_2 q_1' q_2'}\right\} = \frac{c}{8\pi}\varepsilon_1^{1/2}\cos\theta\left|\vec{E}_0\right|^2(1-R). \tag{8}$$

We come to derive the field enhancement factor this way:

$$\eta \equiv \frac{\left|\vec{E}_{SP}(0^+)\right|^2}{\left|\vec{E}_0\right|^2} = \frac{c\left(|q_1|^2 + |k_{SP}|^2\right)\cos\theta(1-R)}{\omega \varepsilon_1^{1/2} k_{SP}'' \mathrm{Re}\left\{\frac{k_{SP}(\varepsilon_1 q_1' + \varepsilon_2 q_2')}{\varepsilon_2 q_1' q_2'}\right\}}. \tag{9}$$

Note that this field enhancement factor is defined as the ratio of field *intensities* and not field *magnitudes*. Weber and Ford used an approximation $\varepsilon_2'' \ll -\varepsilon_2'$. They rationalized this approximation by the non-lossy nature of the noble metals, which were the only materials they dealt with in [11], so they ended up with a much simpler formula. In contrast, we fully calculate the enhancement factors as Eq. (9) removing the approximation to properly deal with the relatively lossy metals in this study. It should be noted that our calculation is only based on the Maxwell equations and involves nothing exotic or physically novel.
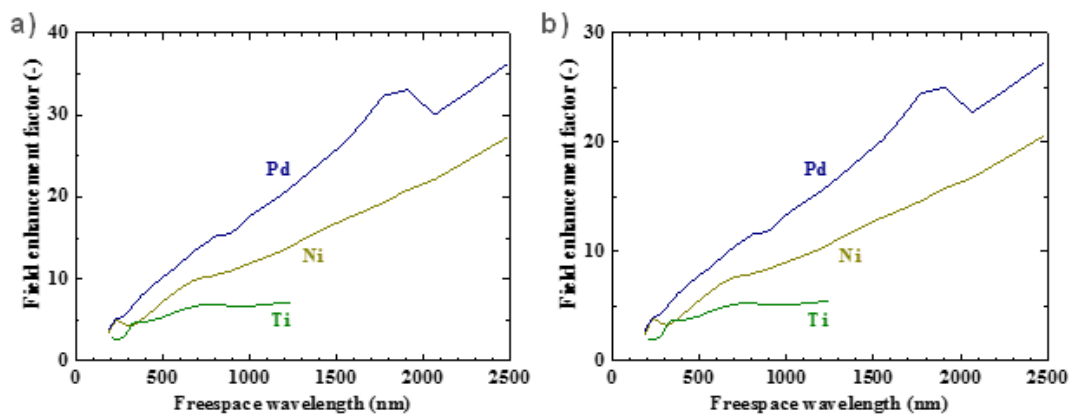
Figure 2. Electromagnetic field enhancement factors on planar Pd, Ni, and Ti surfaces in (a) D_2/vacuum and (b) D_2O.

3. Results and Discussion

Figure 2 shows the calculated spectra of field enhancement factors at the metal surfaces of Pd, Ni, and Ti, which have been conventionally used for deuterium-containing fuel materials in the field of condensed-matter nuclear fusion, in D_2 or vacuum (Fig. 2(a)) and D_2O (Fig. 2(b)). We assumed normal incidence ($\theta = 0$) and perfect coupling of the external field into the surface-plasmon mode ($R = 0$) to determine the maximum possible enhancement in this calculation. Local energy enhancement of a certain degree is seen in the spectra. The metal surfaces can this way concentrate optical or electromagnetic energy in their vicinity. Among all metal elements, Al and the noble metals Ag, Au, and Cu are known to exhibit distinctively higher field enhancement factors than other metals, due to their high conductivity [10,11,20]. A certain level of field enhancement, however, is still attainable even for the metals commonly used for condensed-matter fusion, as seen in Fig. 2. Importantly, a certain number of the electrolysis-type condensed-matter nuclear fusion experiments reported so far may actually have unknowingly benefited from this plasmonic local energy enhancement effect. If the spatial density of the reactive sites and the nuclear-reaction probability had been sufficiently high, the fuel samples would have been highly energy-absorptive and thus the given incident energy would have been almost perfectly absorbed and converted for the reaction excitation, and therefore the electromagnetic enhancement effect we present in this work would have hardly contributed to the nuclear-reaction rate. In reality, however, the situation seen in many experimental reports in the community is likely the very opposite, and therefore the enhancement of the supplied energy density around the nuclear-reaction sites would increase the reaction rates by providing a larger opportunity and a larger amount of energy to be absorbed and then utilized for the excitation.

It should be noted that coupling of incident electromagnetic or optical energy into surface-plasmon modes does not occur at perfectly smooth metal surfaces. In this case, there is no enhancement of the electromagnetic energy, because of the extremely large reflectivity at the metal surface. Surface structures with scales smaller than the wavelength of the external or incident fields are required for efficient plasmon coupling to induce the enhancement effect [1,3,21–24]. The surface structure is not necessarily periodic, but random roughness can also generate surface plasmons [1,25,26]. The possibility of the existence of intrinsic micro/nanoscale roughness or roughness induced in the electrolysis processes on metal surfaces in the past experimental works is easily assumed. It is therefore supposed that there is still some surface-plasmon electromagnetic enhancement effect even for the metal plate samples, not to mention for the metal samples with micro/nanostructures with the abovementioned plasmon-coupling mechanism. It is highly possible

that the reason many of the successful experimental reports have used samples with micro/nanostructures [18,27–30] is partly attributed to the plasmonic enhancement effect. Another evidence for this speculative plasmonic boosting effect is that there have been a number of successful experimental reports with the application of alternative or modulated electrical bias rather than stationary field [31–33], which may have unknowingly excited the surface-plasmon oscillation. Incidentally, we believe that the plasmonic enhancement effect, assuming it exists, is not the sole clue to solve the mystery of the energy supplied to overcome the gigantic Coulomb barrier to produce the fusion reaction observed with visible rates. But it is one of the multiple factors not yet understood, which researchers may have applied without realizing to multiply the chance of a reaction resulting in the production of anomalous experimental outcomes such as excess heat [12,16–18,27–30,33,34], radiation [12–14,19,32], and elemental transmutation [15,34,35].

The electromagnetic model studied in this work can be a useful tool for the improvement of experimental systems, including the sample material structures, in the condensed-matter fusion field. This sort of numerical model, incidentally, is flexible and simple to connect to other models, and may be included in a comprehensive model by combining with transport and reaction submodels [36], for instance. The size aspect of the metal surface structures should also be accounted for the optimizing design of the deuterium-containing metal composite materials used for condensed-matter fusion, because of the scale-dependent bandwidth of plasmon resonance, surface scattering or radiative loss, and electrodynamic damping, as discussed in [8]. The enhancement approach presented in this study may enable fusion with significantly lower deuterium loading than reported so far [37,38]. Note that this plasmonic energy focusing scheme is applicable not only for the conventional electrolysis-type condensed-matter fusion but also with additional optical excitation sources such as lasers, since the electromagnetic field enhancement is equivalent for both systems.

4. Conclusion

In this work, we have quantitatively investigated the enhancement of electromagnetic field energy density around planar metal/dielectric interfaces. We have shown that the metals of Pd, Ni, and Ti commonly used in the field of condensed-matter fusion research intrinsically exhibit a certain degree of field enhancement, not only for their particulate form, but also for plates. Our results indicate that this electromagnetic boosting effect may have been unknowingly produced in the experiments reported so far, particularly for the electrolysis-type ones. Importantly, this plasmonic enhancement occurs in the case of an optical-power incidence as well as an electric-bias application. It is therefore important to design and optimize the experimental systems, including the choice of materials, structures, and operating conditions, while accounting for the plasmonic energy enhancement effect around gas-, vacuum-, or liquid-metal interfaces.

Acknowledgement

References

[1]   H. Raether, *Surface Plasmons on Smooth and Rough Surfaces and on Gratings*, Springer, Berlin, 1988.
[2]   S. Nie and S.R. Emory, *Science* **275** (1997) 1102.
[3]   T.W. Ebbesen, H.J. Lezec, H.F. Ghaemi, T. Thio and P.A. Wolff, *Nature* **391** (1998) 667.
[4]   P. Andrew and W.L. Barnes, *Science* **306** (2004) 1002.
[5]   K. Nakayama, K. Tanabe and H.A. Atwater, *Appl. Phys. Lett.* **93** (2008) 121904.
[6]   J.A. Schuller, E.S. Barnard, W. Cai, Y.C. Jun, J.S. White and M.L. Brongersma, *Nat. Mater.* **9** (2010) 193.
[7]   K. Tanabe, *Nanoscale Res. Lett.* **11** (2016) 236.
[8]   K. Tanabe, *J. Cond. Matter Nucl. Sci.* **24** (2017) 296.
[9]   E.D. Palik (Ed.), *Handbook of Optical Constants of Solids*, Academic Press, Orland, 1985.

[10] K. Tanabe, *J. Phys. Chem. C* **112** (2008) 15721.

[11] W.H. Weber and G.W. Ford, *Opt. Lett.* **6** (1981) 122.

[12] M. Fleischmann, S. Pons and M. Hawkins, *J. Electroanal. Chem.* **261** (1989) 301.

[13] S.E. Jones, E.P. Palmer, J.B. Czirr, D.L. Decker, G.L. Jensen, J.M. Thorne, S.F. Taylor and J. Rafelski, *Nature* **338** (1989) 737.

[14] K.L. Wolf, N.J.C. Packham, D. Lawson, J. Shoemaker, F. Cheng and J.C. Wass, *J. Fusion Ener.* **9** (1990) 105.

[15] Y. Iwamura, M. Sakano and T. Itoh, *Jpn. J. Appl. Phys.* **41** (2002) 4642.

[16] R.L. Mills and S.P. Kneizys, *Fusion Technol.* **20** (1991) 65.

[17] S. Focardi, R. Habel and F. Piantelli, *Nuovo Cimento* **107A** (1994) 163.

[18] A. Kitamura, A. Takahashi, K. Takahashi, R. Seto, Y. Matsuda, Y. Iwamura, T. Itoh, J. Kasagi, M. Nakamura, M. Uchimura, H. Takahashi, T. Hioki, T. Motohiro, Y. Furuyama and M. Kishida, *J. Cond. Matter Nucl. Sci.* **24** (2017) 202.

[19] A. De Ninno, A. Frattolillo, G. Lollobattista, L. Martinis, M. Martone, L. Mori, S. Podda and F. Scaramuzzi, *Europhys. Lett.* **9** (1989) 221.

[20] K. Tanabe, *Jpn. J. Appl. Phys.* **55** (2016) 08RG01.

[21] C.E. Wheeler, E.T. Arakawa and R.H. Ritchie, *Phys. Rev. B* **13** (1976) 2372.

[22] J.B. Pendry, L. Martin-Moreno and F.J. Garcia-Vidal, *Science* **305** (2004) 847.

[23] P. Lalanne and J.P. Hugonin, *Nat. Phys.* **2** (2006) 551.

[24] D. Pacifici, H.J. Lezec, L.A. Sweatlock, R.J. Walters and H.A. Atwater, *Opt. Express* **16** (2008) 9222.

[25] F. Toigo, A. Marvin, V. Celli and N.R. Hill, *Phys. Rev. B* **15** (1977) 5618.

[26] K. Arya, Z.B. Su and J.L. Birman, *Phys. Rev. Lett.* **54** (1985) 1559.

[27] Y. Arata and Y. Zhang, *Jpn. J. Appl. Phys.* **37** (1998) L1274.

[28] G.H. Miley, X. Yang, K. Kim, E. Ziehm, T. Patel, B. Stunkard, A. Ousouf and H. Hora, *J. Cond. Matter Nucl. Sci.* **13** (2014) 411.

[29] M. Swartz, G. Verner, J. Tolleson, L. Wright, R. Goldbaum and P. Hagelstein, *J. Cond. Matter Nucl. Sci.* **15** (2015) 66.

[30] U. Mastromatteo, A. Bertele and F. Celani, *J. Cond. Matter Nucl. Sci.* **15** (2015) 240.

[31] J.R. Granada, R.E. Mayer, G. Guido, P.C. Florido, A. Larreteguy, V.H. Gillette, N.E. Patino, J. Converti and S.E. Gomez, *J. Nucl. Sci. Technol.* **27** (1990) 222.

[32] A. Takahashi, T. Takeuchi, T. Iida and M. Watanabe, *J. Nucl. Sci. Technol.* **27** (1990) 663.

[33] T. Mizuno, T. Akimoto, K. Azumi, M. Kitaichi, K. Kurokawa and M. Enyo, *Fusion Technol.* **29** (1996) 385.

[34] T. Ohmori, M. Enyo, T. Mizuno, Y. Nodasaka and H. Minagawa, *Fusion Technol.* **31** (1997) 210.

[35] T. Hioki, N. Takahashi, S. Kosaka, T. Nishi, H. Azuma, S. Hibi, Y. Higuchi, A. Murase and T. Motohiro, *Jpn. J. Appl. Phys.* **52** (2013) 107301.

[36] K. Tanabe, *Heliyon* **2** (2016) e00057.

[37] E. Storms, *Fusion Technol.* **20** (1991) 433.

[38] M.C.H. McKubre and F.L. Tanzella, *J. Cond. Matter Nucl. Sci.* **4** (2011) 32.